



UNIVERSITY OF
LIVERPOOL

Synthesis of new lithium ion conductors

Thesis submitted in accordance with the requirements
of the University of Liverpool for the
degree of Doctor in Philosophy
by
Leopoldo Enciso Maldonado

January 2017

This page is intentionally left blank

Abstract

Synthesis of new lithium ion conductors

Leopoldo Enciso Maldonado

This thesis reports the synthesis and characterisation of a number of new Li-ion conductors with olivine and NASICON structure types. The new materials have been characterised by chemical analysis, diffraction and spectroscopy in order to establish relationships between the Li-ion conductivity and the crystal structure.

The thesis starts describing Li-ion battery technology. The role of ceramic materials in battery development is highlighted and some of the state-of-the-art materials are introduced. The battery failure mechanism and fire risk are examined. Then defect chemistry and ionic conduction are presented to end with a literature review on families of Li-ion conductors indicating their conductivities and crystallographic features. The experimental techniques used throughout the thesis for the synthesis and characterisation of the new materials are also introduced.

A large fraction of the work in the thesis focuses on the olivine-type structure of general composition LiMPO_4 with M a 2+ cation. The main strategy developed in these chapters was the aliovalent substitution on M site in order to introduce Li-vacancies in the Li-ion diffusion pathways of the structure. A number of new modifications are reported, mainly based on the olivine material LiMgPO_4 . These series follow Vegard's law up to a doping limit after which a plateau is reached. The impurity phases that appear in the plateau have been determined. In general, the synthesis of these new materials have needed higher temperatures than the parent phases, highlighting in this way the role of the entropy of mixing in this type of modification. Li-ion conductivity derived from AC impedance measurements are presented for some of the new samples.

The rest of the work in the thesis is on the NASICON-type structure. A number of Li-ion analogues related to $\text{LiTaAl(PO}_4)_3$ have been investigated. The role of Li and P excess in the distortion of the unit cell has been studied with X-ray diffraction. For one of the related analogues, its phase diagram has been explored in a search for new Li-ion conductors with the NASICON-type structure. Densification methods to enable conductivity measurements have also been developed. Finally, Li-ion conductivity has been determined by AC impedance spectroscopy on a number of new phases. A summary chapter at the end of the thesis summarises the work and highlights the main conclusions and future directions.

This page is intentionally left blank

Acknowledgements

Firstly I am immensely grateful to my supervisor Professor Matthew J Rosseinsky for giving me the excellent opportunity to undertake my PhD in his research group and sending me away to diffraction schools and conferences in the UK, France and Italy. It has been a privilege to be a member of his group. His wise advice has contributed to make me a better researcher. I am also grateful to my secondary supervisor Dr John B Claridge for all his good ideas and helpful teaching.

I would like to thank all the mentors during my PhD for their guidance and help.

I thank the research coordinators of the group for their continuous input and for proofreading the chapters of this thesis.

I am very thankful to all the people who I have worked with over the years, in particular those from the MJR group, for their contributions from which I have learned and improved a number of skills.

Thanks also go to all the instrument scientists and staff at Diamond Light Source and ISIS Neutron Source at Harwell campus for their assistance during the diffraction experiments.

Finally I wish to thank my family and friends who have supported me during my time at the University of Liverpool.

This page is intentionally left blank

Contents

Abstract.....	iii
Acknowledgements.....	v
Contents.....	vii
1. Chapter 1: Introduction	1
1.1 Batteries.....	2
1.1.1 Definitions.....	2
1.1.2 Development.....	4
1.1.3 Structure	4
1.1.3.1 Anode.....	5
1.1.3.2 Cathode.....	7
1.1.3.3 Electrolyte	9
1.1.3.4 Separators.....	10
1.1.3.5 Solid electrolyte interphase	11
1.1.3.6 Current collectors.....	11
1.1.4 Operation	12
1.1.5 Cell voltage.....	13
1.1.6 Failure mechanism	14
1.1.7 Fire risk.....	15
1.2 Li-ion conductivity.....	17
1.2.1 Electrical conductivity	17
1.2.2 Li-ion transport number.....	18
1.2.3 Crystallographic defects.....	19
1.2.4 Ionic conductivity	22
1.2.5 Ionic conduction mechanism	24
1.2.6 Dimensionality of ionic conductors	26
1.3 Families of Li-ion conductors	27
1.3.1 Early Li-ion conductors.....	27
1.3.2 NASICON analogues	29
1.3.3 LISICON.....	31
1.3.4 Thio-LISICON and related phases.....	33
1.3.5 Garnets.....	35
1.3.6 Perovskites.....	36
1.3.7 Argyrodite	38

1.3.8	Olivines.....	40
1.4	Aims of the thesis.....	42
1.5	References	43
2.	Chapter 2: Experimental techniques	51
2.1	Synthetic methods	51
2.1.1	Solid state route.....	51
2.1.2	Pelletising and Pressing.....	52
2.1.3	Buffer pellets.....	53
2.1.4	Planetary mill	53
2.1.5	Furnaces	54
2.1.6	Gas flow synthesis.....	55
2.1.7	Cold isostatic press.....	55
2.2	Crystallography	56
2.2.1	Crystal structures and unit cells.....	56
2.2.2	Translational symmetry and crystal systems	56
2.2.3	Centring of the unit cell and Bravais lattices	57
2.2.4	Atomic positions and symmetry elements	57
2.2.5	Space groups and Wyckoff symbols.....	57
2.2.6	Electron and nuclear densities.....	58
2.3	Diffraction	58
2.3.1	Bragg's law	58
2.3.2	Scattering factors and thermal displacement parameters	59
2.3.3	Absorption.....	61
2.3.4	Structure factors	61
2.3.5	Laboratory instruments	62
2.3.6	Synchrotron.....	63
2.3.7	Neutron diffraction	64
2.3.8	Time-of-flight powder diffractometers.....	65
2.3.8.1	POLARIS.....	66
2.3.8.2	GEM.....	67
2.3.9	Refinements	67
2.3.9.1	Single profile fitting.....	67
2.3.9.2	Pawley refinements	68
2.3.9.3	Rietveld refinements.....	68
2.3.9.4	Criteria of fit	69
2.3.9.5	Errors.....	70

2.3.9.6	Constraints	70
2.3.9.7	Peak shapes.....	70
2.3.9.8	Peak widths	71
2.3.9.9	Multi-histogram refinements.....	71
2.3.10	Indexing.....	72
2.3.11	Direct methods.....	72
2.4	Inductively coupled plasma - optical emission spectroscopy	73
2.5	Fourier transform infrared spectroscopy.....	73
2.6	Electron microscopy.....	74
2.6.1	Transmission electron microscope - energy dispersive X-ray analysis 74	
2.7	Thermogravimetric analysis	74
2.8	AC impedance spectroscopy	75
2.8.1	Electrode preparation	75
2.8.2	Sample environments	77
2.8.3	Instruments.....	78
2.8.4	Impedance measurements	78
2.8.5	Electro-active elements	79
2.9	Density functional theory	81
2.10	Solid state nuclear magnetic resonance	81
2.11	References	82
3.	Chapter 3: New olivine materials.....	85
3.1	Introduction	85
3.2	Density functional theory calculations	90
3.3	The parent material LiMgPO_4	91
3.3.1	Synthesis	91
3.3.2	Characterisation.....	93
3.4	In-doped series.....	98
3.4.1	Synthesis	98
3.4.2	Chemical analysis	103
3.4.3	Diffraction and refinements.....	104
3.4.4	Densification	112
3.4.5	Conductivity measurements	114
3.4.6	NMR	125
3.5	Sc-doped series	127
3.5.1	Synthesis	127

3.6	Ga-doped series	131
3.6.1	Synthesis	131
3.7	In, Ga co-doping series.....	133
3.7.1	Synthesis	133
3.8	In, Li co-doping series.....	134
3.8.1	Synthesis	134
3.9	Zr-doping trials.....	137
3.9.1	Synthesis	137
3.10	Mg-doped series	142
3.10.1	Synthesis	142
3.10.2	Densification	144
3.10.3	Conductivity measurements	145
3.11	Summary and Conclusions	149
3.12	Appendix 3.1: TEM-EDX spectra of Olivine samples.....	152
3.12.1	Sample of nominal composition $\text{Li}_{0.9}\text{Mg}_{0.9}\text{In}_{0.1}\text{PO}_4$	152
3.12.2	Sample of nominal composition ${}^7\text{Li}_{0.9}\text{Mg}_{0.9}\text{In}_{0.1}\text{PO}_4$	155
3.13	References	158
4.	Chapter 4: New olivine cathode materials.....	161
4.1	Introduction	161
4.2	Parent LiFePO_4	164
4.2.1	Finding a suitable reaction and setup.....	164
4.2.2	Optimised synthesis of the parent LiFePO_4	165
4.2.3	Diffraction and refinements.....	166
4.2.3.1	Ordered model at room temperature for LiFePO_4	166
4.2.3.2	Testing the model: cation occupancy and Li-Fe anti site defects 168	
4.3	In-doped series.....	171
4.3.1	Finding the right temperature for the synthesis.....	171
4.3.2	Optimised Synthesis of the In-doped series	173
4.3.3	Diffraction and refinements.....	176
4.3.3.1	Ordered model at room temperature for $\text{Li}_{0.92}\text{Fe}_{0.92}\text{In}_{0.08}\text{PO}_4$...	176
4.3.3.2	Ordered model at room temperature for $\text{Li}_{0.96}\text{Fe}_{0.96}\text{In}_{0.04}\text{PO}_4$...	182
4.3.3.3	Variable temperature diffraction for $\text{Li}_{0.92}\text{Fe}_{0.92}\text{In}_{0.08}\text{PO}_4$	183
4.3.3.4	Refined occupancies at room temperature	185
4.3.3.5	Graphic representation of the ADPs	185
4.3.3.6	Table of structural parameters for all combined refinements .	187

4.3.3.7	Structure solution of $\text{LiFeIn}(\text{PO}_4)_2$ and $\text{LiMgIn}(\text{PO}_4)_2$	189
4.4	ICP-OES.....	195
4.5	FTIR-ATR.....	195
4.6	Cathode testing.....	196
4.7	Summary, conclusions and future work	201
4.8	References	204
5.	Chapter 5: New NASICON analogue materials.....	207
5.1	Introduction	207
5.1.1	From the NASICON-type structure to the lithium analogues	207
5.1.2	Polymorphism	210
5.1.3	The Li sites in the α -polymorph	212
5.1.4	Opportunities for variation	213
5.1.5	Other considerations	214
5.1.6	Exploring anisotropic strain and structural distortion as potential enhancers of conductivity in $\text{LiTaAl}(\text{PO}_4)_3$ related samples.....	215
5.1.7	Calcium doping of $\text{LiTaAl}(\text{PO}_4)_3$ related samples.....	216
5.1.8	New combinations of elements that retain the NASICON-type structure: Ta-Mg-Ga.....	217
5.2	Anisotropic strain and ionic conductivity in $\text{LiTaAl}(\text{PO}_4)_3$ related samples 219	
5.2.1	Synthesis	219
5.2.1.1	Revisiting the selected composition	219
5.2.1.2	Scaling up selected samples.....	227
5.2.2	TEM-EDX.....	228
5.2.3	Diffraction and refinements.....	230
5.2.4	Densification	232
5.2.5	Conductivity of $\text{Li}_{0.925}\text{Ta}_{1.062}\text{Al}_{0.938}\text{P}_{3.16}\text{O}_{12+x}$ sintered at 900 °C and 1000 °C	234
5.3	Li-Ta-Ca-Al-P-O series constrained to $\text{Li}_{2x}[\text{Ta}_{1.55-x}\text{Ca}_{0.11}\text{Al}_{0.33+x}](\text{PO}_4)_3$	238
5.3.1	Synthesis	238
5.3.1.1	Samples of $\text{Li}_{1.55}\text{Ta}_{0.78}\text{Ca}_{0.11}\text{Al}_{1.11}\text{P}_3\text{O}_{12}$ with a range of P excess	238
5.3.1.2	$\text{Ca}_{0.11}$ line exploration.....	242
5.3.1.3	Scaled up sample	245
5.3.2	TEM-EDX.....	247
5.3.3	Diffraction and refinements.....	249
5.3.4	Densification	252
5.3.5	Conductivity of $\text{Li}_{0.734}\text{Ta}_{1.187}\text{Ca}_{0.108}\text{Al}_{0.705}\text{P}_3\text{O}_{12}$ sintered at 1100 °C	256

5.4	Li-Ta-Ga-Mg-P-O series	261
5.4.1	Synthesis	261
5.4.2	Diffraction and refinements.....	270
5.4.3	Densification	272
5.4.4	Conductivity of $\text{Li}_{0.6}\text{Ta}_{1.2}\text{Ga}_{0.8}\text{P}_3\text{O}_{12}$ and $\text{Li}_{0.86}\text{Ta}_{1.18}\text{Mg}_{0.22}\text{Ga}_{0.6}\text{P}_3\text{O}_{12}$ 273	
5.5	Summary, conclusions and further work.....	276
5.6	Appendix 5.1: TGA of selected reactants.....	279
5.7	Appendix 5.2: Structure solution of $\text{Ta}_{0.5}\text{Al}_{0.5}\text{P}_2\text{O}_7$	281
5.8	Appendix 5.3: TEM-EDX spectra of NASICON samples.	283
5.8.1	Sample of overall composition $\text{Li}_{0.925}\text{Ta}_{1.062}\text{Al}_{0.938}\text{P}_{3.16}\text{O}_{12+x}$ (sample 1). 283	
5.8.2	Sample of overall composition $\text{Li}_{0.953}\text{Ta}_{1.062}\text{Al}_{0.938}\text{P}_{3.64}\text{O}_{12+x}$ (sample 5). 286	
5.8.3	Ca-doped sample.	289
5.9	References	292
6.	Chapter 6: Summary	295

Chapter 1

Introduction

The development of new ceramic materials with potential application in Li-ion battery technologies is the leitmotiv of this thesis. Therefore the thesis lies in the field of fundamental research where the novelty of the materials along with their property assessment are the major goals.

Ceramic materials have already been very useful during the development of the Li-ion battery. These have ranged from the layered oxide LiCoO_2 to the spinel LiMn_2O_4 and the olivine LiFePO_4 , and have been commonly used as part of the cathode of commercial Li-ion batteries [1].

Ceramic materials are still a promising approach for the substitution of the liquid organic electrolytes currently used for building Li-ion batteries. Removing these organic liquids from the manufacturing of batteries would eliminate the fuel component that feeds the thermal runaway of a battery catching fire [2].

Along with the progressive depletion of fossil fuels, renewable energies will take over the role of energy generation [3]. However renewables are intermittent and therefore large energy storage systems will be needed to enable the success of this technology [4]. It is expected that new materials will support the evolution of the energy production industry during the next few decades [5].

The aim of this thesis is to explore through synthesis the field of new solid state Li-ion conductors in order to discover new materials with potential application mainly as solid state electrolytes. These new materials have been prepared and characterised with a range of techniques that are presented in the second chapter. Chapters three and five will explore new Li-ion conductors with the focus on electrolyte applications while chapter four will focus on a similar approach for cathode applications. Chapter one introduces the work presented in the thesis. This chapter has been organised in four main sections that are described below.

Batteries. Batteries are electrochemical devices for energy storage. The technology is consolidated for portable electronics, growing very fast for electric vehicles [6] and will play an important role in future grid energy distribution [7]. This section explains the basics of the technology and its application. It also introduces the reasons for pursuing the quest of new materials presented in this thesis.

Li-ion conductivity. Li-ion conductivity is one of the limiting properties that enables a material to be used for building Li-ion batteries [8]. This section introduces the term and the underlying physical phenomena that make it important for this thesis.

Families of Li-ion conductors. This section presents a literature review on prominent families of Li-ion conductors with their conductivities, compositions and crystal structures. It also explains which limitations of these materials motivate the research of this thesis.

Aims of the thesis. In this section, the motivations and objectives for this thesis are presented.

1.1 Batteries

Batteries are devices for energy storage and conversion. These devices can work as electrical generators by direct conversion of chemical energy to electricity at the cathode and anode through redox reactions. A charged battery stores chemical energy in the form of electrochemical potential.

1.1.1 Definitions

The discharge is the process in which, after connecting an external circuit or load, favoured redox reactions drive the production of electrical energy. The electrical energy has the form of an electric potential that can be sustained by the electric current supplied from anode to cathode. At the same time as the electrons are supplied to the external circuit, an equivalent charge of ions move from anode to cathode through the electrolyte. The progression of this reaction changes the concentration of carriers at the anode and cathode. When the carrier concentration

at the anode is low and the chemical potential has fallen below usable limits, the battery is said to be discharged.

The charge of a battery can be performed by reversing the previous process of discharge. This can be achieved by connecting an electric generator that is able to pump the carriers from cathode to anode. In this way the battery converts the electric energy supplied by the generator in chemical energy that restores the electrochemical potential of the battery.

In general, the reaction at the anode happens at lower potential than the cathode and that is why it is usually called negative electrode, while the cathode is the positive electrode.

Open circuit voltage, V_{oc} or E , is the electric potential exhibited by the battery when no current is flowing, i.e. in equilibrium.

The state of charge of a battery is the fraction of chemical energy still remaining in the battery compared with the state of full charge (when the V_{oc} is maximum).

Primary batteries are intended for a single use, i.e. after fabrication they can be used until they become exhausted and then they are discarded. These batteries are fabricated in the charged state.

Secondary batteries can be used until exhausted but then they can be restored to the original charged state by an electric current flowing in the opposite direction than during discharge. These batteries are usually fabricated in the discharged state [9].

The energy density of a battery relates to the amount of work that a battery can do per unit volume or unit mass. The power density of a battery is related with how fast this work can be done.

Two of the most remarkable advantages of Li-ion batteries compared to other battery technologies are the high energy density and high power densities. Li-ion batteries are relatively light-weight and allow for relatively fast cycles of charge/discharge.

1.1.2 Development

One early milestone in battery history was the Volta cell in 1782, composed of a stack of zinc and silver disks, which was a primary battery. Later in 1859 Planté invented the cell $\text{PbO}_2/\text{dilute H}_2\text{SO}_4/\text{Pb}$, which was a secondary battery [10]. Between these and the commercialisation of the Li-ion battery in 1991 by Sony there were multiple milestones including technologies such as the Li/LiI/I_2 cell, a primary battery developed for pacemakers [11], or the nickel-cadmium and nickel-metal hydride cells which are secondary batteries [12].

From the several technologies available, this thesis focuses on materials for Li-ion batteries. Reducing the risk of batteries catching fire is one of the main motivations for pursuing the discovery of new Li-ion conductors that could potentially replace the most dangerous component in the battery, the organic liquid electrolyte.

1.1.3 Structure

The Li-ion battery is made of two electrodes, positive and negative, separated by the electrolyte. The two electrodes are connected to the external circuit by metallic current collectors. Each component of the Li-ion battery has a particular function and the materials used will have to meet a set of requirements that are presented below. The schematic structure of a battery can be seen in figure 1.1.

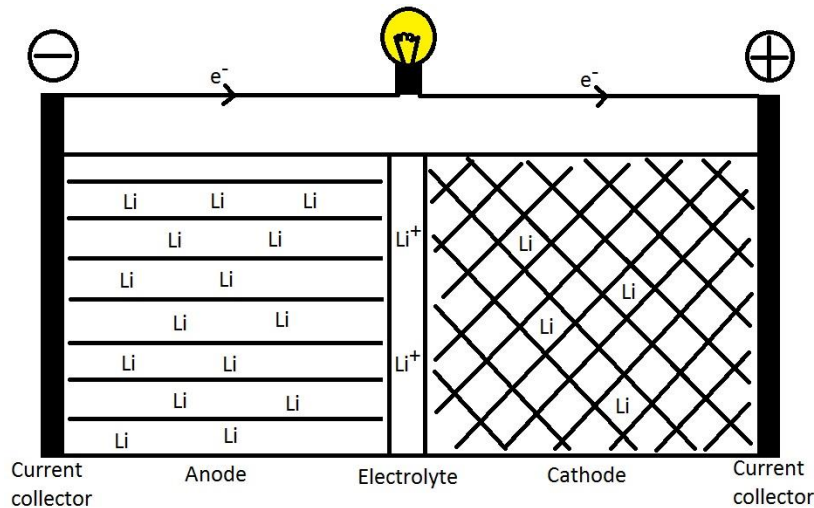


Figure 1.1. Diagram of a battery connected to a bulb. During the discharge of the battery, the Li-ions move from the anode to the cathode through the electrolyte at the same time that the electrons move also from anode to cathode but through the current collectors and the external circuit (cables and bulb).

1.1.3.1 Anode

The anode is a material in contact with the electrolyte and the current collector of the negative terminal of the battery. It has to be chemically stable during charge/discharge and able to reversibly intercalate Li-ions during the normal operation of the battery. It also needs to be a good electronic conductor in order to allow the electrons to flow from/to the current collector to/from the vicinity of the intercalated Li-ions. Therefore anodes have to be mixed ionic-electronic conductors, MIEC.

The anode material can be Li-metal, carbonaceous or ceramic. The electrochemical potential of each of these vs Li/Li⁺ alongside with the electrochemical potential of the cathode material vs Li/Li⁺ determines the potential of the cell. The anode of commercial Li-ion batteries is generally made of a carbonaceous materials such as graphite for the reasons outlined below.

The ideal choice would be Li-metal due to having the largest Li capacity. One of the limitations is the low melting point of Li, 180 °C, which involves safety concerns. The major limitation with Li-metal anodes is that it is impossible to achieve the level

of passivation needed for a safe and durable operation, especially if the battery is operated at high charge rates. The Li deposition at the anode promotes volume changes that continuously degrade the passivation layer by dendrite formation. The dendrites are then passivated again, consuming more electrolyte in the process. Electrolyte depletion along with internal short due to dendrites reaching the cathode are two important drawbacks of this cell configuration. Because of that other materials are used as anodes.

Graphite has an electrochemical potential close to Li/Li^+ , about 0.1 V vs Li/Li^+ [13]. This allow to take advantage of most of the electrochemical potential of the cathode. For a fixed amount of charge transfer, the higher the V_{oc} the higher the energy. On the other hand, the change in volume for graphite anodes is small enough for allowing the passivation layer to remain stable during normal operation conditions [14]. This along with the low potential of Li insertion in graphite vs Li/Li^+ has made of the "rocking chair" battery concept [15] a commercial success.

A ceramic material that would be a safer alternative to graphite is the spinel $\text{Li}_4\text{Ti}_5\text{O}_{12}$, $\text{Li}_3[\text{LiTi}_5]\text{O}_{12}$, which intercalates Li up to the ordered rock salt $\text{Li}_7\text{Ti}_5\text{O}_{12}$. It has a very flat electrochemical potential of 1.55 V vs Li/Li^+ due to the two phases redox reaction [16]. It also forms much less solid electrolyte interphase than graphite due to having an electrochemical potential that lies within the stability window of common organic liquid electrolytes. This allows higher charging rates, even at low temperatures, with no Li plating, which also contributes to the safety of the cell. In addition it is subject to lower mechanical stress than graphite during cycling due to its "zero strain" property with only 0.2 % volume change.

One drawback of the cells made with $\text{Li}_4\text{Ti}_5\text{O}_{12}$ is the lower energy density with respect to cells made with graphite. This is due to the lower specific capacity of the spinel and also because the resulting open circuit voltage of the cell is lower than with graphite, e.g. for a cell with LiCoO_2 cathode the V_{oc} would be about 2.4 V when using $\text{Li}_4\text{Ti}_5\text{O}_{12}$ anode and not 3.7 V as is the case for graphite. This represents about a 30 % energy loss for cells of the same capacity. $\text{Li}_4\text{Ti}_5\text{O}_{12}$ can also exhibit release of the gasses H_2 , CO_2 and CO due to reaction with the electrolyte upon cycling [17].

There are other anode materials, such as silicon, but due to different reasons graphite remains as the anode of choice for commercial cells.

1.1.3.2 Cathode

The cathode is the analogue material to the anode in the positive half of the battery. It is in contact with the positive current collector and the electrolyte and therefore has to be chemically stable during normal charge and discharge of the battery, including structural stability in the Li intercalation ranges used [18]. It needs to have good ionic and electronic conductivities and therefore has to be again a mixed ionic-electronic conductor. The cathodes of commercial Li-ion batteries are generally made of ceramic materials in the form of Li-containing transition metal oxides such as LiCoO_2 or LiMn_2O_4 . These electrochemically active material make a composite with an electronically conducting material and a binder. The composite is then cast on the current collector to build the cell [19].

LiCoO_2 has higher cycle life than LiNiO_2 or LiMn_2O_4 [20]. For LiCoO_2 the lowest reversible delithiation is up to $\text{Li}_{0.5}\text{CoO}_2$ [21]. If the cell is overcharged and the delithiation goes beyond, LiCoO_2 transforms to the electrochemically less active cubic spinel which involves capacity loss [22].

One reason why LiCoO_2 has been adopted as cathode material was its high electrochemical potential of 4.2 V vs. Li/Li^+ which gives a large V_{oc} when used with anodes of low electrochemical potential such as Li-metal or graphite. This property leads to high energy density cells. That along with good cycling properties are the main reasons why LiCoO_2 /graphite cells are common in the market. The drawbacks of this cathode material are poor safety due to the potential release of O_2 if abused and relatively high cost along with toxicity [18].

The spinel LiMn_2O_4 is a cathode material that has lower cost and toxicity than LiCoO_2 and therefore is an attractive cathode material. One drawback is that it shows larger capacity fading than LiCoO_2 . One reason for capacity loss is the Mn^{2+} dissolution into the electrolyte, especially at high temperature. LiMn_2O_4 can be delithiated to $\lambda\text{-Mn}_2\text{O}_4$ which has same symmetry as LiMn_2O_4 but smaller unit cell volume [18].

LiMn_2O_4 has a slightly higher electrochemical potential than LiCoO_2 vs Li/Li^+ exhibiting two close plateaus. Modification of this material with Ni, e.g. $\text{LiNi}_{0.5}\text{Mn}_{1.5}\text{O}_4$ has shown a higher electrochemical potential, about 4.75 V vs. Li/Li^+ , with good cycling properties, which produces higher energy density cells. Currently,

the organic liquid electrolytes formulated for these high voltage cells require additives to increase electrolyte stability. An alternative could be to engineer a solid electrolyte interphase in the cathode similar to that developed for the anode interphase. A battery made with this high voltage spinel and with $\text{Li}_4\text{Ti}_5\text{O}_{12}$ as anode could be an interesting candidate for the future due to a safer operation [23].

LiFePO_4 is another electroactive intercalation electrode material which exhibits a very flat single plateau. It is due to being a two phases electrode, with the delithiated version being FePO_4 . The electrochemical potential is 3.5 V vs Li/Li^+ . One major drawback of this material is having poor electronic and ionic conductivities [24]. However LiFePO_4 conductivities can be increased with strategies such as nanosizing or addition of conductive carbon during production of the LiFePO_4 material [25]. LiFePO_4 is safer than common layered oxides such as LiCoO_2 due to the strong bonding of oxygen in the phosphate group. Therefore this cathode material is more resilient against thermal runaway [26]. The lower price and toxicity of Fe are additional advantages that make of this material one of the preferred cathodes for the close future. The lower electrochemical potential vs Li/Li^+ is a disadvantage with respect to LiCoO_2 due to the lower V_{oc} of the cells made with LiFePO_4 .

There is also an emerging category of cathode materials known as layered Li-rich NMC phases. The major feature of this category is the higher specific capacity with respect to traditional transition metal layered oxides such as LiCoO_2 . These materials derive from LiCoO_2 by partial or total substitution of Co by Ni, Mn and Li at the same time. This is a step further with respect to the layered NMC, e.g. $\text{Li}[\text{Ni}_{1/3}\text{Mn}_{1/3}\text{Co}_{1/3}]\text{O}_2$, which did provide higher specific capacity than LiCoO_2 and is currently used in several applications. The drawbacks of Li-rich NMC materials are voltage decay with cycling, capacity fading and poor kinetics. Currently a large amount of research is trying to make of Li-rich NMC phases a material with practical applications [27].

1.1.3.3 Electrolyte

The electrolyte is the layer component that separates the anode from the cathode. In order to avoid self-discharge of the battery, it has to be an electronic insulator. On the other hand, the ionic conductivity of the electrolyte has to be high enough so that the ion transport is allowed between electrodes.

The electrolyte has to be chemically stable against both electrodes, i.e. anode and cathode during normal cycling of the battery. The most conventional type of electrolyte is the organic liquid electrolyte made of a Li salt such as LiPF_6 dissolved in mixtures of solvents. These are commonly organic solvents such as ethylene carbonate (EC), dimethyl carbonate (DMC), ethyl methyl carbonate (EMC), etc. The formula of the liquid electrolyte is normally completed with additives such as flame-retardants and "redox shuttles" [28]. The reasons for using these organic liquid electrolytes are the electrochemical stability of LiPF_6 , the temperature range in which can be used and also due to its high overall ionic conductivity of about $10^{-2} \text{ S cm}^{-1}$, although part of this conductivity is attributed to anions of the electrolyte [29].

The introduction of cathodes with high electrochemical potential vs Li/Li^+ is demanding new electrolytes that are stable in a wider voltage window [30]. The use of surface reactive additives has the goal of creating protective layers in the electrolyte/electrode interphase [31]. A step further would be the complete substitution of the liquid electrolyte by a solid state electrolyte with decomposition voltage larger than the open circuit voltage of the cell.

In the field of solid state electrolytes, an early achievement was the LiI electrolyte used as solid electrolyte in pacemaker's battery [11]. Nowadays the research in solid electrolytes is focused in finding solid state alternatives to the organic liquid electrolyte. The use of solid state electrolytes is imperative in the field of micro batteries. Complex architectures can be achieved by deposition manufacturing technologies. There are currently available thin film micro batteries that use solid state electrolyte [32].

This thesis focuses on the field of crystalline materials. Several Li-containing halides, nitrides, oxy-salts and sulphides are known as Li-ion conductors. General requirements for these materials in order to have a high Li-ion conductivity are a

high concentration of mobile ions, sufficient fraction of vacancies or interstitials and low activation energy for ion hopping [33]. In addition, the electronic conductivity of the material has to be negligible which is achieved by using elements with strongly preferred oxidation state in the formulation of the solid electrolyte.

Some of the state-of-the-art materials in the field of Li-ion solid state electrolytes are perovskites, Li-ion analogues of sodium superionic conductors (NASICON), lithium superionic conductors (LISICON), Thio-LISICON and garnets [34]. Materials with these crystal structures, their compositions, structural features, conductivity properties and limitations are widely presented and discussed later on, representing a large fraction of this chapter.

1.1.3.4 Separators

The separator is a porous polymer layer that separates both electrodes of the battery. Common materials for this purpose are polyethylene (PE) or polypropylene (PP). The separator lay in the region of the electrolyte and has pores that allow ion migration but avoid contact between anode and cathode. The separator layers made of PE or PP have melting points of about 130 °C and 165 °C respectively.

Multilayers made of both PE and PP are also common [35]. This is a safety shutdown mechanism to prevent the dangerous thermal runaway, e.g. if the battery is subject to a very high discharge rate, the heat produced will melt the polymer layer closing the pores, stopping the electrochemical reactions, and preventing further temperature increase. The shutdown temperature, which depends on the melting temperature of the polymer layers, can be tuned by varying the composition of the polymers [36]. Cellulose based separators have also been investigated resulting in better electrochemical performance but without the shutdown mechanism [37].

1.1.3.5 Solid electrolyte interphase

The liquid electrolyte is not stable at low potential and the electrolyte reduction along with the corrosion of the negative electrode builds a passivation thin layer during the initial cycles of the cell. The composition of this interface, known as solid electrolyte interphase or SEI, is dictated by the chemicals available in the electrolyte and their irreversible electrochemical reactions.

If the composition of the electrolyte is wisely chosen, this accounts for an initial capacity loss that stabilises after a few cycles. It has been shown that if graphite is the chosen anode material, its surface modification with reactive gasses such as CO_2 subject to a specific heat treatment can reduce the capacity loss during SEI formation [38].

When the electrolyte is formulated with Li salts that do not produce significant amounts of HF, such as LiClO_4 or LiAsF_6 , the SEI products are derived from solvents reduction and the major components of the SEI are Li carboxylates and alkoxides. If the Li salt can produce larger amounts of HF, such as for LiPF_6 with conditions for hydrolysis, the SEI chemistry is dominated by LiF and Li alkoxides [39].

Another possible problem of the low potential is lithium plating during charge at low temperatures, which also causes aging of the battery in the form of capacity loss and impedance increase.

Lithium plating at the anode occurs dendritically and further passivation through SEI formation causes further capacity loss. Dendritic filaments may reach the cathode causing a local short. The low melting temperature of metallic Li, $180\text{ }^\circ\text{C}$, can trigger under this situation a thermal runaway [38].

1.1.3.6 Current collectors

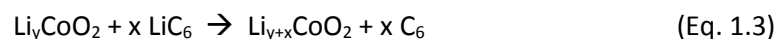
The current collectors are made of metallic materials such as copper and aluminium, for the anode and cathode respectively, which collect the electrons from the electrodes and guide them to the external circuit. The current collectors are generally very thin plates of metal where the electrode is cast on when building the battery. These metal plates have to be chemically stable against the

corresponding electrode material during normal operation of the battery in order to avoid corrosion [40].

1.1.4 Operation

During charge of the battery, the Li-ions and electrons move from the cathode to the anode. The Li-ions move through the electrolyte at the same time as the electrons move through the current collectors and the external circuit. During discharge the movement of ions and electrons is in the opposite direction but following the same pathways.

The operation of a cell made of graphite anode, LiCoO_2 cathode and organic liquid electrolyte is presented here. The discharge half-reactions of the anode and the cathode are shown in equations 1.1 and 1.2 respectively, where x represents the charge transferred during the discharge and y is related to the previous state of charge of the battery. During discharge, one Li-ion is de-intercalated from the graphite of the anode and one electron is released to the current collector of the negative electrode. On the cathode, the Li-ions and the electrons that arrive during discharge lithiate the cathode material through a redox process in which Li_yCoO_2 is transformed into LiCoO_2 . Equation 1.2 shows a partially lithiated cathode represented as Li_yCoO_2 . The full reaction of the cell is shown in equation 1.3.



1.1.5 Cell voltage

The open circuit potential, E , corresponding to a Li intercalation reaction is proportional to the difference in chemical potential of Li in the anode and in the cathode as shown in equation 1.4.

$$E = - \frac{\mu_{Li}^{cathode} - \mu_{Li}^{anode}}{ze} \quad (\text{Eq. 1.4})$$

Where z is the number of electrons transferred and e is the electronic charge. If the anode is Li-metal, μ_{Li}^{anode} can be considered constant while $\mu_{Li}^{cathode}$ will depend on the state of charge [41].

The chemical potential is determined by the energy used in electron and Li^+ transfer, being the Li^+ transfer the largest contributor. The energy related to electron transfer depends on the energy needed to remove the electron from the electrode, known as work function. The energy related to Li^+ transfer depends on the electrostatic interactions with the electrode which are related to the crystal structure and the coordination environment of Li.

It has been traditionally thought that the Li intercalation potential derives from the redox potential of the transition metal, which oxidation state is believed to change after Li^+ insertion. But more recently it is being thought that the oxygen ions are in part responsible for the electron exchange.

Calculations have shown that a significant fraction of electron transfer occurs with oxygen rather than with the transition metal of the cathode. They have also shown that the electron transfer contribution to oxygen and the transition metal varies with the state of charge of the cell [41].

There is experimental evidence that supports these results. Work from Sathiya et al. [42] have tried to explain why Li-rich NMC layered oxides have higher reversible capacities than the transition metal can explain. They have used the related and simpler model compound $\text{Li}_2\text{Ru}_{1-\gamma}\text{Sn}_\gamma\text{O}_3$ to show that the high capacity is in part explained by the reversible anionic redox activity from oxide to peroxide. Following similar idea, McCalla et al. [43] have also shown evidence of the peroxo-like dimers on the model compound Li_2IrO_3 by using transmission electron microscopy and neutron diffraction.

Doping a cathode material with no transition metals would increase the participation of oxygen in the electron exchange during Li⁺ insertion with respect to the transition metal, leading to an increased Li⁺ intercalation voltage while retaining its electrochemical activity. This has been shown by Ceder et al. [44] with aluminium doping into LiCoO₂. This means that the intercalation potential of the electrodes can be "quantum-engineered".

Thermodynamic stability requires that μ_{Li}^{anode} and $\mu_{Li}^{cathode}$ lie within the stability electrochemical potential window of the electrolyte, Eg. When μ_{Li}^{anode} is below the Eg limit or $\mu_{Li}^{cathode}$ is above the Eg limit, the solid electrolyte interface is formed in the electrode/electrolyte boundary from irreversible redox reactions until passivation is achieved.

1.1.6 Failure mechanism

The failure mechanisms with major safety risk are:

- Short derived from dendrite formation.
- Temperature increase due to over abuse.
- Short derived from mechanical deformation or punching.

All these can produce thermal runaway that can end up in a fire. In order to minimise the risk, some of the protection technologies in place are:

- The shutdown mechanism implemented in multilayer separators and already presented in that section.
- The selection of a more thermally stable cathode materials: It has been shown that the onset temperature for self-sustained thermal runaway of LiCoO₂ and LiFePO₄ are 150 and 310 °C respectively [26], showing the higher thermal stability of the olivine with respect to the layered oxide due to the strong P-O bond in the oxyanion. This indicates that batteries made with a LiFePO₄ cathode would have an increased thermal resistance especially if it would have a non-flammable electrolyte, e.g. a ceramic Li-ion conductor.

- The selection of more thermally stable anodes: One of the reasons why Li-metal was discarded as anode was its low melting point of 180 °C. The exothermic reaction of graphite at different states of charge has been shown to happen above 250 °C [45] which is higher than the 150 °C discussed above for LiCoO₂.
- There are other safety measures such as vent valves, thermal fuses, positive temperature coefficient materials or redox shuttles [46].

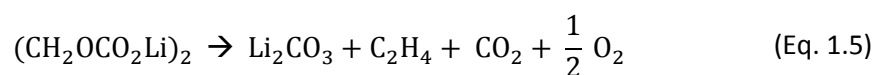
1.1.7 Fire risk

The thermal runaway mechanism is overall well known, although different cell types respond differently to it [2].

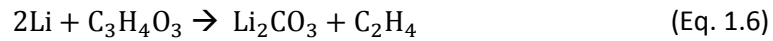
Thermal runaway and explosion has been studied in pouch cells by overcharging, nail penetration and impact. These over abuse tests end up with the battery catching fire [47].

The fire risk is due to the presence of the organic liquid electrolyte that provide the fuel to the combustion reaction that can use O₂ released from the thermal decomposition of a partially delithiated cathode.

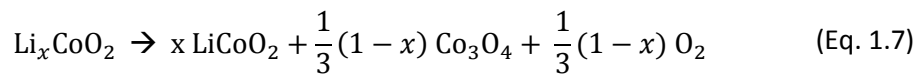
The series of events that lead to a fire starts with a temperature increase due to heat that cannot be dissipated. When the temperature reaches 90 – 120 °C, the metastable components of the solid electrolyte interface, SEI, decompose exothermically [2], e.g. as shown in equation 1.5.



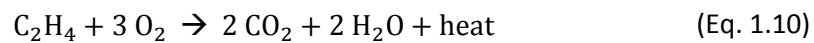
As the temperature raise from SEI decomposition, the intercalated Li reacts with the solvents of the electrolyte to release hydrocarbons from about 100 °C, e.g. as can happen for ethylene carbonate [48] which reaction is shown in equation 1.6.



These processes increase the pressure inside the cell. When the temperature is above 130 °C, the separator melts allowing local shorts to happen between the electrodes. This produces hotspots where the cathode decomposes or disproportionates [49], e.g. the thermal decomposition of Li_xCoO_2 can be written as shown in equations 1.7 to 1.9.



Thus, the thermal decomposition produces O_2 available for combustion. At this stage gasses and solvents are above the flash point with oxygen available and pressure growing up. As soon as the auto ignition temperature of the mixture is reached, the combustion is triggered. Common combustion reactions such as the one shown in equation 1.10 raise rapidly the temperature and initiate the fire or cause the explosion.



If the safety vent opens before the start of the combustion, the flammable mixture escapes. If the safety vent opens with the combustion started, the burning mixture escapes producing a fire. If the safety vent does not open or is not present, the pressure caused by the burning mixture breaks the battery case causing an explosion.

There are other reactions happening during the thermal runaway of the cell [2], but the set shown here is representative of the fire risk of the cell and how it catches fire.

1.2 Li-ion conductivity

1.2.1 Electrical conductivity

Electrical conductivity is generally measured from samples with a regular shape. In general the resistance, R , is measured first. The conductivity, σ , can be obtained from the resistance by applying the geometrical factor that takes into account the thickness of the sample, t , and the area of the sample electrodes, a . This relationship is shown in equation 1.11.

$$\sigma = \frac{1}{R} \cdot \frac{t}{a} \quad (\text{Eq. 1.11})$$

The conductivity measured in this way is the total conductivity. The conductivity can be due to different charge carriers, e.g. electrons and ions. The total conductivity, σ_{total} , can be split in partial conductivities, e.g. $\sigma_{\text{electronic}}$ and σ_{ionic} , as shown in equation 1.12.

$$\sigma_{\text{total}} = \sigma_{\text{electronic}} + \sigma_{\text{ionic}} \quad (\text{Eq. 1.12})$$

This can be split further, e.g. the electronic conductivity can be split in electron and electron hole components and the ionic conductivity in cationic and anionic components as shown in equation 1.13.

$$\sigma_{\text{total}} = \sigma_{\text{electrons}} + \sigma_{\text{electron_holes}} + \sigma_{\text{cations}} + \sigma_{\text{anions}} \quad (\text{Eq. 1.13})$$

One can split some of these again, e.g. the cationic conductivity could be split in cationic conductivity due to vacancies or cationic conductivity due to interstitials.

A compact way of writing this is by using a summation that includes all the components for each i^{th} carrier as shown in equation 1.14.

$$\sigma_{total} = \sum_i \sigma_i \quad (\text{Eq. 1.14})$$

The partial contribution from each i^{th} carrier is known as the transport number or transference number, t_i , and can be calculated as shown in equation 1.15.

$$t_i = \frac{\sigma_i}{\sigma_{total}} \quad (\text{Eq. 1.15})$$

The summation of all transport numbers for all species in a system add up to one as shown in equation 1.16.

$$\sum_i t_i = 1 \quad (\text{Eq. 1.16})$$

For a material with different types of charge carriers, each partial conductivity, σ_i , can be written as a function of the i^{th} carrier concentration, n_i , its mobility, μ_i , and the species charge, z_i , as shown in equation 1.17.

$$\sigma_i = n_i z_i e \mu_i \quad (\text{Eq. 1.17})$$

One type of carrier often predominates in an oxide under particular conditions of temperature and oxygen partial pressure, pO_2 . Electronic mobility is normally much higher than ionic mobility.

1.2.2 Li-ion transport number

The Li-ion transport number, or transference number, indicates which fraction of the total electric current in a material is produced by Li-ions. It can be defined as a function of partial conductivities as shown in equation 1.18.

$$t_{Li-ion} = \frac{\sigma_{Li-ion}}{\sigma_{total}} \quad (\text{Eq. 1.18})$$

In solid state Li-ion conductors the Li-ion transport number is practically one, meaning that the contribution to the electric current from carriers other than Li-ions is negligible.

This is not the case with liquid organic electrolytes which have Li-ion transference numbers in the range 0.2 – 0.5 and overall ionic conductivities of $10^{-2} \text{ S cm}^{-1}$ at room temperature [50].

Pure ionic liquids have only one cation and one anion, but if a lithium salt is dissolved in an ionic liquid the resulting solution is more complex and the transference number for Li-ion can be as low as 0.1.

AC impedance can provide information about the overall ionic conductivity, i.e. $\sigma_{\text{overall_ionic}} = \sigma_{\text{cations}} + \sigma_{\text{anions}}$. If individual transport numbers are required other techniques such as pulsed field gradient NMR can be used, which allow for the determination of individual coefficients of self-diffusion for anions and cations [29].

This means that the target conductivity for a functional solid state electrolyte is about a half the value of common liquid organic electrolytes. In other words, this sets a minimum value of ionic conductivity of about $5 \times 10^{-3} \text{ S cm}^{-1}$ for practical solid state electrolytes.

1.2.3 Crystallographic defects

A crystalline solid has to meet several requirements in order to host an ionic conduction mechanism, such as having vacant sites for adjacent Li-ions to hop into and having Li-sites close enough so that the energy barrier is low, i.e. low activation energy or E_a .

The vacancies can be intrinsic, if they are due to Frenkel or Schottky defects; or extrinsic if they have been created by aliovalent substitution. These are known as point defects.

Schottky defects are vacancies in the crystal due to missing atoms that overall keep the charge balance. It can be seen as an integer number of formula units that have migrated from the bulk to the surface of the crystal, leaving vacancies in the bulk. If the ionic crystal has a formula MX, these vacancies are known as Schottky pairs.

Frenkel defects are vacancies on normal sites that have been generated because the ion has migrated to a vacant interstitial site. This usually happens with small ions that have appropriate interstitial vacancies close to them [51].

Although the creation of a defect is an endothermic process, defect formation is a thermodynamically favoured process balanced by the large increase in entropy. Its formation free energy, ΔG , is given by equation 1.19.

$$\Delta G = \Delta H - T \Delta S \quad (\text{Eq. 1.19})$$

Where ΔH is the formation enthalpy for one intrinsic defect, T is the absolute temperature and ΔS is the entropy change.

The entropy change, ΔS , can be estimated by using the configurational entropy from the Boltzmann formula shown in equation 1.20.

$$S = k \ln W \quad (\text{Eq. 1.20})$$

Where k is the Boltzmann constant, $1.38 \times 10^{-23} \text{ J K}^{-1}$, and W is the number of ways of distributing the defects at random in the crystal [51].

Intrinsic defects are statistically generated by temperature. The concentration of Schottky defects in a crystal with stoichiometry 1:1 of formula MX , n_s , is shown in equation 1.21.

$$n_s = N \cdot e^{\left(\frac{-\Delta H_s}{2kT}\right)} \quad (\text{Eq. 1.21})$$

Where N is the concentration of anions which is equal to the concentration of cations, ΔH_s is the formation enthalpy for one Schottky intrinsic defect, k is the Boltzmann constant and T is the absolute temperature in Kelvin.

The concentration of Frenkel defects in a crystal, n_f , is shown in equation 1.22.

$$n_f = \sqrt{NN_i} \cdot e^{\left(\frac{-\Delta H_f}{2kT}\right)} \quad (\text{Eq. 1.22})$$

Where N is the concentration of ionic sites in the crystal, N_i is the concentration of available interstitial sites, ΔH_F is the formation enthalpy for one Frenkel intrinsic defect.

In general, the number of intrinsic vacancies is negligible at low temperature, where the extrinsic vacancies drives the conductivity. On the other hand the number of intrinsic vacancies is increased exponentially with temperature and is responsible for the conductivity behaviour at high temperature.

For the determination of the crossover temperature of the extrinsic and intrinsic regions one needs to know the fraction of extrinsic defects, n_{extr}/N , which is temperature independent and the formation enthalpy for each intrinsic defect, e.g. ΔH_S for a Schottky defect. Then by doing $n_{extr}/N = n_s/N$ as shown in equation 1.23, the crossover temperature, T_{cr} , can be calculated by solving the equation for T_{cr} .

$$\frac{n_{extr}}{N} = e^{\left(\frac{-\Delta H_S}{2kT_{cr}}\right)} \quad (\text{Eq. 1.23})$$

As graphical example, using a fraction of extrinsic defects $n_{extr}/N = 0.001$ and a formation enthalpy for each Schottky defect of $\Delta H_S = 1$ eV the plot in figure 1.2. is obtained. It can be seen that in the extrinsic and intrinsic regions, the total fraction of defects, $(n_{extr} + n_{intr})/N$, corresponds to the extrinsic and intrinsic fractions of defects respectively. For this example the crossover temperature, T_{cr} , is about 570 °C.

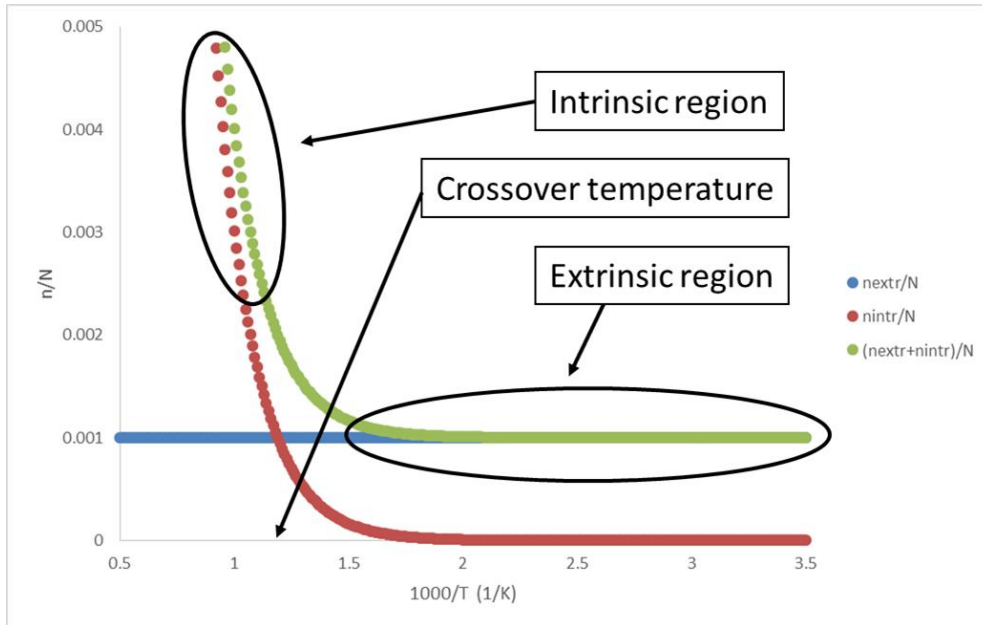


Figure 1.2. Fraction of intrinsic, extrinsic and (intrinsic + extrinsic) defects as a function of $1000/T$. T is absolute temperature. The extrinsic region is dominated by the extrinsic defects at temperatures below T_{cr} . The intrinsic region is dominated by the intrinsic defects at temperatures above T_{cr} .

1.2.4 Ionic conductivity

Low values of Li-ion conductivity have been one of the main reasons that has prevented further developments in Li-ion battery technology [8]. As introduced earlier in this chapter, a reasonable ionic conductivity for a solid electrolyte would be $5 \times 10^{-3} \text{ S cm}^{-1}$. Lower values of ionic conductivity would imply limiting the charge/discharge rates of the battery.

In the words of A. R. West [52] “The electrical properties of materials depend on whether they are conductors or dielectrics (insulators) and, in the former, whether the current carriers are electrons or ions.”

Those materials that are electrical conductors in which the carriers are ions are known as ionic conductors and are characterised by their ionic conductivity. If in addition, the electronic conductivity of these materials is negligible, then they are called electrolytes, i.e. electrolytes are ionic conductors and electronic insulators at the same time [53].

In sintered ceramic electrolytes, made of different grains of material, bulk Li-ion conductivity occurs within the crystal structure along the diffusion pathways when the Li-ions move or hop from site to site. The conductivity through the grain boundaries is in general lower than within the grains [50].

The mobile ions are called the working ions. The higher the mobility, μ , and concentration, n , of the working ions of an electrolyte, the higher the conductivity. This relationship can be seen in equation 1.24 which can be used for electrons as well in which case $z = 1$.

$$\sigma = n z e \mu \quad (\text{Eq. 1.24})$$

Ionic conduction is a process mediated by vacancies or interstitials. Defects tend to aggregate together to form defect clusters. Interstitials aggregate due to the local distortion caused by the defect. The cluster of two interstitials is known as split interstitial. Vacancies in ionic crystals aggregate when they have opposite charges. The basic pairs are made of vacancy/vacancy or impurity/vacancy. These are dipolar and can attract each other to form larger clusters [52]. Defect clustering reduces the ionic conductivity of the material because it can be associated with ion trapping.

The ion diffusion coefficient, D , and the ionic conductivity, σ , are related by the Nernst-Einstein relation shown in equation 1.25, where k_B is the Boltzmann constant, T is the absolute temperature, N is the concentration of the Li-ions (number of ions per unit volume) and q is the charge of the Li-ion.

$$D = \frac{\sigma k_B T}{N q^2} \quad (\text{Eq. 1.25})$$

Diffusion is a thermally activated process [54] that often follows an Arrhenius type equation over a wide range of temperatures. The diffusion coefficient, D , can be written as shown in equation 1.26.

$$D = D_0 \cdot e^{\left(\frac{-Q}{RT}\right)} \quad (\text{Eq. 1.26})$$

Where D_0 is the pre-exponential factor, Q is the activation energy of diffusion, R is the universal gas constant and T is the absolute temperature in Kelvin. Therefore

the conductivity will be an activated process as well and it will be shown in the next section.

If the diffusion coefficient is calculated from conductivity measurements by using the Nernst-Einstein relationship, D_{calc} , its value is generally different than the one obtained from direct measurements, D_{meas} . This disagreement is attributed to the presence of the electric field in the conductivity measurements, which influences the direction of the ion hopping [55]. The relationship between both is known as the Haven ratio and is shown in equation 1.27.

$$H_r = \frac{D_{meas}}{D_{calc}} \quad (\text{Eq. 1.27})$$

1.2.5 Ionic conduction mechanism

The hopping mechanism is usually used to explain the ionic conductivity process in crystalline ion conductors. This model explains the ion transport by allowing hops between neighbouring Li sites within the structure [56].

Ionic conduction is a defect mediated mechanism [57], i.e. either vacancies or interstitials are needed in order to enable the hopping mechanism. The origin of the defects can be intrinsic or extrinsic, e.g. derived from aliovalent doping.

Without the presence of defects the charge transport is not possible because the ions cannot hop, as shown in figure 1.3.a. If a defect, e.g. a vacancy, is present the ion transport is possible. In figure 1.3.b it can be seen that either ion B or ion D can hop from their site to site 3. This can also be seen as vacancy hopping, e.g. if the ion B hops from site 2 to site 3, the vacancy on site 3 would move to site 2. This can be extended to 2D or 3D diffusion pathways, but whichever the dimensionality, the crystallographic defect needs to be present in order to enable the ion transport.

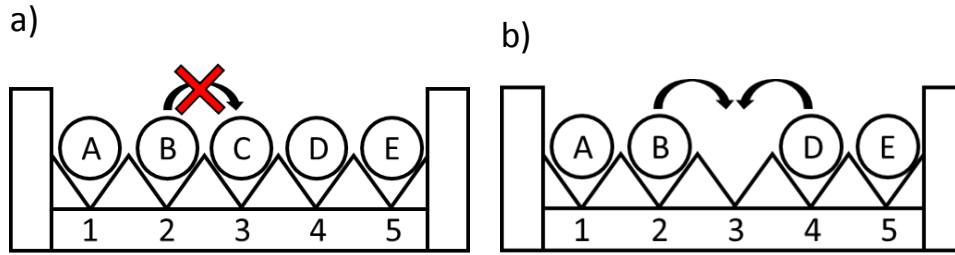


Figure 1.3. Panel a) shows a 1D diffusion pathway with all sites, 1 to 5, occupied by ions A to E. Ion B cannot hop from site 2 to 3 because site 3 is occupied by ion C. Panel b) shows the same diffusion pathway with a vacancy defect on site 3. In this situation, either ion B or ion D can hop from their site to site 3.

This transport process has an associated energy barrier. Lower energy barrier means easier hopping and higher ionic conductivity. The higher the temperature, the easier the migration of the ion between adjacent sites of the lattice. Therefore this energy barrier, called activation energy, is temperature dependent as it was anticipated in the previous section while discussing the diffusion coefficient. Because of that, the experimental conductivity results can be fitted to the Arrhenius equation, see equation 1.28, and used to produce an Arrhenius plot [52].

$$\sigma = A \cdot e^{\left(\frac{-E_a}{RT}\right)} \quad (\text{Eq. 1.28})$$

Where σ is the conductivity, A is the pre-exponential factor, E_a is the activation energy, R is the universal gas constant and T is the absolute temperature in Kelvin.

There is an extension of the Arrhenius expression known as the modified Arrhenius equation [58] and used by some authors that is shown in equation 1.29.

$$\sigma \cdot T = A_T \cdot e^{\left(\frac{-E_a}{RT}\right)} \quad (\text{Eq. 1.29})$$

Where the pre-exponential factor, A_T , includes a reciprocal temperature term. The latter equation can be deduced from the random walk theory but the former

equation is simpler to use because the conductivity can be read directly from the plot. In general both give same activation energies within error [53].

1.2.6 Dimensionality of ionic conductors

The crystalline solids studied here are non-molecular solids. These extended structures are made from atoms and ions coming together with ionic or covalent bonding. The mobile ions are arranged within the solid forming the sub lattice of the diffusion pathways.

Depending on the structure type of the crystal, these diffusion pathways can be organised in parallel channels, parallel flat networks or interconnected channels along all crystallographic directions, which are known as 1D, 2D and 3D diffusion pathways respectively. Examples of crystal structures with 1D conduction pathways are olivine or hollandite materials, with 2D conduction pathways are spinel or layered oxide materials and with 3D conduction pathways are garnet or NASICON materials.

The dimensionality of the conduction pathways is not always deduced straightaway from the crystal structure, e.g. initially it was not clear if Li diffusion in LiFePO_4 was a 1D or 2D process [24] until single crystal conductivity measurements along the crystallographic axes showed that the conduction along the b crystallographic axis is greatly favoured [59], which is in agreement with the fact that the lowest Li-Li distance in the Li sub lattice of LiFePO_4 is found along the b axis.

The dimensionality of the conduction sub lattice is one of the factors controlling ionic conductivity. 1D and 2D diffusion pathways lead to an anisotropic nature of the ion diffusion, while 3D diffusion pathways lead to an isotropic nature of the conduction in the solid. While for a single crystal the orientation can be chosen, for a well sintered polycrystalline sample, with negligible grain boundary effects, the conductivity will be similar to that of the single crystal only in the case of 3D conductors [60]. In the case of 1D and 2D conductors, the well sintered polycrystalline sample will exhibit an intermediate conductivity with respect to those measured in the single crystal for each direction. The 1D materials remain as useful models for studying the fundamentals of the conduction mechanisms [61],

knowledge that later on can be extrapolated to 2D and 3D materials and can be used for the design of new functional materials.

1.3 Families of Li-ion conductors

This section presents a literature review about families of Li-ion conductors. Whenever possible the conductivity at room temperature is cited along with features of the crystallographic structure that have been pointed to influence conductivity. The major area of interest for this thesis is the field of crystalline Li-ion conductors. For that reason glass and polymer Li-ion conductors are not reviewed in this section. The Li-ion conductivity within a family can change up to 6 orders of magnitude which suggest that structure tuning can be a way of improving conductivity [50]. The major limitations for most of the known materials are either low ionic conductivity, which should be higher than $5 \times 10^{-3} \text{ S cm}^{-1}$ at room temperature, or other problems such as ageing or chemical stability.

1.3.1 Early Li-ion conductors

These are early Li-ion conductors in the form of halides, nitrides and compounds that contain oxyanions. From the Li halides, only LiI is relatively conducting at room temperature with $\sigma = 5 \times 10^{-7} \text{ S cm}^{-1}$. The other Li halides are almost insulators. LiI is isostructural to NaCl [62]. The solid solution of LiI with CaI_2 at 1% increases the Li-ion conductivity up to $\sigma = 10^{-5} \text{ S cm}^{-1}$ at 28 °C. The conductivity decrease to $\sigma = 10^{-6} \text{ S cm}^{-1}$ at 28 °C after 500 hours [63]. When a composite is made with LiI and 40 % Al_2O_3 the Li-ion conductivity can be stabilised at about $\sigma = 10^{-5} \text{ S cm}^{-1}$ at 25 °C [64].

From the Li nitrides, the layered compound Li_3N is made of Li_2N layers containing Li^+ between the layers. This produces a strong anisotropy in the conductivity with an in-plane conductivity of $\sigma = 1.2 \times 10^{-3} \text{ S cm}^{-1}$ and a conductivity perpendicular to the plane of $\sigma = 10^{-5} \text{ S cm}^{-1}$ at room temperature [65]. A sample randomly oriented shows a conductivity value of $\sigma = 7 \times 10^{-4} \text{ S cm}^{-1}$ at room temperature [62]. The

disadvantages of this material are its self-ignition in air, especially of finely divided specimens, and its low thermodynamic decomposition potential of 0.44 V. This potential is calculated from the free energy of formation and it is smaller with increasing temperature, making the material unsuitable for being used as electrolyte of a cell with open circuit potential higher than 0.44V at high temperatures. At room temperature the decomposition is inhibited kinetically [66]. Other derivatives such as the $\text{Li}_3\text{N-LiCl}$ system decompose at higher voltages but have lower conductivity [67].

Other early Li-ion conductors have been the spinel Li_2CdCl_4 , in which Cd is on octahedral sites and Li is distributed between octahedral and tetrahedral sites. Non-stoichiometry improves Li-ion conductivity with a maximum for $\text{Li}_{1.9}\text{Cd}_{1.05}\text{Cl}_4$ of about $\sigma = 5 \times 10^{-6} \text{ S cm}^{-1}$ at room temperature [68].

The last early electrolytes presented in this section will be some oxyacid salts of lithium. These are important because some of the following families are built on their tetrahedral sub-units, e.g. olivine or LISICON materials that will be introduced later. The phase $\gamma\text{-II Li}_3\text{PO}_4$ is based on a hexagonal closed packed oxide network with all the cations in tetrahedral coordination. It has a conductivity value of about $\sigma = 10^{-9} \text{ S cm}^{-1}$ at 300 °C. On the other hand, Li_4SiO_4 has a conductivity of $\sigma = 5 \times 10^{-9} \text{ S cm}^{-1}$ at room temperature [69]. The Al-doped composition $\text{Li}_{2.5}\text{Al}_{0.5}\text{SiO}_4$ has a conductivity of $\sigma = 3 \times 10^{-5} \text{ S cm}^{-1}$ at 100 °C [70]. Finally, samples from the solid solution of Li_3PO_4 and Li_4SiO_4 have been shown to have higher conductivity than the end members. For the formula $\text{Li}_{3+x}\text{P}_{1-x}\text{Si}_x\text{O}_4$, the better conductivity is for $x = 0.5$ with $\sigma = 3 \times 10^{-6} \text{ S cm}^{-1}$ at room temperature [71].

The major limitation of all these early conductors is that they do not reach the target conductivity for practical applications, i.e. $5 \times 10^{-3} \text{ S cm}^{-1}$. The rest of the families of Li-ion conductors presented here have recently been or are currently hot topics in Li-ion conductors' literature. A brief description of each family is given in the following sections along with the motivations for further research.

1.3.2 NASICON analogues

NASICON means “Sodium(NA)-Super-Ionic-CONductor”. The NASICON-type structure was described in 1968 for the compositions $\text{NaZr}_2(\text{PO}_4)_3$, $\text{NaGe}_2(\text{PO}_4)_3$ and $\text{NaTi}_2(\text{PO}_4)_3$ [72]. The crystal structure is a framework of PO_4 tetrahedra and ZrO_6 octahedra with corner sharing connection in alternating sequences as can be seen in figure 1.4. This framework has a rhombohedral cell commonly described in the hexagonal setting of space group $R\bar{3}c$. The crystal structure has a three dimensional network of channels. The relatively high ionic conductivity is due to this 3D diffusion pathway in which there are two sites partially occupied by the alkali metal ions. This enables the ion migration through the hopping mechanism that is responsible for the ionic conductivities measured in these materials. [50].

The study of the solid solution $\text{Na}_{1+x}\text{Zr}_2\text{P}_{3-x}\text{Si}_x\text{O}_{12}$ showed that for $x = 2$ the Na-ion conductivity was of $\approx 0.2 \text{ S cm}^{-1}$ at $300 \text{ }^\circ\text{C}$ with $E_a \approx 0.29 \text{ eV}$ [73]. This is due to the Na-ions occupying 3 out of 4 available sites for Na, which leaves a vacancy for ion hopping [51]. This conductivity was relatively high compared with other Na-ion conductors and this structure-type was known as NASICON.

The Li-containing NASICON analogues are materials with the NASICON-type structure in which the mobile species is the Li-ion. These materials have been investigated as Li-ion conductors. Materials of composition $\text{LiM}_2\text{P}_3\text{O}_{12}$ with $M = \text{Zr}, \text{Ge}, \text{Hf}$ and Ti have shown total conductivities of 10^{-10} , 10^{-7} , 10^{-7} and $10^{-6} \text{ S cm}^{-1}$ respectively. The activation energies of the bulk were e.g. 0.30 eV for $M = \text{Ti}$ and 0.43 eV for $M = \text{Hf}$ [74].

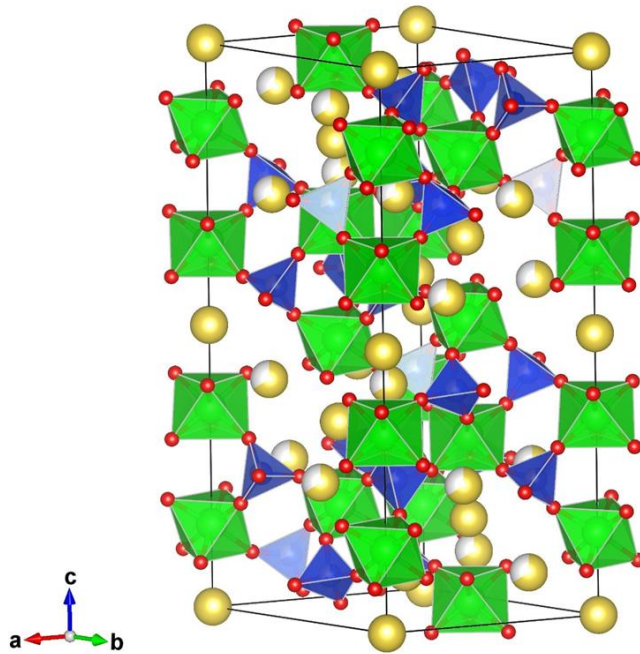


Figure 1.4. Unit cell of $\text{Na}_3\text{Zr}_2\text{Si}_2\text{PO}_{12}$ plotted with VESTA [75] from the structural model of Didisheim et al. [76]. Zr octahedra and Si/P tetrahedra are shown in green and blue respectively. Na atoms are shown in yellow. Partial occupancies are represented with pie chart style plots.

These materials have also been prepared with two different atoms on the M site. In order to keep the overall 4+ charge on the M site, couples 5+/3+ were tried. Such is the case for $\text{LiTaAlP}_3\text{O}_{12}$ that has a total ionic conductivity of $6.5 \times 10^{-7} \text{ Scm}^{-1}$ with $E_a = 0.47 \text{ eV}$ at $30 \text{ }^\circ\text{C}$ [77]. Aliovalent doping was attempted as well in order to increase the Li content, e.g. the series $\text{Li}_{1+x}[\text{Ge}_{2-x}\text{Al}_x](\text{PO}_4)_3$ has been studied showing for $x = 0.4$, $\text{Li}_{1.4}[\text{Ge}_{1.6}\text{Al}_{0.4}](\text{PO}_4)_3$, a total conductivity of $\approx 10^{-4} \text{ Scm}^{-1}$ and $E_a \approx 0.43 \text{ eV}$ at $23 \text{ }^\circ\text{C}$ [78].

The composition $\text{Li}_{1.3}\text{Al}_{0.3}\text{Ti}_{1.7}(\text{PO}_4)_3$ has shown the best bulk Li-ion conductivity to date at room temperature for NASICON analogues. The bulk conductivity at 298 K is $\sigma_b = 3 \times 10^{-3} \text{ S cm}^{-1}$ and the total conductivity is $\sigma_t = 7 \times 10^{-4} \text{ S cm}^{-1}$. The activation energy for the total conductivity between room temperature and $200 \text{ }^\circ\text{C}$ is 0.20 eV, while above $200 \text{ }^\circ\text{C}$ it is 0.35 eV. The Arrhenius plot of the total conductivity shows a gentle curve with no phase transition observed in differential thermal analysis

[79]. The total conductivity of these materials is not high enough for practical applications. In addition, the titanium ion can be reduced at low potentials.

1.3.3 LISICON

LISICON means “Lithium-Super-Ionic-CONductor”. The structure type of this family is different to the NASICON-type structure. These materials have frameworks derived from γ - Li_3PO_4 which has space group $Pnma$. It is based on a hexagonal closed packed oxide network with all cations in tetrahedral coordination as can be seen in figure 1.5.a. There are two sites for Li, 8d and 4c, with 1D chains along the a-axis [50].

A LISICON is formed when interstitial lithium ions are incorporated into phases such as γ - Li_3PO_4 , γ - Li_3AsO_4 , γ - Li_3VO_4 or γ - $\text{Li}_2\text{ZnGeO}_4$. These phases are called γ -tetrahedral structures [53].

The solid solution between γ - Li_3PO_4 and Li_4SiO_4 produces the series $\text{Li}_{3+x}(\text{P}_{1-x}\text{Si}_x)\text{O}_4$ for $0 < x < 0.4$. The solid solution of γ - $\text{Li}_2\text{ZnGeO}_4$ with Li_4GeO_4 produces the series $\text{Li}_{2+2x}\text{Zn}_{1-x}\text{GeO}_4$ for $0.15 < x < 0.85$ [80]. These solid solutions, that are equivalent to aliovalent doping of the tetrahedral phases, introduce partially occupied interstitial Li sites that reduce the distance between Li sites and enable the hopping mechanism. This leads to large increases in Li-ion conductivity for the doped phases with respect to the tetrahedral parent materials.

The original LISICON is the nonstoichiometric compound $\text{Li}_{2+2x}\text{Zn}_{1-x}\text{GeO}_4$, that reaches a maximum of conductivity for $x = 0.4 - 0.5$. The interstitial Li sites can be seen in figure 1.5.b for $\text{Li}_3\text{Zn}_{0.5}\text{GeO}_4$. The conductivity for $x = 0.4$ is comparable to other LISICON materials at $300\text{ }^\circ\text{C}$, $\sigma = 0.1\text{ S cm}^{-1}$. At room temperature the conductivity is low, $4 \times 10^{-8}\text{ S cm}^{-1}$, compared with other materials such as $\text{Li}_{3.4}(\text{Si}_{0.4}\text{V}_{0.6})\text{O}_4$ with a conductivity of $\sigma = 1 \times 10^{-5}\text{ S cm}^{-1}$. $\text{Li}_{2+2x}\text{Zn}_{1-x}\text{GeO}_4$ has the problem of ageing at room temperature, i.e. the conductivity gradually decreases with time. It has been shown that the introduction of large number of Li-ion vacancies in $\text{Li}_2\text{ZnGeO}_4$ does not lead to high conductivities whereas the introduction of interstitial lithium does [81].

The ageing of $\text{Li}_{2+2x}\text{Zn}_{1-x}\text{GeO}_4$ was described for a sample stored in vacuum for 28 days which showed a conductivity 100 times lower than for a freshly prepared sample. The aged sample showed also slightly higher E_a . This could not be explained with powder X-ray diffraction data. The cause of the ageing was initially attributed to changes in the mechanism of conduction, in particular with the formation of defect clusters. In a later publication the ageing effect was attributed to the formation of clusters by the trapping of mobile Li-ions [80]. Finally the study with high resolution powder neutron diffraction, at room temperature first [82] and at higher temperatures up to 500 °C later [83], showed the different substructures of the defect clusters that explain the aging effect.

The solid solution $\text{Li}_{4-x}(\text{Ge}_{1-x}\text{V}_x)\text{O}_4$ does not show the ageing problem. From this series, the composition $\text{Li}_{3.6}(\text{Ge}_{0.6}\text{V}_{0.4})\text{O}_4$ has a conductivity of $\sigma = 4 \times 10^{-5} \text{ S cm}^{-1}$ at 18 °C with $E_a = 0.44 \text{ eV}$ [84]. In addition to the ageing problem, none of these materials reach the target conductivity for a practical application.

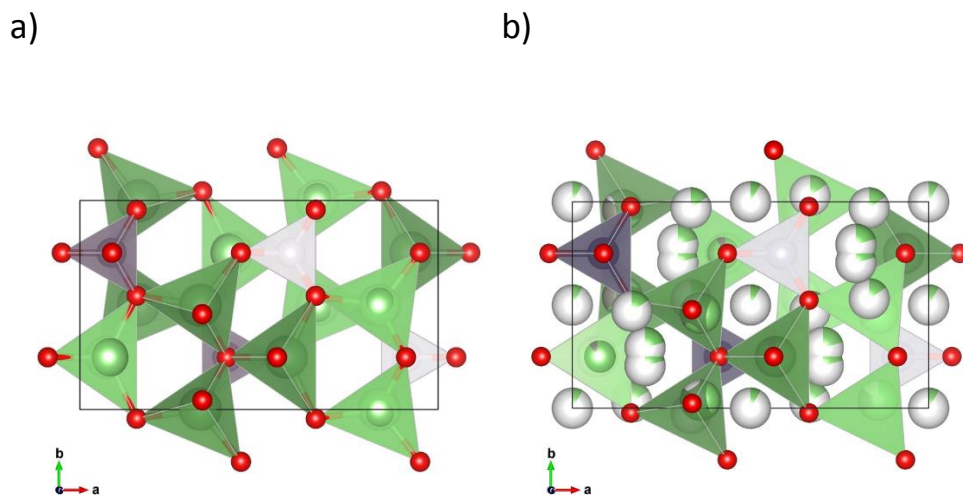


Figure 1.5. a) Unit cell of Li_3PO_4 plotted with VESTA [75] from the structural model of Yakubovich et al. [85] with PO_4 and LiO_4 tetrahedra in purple and green respectively. b) Unit cell of $\text{Li}_3\text{Zn}_{0.5}\text{GeO}_4$ plotted with VESTA [75] from the structural model of Abrahams et al. [82] with GeO_4 and LiO_4 tetrahedra in purple and green respectively. Li and Zn atoms are shown in green and grey respectively. Fractional occupancies are represented with pie chart style plots.

1.3.4 Thio-LISICON and related phases

The Thio-LISICON family is formed when the O atom of LISICON materials is replaced with the S atom. A number of new materials discovered by Kanno et al. [86] were structurally related to the LISICON family such as Li_4GeS_4 or $\text{Li}_2\text{ZnGeS}_4$.

The crystallographic features are similar to those in the LISICON family, but based on a hexagonal close packed sulphide network. Some of the compositions are isostructural to the LISICON oxide analogues and therefore related to the $\gamma\text{-Li}_3\text{PO}_4$ structure type. Again the excess lithium is accommodated on partially occupied interstitial sites that promote the hopping mechanism.

For the case of Li_4GeS_4 the conductivity is 2×10^{-7} at 25 °C [86]. Li interstitials were introduced in Li_4SiS_4 by substitution of Al^{3+} for Si^{4+} , giving the series $\text{Li}_{4+x}\text{Si}_{1-x}\text{Al}_x\text{S}_4$. Li vacancies were also introduced in Li_4SiS_4 by substitution of P^{5+} for Si^{4+} to give the series $\text{Li}_{4-x}\text{Si}_{1-x}\text{P}_x\text{S}_4$. In both cases the conductivity increased with respect to the parent material. The best conductivity was for $\text{Li}_{3.4}\text{Si}_{0.4}\text{P}_{0.6}\text{S}_4$ which has an ionic conductivity of $6.4 \times 10^{-4} \text{ S cm}^{-1}$ at 27 °C with $E_a = 0.29 \text{ eV}$ [87].

The larger ionic radius along with the more polarisable nature of the sulphide ion with respect to the oxide ion may be responsible for the higher conductivities observed in the sulphur substituted samples [86].

One of the best conductors in this family is $\text{Li}_{3.25}\text{Ge}_{0.25}\text{P}_{0.75}\text{S}_4$ with a conductivity of $2.2 \times 10^{-3} \text{ S cm}^{-1}$ at 25 °C and $E_a = 0.21 \text{ eV}$ [88].

Another set of phases related with the thio-LISICON family, having a new structure type, was discovered with higher conductivities than those presented so far. The general formula is $\text{Li}_{10}\text{MP}_2\text{S}_{12}$ with $M = \text{Si, Ge and Sn}$ [89-91].

The space group of these compositions is $P4_2/nmc$. The PS_4 and MS_4 tetrahedra do not share any S atom between them. One of the P atoms of $\text{Li}_{10}\text{MP}_2\text{S}_{12}$ sits on the 2b site while M and the second P share the 4d site. There are 4 sites for Li namely 4c, 4d, 8f and 16h. Li on the 4d site is in octahedral coordination. It is thought that Li on this site is less mobile, playing in this way a more structural role. On the other hand, it is also thought that this Li atom works also as a gateway between the 1D Li channels that develop along the backbone of the structure. The other three sites host Li in tetrahedral coordination. The tetrahedral Li is considered the species with

high mobility in the structure. These sites are partially occupied and relatively close to each other. The crystal structure of $\text{Li}_{10}\text{GeP}_2\text{S}_{12}$ is shown in figure 1.6.

$\text{Li}_{10}\text{SiP}_2\text{S}_{12}$ has an ionic conductivity of $2.3 \times 10^{-3} \text{ S cm}^{-1}$ with $E_a = 0.20 \text{ eV}$ [89]. $\text{Li}_{10}\text{SnP}_2\text{S}_{12}$ has an ionic conductivity of $4 \times 10^{-3} \text{ S cm}^{-1}$ with $E_a = 0.27 \text{ eV}$ [90]. The best ionic conductivity recorded so far has been the one for $\text{Li}_{10}\text{GeP}_2\text{S}_{12}$ which has an ionic conductivity of $1.2 \times 10^{-2} \text{ S cm}^{-1}$ with $E_a = 0.25 \text{ eV}$ [91].

The solid solutions $\text{Li}_{10}\text{GeP}_2\text{S}_{12} - \text{Li}_{10}\text{SnP}_2\text{S}_{12}$ and $\text{Li}_{10}\text{GeP}_2\text{S}_{12} - \text{Li}_{10}\text{SiP}_2\text{S}_{12}$ have been studied, but the new samples have not hit the conductivity value for $\text{Li}_{10}\text{GeP}_2\text{S}_{12}$ [92]. Although some of these conductivities are in range for practical applications, sulphides present a number of disadvantages such as water sensitivity with potential release of H_2S , need of inert atmosphere for manipulation and lower stability than other solid electrolytes [93]. In addition, the high volatility of sulphur makes the control of the stoichiometry difficult during the synthesis of these materials. Finally, computational studies have found $\text{Li}_{10}\text{GeP}_2\text{S}_{12}$ to be unstable against Li-metal [50].

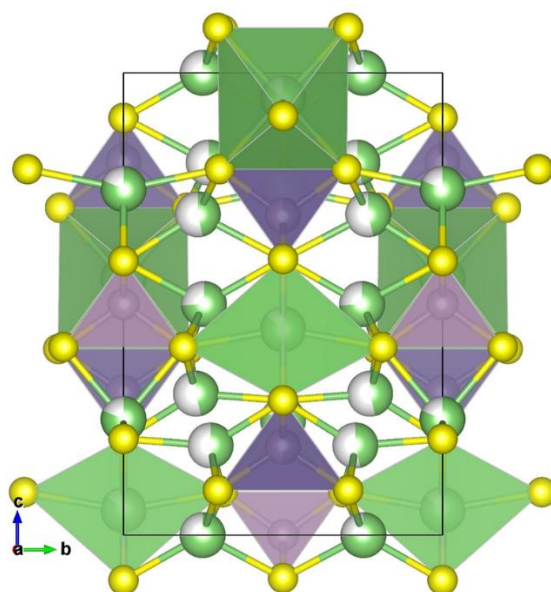


Figure 1.6. Unit cell of $\text{Li}_{10}\text{GeP}_2\text{S}_{12}$ plotted with VESTA [75] from the structural model of Kuhn et al. [94]. P/Ge tetrahedra are shown in purple. S atoms are shown in yellow. LiO_6 octahedra are shown in green. Li atoms in tetrahedral coordination are shown as white/green spheres. Partial occupancies are represented with pie chart style plots.

1.3.5 Garnets

Li-ion conducting garnets have the general formula $\text{Li}_n\text{A}_3\text{B}_2\text{O}_{12}$ with the structure type of $\text{Ca}_3\text{Al}_2\text{Si}_3\text{O}_{12}$. The crystal structure of the orthosilicate $\text{Ca}_3\text{Al}_2\text{Si}_3\text{O}_{12}$ has the cubic space group $la\bar{3}d$ and is made of SiO_4 tetrahedra, AlO_6 octahedra and CaO_8 dodecahedra with edge-sharing connectivity as can be seen in figure 1.7.a. In $\text{Li}_n\text{A}_3\text{B}_2\text{O}_{12}$, A is the dodecahedral site, B is the octahedral site and n generally varies between 3 and 7. For n = 3, Li occupies the tetrahedral site, e.g. $\text{Li}_3\text{Nd}_3\text{Te}_2\text{O}_{12}$ for which the conductivity is as low as $\sigma = 10^{-5} \text{ S cm}^{-1}$ at 600 °C with an activation energy of 1.22 eV [95]. The large increase in conductivity for these materials happens when n is greater than 3. The extra lithium partially occupies interstices of the structure that make a three dimensional network of closer Li sites as can be seen in figure 1.7.b. The value of n can be tuned by changing the valence of the cations A and B.

For example, two members of the garnet family with n = 5 are $\text{Li}_5\text{La}_3\text{Nb}_2\text{O}_{12}$ with a conductivity of about $\sigma = 10^{-5} \text{ S cm}^{-1}$ at 22 °C and an activation energy of 0.43 eV [96] and $\text{Li}_5\text{La}_3\text{Ta}_2\text{O}_{12}$ with a conductivity of $10^{-6} \text{ S cm}^{-1}$ at room temperature and an activation energy of 0.57 [97]. These two conductivities are much higher than the conductivity of $\text{Li}_3\text{Nd}_3\text{Te}_2\text{O}_{12}$ at room temperature.

Materials of the family with n = 6 can show even higher conductivities, e.g. the composition $\text{Li}_6\text{BaLa}_2\text{Ta}_2\text{O}_{12}$ has a total Li-ion conductivity of about $\sigma = 4 \times 10^{-5} \text{ S cm}^{-1}$ at room temperature with an activation energy of 0.40 eV [98].

Materials with n = 7 can also be made, e.g. the composition $\text{Li}_7\text{La}_3\text{Zr}_2\text{O}_{12}$ shows a bulk Li-ion conductivity of about $\sigma = 3 \times 10^{-4} \text{ S cm}^{-1}$ and a total Li-ion conductivity of about $\sigma = 1 \times 10^{-4} \text{ S cm}^{-1}$ at 25 °C, with activation energy of 0.34 eV [99].

Finally, the composition $\text{Li}_{6.55}\text{Ga}_{0.15}\text{La}_3\text{Zr}_2\text{O}_{12}$ shows a total Li-ion conductivity of $\sigma = 1.3 \times 10^{-3} \text{ S cm}^{-1}$ at 24 °C with an activation energy of 0.3 eV [100]. This value is among the highest conductivities reported for garnets to date. These conductivities are still below the target value for practical application. In addition, $\text{Li}_7\text{La}_3\text{Zr}_2\text{O}_{12}$ has been shown to react with LiCoO_2 to form La_2CoO_4 , which induces a poor lithium insertion/extraction behaviour [101].

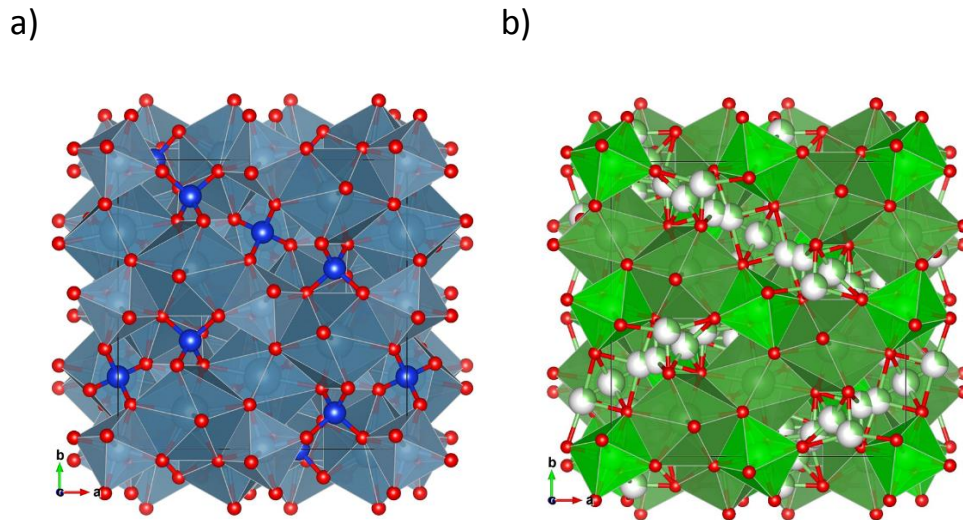


Figure 1.7. a) Unit cell of $\text{Ca}_3\text{Al}_2\text{Si}_3\text{O}_{12}$ plotted with VESTA [75] from the structural model of Abrahams et al. [102] with AlO_6 octahedra and CaO_8 dodecahedra in blue. Si and O are shown in blue and red respectively. b) Unit cell of $\text{Li}_7\text{La}_3\text{Zr}_2\text{O}_{12}$ plotted with VESTA [75] from the structural model of Geiger et al. [103] with ZrO_6 octahedra and LaO_8 dodecahedra in light green and dark green respectively. Li and O are shown in green and red respectively. Fractional occupancies are represented with pie chart style plots.

1.3.6 Perovskites

The perovskite mineral is made of CaTiO_3 and was named after Russian mineralogist Lev Perovski. Its crystal structure was discussed by Goldschmidt in 1926 [104]. Materials that are isostructural to CaTiO_3 are also called perovskites.

Perovskite materials have the general formula ABO_3 . A is the larger cation, usually a rare-earth or alkaline-earth metal-ion. B is the smaller cation and O is the oxide ion. The smaller cation presents octahedral coordination and the BO_6 octahedra are linked to each other by corner sharing. The larger A cation shows 12-fold coordination and sits in the voids of the network of linked BO_6 octahedra. The octahedral connectivity and the A site for Li and Nd can be seen in figure 1.8 for the perovskite $\text{Li}_{0.35}\text{Nd}_{0.55}\text{TiO}_3$. The tolerance factor defined by Goldschmidt is the ratio between A-O and B-O bond lengths and is used to predict the stability of the perovskite structure [52, 105].

Li can be introduced on the A site of the structure by aliovalent doping [50], although compositions with Li on both A and B sites have also been described [106].

The total ionic conductivity of e.g. $\text{Nd}_{0.55}\text{Li}_{0.34}\text{TiO}_3$ is $8 \times 10^{-8} \text{ S cm}^{-1}$ with $E_a = 0.53 \text{ eV}$ while for $\text{Pr}_{0.55}\text{Li}_{0.34}\text{TiO}_3$ is $1 \times 10^{-6} \text{ S cm}^{-1}$ with $E_a = 0.47 \text{ eV}$ at 300K. The trend for these conductivity values follows the increasing ionic radius of the rare-earth element in the order $\text{Sm}^{3+} < \text{Nd}^{3+} < \text{Pr}^{3+} < \text{La}^{3+}$. The A site of the perovskite is in the middle of eight linked BO_6 octahedra and plays the role of spacer for the Li-ions [107]. The increase in unit cell volume produced by larger ions on the A site leads to increase the size of the square-planar bottlenecks of the diffusion pathways.

One of the best Li-ion conductors in this family is $\text{Li}_{0.34}\text{La}_{0.51}\text{TiO}_{2.94}$ with a bulk ionic conductivity of $10^{-3} \text{ S cm}^{-1}$ at room temperature and a total ionic conductivity of $2 \times 10^{-5} \text{ S cm}^{-1}$ at room temperature [108]. This conductivity was slightly improved by doping with Sr. Samples of the system $[(\text{La}_{0.5}\text{Li}_{0.5})_{1-x}\text{Sr}_x]\text{TiO}_3$ with $x = 0.05$ and 0.1 had larger unit cell volume and higher bulk ionic conductivity, $1.5 \times 10^{-3} \text{ S cm}^{-1}$ at room temperature, than samples with $x = 0$. For the compositions with $x = 0.05$ and 0.1 the grain boundary or the total conductivity values were not given [109].

For $\text{Li}_{0.34}\text{La}_{0.51}\text{TiO}_{2.94}$, the total ionic conductivity is lower than the bulk ionic conductivity because it includes the grain boundary contribution. The total impedance is the addition of the bulk impedance and the grain boundary impedance, $Z_{\text{total}} = Z_{\text{bulk}} + Z_{\text{gb}}$, because in the equivalent circuit they are in series. The grain boundary impedance is in general higher than the bulk impedance and that is why the total conductivity is lower than the bulk conductivity. The total conductivity is the property of interest for practical applications. In general the studies focus in the bulk conductivity because with proper processing of the materials the grain boundary contribution can be minimised.

The major limitation for materials in this family are either a low Li-ion conductivity value or the reaction with other materials of the battery. The titanium ion can be reduced when in contact with low voltage electrodes and therefore these materials cannot be used as electrolytes in cells with lithium metal or graphite as negative electrodes [50] because the electrochemical potential of these anode materials vs Li/Li^+ is lower than the electrochemical intercalation potential of Li into the perovskite vs Li/Li^+ . A practical application of these materials as electrolyte would require an anode with a Li intercalation potential higher than 2.8 V vs Li/Li^+ [110].

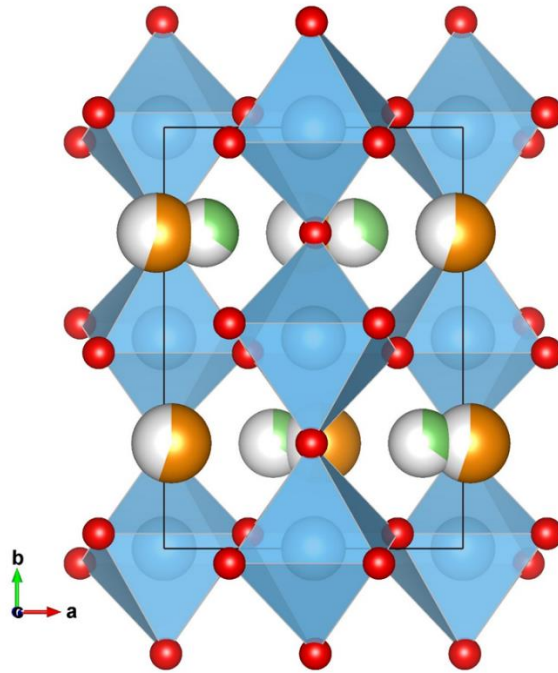


Figure 1.8. Unit cell of $\text{Li}_{0.35}\text{Nd}_{0.55}\text{TiO}_3$ plotted with VESTA [75] from the structural model of Skakle et al. [111]. TiO_6 octahedra are shown in blue. O atoms are shown in red. Nd and Li are shown as white/orange and white/green spheres on the A site of the perovskite. Partial occupancies are represented with pie chart style plots.

1.3.7 Argyrodite

Argyrodite is a relatively new family of Li-ion conductors related to the mineral Ag_8GeS_6 . Other argyrodites were already known as fast Ag^+ and Cu^+ ion conductors, e.g. compounds with formulae $\text{Ag}_6\text{PS}_5\text{X}$ and $\text{Cu}_6\text{PSe}_5\text{X}$ with $\text{X} = \text{Br}, \text{I}$ [112]. Although the phase Li_7PS_6 is known since 1976 [113], the argyrodites Li analogues $\text{Li}_6\text{PS}_5\text{X}$ with $\text{X} = \text{Cl}, \text{Br}$ and I were published in 2008 by Deiseroth et al. showing preliminary AC impedance conductivities of $10^{-3} - 10^{-2} \text{ S cm}^{-1}$ at room temperature [114].

Most of these Li-containing chalcogenides have a face-centred-cubic structure with space group $F\bar{4}3m$. The structure is based on a tetrahedral close packed network of anions with P atoms on the tetrahedral 4b sites. The PS_4 tetrahedra do not share any atoms between each other. Li is on sites 48h and 24g forming a network of

partially occupied positions close to each other that enable the hopping mechanism. The unit cell of $\text{Li}_6\text{PS}_5\text{Br}$ can be seen in figure 1.9.

Deiseroth et al. [115] showed that Li_7PS_6 has a bulk conductivity at 40 °C of $1.6 \times 10^{-6} \text{ S cm}^{-1}$ with $E_a = 0.16 \text{ eV}$. Conductivities for the substituted samples $\text{Li}_6\text{PS}_5\text{X}$ with $X = \text{Cl}, \text{Br}$ were 2×10^{-3} and $7 \times 10^{-3} \text{ S cm}^{-1}$ respectively at room temperature [116]. Compositions such as $\text{Li}_{7-x}\text{PS}_{6-x}\text{I}_x$ have also been studied. For $\text{Li}_6\text{PS}_5\text{I}$ the measured conductivity was $3.6 \times 10^{-7} \text{ S cm}^{-1}$ at room temperature with an activation energy of $E_a = 0.32 \text{ eV}$ [117].

The substitution of S by O leads to a decrease in conductivity, e.g. $\text{Li}_6\text{PO}_5\text{X}$ with $X = \text{Cl}$ shows a conductivity of about $10^{-9} \text{ S cm}^{-1}$ at room temperature with an activation energy of about 0.66 eV [118].

It has been shown by Rao et al. [119] that when a stoichiometric precursor of $\text{Li}_6\text{PS}_5\text{Cl}$ is annealed at low temperatures, e.g. 80 °C, the main crystalline phase is Li_7PS_6 . When the same precursor is annealed at temperatures above 250 °C the phase $\text{Li}_6\text{PS}_5\text{Cl}$ is formed with a conductivity of $10^{-3} \text{ S cm}^{-1}$ at room temperature and with an activation energy of $E_a = 0.16 \text{ eV}$.

Boulineau et al. showed that the electronic conductivity for $\text{Li}_6\text{PS}_5\text{X}$ is in the range $10^{-9} - 10^{-8} \text{ S cm}^{-1}$ at room temperature [120]. This value is low but relatively not negligible, which could be a limiting factor in practical applications for being in the boundary of insulators and semiconductors, i.e. the self-discharge rate would be higher than for a better electronic insulator. In addition, the high S content of some of these compositions could make them exhibit some of the limitations discussed for the Thio-LISICON materials and related phases.

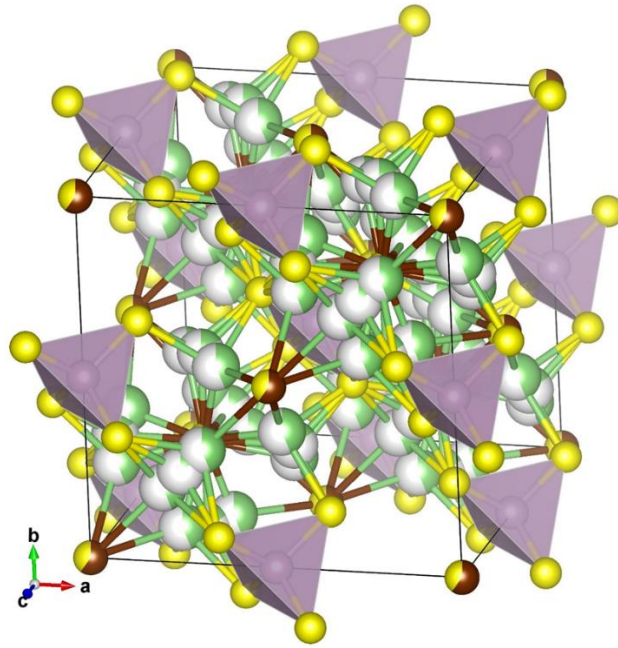


Figure 1.9. Unit cell of $\text{Li}_6\text{PS}_5\text{Br}$ plotted with VESTA [75] from the structural model of Deiseroth et al. [114]. PS_4 tetrahedra are shown in purple. S, Br and Li atoms are shown in yellow, brown and green respectively. Partial occupancies are represented with pie chart style plots.

1.3.8 Olivines

The olivine mineral owes its name to the green colour of forsterite, Mg_2SiO_4 , which resembles the colour of the olive. The olivine materials have become popular as cathodes because of LiFePO_4 [121] which is being optimised and used as cathode material for being less toxic, safer and more sustainable than LiCoO_2 and LiMn_2O_4 .

The olivine structure type has general formula ABXO_4 . It is made of AO_6 and BO_6 octahedra and XO_4 tetrahedra. The edge sharing AO_6 octahedra develop 1D channels along the b crystallographic axis as can be seen in figure 1.10 for LiFePO_4 . The BO_6 octahedra are linked by edge sharing to the XO_4 tetrahedra. These octahedron-tetrahedron units link to each other by corner sharing and leave through them the voids that host the 1D chains of edge sharing AO_6 octahedra.

The Li-ion diffusion within this structure happens along the 1D chains. This has been visualised in a sample of $\text{Li}_{0.6}\text{FePO}_4$ by using neutron diffraction and the maximum entropy method [122].

This structure type has not been thoroughly studied as a Li-ion conductor for electrolyte applications and presents an exciting opportunity for development during this thesis in order to identify new families of potential solid state electrolytes. A number of olivine materials were computationally screened for application as solid electrolytes and one of such materials is LiMgPO_4 [123]. However, it was noted that the improvement in Li-ion conductivity would need Li-vacancies which can be introduced chemically by aliovalent substitution.

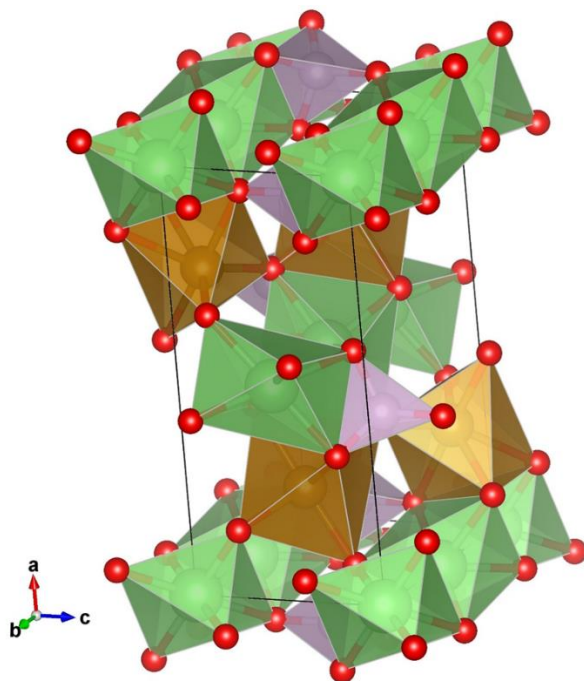


Figure 1.10. Unit cell of LiFePO_4 plotted with VESTA [75] from the structural model of Yakubovich et al. [124]. PO_4 tetrahedra are shown in purple. O, Fe and Li atoms are shown in red, brown and green respectively.

1.4 Aims of the thesis

In order to develop a future Li-ion battery technology that will be safer, cheaper and better performer than current batteries, new solid state electrolytes will be needed. The literature review of this chapter has shown that all the known materials present limitations. One of the major obstacles is the low Li-ion conductivity in solids. When the known materials achieve high conductivity values, these materials present other limitations such as ageing or lack of chemical stability. The manufacture of all solid state Li-ion batteries with the known materials would lead to batteries of lower quality than those currently in use.

This thesis will pursue the discovery of new materials with high Li-ion conductivities, in the range $10^{-3} - 10^{-2} \text{ S cm}^{-1}$ at room temperature, but with no chemical stability issues. A way to achieve this is the identification of new families of Li-ion conductors, e.g. within the olivine-type structure.

The conductivity increase will be attempted through addition of extrinsic defects to stable materials, in particular Li-vacancy introduction by aliovalent doping or synthesis of solid solutions. Another approach will be to investigate the effect of phosphorous excess in phosphate Li-ion conductors. Finally the exploration of new synthetic spaces will be used for the identification of new phases.

1.5 References

1. Tarascon, J.-M. and M. Armand, *Issues and challenges facing rechargeable lithium batteries*. Nature, 2001. **414**(6861): p. 359-367.
2. Wang, Q., P. Ping, X. Zhao, G. Chu, J. Sun, and C. Chen, *Thermal runaway caused fire and explosion of lithium ion battery*. Journal of power sources, 2012. **208**: p. 210-224.
3. Poizot, P. and F. Dolhem, *Clean energy new deal for a sustainable world: from non-CO₂ generating energy sources to greener electrochemical storage devices*. Energy & Environmental Science, 2011. **4**(6): p. 2003-2019.
4. Lindley, D., *Smart grids: The energy storage problem*. Nature, 2010. **463**(7277): p. 18.
5. Armand, M. and J.-M. Tarascon, *Building better batteries*. Nature, 2008. **451**(7179): p. 652-657.
6. Khaligh, A. and Z. Li, *Battery, ultracapacitor, fuel cell, and hybrid energy storage systems for electric, hybrid electric, fuel cell, and plug-in hybrid electric vehicles: State of the art*. IEEE transactions on Vehicular Technology, 2010. **59**(6): p. 2806-2814.
7. Dunn, B., H. Kamath, and J.-M. Tarascon, *Electrical energy storage for the grid: a battery of choices*. Science, 2011. **334**(6058): p. 928-935.
8. Park, M., X. Zhang, M. Chung, G.B. Less, and A.M. Sastry, *A review of conduction phenomena in Li-ion batteries*. Journal of Power Sources, 2010. **195**(24): p. 7904-7929.
9. Winter, M. and R.J. Brodd, *What are batteries, fuel cells, and supercapacitors?* Chemical reviews, 2004. **104**(10): p. 4245-4270.
10. Julien, C., A. Mauger, A. Vijn, and K. Zaghib, in *Lithium Batteries: Science and Technology*. 2016, Springer International Publishing: Cham.
11. Greatbatch, W., J.H. Lee, W. Mathias, M. Eldridge, J.R. Moser, and A.A. Schneider, *The solid-state lithium battery: a new improved chemical power source for implantable cardiac pacemakers*. IEEE Transactions on Biomedical Engineering, 1971(5): p. 317-324.
12. Scrosati, B., *History of lithium batteries*. Journal of solid state electrochemistry, 2011. **15**(7-8): p. 1623-1630.
13. Nitta, N., F. Wu, J.T. Lee, and G. Yushin, *Li-ion battery materials: present and future*. Materials Today, 2015. **18**(5): p. 252-264.
14. Aurbach, D., E. Zinigrad, Y. Cohen, and H. Teller, *A short review of failure mechanisms of lithium metal and lithiated graphite anodes in liquid electrolyte solutions*. Solid state ionics, 2002. **148**(3): p. 405-416.
15. Tarascon, J. and D. Guyomard, *The Li_{1+x}Mn₂O₄/C rocking-chair system: a review*. Electrochimica Acta, 1993. **38**(9): p. 1221-1231.
16. Kitta, M., T. Akita, S. Tanaka, and M. Kohyama, *Two-phase separation in a lithiated spinel Li₄Ti₅O₁₂ crystal as confirmed by electron energy-loss spectroscopy*. Journal of Power Sources, 2014. **257**: p. 120-125.
17. He, Y.-B., B. Li, M. Liu, C. Zhang, W. Lv, C. Yang, J. Li, H. Du, B. Zhang, Q.-H. Yang, J.-K. Kim, and F. Kang, *Gassing in Li₄Ti₅O₁₂-based batteries and its remedy*. Scientific Reports, 2012. **2**: p. 913.
18. Gabrisch, H., Y. Ozawa, and R. Yazami, *Crystal structure studies of thermally aged LiCoO₂ and LiMn₂O₄ cathodes*. Electrochimica acta, 2006. **52**(4): p. 1499-1506.

19. Yoshio, M., R.J. Brodd, and A. Kozawa, *Lithium-ion batteries*. Vol. 1. 2009: Springer.
20. Choi, S.H., J. Kim, and Y.S. Yoon, *A TEM study of cycled nano-crystalline HT-LiCoO₂ cathodes for rechargeable lithium batteries*. Journal of power sources, 2004. **135**(1): p. 286-290.
21. Etacheri, V., R. Marom, R. Elazari, G. Salitra, and D. Aurbach, *Challenges in the development of advanced Li-ion batteries: a review*. Energy & Environmental Science, 2011. **4**(9): p. 3243-3262.
22. Gabrisch, H., R. Yazami, and B. Fultz, *A transmission electron microscopy study of cycled LiCoO₂*. Journal of power sources, 2003. **119**: p. 674-679.
23. Patoux, S., L. Daniel, C. Bourbon, H. Lignier, C. Pagano, F. Le Cras, S. Jouanneau, and S. Martinet, *High voltage spinel oxides for Li-ion batteries: From the material research to the application*. Journal of Power Sources, 2009. **189**(1): p. 344-352.
24. Ellis, B.L., K.T. Lee, and L.F. Nazar, *Positive electrode materials for Li-ion and Li-batteries*. Chemistry of Materials, 2010. **22**(3): p. 691-714.
25. Biendicho, J.J. and A.R. West, *Thermally-induced cation disorder in LiFePO₄*. Solid State Ionics, 2011. **203**(1): p. 33-36.
26. Jiang, J. and J. Dahn, *ARC studies of the thermal stability of three different cathode materials: LiCoO₂; Li[Ni_{0.1}Co_{0.8}Mn_{0.1}]O₂; and LiFePO₄, in LiPF₆ and LiBoB EC/DEC electrolytes*. Electrochemistry Communications, 2004. **6**(1): p. 39-43.
27. Rozier, P. and J.M. Tarascon, *Review—Li-rich layered oxide cathodes for next-generation Li-ion batteries: chances and challenges*. Journal of The Electrochemical Society, 2015. **162**(14): p. A2490-A2499.
28. Zhang, S.S., *A review on electrolyte additives for lithium-ion batteries*. Journal of Power Sources, 2006. **162**(2): p. 1379-1394.
29. Fromling, T., M. Kunze, M. Schonhoff, J. Sundermeyer, and B. Roling, *Enhanced lithium transference numbers in ionic liquid electrolytes*. The Journal of Physical Chemistry B, 2008. **112**(41): p. 12985-12990.
30. Kraysberg, A. and Y. Ein-Eli, *Higher, Stronger, Better... □ A Review of 5 Volt Cathode Materials for Advanced Lithium-Ion Batteries*. Advanced Energy Materials, 2012. **2**(8): p. 922-939.
31. Aurbach, D., Y. Talyosef, B. Markovsky, E. Markevich, E. Zinigrad, L. Asraf, J.S. Gnanaraj, and H.-J. Kim, *Design of electrolyte solutions for Li and Li-ion batteries: a review*. Electrochimica Acta, 2004. **50**(2): p. 247-254.
32. Wang, Y., B. Liu, Q. Li, S. Cartmell, S. Ferrara, Z.D. Deng, and J. Xiao, *Lithium and lithium ion batteries for applications in microelectronic devices: A review*. Journal of Power Sources, 2015. **286**: p. 330-345.
33. Kim, J.G., B. Son, S. Mukherjee, N. Schuppert, A. Bates, O. Kwon, M.J. Choi, H.Y. Chung, and S. Park, *A review of lithium and non-lithium based solid state batteries*. Journal of Power Sources, 2015. **282**: p. 299-322.
34. Knauth, P., *Inorganic solid Li ion conductors: An overview*. Solid State Ionics, 2009. **180**(14): p. 911-916.
35. Zhang, S.S., *A review on the separators of liquid electrolyte Li-ion batteries*. Journal of Power Sources, 2007. **164**(1): p. 351-364.
36. Chung, Y., S. Yoo, and C. Kim, *Enhancement of meltdown temperature of the polyethylene lithium-ion battery separator via surface coating with polymers having high thermal resistance*. Industrial & Engineering Chemistry Research, 2009. **48**(9): p. 4346-4351.

37. Zhang, J., Z. Liu, Q. Kong, C. Zhang, S. Pang, L. Yue, X. Wang, J. Yao, and G. Cui, *Renewable and superior thermal-resistant cellulose-based composite nonwoven as lithium-ion battery separator*. ACS applied materials & interfaces, 2012. **5**(1): p. 128-134.
38. Buqa, H., R.I. Blyth, P. Golob, B. Evers, I. Schneider, M. Santis Alvarez, F. Hofer, F. Netzer, M. Ramsey, and M. Winter, *Negative electrodes in rechargeable lithium ion batteries - Influence of graphite surface modification on the formation of the solid electrolyte interphase*. Ionics, 2000. **6**(3): p. 172-179.
39. Aurbach, D., *Electrode-solution interactions in Li-ion batteries: a short summary and new insights*. Journal of power sources, 2003. **119**: p. 497-503.
40. Braithwaite, J.W., A. Gonzales, G. Nagasubramanian, S.J. Lucero, D.E. Peebles, J.A. Ohlhausen, and W.R. Cieslak, *Corrosion of lithium-ion battery current collectors*. Journal of The Electrochemical Society, 1999. **146**(2): p. 448-456.
41. Aydinol, M. and G. Ceder, *First-Principles Prediction of Insertion Potentials in Li-Mn Oxides for Secondary Li Batteries*. Journal of the Electrochemical Society, 1997. **144**(11): p. 3832-3835.
42. Sathiya, M., G. Rousse, K. Ramesha, C.P. Laisa, H. Vezin, M.T. Sougrati, M.L. Doublet, D. Foix, D. Gonbeau, W. Walker, A.S. Prakash, M. Ben Hassine, L. Dupont, and J.M. Tarascon, *Reversible anionic redox chemistry in high-capacity layered-oxide electrodes*. Nat Mater, 2013. **12**(9): p. 827-35.
43. McCalla, E., A.M. Abakumov, M. Saubanere, D. Foix, E.J. Berg, G. Rouse, M.L. Doublet, D. Gonbeau, P. Novak, G. Van Tendeloo, R. Dominko, and J.M. Tarascon, *Visualization of O-O peroxo-like dimers in high-capacity layered oxides for Li-ion batteries*. Science, 2015. **350**(6267): p. 1516-21.
44. Ceder, G., Y.-M. Chiang, D. Sadoway, M. Aydinol, Y.-I. Jang, and B. Huang, *Identification of cathode materials for lithium batteries guided by first-principles calculations*. Nature, 1998. **392**(6677): p. 694-696.
45. Yang, H., H. Bang, K. Amine, and J. Prakash, *Investigations of the exothermic reactions of natural graphite anode for Li-ion batteries during thermal runaway*. Journal of the Electrochemical Society, 2005. **152**(1): p. A73-A79.
46. Balakrishnan, P., R. Ramesh, and T.P. Kumar, *Safety mechanisms in lithium-ion batteries*. Journal of Power Sources, 2006. **155**(2): p. 401-414.
47. Doh, C.-H., D.-H. Kim, H.-S. Kim, H.-M. Shin, Y.-D. Jeong, S.-I. Moon, B.-S. Jin, S.W. Eom, H.-S. Kim, and K.-W. Kim, *Thermal and electrochemical behaviour of C/Li_xCoO₂ cell during safety test*. Journal of Power Sources, 2008. **175**(2): p. 881-885.
48. Spotnitz, R. and J. Franklin, *Abuse behavior of high-power, lithium-ion cells*. Journal of Power Sources, 2003. **113**(1): p. 81-100.
49. Jiang, J. and J. Dahn, *Effects of particle size and electrolyte salt on the thermal stability of Li_{0.5}CoO₂*. Electrochimica acta, 2004. **49**(16): p. 2661-2666.
50. Bachman, J.C., S. Muy, A. Grimaud, H.H. Chang, N. Pour, S.F. Lux, O. Paschos, F. Maglia, S. Lupart, P. Lamp, L. Giordano, and Y. Shao-Horn, *Inorganic Solid-State Electrolytes for Lithium Batteries: Mechanisms and Properties Governing Ion Conduction*. Chem Rev, 2016. **116**(1): p. 140-62.
51. Smart, L.E. and E.A. Moore, *Solid state chemistry: an introduction*. 2012: CRC press.

52. West, A.R., *Basic solid state chemistry*. Vol. 36. 1999: John Wiley & Sons New York.
53. Bruce, P.G., *Solid state electrochemistry*. Vol. 5. 1997: Cambridge University Press.
54. Wu, X. and Y.F. Zheng, *Compensation effect for electrical conductivity and its applications to estimate oxygen diffusivity in minerals*. Journal of Geophysical Research: Solid Earth, 2003. **108**(B3).
55. Dudney, N.J., W.C. West, and J. Nanda, *Handbook of Solid State Batteries*. Vol. 6. 2015: World Scientific.
56. Catlow, C.R.A., *Atomistic mechanisms of ionic transport in fast-ion conductors*. Journal of the Chemical Society, Faraday Transactions, 1990. **86**(8): p. 1167-1176.
57. Catlow, C.R.A., *Defect processes and migration mechanisms in solid state ionics*. Materials Science and Engineering: B, 1992. **12**(4): p. 375-382.
58. McNaught, A.D. and A. Wilkinson, *IUPAC. Compendium of Chemical Terminology, 2nd ed. (the "Gold Book")*. Vol. 1669. 1997: Blackwell Science Oxford.
59. Li, J., W. Yao, S. Martin, and D. Vaknin, *Lithium ion conductivity in single crystal LiFePO₄*. Solid State Ionics, 2008. **179**(35): p. 2016-2019.
60. Hagenmuller, P. and W. Van Gool, *Solid electrolytes: general principles, characterization, materials, applications*. 1978: Academic Press.
61. Onoda, Y., M. Watanabe, Y. Fujiki, S. Yoshikado, T. Ohachi, and I. Taniguchi, *NMR study of one dimensional ionic conductor A_xGa₈Ga_{8+x}Ti_{16-x}O₅₆ (A = Cs, Rb)*. Solid State Ionics, 1989. **35**(3-4): p. 387-394.
62. Gellings, P.J. and H. Bouwmeester, *Handbook of solid state electrochemistry*. 1997: CRC press.
63. Schlaikjer, C.R. and C.C. Liang, *Ionic conduction in calcium doped polycrystalline lithium iodide*. Journal of The Electrochemical Society, 1971. **118**(9): p. 1447-1450.
64. Liang, C., *Conduction Characteristics of the Lithium Iodide-Aluminum Oxide Solid Electrolytes*. Journal of The Electrochemical Society, 1973. **120**(10): p. 1289-1292.
65. Alpen, U.v., A. Rabenau, and G. Talat, *Ionic conductivity in Li₃N single crystals*. Applied Physics Letters, 1977. **30**(12): p. 621-623.
66. Rabenau, A., *Lithium nitride and related materials case study of the use of modern solid state research techniques*. Solid State Ionics, 1982. **6**(4): p. 277-293.
67. Hartwig, P., W. Weppner, and W. Wichelhaus, *Fast ionic lithium conduction in solid lithium nitride chloride*. Materials Research Bulletin, 1979. **14**(4): p. 493-498.
68. Kanno, R., Y. Takeda, K. Takada, and O. Yamamoto, *Ionic Conductivity and Phase Transition of the Spinel System Li_{2-2x}M_{1+x}Cl₄ (M= Mg, Mn, Cd)*. Journal of The Electrochemical Society, 1984. **131**(3): p. 469-474.
69. Hu, Y.W., I. Raistrick, and R.A. Huggins, *Ionic Conductivity of Lithium Orthosilicate—Lithium Phosphate Solid Solutions*. Journal of the Electrochemical society, 1977. **124**(8): p. 1240-1242.
70. Garcia, A., G. Torres-Trevino, and A.R. West, *New lithium ion conductors based on the γ-LiAlO₂ structure*. Solid State Ionics, 1990. **40**: p. 13-17.
71. Rodger, A., J. Kuwano, and A. West, *Li⁺ ion conducting γ solid solutions in the systems Li₄XO₄-Li₃YO₄: X= Si, Ge, Ti; Y= P, As, V; Li₄XO₄-LiZO₂: Z= Al, Ga, Cr and Li₄GeO₄-Li₂CaGeO₄*. Solid State Ionics, 1985. **15**(3): p. 185-198.

72. Hagman, L.O. and P. Kierkegaard, *The crystal structure of $\text{NaMe}_2^{\text{IV}}(\text{PO}_4)_3$; $\text{Me}^{\text{IV}} = \text{Ge, Ti, Zr}$* . Acta Chem. Scand, 1968. **22**(6): p. 1822-32.
73. Goodenough, J., H.-P. Hong, and J. Kafalas, *Fast Na^+ -ion transport in skeleton structures*. Materials Research Bulletin, 1976. **11**(2): p. 203-220.
74. Aono, H., E. Sugimoto, Y. Sadaoka, N. Imanaka, and G.y. Adachi, *The Electrical Properties of Ceramic Electrolytes for $\text{LiM}_x\text{Ti}_{2-x}(\text{PO}_4)_3 + y\text{Li}_2\text{O}$, $M = \text{Ge, Sn, Hf, and Zr}$ Systems*. Journal of The Electrochemical Society, 1993. **140**(7): p. 1827-1833.
75. Momma, K. and F. Izumi, *VESTA 3 for three-dimensional visualization of crystal, volumetric and morphology data*. Journal of Applied Crystallography, 2011. **44**(6): p. 1272-1276.
76. Didisheim, J.-J., E. Prince, and B. Wuensch, *Neutron Rietveld analysis of structural changes in NASICON solid solutions $\text{Na}_{1+x}\text{Zr}_2\text{Si}_x\text{P}_{3-x}\text{O}_{12}$ at elevated temperatures: $x = 1.6$ and 2.0 at 320°C* . Solid State Ionics, 1986. **18**: p. 944-958.
77. Thangadurai, V., A.K. Shukla, and J. Gopalakrishnan, *New lithium-ion conductors based on the NASICON structure*. Journal of Materials Chemistry, 1999. **9**(3): p. 739-741.
78. Yamamoto, H., M. Tabuchi, T. Takeuchi, H. Kageyama, and O. Nakamura, *Ionic conductivity enhancement in $\text{LiGe}_2(\text{PO}_4)_3$ solid electrolyte*. Journal of power sources, 1997. **68**(2): p. 397-401.
79. Aono, H., E. Sugimoto, Y. Sadaoka, N. Imanaka, and G.y. Adachi, *Ionic conductivity of solid electrolytes based on lithium titanium phosphate*. Journal of the electrochemical society, 1990. **137**(4): p. 1023-1027.
80. Bruce, P. and A. West, *Ion trapping and its effect on the conductivity of LISICON and other solid electrolytes*. Journal of Solid State Chemistry, 1984. **53**(3): p. 430-434.
81. Bruce, P. and A. West, *Ionic conductivity of LISICON solid solutions, $\text{Li}_{2+2x}\text{Zn}_{1-x}\text{GeO}_4$* . Journal of Solid State Chemistry, 1982. **44**(3): p. 354-365.
82. Abrahams, I., P. Bruce, W. David, and A. West, *A re-examination of the lisicon structure using high-resolution powder neutron diffraction: evidence for defect clustering*. Acta Crystallographica Section B: Structural Science, 1989. **45**(5): p. 457-462.
83. Bruce, P., I. Abrahams, and A. West, *Defect clustering in lisicon solid electrolytes*. Solid State Ionics, 1990. **40**: p. 293-299.
84. Kuwano, J. and A.R. West, *New Li^+ ion conductors in the system, $\text{Li}_4\text{GeO}_4\text{-Li}_3\text{VO}_4$* . Materials Research Bulletin, 1980. **15**(11): p. 1661-1667.
85. Yakubovich, O. and V. Urusov, *Electron density distribution in lithiophosphatite Li_3PO_4 . Crystallochemical features of orthophosphate groups with hexagonal close packing*. Kristallografiya, 1997. **42**(2): p. 301-308.
86. Kanno, R., T. Hata, Y. Kawamoto, and M. Irie, *Synthesis of a new lithium ionic conductor, thio-LISICON—lithium germanium sulfide system*. Solid State Ionics, 2000. **130**(1): p. 97-104.
87. Murayama, M., R. Kanno, M. Irie, S. Ito, T. Hata, N. Sonoyama, and Y. Kawamoto, *Synthesis of new lithium ionic conductor thio-LISICON—lithium silicon sulfides system*. Journal of Solid State Chemistry, 2002. **168**(1): p. 140-148.
88. Kanno, R. and M. Murayama, *Lithium Ionic Conductor Thio-LISICON: The $\text{Li}_2\text{S-GeS}_2\text{-P}_2\text{S}_5$ System*. Journal of The Electrochemical Society, 2001. **148**(7): p. A742-A746.

89. Whiteley, J.M., J.H. Woo, E. Hu, K.-W. Nam, and S.-H. Lee, *Empowering the lithium metal battery through a silicon-based superionic conductor*. Journal of the Electrochemical Society, 2014. **161**(12): p. A1812-A1817.
90. Bron, P., S. Johansson, K. Zick, J.r. Schmedt auf der Günne, S. Dehnen, and B. Roling, *Li₁₀SnP₂S₁₂: an affordable lithium superionic conductor*. Journal of the American Chemical Society, 2013. **135**(42): p. 15694-15697.
91. Kamaya, N., K. Homma, Y. Yamakawa, M. Hirayama, R. Kanno, M. Yonemura, T. Kamiyama, Y. Kato, S. Hama, and K. Kawamoto, *A lithium superionic conductor*. Nature materials, 2011. **10**(9): p. 682-686.
92. Kato, Y., R. Saito, M. Sakano, A. Mitsui, M. Hirayama, and R. Kanno, *Synthesis, structure and lithium ionic conductivity of solid solutions of Li₁₀(Ge_{1-x}M_x)P₂S₁₂ (M = Si, Sn)*. Journal of Power Sources, 2014. **271**: p. 60-64.
93. Cao, C., Z.-B. Li, X.-L. Wang, X.-B. Zhao, and W.-Q. Han, *Recent advances in inorganic solid electrolytes for lithium batteries*. Frontiers in Energy Research, 2014. **2**: p. 25.
94. Kuhn, A., J. Köhler, and B.V. Lotsch, *Single-crystal X-ray structure analysis of the superionic conductor Li₁₀GeP₂S₁₂*. Physical Chemistry Chemical Physics, 2013. **15**(28): p. 11620-11622.
95. O'Callaghan, M.P., D.R. Lynham, E.J. Cussen, and G.Z. Chen, *Structure and Ionic-Transport Properties of Lithium-Containing Garnets Li₃Ln₃Te₂O₁₂ (Ln = Y, Pr, Nd, Sm-Lu)*. Chemistry of materials, 2006. **18**(19): p. 4681-4689.
96. Thangadurai, V., S. Narayanan, and D. Pinzaru, *Garnet-type solid-state fast Li ion conductors for Li batteries: critical review*. Chemical Society Reviews, 2014. **43**(13): p. 4714-4727.
97. Gao, Y., X. Wang, W. Wang, and Q. Fang, *Sol-gel synthesis and electrical properties of Li₅La₃Ta₂O₁₂ lithium ionic conductors*. Solid State Ionics, 2010. **181**(1): p. 33-36.
98. Thangadurai, V. and W. Weppner, *Li₆Ala₂Ta₂O₁₂ (A = Sr, Ba): Novel Garnet-Like Oxides for Fast Lithium Ion Conduction*. Advanced Functional Materials, 2005. **15**(1): p. 107-112.
99. Li, Y., J.-T. Han, C.-A. Wang, S.C. Vogel, H. Xie, M. Xu, and J.B. Goodenough, *Ionic distribution and conductivity in lithium garnet Li₇La₃Zr₂O₁₂*. Journal of Power Sources, 2012. **209**: p. 278-281.
100. Bernuy-Lopez, C., W. Manalastas Jr, J.M. Lopez del Amo, A. Aguadero, F. Aguesse, and J.A. Kilner, *Atmosphere controlled processing of Ga-substituted garnets for high Li-ion conductivity ceramics*. Chemistry of Materials, 2014. **26**(12): p. 3610-3617.
101. Kim, K.H., Y. Iriyama, K. Yamamoto, S. Kumazaki, T. Asaka, K. Tanabe, C.A. Fisher, T. Hirayama, R. Murugan, and Z. Ogumi, *Characterization of the interface between LiCoO₂ and Li₇La₃Zr₂O₁₂ in an all-solid-state rechargeable lithium battery*. Journal of Power Sources, 2011. **196**(2): p. 764-767.
102. Abrahams, S. and S. Geller, *Refinement of the structure of a grossularite garnet*. Acta Crystallographica, 1958. **11**(6): p. 437-441.
103. Geiger, C.A., E. Alekseev, B. Lazic, M. Fisch, T. Armbruster, R. Langner, M. Fechtelkord, N. Kim, T. Pettke, and W. Weppner, *Crystal chemistry and stability of "Li₇La₃Zr₂O₁₂" garnet: a fast lithium-ion conductor*. Inorganic chemistry, 2010. **50**(3): p. 1089-1097.
104. Goldschmidt, V.M., *Die gesetze der krystallochemie*. Naturwissenschaften, 1926. **14**(21): p. 477-485.

105. Huggins, R., *Advanced batteries: materials science aspects*. 2008: Springer Science & Business Media.
106. Santibáñez-Mendieta, A.B., C. Didier, K.K. Inglis, A.J. Corkett, M.J. Pitcher, M. Zanella, J.F. Shin, L.M. Daniels, A. Rakhmatullin, M. Li, M.S. Dyer, J.B. Claridge, F. Blanc, and M.J. Rosseinsky, *La₃Li₃W₂O₁₂: Ionic Diffusion in a Perovskite with Lithium on both A- and B-Sites*. *Chemistry of Materials*, 2016. **28**(21): p. 7833-7851.
107. Itoh, M., Y. Inaguma, W.-H. Jung, L. Chen, and T. Nakamura, *High lithium ion conductivity in the perovskite-type compounds Ln₁₂Li₁₂TiO₃ (Ln = La, Pr, Nd, Sm)*. *Solid State Ionics*, 1994. **70**: p. 203-207.
108. Inaguma, Y., C. Lique, M. Itoh, T. Nakamura, T. Uchida, H. Ikuta, and M. Wakihara, *High ionic conductivity in lithium lanthanum titanate*. *Solid State Communications*, 1993. **86**(10): p. 689-693.
109. Inaguma, Y., L. Chen, M. Itoh, and T. Nakamura, *Candidate compounds with perovskite structure for high lithium ionic conductivity*. *Solid State Ionics*, 1994. **70**: p. 196-202.
110. Bohnke, O., C. Bohnke, and J. Fourquet, *Mechanism of ionic conduction and electrochemical intercalation of lithium into the perovskite lanthanum lithium titanate*. *Solid State Ionics*, 1996. **91**(1): p. 21-31.
111. Skakle, J.M., G.C. Mather, M. Morales, R.I. Smith, and A.R. West, *Crystal structure of the Li⁺ ion-conducting phases, Li_{0.5-3x}Re_{0.5+x}TiO₃: RE = Pr, Nd; x ≈ 0.05*. *Journal of Materials Chemistry*, 1995. **5**(11): p. 1807-1808.
112. Beeken, R., J. Garbe, J. Gillis, N. Petersen, B. Podoll, and M. Stoneman, *Electrical conductivities of the Ag₆PS₅X and the Cu₆PSe₅X (X = Br, I) argyrodites*. *Journal of Physics and Chemistry of Solids*, 2005. **66**(5): p. 882-886.
113. Brice, J.F., *Preparation and Study of 2 Ternary Lithium-Phosphorus Sulfides - Li₈P₂S₉ and Li₇PS₆*. *Comptes Rendus Hebdomadaires Des Seances De L Academie Des Sciences Serie C*, 1976. **283**(13): p. 581-584.
114. Deiseroth, H.J., S.T. Kong, H. Eckert, J. Vannahme, C. Reiner, T. Zais, and M. Schlosser, *Li₆PS₅X: A Class of Crystalline Li-Rich Solids With an Unusually High Li⁺ Mobility*. *Angewandte Chemie International Edition*, 2008. **47**(4): p. 755-758.
115. Deiseroth, H.J., J. Maier, K. Weichert, V. Nickel, S.T. Kong, and C. Reiner, *Li₇PS₆ and Li₆PS₅X (X: Cl, Br, I): Possible Three-dimensional Diffusion Pathways for Lithium Ions and Temperature Dependence of the Ionic Conductivity by Impedance Measurements*. *Zeitschrift für anorganische und allgemeine Chemie*, 2011. **637**(10): p. 1287-1294.
116. Rao, R.P. and S. Adams, *Studies of lithium argyrodite solid electrolytes for all-solid-state batteries*. *physica status solidi (a)*, 2011. **208**(8): p. 1804-1807.
117. Pecher, O., S.T. Kong, T. Goebel, V. Nickel, K. Weichert, C. Reiner, H.J. Deiseroth, J. Maier, F. Haarmann, and D. Zahn, *Atomistic Characterisation of Li⁺ Mobility and Conductivity in Li_{7-x}PS_{6-x}I_x Argyrodites from Molecular Dynamics Simulations, Solid-State NMR, and Impedance Spectroscopy*. *Chemistry—A European Journal*, 2010. **16**(28): p. 8347-8354.
118. Kong, S.T., H.J. Deiseroth, J. Maier, V. Nickel, K. Weichert, and C. Reiner, *Li₆PO₅Br and Li₆PO₅Cl: The first Lithium-Oxide-Argyrodites*. *Zeitschrift für anorganische und allgemeine Chemie*, 2010. **636**(11): p. 1920-1924.

119. Rao, R.P., N. Sharma, V. Peterson, and S. Adams, *Formation and conductivity studies of lithium argyrodite solid electrolytes using in-situ neutron diffraction*. *Solid State Ionics*, 2013. **230**: p. 72-76.
120. Boulineau, S., M. Courty, J.-M. Tarascon, and V. Viallet, *Mechanochemical synthesis of Li-argyrodite $\text{Li}_6\text{PS}_5\text{X}$ ($\text{X} = \text{Cl}, \text{Br}, \text{I}$) as sulfur-based solid electrolytes for all solid state batteries application*. *Solid State Ionics*, 2012. **221**: p. 1-5.
121. Zaghbi, K., A. Guerfi, P. Hovington, A. Vijn, M. Trudeau, A. Mauger, J.B. Goodenough, and C.M. Julien, *Review and analysis of nanostructured olivine-based lithium rechargeable batteries: Status and trends*. *Journal of Power Sources*, 2013. **232**: p. 357-369.
122. Nishimura, S.-i., G. Kobayashi, K. Ohoyama, R. Kanno, M. Yashima, and A. Yamada, *Experimental visualization of lithium diffusion in Li_xFePO_4* . *Nature materials*, 2008. **7**(9): p. 707-711.
123. Jalem, R., T. Aoyama, M. Nakayama, and M. Nogami, *Multivariate Method-Assisted Ab Initio Study of Olivine-Type LiMXO_4 (Main Group M^{2+} - X^{5+} and M^{3+} - X^{4+}) Compositions as Potential Solid Electrolytes*. *Chemistry of Materials*, 2012. **24**(7): p. 1357-1364.
124. Yakubovich, O., E. Belokoneva, V. Tsirel'son, and V. Urusov, *Electron density distribution in synthetic triphylite LiFePO_4* . *Vestnik Moskovskogo Universiteta, Geologiya*, 1990. **45**: p. 93-99.

Chapter 2

Experimental techniques

2.1 Synthetic methods

2.1.1 Solid state route

During this thesis all the syntheses have been performed by using ceramic synthesis, i.e. by heating at high temperatures homogeneous precursors. These precursors have been prepared by grinding and mixing of reactants, either with pestle and mortar or with planetary mill. In this thesis pestle and mortar have been used generally for small scale samples up to 3 grams and mechanical milling for larger scale samples, e.g. 6 grams.

The governing process to form the products from the precursors is the ion diffusion in the solid. The kinetics for this process are very slow and the activation energy very high. That is why high temperatures, sometimes close to the melting point, are needed [1]. This synthetic method usually produces the thermodynamic product. When meta-stable phases are required, solution methods at lower temperatures are generally used [2].

The ceramic synthesis is ideal for exploratory studies. Among the traditional methods, it is the easiest to follow. Once the stoichiometric amounts have been weighed out with enough accuracy, these are mixed and then loaded in a crucible. The grinding/mixing step can be made either under dry or wet conditions. When the wet grinding is chosen, common solvents are ethanol or acetone. The precursor can then be loaded in the crucible either as loose powder or as a pellet. The crucible is usually made of alumina, zirconia or platinum.

It is good practice to work with furnaces that have been calibrated in the ranges of temperature of the reaction. Working with care, high quality samples can be prepared by using ceramic synthesis.

The details for the synthesis of each material are presented in the section in which the material is discussed.

2.1.2 Pelletising and Pressing

Pelletising is a process in which a material is compressed into the shape of a pellet. It involves loading a cylinder template, known as pellet die, with the powder and using a plunger to apply pressure and compact the solid until it forms a rigid body. The pressure is usually applied with a hydraulic press with an indicating gauge that reads the applied load.

During this thesis, pelletising for synthesis has been done at the lowest pressure that allowed for a rigid solid piece to be manipulated for being placed inside the crucible. Pelletising for property measurements has been done at the lowest possible pressure as well. Using relatively high pressures usually results in broken pellets after extraction from the pellet die or contaminated pellets by the material of the pellet die.

It is important to translate loads in the press into actual uniaxial pressures in the pellet. This is made by means of equation 2.1.

$$P = m g / A \quad (\text{Eq. 2.1})$$

Where P is the pressure in Pascal, m is the load in Kg, g is the standard acceleration due to gravity, i.e. approx. 9.81 m/s² and A is the area of the pellet in m².

Using equation 2.1 a table of standard pressures for different pellet diameters can be made as is shown in table 2.1. High load is generally used for oxide materials for which the pellet is hard to form. Low load is used for powders that form pellets very easily. In general it is good practice to try the low load first.

Table 2.1. Approximate standard loads for different pellet die sets.

Pellet die diameter	High load	Low load
5 mm	150 Kg	2.5 Kg
8 mm	400 Kg	6 Kg
10 mm	600 Kg	10 Kg
13 mm	1000 Kg	16 Kg
20 mm	2400 Kg	40 Kg
32 mm	6000 Kg	100 Kg
Uniaxial pressure in the pellet:	74 MPa	1.2 MPa

2.1.3 Buffer pellets

Crucibles are made of materials that aim to be inert at the reaction temperature or towards the reaction mixture. However this inertness cannot always be guaranteed. A method repeatedly used during this thesis to isolate the reaction from the crucible has been to place a buffer pellet between both. If there is reaction between the precursor and the crucible, this contamination will affect the buffer pellet, but in general it will not reach the main pellet.

The main sample is commonly prepared from a pressed pellet of the precursors. A buffer pellet is another pellet made of the same precursor that generally uses a minor fraction of it, e.g. 1.5 grams of precursor can be split in 1.2 grams for the sample and about 0.3 grams for the buffer pellet. If the synthesis is for a large batch, the large main pellet can be supported on three small pellets in order to save precursor.

2.1.4 Planetary mill

Mechanical milling is convenient when either the sample size is large or either a better mixing is required. High energy mechanical milling is also useful when reduction of particle size is required [3].

Mechanical milling allows for an effortless repetition of the milling process. For most types of mills, e.g. the planetary mill, the intensity of the milling can be set. A sensible combination of milling media, speed and time must be used in order to achieve an effective reduction in particle size or homogenisation without incurring contamination of the sample with traces of milling media.

A planetary mill is a type of mill in which pots loaded with sample and milling media are mounted off centre of a rotating disk. The disk rotates at the same time that the pots are rotated uniaxially. Both movements happen in opposite directions causing the balls of the milling media to collide between them, the sample and the pot [4].

During this thesis the planetary mill Pulverisette 7 has been used along with zirconia milling media in order to mix reactants to prepare precursors. The second target for which it has been used has been to reduce particle size of ceramics during the processing for densification. The samples presented during this thesis have not shown zirconia contamination when studied by powder X-ray diffraction.

Commonly, 45 ml zirconia pots with 10 mm zirconia balls have been used in this thesis as milling media. Typical sample loads have been in the range 1 – 10 grams, generally loaded with 20 ml of ethanol. The number of balls used per pot ranged from 3 to 7 depending of the size of the sample. Finally, the mills have been used at 350 rpm, with milling/resting times of 10 – 15 minutes and total milling time ranging from 2 hours to 7 hours.

2.1.5 Furnaces

The ceramic route makes use of high temperatures, generally in the range 600 – 1600 °C. There are several types of furnaces, being the most common the box furnace followed by the tube furnace. The box furnace is ideal for reactions that can be carried out in open atmosphere while the tube furnace is more suited for reactions that require special atmospheres such as oxygen or argon. Common furnaces are powered by electricity and their chamber temperature is probed through thermocouples. Very specific temperature programs can be run in modern furnaces through the integrated programmers. The power delivered to the heating

elements of the furnace is controlled by a feedback loop connected to the thermocouple through a proportional-integral-derivative controller, PID controller. The PID controller is generally calibrated for a range of temperatures and allow for the target temperature to be reached as soon as possible and avoiding potential overshoots. Temperature calibration for the range of use is good practice.

2.1.6 Gas flow synthesis

Some reactions are air sensitive and have to be carried out in inert atmospheres in order to achieve success. Other reactions or measurements need to be run under specific atmospheres. The underlying reasons can be to keep/force an oxidation state or to prevent reaction with CO₂ among others. In these cases the tube furnace is the choice. The tube furnace is then setup with an appropriate working tube and after loading the sample, the ends are sealed with endcaps and the corresponding gaskets. Bottles of compressed gases with appropriate regulators are common sources of the required gases. The outlet of the setup is usually connected to two gas washing bottles connected in series, with the last one containing enough oil to produce bubbling. The setup is then tested for leaks. The flow rate can be set by observing the bubbling rate, although flowmeters can be used. The flow rate slightly alters the chamber temperature. If the setup is for measurements, a thermocouple next to the sample is needed to probe the temperature when the properties are being measured.

2.1.7 Cold isostatic press

A laboratory cold isostatic press, CIP, from Autoclave Engineers has been used during this thesis for densification of pellets for property measurements. After forming the pellets by uniaxial pressing, these are loaded in bags that are sealed under vacuum. These bags are then immersed in hydraulic fluid inside a high pressure tank. The pressure is then increased by pumping hydraulic fluid inside the tank. When the set pressure of 30 Kpsi, i.e. 207 MPa, is reached, this acts in all directions against the pellets. During this thesis the CIP has always been used at its

maximum working pressure of 207 MPa. The pressure helps to arrange and increase the powder packing in the pellet. The pressure is then released and the samples are retrieved. After this process the pellets are ready for sintering. The sintering conditions of each material are presented in their corresponding section.

2.2 Crystallography

2.2.1 Crystal structures and unit cells

Inorganic solids are made of arrangements of atoms or ions. When the elements show long range order, they are said to form a crystal. Crystals are characterised by their unit cell. Within the array of atoms of a crystal, a repetitive pattern can be found. This repetitive pattern can be enclosed within a parallelepiped. If it is the smallest parallelepiped that can describe the crystal by repetition in all three directions of space, then it is called the unit cell [1].

2.2.2 Translational symmetry and crystal systems

The repetition along the three axis of the unit cell is called the translational symmetry. The three axis of the unit cell can be orthogonal between them or can be tilted. The cell edges can also be of the same length or of different length. The variety of relationships between all these elements leads to the 7 crystal systems which are cubic, tetragonal, orthorhombic, monoclinic, triclinic, hexagonal and trigonal. The two main structures discussed during this thesis exhibit orthorhombic and hexagonal unit cell, e.g. the orthorhombic unit cell has the three edges of the parallelepiped of different size to each other while the angle between any two is 90° [5].

2.2.3 Centring of the unit cell and Bravais lattices

Depending on how the atoms are arranged within the unit cell, different centring can be described namely primitive, body-centred, face-centred and base-centred. Each crystal system can adopt from one to all the centring, e.g. a triclinic cell is always primitive while an orthorhombic cell can show any of the centring. When considering all the crystal systems with all the possible centring, the 14 Bravais lattices appear. Some Bravais lattices are equivalent to describe a crystal, e.g. for a face centred tetragonal lattice, the corresponding body centred tetragonal lattice can be found [1].

2.2.4 Atomic positions and symmetry elements

The position of the atoms within the unit cell are described by their atomic coordinates. These are fractional coordinates, from 0 to 1, within the reference framework of the unit cell. The contents of the cell are described by listing the type of atoms and their atomic positions. When symmetry elements can be found within the unit cell, some atom positions can be related to others by symmetry operations. All these are called equivalent positions and can be described by the position of one atom and the corresponding collection of symmetry elements [6].

2.2.5 Space groups and Wyckoff symbols

When considering all the crystal systems with all the possibilities of symmetry operations the 230 space groups arise [5]. When the highest symmetry has been found for a unit cell, the number of atoms that are used to describe the contents of the cell is minimum. This set of atoms is called the asymmetric unit and along with the space group builds up the contents of the unit cell. The multiplicity of each atom of the asymmetric unit along with its symmetry are used to give a name to all the equivalent positions, which is known as Wyckoff symbol [7].

2.2.6 Electron and nuclear densities

Each atom or ion in the unit cell is located in a so called lattice point. Each atom has associated an electron density related to the number of electrons for the corresponding configuration. Within the unit cell exists an electron density map that shows density maxima around the lattice points. The electron density is what is probed by X-ray diffraction to locate the atoms and solve the crystal structures. On the other hand, the nuclei of the atoms that has associated the corresponding nuclear density map is what is probed by neutron diffraction. Bond lengths derived from neutrons and X-rays can be slightly different due to distortions of the electron density [6].

The next section is devoted to the diffraction techniques and will highlight how they can help with the identification and refinement of crystal structures.

2.3 Diffraction

Diffraction was used during this thesis for characterisation of the materials synthesised. Phase identification was performed with the search-match software X'pert Highscore Plus [8]. The Rietveld method was used routinely for confirmation of the phases. The Rietveld refinements were performed by using the software Topas academic version 5 [9]. The starting structural models for Rietveld refinements were routinely obtained from the inorganic crystal structure database, ICSD [10]. During this thesis, laboratory powder X-ray diffraction was used for initial identification and selection of samples. Synchrotron X-ray diffraction and neutron diffraction were used to characterise the best samples.

2.3.1 Bragg's law

When the X-ray or neutron beam hits a crystal, the geometry of the experiment will determine if a reflection will be detected or not. This diffraction condition is known as the Bragg's law and is shown in equation 2.2, where λ is the wavelength of the

radiation, d_{hkl} is the interplanar spacing for the reflection (hkl) and θ is the diffraction angle [6].

$$\lambda = 2 d_{hkl} \sin\theta \quad (\text{Eq. 2.2})$$

2.3.2 Scattering factors and thermal displacement parameters

The scattering factors indicate how intense an atom or ion will diffract the incident radiation. The scattering factors show a dependence with $\sin\theta/\lambda$, with the maximum value corresponding to when the diffraction angle is 0. For growing diffraction angles, the scattering factor becomes smaller. The scattering functions have been fitted to parametric curves and their parameters tabulated, e.g. Cromer-Mann coefficients [11]. The scattering factor is commonly measured in number of electrons and its value is commonly indicated as $f^0(\sin\theta/\lambda)$.

If anomalous dispersion is present, then the scattering factor becomes a complex quantity [12] defined as $f = f^0 + f' + i f''$, where i is the imaginary unit showing that f'' is shifted 90 ° with respect to f^0 and f' .

If the thermal displacement parameter is considered, the scattering factor is weakened by the Debye-Waller factor [13], B , as shown in equation 2.3.

$$f_B = f e^{-B\left(\frac{\sin\theta}{\lambda}\right)^2} \quad (\text{Eq. 2.3})$$

The Debye-Waller factor B is related to the mean displacement of a vibrating atom by the Debye-Waller relationship shown in equation 2.4, where u is the displacement of a vibrating atom measured in Å and $\langle x \rangle$ means the mean of x . The units of the Debye-Waller factor are Å². Some authors publish U_{iso} values instead of B values. B is commonly referred to as the isotropic displacement parameter or B_{iso} .

$$B = 8 \pi^2 \langle u \rangle^2 = 8 \pi^2 U_{iso} \quad (\text{Eq. 2.4})$$

The $\langle u \rangle$ value refers to the isotropic average. If the displacement of a vibrating atom is different in different directions, then the anisotropic average $\langle u_{ij} \rangle$ can be defined, where the 3x3 tensor u_{ij} replaces u . These anisotropic displacement parameters, ADPs, are used to describe the anisotropic displacement ellipsoid. In Topas academic version 5 [9] the outputs for Biso are B values, but the outputs for the ADPs are U_{ij} values.

The plot of the scattering factor for the indium atom is shown in figure 2.1, for both, full occupancy and half occupancy. The scattering at low angles is meaningful for determination of occupancies, while B-factors are not distinguished at low angles. That is due to the $\sin\theta$ contribution in the exponential relationship shown in equation 2.3. The scattering at high angles contains the information of the occupancies mixed with the B-factors.

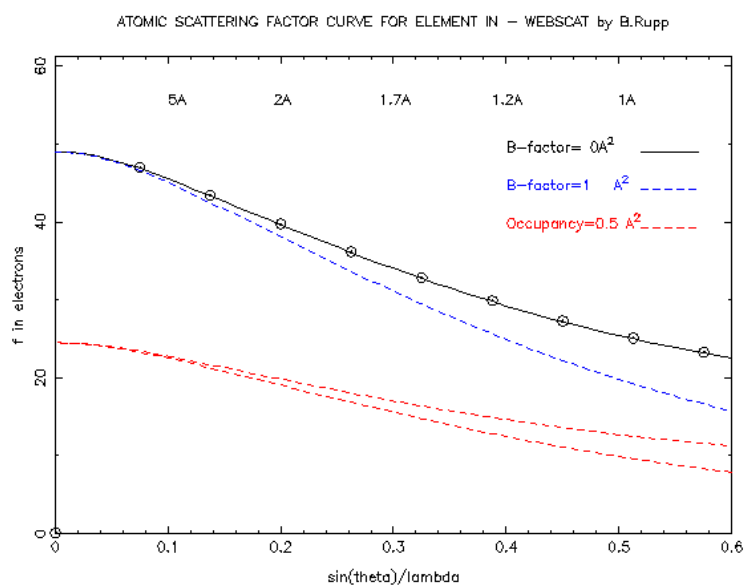


Figure 2.1. Calculated scattering factors for the indium atom, atomic number 49, for a thermal displacement parameter of 0 \AA^2 , black, or 1 \AA^2 , blue. Also for an occupancy of 0.5, with thermal displacement parameter of 0 \AA^2 , upper red, or 1 \AA^2 , lower red. The $\sin\theta/\lambda$ dependency can be observed. Calculation and output plot from www.ruppweb.org [13]. Image reproduced with permission of Dr Bernhard Rupp.

In extended structures made of ions, the ions usually adopt the electronic structure of noble gases. This makes it hard to distinguish by X-ray diffraction between isoelectronic ions, i.e. ions that adopt the same noble gas electronic structure.

2.3.3 Absorption

A fraction of the X-rays can be absorbed by the sample. This fraction is lost for diffraction. The composition of a sample is what determines its absorption coefficient μ . In general, heavier elements will absorb more and longer wavelengths will be absorbed more. If the sample is contained in a capillary of radius R , the transmitted intensity, I_t , is calculated as shown in equation 2.5. During this thesis the absorption calculations have been performed with the web app from Argonne National Laboratory [14].

$$I_t = I_0 e^{-2\mu R} \quad (\text{Eq. 2.5})$$

2.3.4 Structure factors

The structure factors are complex quantities that are used to describe the diffraction model. The calculation of the structure factors for each reflection make use of the Miller indices of the reflection, (h,k,l) , the atomic coordinates for each j^{th} atom, (x_j, y_j, z_j) , and the scattering factor for each j^{th} atom, f_j [13]. The expression is shown in equation 2.6, where the sum covers the n atoms in the structure and i is the imaginary unit.

$$F_{hkl} = \sum_{j=1}^n f_j e^{2\pi i(hx_j + ky_j + lz_j)} \quad (\text{Eq. 2.6})$$

The intensity of each reflection in a diffraction pattern, I_{hkl} , is proportional to the amplitude of the structure factor squared and other contributions such as the

Lorentz polarisation factor, LP, or the absorption, A [13]. This relationship is shown in equation 2.7.

$$I_{hkl} = |F_{hkl}|^2 LP A \quad (\text{Eq. 2.7})$$

When a structure refinement is run, the structure factors along with several of the instrumental factors are used to build the diffraction model that is compared with the diffraction data.

2.3.5 Laboratory instruments

During this thesis two laboratory diffractometers were used routinely.

The first one was a Panalytical X'pert Pro with Co $K\alpha_1$ radiation, $\lambda = 1.789 \text{ \AA}$, operating in Bragg Brentano geometry, also known as reflection mode, and using an X'Celerator detector. For lattice parameters determination the diffraction patterns were collected in the range $5^\circ < 2\theta < 130^\circ$. The step size was of 0.0167° and the time per step was of 0.47 seconds. For routine phase identification shorter range was generally used, such as $5^\circ < 2\theta < 70^\circ$. Samples for this instrument were prepared in a number of different ways. Powders were either stuck to a glass slide by using grease or loaded in a backfilled holder. Pellets were loaded in pellet holders or in backfilled holders and fixed in the right position with the aid of reusable putty-like adhesive.

The second instrument was a Bruker D8 Advance with Cu $K\alpha_1$ radiation, $\lambda = 1.54 \text{ \AA}$, operating in Debye-Scherrer geometry, also known as transmission mode. The diffraction patterns were routinely collected in the range $5^\circ < 2\theta < 60^\circ$ for one hour. The samples for this instrument were prepared in a plastic sample holder, either by sticking the sample to an adhesive tape with no X-ray reflections, or by placing the powder between two layers of a thin plastic film transparent to X-rays.

Both instruments rotate the samples during data collection in order to improve the powder average. The data generated with these instruments are in the format of intensity versus 2θ .

2.3.6 Synchrotron

During this thesis, the best samples, in general the purest samples, were sent to Diamond Light Source at Harwell campus, UK. These samples were loaded in borosilicate or quartz capillaries and subject to X-ray diffraction with the powder diffractometer of the beamline I11. The I11 powder diffractometer is equipped with two different detectors, a position sensitive detector, PSD, and a multi-analyser crystal detector, MAC.

The main feature of the synchrotron radiation is its high intensity. This produces high quality diffraction patterns very fast, in seconds when using the PSD detector. On the other hand, very high resolution can be achieved with the MAC detectors that produce very sharp reflections with an original step size of 0.001° . It is common practice to collect several scans from the same sample and summing them together. In general the datasets are also re-binned to a larger step size such as 0.002° or 0.003° .

Synchrotrons generate the X-ray radiation by accelerating electrons. The electron beam is generated in the electron gun and subject to initial acceleration by means of a linear accelerator or LINAC. The beam is then subject to a second energy increase in the booster synchrotron, where it reaches the energy that will conserve in the storage ring, 3 GeV. The storage ring is the main synchrotron. The storage ring is made of linear segments with bending magnets in their connections. The bending magnets curve the trajectory of the electrons. In this process the electron suffers an acceleration that induces the emission of X-ray radiation that is then directed to the beamlines. The second method for producing X-ray radiation for the beam lines is the use of undulators, which are devices that induce oscillation in the beam. This is again an acceleration that causes the electrons to produce X-ray radiation. The pathway of the electron beam from its generation in the electron gun until the production of radiation for the beamlines can be seen in figure 2.2.

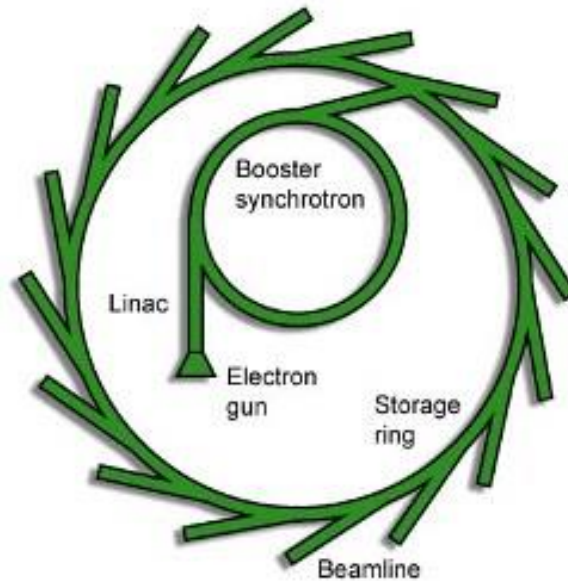


Figure 2.2. Schematic diagram showing the pathway of the electron beam and the extraction of radiation from the storage ring to the beamlines. From www.diamond.ac.uk/Home/About/How-Diamond-Works.html. Image reproduced with permission: Courtesy Diamond Light Source.

2.3.7 Neutron diffraction

Neutron diffraction is used to complete structural details of the sample that X-ray diffraction cannot retrieve. The reason is that X-rays are diffracted by the electrons of the atom while neutrons are diffracted by the nuclei of the atoms [6].

The electron density is very low around light atoms which produce a weak X-ray diffraction. These light atoms can be located in the crystal structures by neutron diffraction because the interaction is with the nuclei.

During this thesis, the powder neutron diffraction experiments were performed at ISIS pulsed neutron source, at Harwell campus, UK. The neutron data presented in this thesis were collected with the diffractometers POLARIS and GEM.

ISIS is a pulsed neutron source. Hydride ions are produced using an electric discharge and accelerated initially with a linear accelerator or LINAC up to 70 MeV. Then they are injected into a synchrotron. When the H^- is injected into the synchrotron, the two electrons of the ion are removed, leaving a proton. The proton

beam is then accelerated in the synchrotron up to 800 MeV. The beam is then extracted from the synchrotron through a kicker magnet and sent to a tungsten target where the neutrons are produced through a process called spallation. From the target, the neutrons are sent to the instruments where they interact with the samples. A diagram of this process can be seen in figure 2.3.

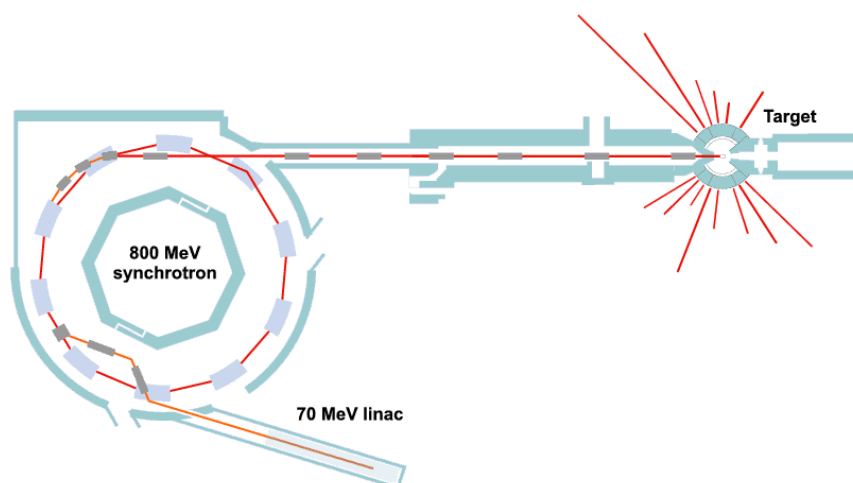


Figure 2.3. Schematic diagram of ISIS showing the generation of the beam and target station 1. From <http://pd.chem.ucl.ac.uk/pdnn/inst3/pulsed.htm>. Image reproduced with permission of Dr Jeremy Karl Cockcroft.

2.3.8 Time-of-flight powder diffractometers

Neutron spallation sources produce pulses of neutrons with an energy distribution instead of a constant wavelength. Because of that, the instruments used in these sources do not operate in angle dispersive mode measuring intensity versus 2θ . Instead, these instruments operate in energy dispersive mode, measuring energy and direction of the diffracted neutrons, which finally translates into a pattern of intensity versus time-of-flight, TOF.

The relationship that relates the time of flight, t , with the d -spacing makes use of the diffractometer constants $difA$, $difC$ and t_0 and is presented in equation 2.8.

$$t = difC d + difA d^2 + t_0 \quad (\text{Eq. 2.8})$$

These parameters are obtained from the refinement of data collected from standard reference materials. The constant difA is sample dependent. It is the t^2 contribution to the time of flight vs d-spacing relationship and is generally refined. The constant t0 is instrument dependent and must remain at the value of calibration. The constant difC is the linear relationship between the time of flight and the d-spacing. In a multi-histogram refinement difC may be refined for the lower resolution histograms [15].

The linear relationship between the time of flight and the d-spacing can be obtained by using the de Broglie equation and the Bragg's law, see equation 2.9.

$$\frac{h}{mv} = \frac{ht}{mL} = 2d \sin\theta \quad (\text{Eq. 2.9})$$

Where h is Plank's constant, t is the time of flight, m is the neutron mass, L is the total flight path from moderator to detector, d is the interplanar spacing for each reflection and θ is the scattering angle. Solving for t in equation 2.9 yields equation 2.10 which relates d-spacing and t.

$$t = 2d \frac{mL}{h} \sin\theta \quad (\text{Eq. 2.10})$$

2.3.8.1 POLARIS

POLARIS is a high intensity, medium resolution powder diffractometer [16]. It is able to measure relatively small samples in short periods of time. Along with speed, the variety of sample environments is another of its strengths. A representation of the diffractometer is shown in figure 2.4.

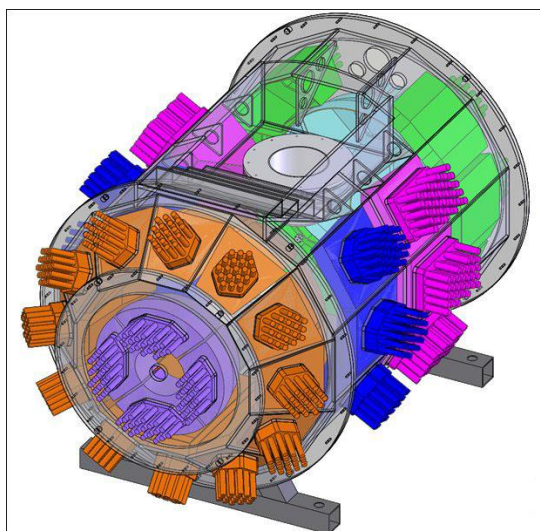


Figure 2.4. The vacuum tank of the POLARIS diffractometer showing the detector panels for each bank in different colours: green, pink, blue, orange and purple for banks 1, 2, 3, 4 and 5 respectively. The staircase and the opening to introduce the samples are visible on the top of the tank. From <http://www.isis.stfc.ac.uk/instruments/polaris/polaris4643.html>. Image reproduced with permission of Dr Stephen Hull.

2.3.8.2 GEM

GEM is the general materials diffractometer [17]. It operates with high intensity and high resolution. It can be used either for disordered materials or for crystalline powders. The GEM detectors cover a scattering angle in the range $1.1 - 169.3^\circ$. The incident flight path is 17 m. There is a variety of sample environments available such as the high temperature furnace.

2.3.9 Refinements

2.3.9.1 Single profile fitting

This is the simplest refinement possible. It is used to fit a single peak. It only needs background, peak shape, position and initial intensity. The refinement of single

profiles are very useful for obtaining accurate 2θ positions for indexing. This type of refinement was performed with the software Topas academic version 5 [9].

2.3.9.2 Pawley refinements

The Pawley refinement [18] of a diffraction pattern is an intensity extraction method. It is used either when the crystal structure is not known or when structural information is not needed. These refinements are faster to setup than structural refinements and are very useful e.g. to check phase purity or to measure lattice parameters. The only input data needed is cell parameters, space group, peak shape and background. The software Topas academic version 5 [9] was used to perform these type of refinements.

2.3.9.3 Rietveld refinements

Rietveld refinement, also known as the full profile method, was initially introduced by Hugo Rietveld for neutron diffraction [19]. During this thesis the Rietveld refinements have been carried out with the software Topas academic version 5 [9]. The Rietveld method is a structure refinement method and therefore it needs an appropriate starting model. Generally isostructural or related models from literature are used. In practice these models are commonly retrieved from the inorganic crystal structure database or ICSD [10].

The method works by comparing the diffraction data with a simulation of the diffraction pattern that takes into account the crystal structure. The refinement is run several times. In each run one or several parameters are refined. This is commonly known as the turn-on sequence of parameters. The usual order in the turn-on sequence is: scale and zero error, background and lattice parameters, peak shape, atomic positions, displacement parameters and occupancies, unstable peak shape parameters and anisotropic displacement parameters. The activation of too many parameters at the same time can cause the refinement to diverge. In addition, some of these parameters are strongly correlated and cannot be refined

together. When this is the case, the common practice is to fix the rest of the parameters and refine one at a time.

2.3.9.4 Criteria of fit

The quality of the refinement is assessed by similarity of the data and the model. The refinement fit factors are formal ways of quantifying this similarity. The most useful factor for quantifying the general progression of a refinement is the weighted profile factor or R_{wp} , which expression is presented in equation 2.11 where $y_{i,obs}$ is the observed intensity at the i^{th} step, $y_{i,calc}$ is the calculated intensity at the i^{th} step and $w_i = 1/y_{i,calc}$. The smaller the R_{wp} becomes, the better the fit. The best value expected taking into account the number of observations, N , and the number of refined parameters, P , is R_{exp} which is shown in equation 2.12. The goodness of fit, GOF or also known as χ , is another fit factor commonly used. It is defined by using R_{wp} and the expected R value or R_{exp} and is shown in equation 2.13 [20].

$$R_{wp} = \sqrt{\frac{\sum w_i (y_{i,obs} - y_{i,calc})^2}{\sum w_i y_{i,obs}^2}} \quad (\text{Eq. 2.11})$$

$$R_{exp} = \sqrt{\frac{N - P}{\sum w_i y_{i,obs}^2}} \quad (\text{Eq. 2.12})$$

$$GOF = \chi = \frac{R_{wp}}{R_{exp}} \quad (\text{Eq. 2.13})$$

2.3.9.5 Errors

The least squares method in which the Rietveld method is based, produces a set of estimated standard deviations or e.s.d., one per refined parameter. These are commonly used as the error of the parameter in the refinement and refers to the precision [21]. In general the e.s.d. is smaller than the experimental error.

2.3.9.6 Constraints

During this thesis the most common constraint [21] used in refinements have been the compositional constraints. These allow e.g. to refine two atoms on one site from a single histogram or three atoms on one site if two histograms are collected at different wavelengths or with different type of radiation.

2.3.9.7 Peak shapes

A set of different peak shapes are available in order to fit accurately the reflection profiles produced by the combination of instrument and sample contributions. The most common PXRD peak shapes are Pseudo Voigt, Pearson VII, TCHZ and Stephens anisotropic. Pseudo Voigt, probably the most common when studying laboratory PXRD patterns, is built up of a fraction of Gaussian, $G(x)$, and a fraction of Lorentzian, $L(x)$ [22]. The fraction of Lorentzian is called the Lorentzian mixing parameter, η , which is refined in the range 0 – 1. The formal definition of the Pseudo-Voigt peak shape is shown in equation 2.14.

$$PV(x) = \eta L(x) + (1-\eta) G(x) \quad (\text{Eq. 2.14})$$

2.3.9.8 Peak widths

The powder diffraction patterns that result from an angle dispersive instrument show a peak width dependency with the diffraction angle that is commonly modelled with the Caglioti relationship [23] shown in equation 2.15, where $H(\theta)$ is the peak width and θ the diffraction angle. U , V and W are the parameters that are commonly refined.

$$H(\theta) = \sqrt{U \tan^2 \theta + V \tan \theta + W} \quad (\text{Eq. 2.15})$$

2.3.9.9 Multi-histogram refinements

Combined refinements [21] make use of several diffraction patterns collected with different wavelengths or types of radiation. During this thesis, combined refinements have been performed with X-ray and neutron powder diffraction patterns simultaneously. Each diffraction pattern used in a combined refinement is commonly named histogram. In addition, the neutron TOF diffractometers usually produce sets of data from different banks of detectors in order to cover a wider range of reflections of the sample. This means that some of the combined refinements of this thesis ended up with up to 4 or 5 histograms that actually represented two types of radiation only.

The main motivation for the combined refinements during this thesis has been to allow light atoms such as lithium or oxygen to be located with higher reliability in the new materials.

Combined refinements are also useful when the scattering factors of two or more atoms in a sample are similar for the initial type of radiation used. In these cases, adding a second wavelength or a different type of radiation in which the scattering factor is different, helps to distinguish them and increase the reliability of the refinement.

Another motivation for using several wavelengths in the same refinement is to be able to refine the occupancy of different atoms on the same site. For a single

wavelength refinement, only two different atoms can be identified on a single site when a compositional constraint is used. If n wavelengths are carefully selected, up to $n+1$ atoms can be identified on the same single site if the compositional constraint is used.

2.3.10 Indexing

Indexing is a technique for finding a suitable unit cell for a diffraction pattern. For a successful indexing of a powder diffraction pattern, the position of the reflections have to be known as accurately as possible, and the zero error should be corrected if possible. For indexing a diffraction pattern, only the first 20 – 25 reflections of the pattern should be used [24].

During this thesis the initial position of the peaks were collected either manually or by automating the peak identification on the pattern with Fullprof [25]. The position of the peaks were then refined by single profile fitting with Topas academic version 5 [9]. The proper indexing was carried out with the program TREOR 90 [26]. The solutions were ranked following the figure of merit M_{20} [27]. Finally the best solution was accepted if it was able to produce a satisfactory Pawley refinement.

2.3.11 Direct methods

Direct methods are types of ab initio methods for structure solution from diffraction data. In other words, direct methods derive structural information such as structure factor phases or atomic coordinates by mathematical means from the set of intensities extracted from the diffraction pattern of a sample. The method works because the phase and amplitude of a structure factor are related through the electron density [5]. During this thesis the software used for structure solution with direct methods was EXPO2014 [28].

2.4 Inductively coupled plasma - optical emission spectroscopy

Inductively coupled plasma - optical emission spectroscopy, ICP-OES, is a technique for elemental analysis. Prior to injection, the sample is properly digested until a perfect dissolution is achieved. For this purpose, stirring and hot concentrated nitric acid was used in this thesis. When the solution is injected in the machine, the plasma torch dissociates it into excited atoms and ions that emit characteristic radiation. The emitted radiation is then measured allowing for identification and quantification. ICP-OES is a very sensitive technique that allow for measurements of concentrations in the range of ppb depending of the elements [29].

2.5 Fourier transform infrared spectroscopy

Fourier transform infrared spectroscopy, FTIR spectroscopy, is a spectroscopic technique that can be used to study the vibrational motions of atoms in solids. When a vibrational mode is IR active, it produces an absorption band in the IR spectrum. Different vibrational modes will absorb IR radiation of different energies. Absorption of the appropriate radiation excites the vibrational modes to higher energy states. The resulting spectra from solids are usually complex. This type of analysis gives information on local structure and can be used with crystalline and amorphous materials [30]. During this thesis this technique was used for checking if a particular reactant was still present at the end of the reaction. This was made by comparison, searching for the intense bands of the reactant in the products. The measurements of the powders were carried out by using a Bruker Optics FTIR Tensor 27 spectrometer with an attenuated total reflectance, ATR, device attached to the spectrometer.

2.6 Electron microscopy

2.6.1 Transmission electron microscope - energy dispersive X-ray analysis

The transmission electron microscope, TEM, was used in this thesis for energy dispersive X-ray analysis, EDX. This is a technique in which the electron beam hits the sample causing some of the electrons of individual atoms to be excited. When these energy levels are filled again with electrons from higher energy levels, X-ray radiation is emitted. The wavelength of this radiation is characteristic of each element. Therefore, the spectra produced by the instrument allow for identification of the elements in the sample. The relative intensities allow for determination of the ratio of the elements present in the sample. The error of these measurements is generally in the range of 5 – 10 %. These measurements were performed by Dr Marco Zanella. The samples were prepared by spreading the powders on a carbon coated Cu or Au TEM grid and measured by using a JEOL 2000FX Transmission Electron Microscope (TEM) equipped with an EDAX Energy Dispersive X-ray Spectroscopy (EDX) detector.

2.7 Thermogravimetric analysis

Thermogravimetric analysis, TGA, is a technique that measures the change in weight of a sample as a function of temperature. This experiment can be run in different atmospheres such as air, nitrogen or oxygen. During this thesis this technique has been used to determine if a reactant experienced weight loss during heating in order to be able to correct the stoichiometry. These experiments were carried out in Pt pans with flow of dry air by using a TA instruments Q600 SDT.

2.8 AC impedance spectroscopy

AC impedance spectroscopy, ACIS, is a well-established technique for electrical characterisation of materials [31]. The cell is generally a piece of material with a regular shape, usually a pellet that enables the measurement of its dimensions for computation of its geometry. Plane parallel sides of the piece of material are covered with a conducting material to act as electrode.

2.8.1 Electrode preparation

The electrode contacts for AC impedance measurements have been prepared during this thesis either with gold or with silver paste. Both sides of the pellet were painted with the paste. When the gold paste was used, gold mesh and gold wire tied to the mesh were added during this stage in order to provide wiring to the pellet as shown in figure 2.5. Then the electrode was dried at 200 °C and finally fired at 600 °C for 1 hour. On the other hand, when silver paste was used, silver wires without mesh were connected to the electrodes by using silver paste. In this case, to help make better adhesion, the end of the wires were folded in the region of contact with the silver paste and the electrode. Silver paste electrodes were dried at 100 – 150 °C for 30 – 60 minutes.

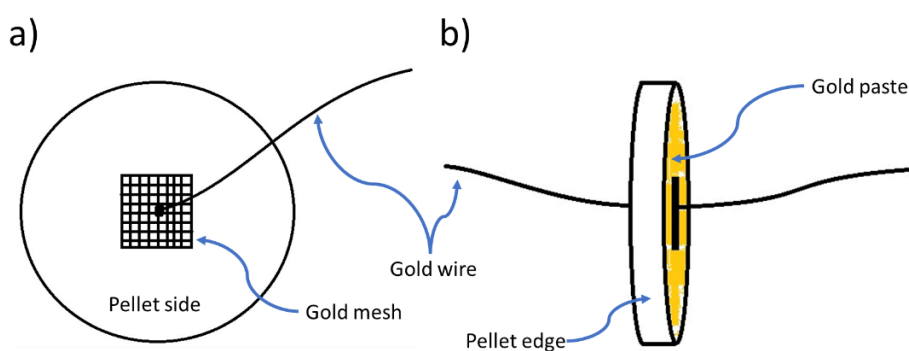


Figure 2.5. Gold electrodes mounting: a) Pellet side showing how the gold mesh and wire were mounted. The gold wire is tied to the mesh. b) Pellet in perspective showing the final connections.

The use of gold as contact electrodes has to be cautious. Gold migration from gold contacts has been reported as a problem for materials such as photovoltaics or light-emitting diodes, LED's.

For some authors, the problem was that if they make a very thin photovoltaic cell, less than 100 nm, it suffers of shorting between the two metal electrodes due to the metal migration of the gold electrode. Suemori et al. [32] showed that the migration into the film occurs during the vacuum deposition of the electrode along the grain boundaries of the polycrystalline film up to a depth of more than 100 nm.

The gold migration has previously been observed as sub-micron sized gold particles located next to the gold-based p-contact of LED's. Chin et al. [33] concluded that gold migration occurs during device processing and ageing. In particular, increasing the ageing time from 100 hours to 1000 hours produced an increase in gold migration range as well. They proposed that during ageing, the gold migrates following the paths of the device with higher current densities.

More recently Domanski et al. [34] have focused their attention on the gold metal electrode of state-of-the-art perovskite solar cells. They have shown that working temperatures of 70 °C are enough for inducing gold migration into the active layer, leading in this way to degradation of the device performance. They also showed that this problem can be mitigated by adding a Cr protective thin layer between the gold electrode and the device.

During this thesis the gold electrodes were painted with gold paste rather than vacuum deposited. This is a different process respect to those discussed above, although the migration mechanism could still be present. One of the reasons why gold migration is so important in the systems discussed above is because the thickness of the device is in the range that gold can migrate, i.e. hundreds of nm. The pellets measured in this thesis have a thickness in the mm scale, which is several orders of magnitude larger than the gold migration range. There is no evidence that gold migration has affected the measurements presented in this thesis, although this has not been studied because the main target of the measurements was to produce an initial assessment of the conductivities of the new materials.

2.8.2 Sample environments

The measurements are routinely made at different temperatures in ranges from room temperature to e.g. 500 °C. The samples are generally run in a flowing gas, e.g. dry air, oxygen or argon. During this thesis dry air means compressed air from a bottle or from the central line of the lab passed through a desiccant material.

In order to control temperature and atmosphere, a tube furnace has been used for measurements. The sample is mounted in a sample holder that has a thermocouple close to the sample as shown in figure 2.6. The sample holder is then installed in the tube furnace leaving the set of sample and thermocouple in the centre of the working tube. The other end is sealed and the appropriate gas can be flowed. Then the temperature program can be run. The AC impedance measurements are then performed. During this thesis the measurements have been controlled with the software SMaRT from Solartron and the Eurotherm iTools software. The precision in temperature during measurements has typically been better than ± 1 °C.

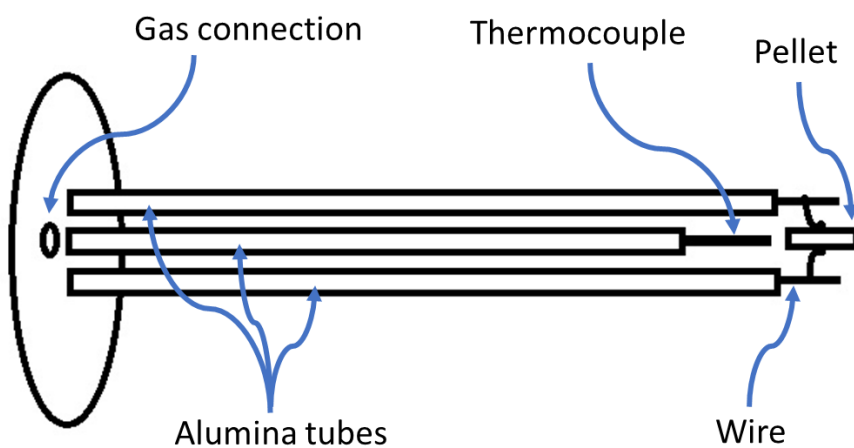


Figure 2.6. Diagram of the sample holder used during this thesis for AC impedance measurements under controlled atmospheres. The end with the gas connection is fitted to the working tube of the tube furnace with an air tight connection. The other end of the working tube has an air tight lid with another gas connection. Standard tubing allows to flow a range of controlled atmospheres.

2.8.3 Instruments

During this thesis, AC impedance measurements were performed by using a Solartron 1255HF or 1255B frequency response analyser coupled with a Solartron 1296 dielectric interface or either with a Solartron 1260 alone.

The most common frequency ranges used were from 0.001 Hz to 1 MHz or from 0.01 Hz to 1 MHz. The temperature ranges were either 25 – 500 °C or 25 – 300 °C. Measurements were performed in dry air unless otherwise stated.

2.8.4 Impedance measurements

The impedance of a sample, $Z(\omega)$, is a complex quantity that indicates the ratio between an AC voltage applied to the sample, $V(\omega)$, and the resulting AC current through the sample, $I(\omega)$ as shown in equation 2.16.

$$Z(\omega) = \frac{V(\omega)}{I(\omega)} \quad (\text{Eq. 2.16})$$

The impedance has real and imaginary components, $Z'(\omega)$ and $Z''(\omega)$ respectively, which can be written as it is shown in equation 2.17. These two components are also frequency dependent. The letter i is the imaginary unit and is written by convention to indicate the imaginary component.

$$Z(\omega) = Z'(\omega) + i Z''(\omega) \quad (\text{Eq. 2.17})$$

The second way of decomposing the impedance is in amplitude and phase, $|Z(\omega)|$ and $\varphi(\omega)$ respectively. These two quantities can be defined from the real and imaginary components of the impedance as shown in equation 2.18 and equation 2.19.

$$|Z(\omega)| = \sqrt{[Z'(\omega)]^2 + [Z''(\omega)]^2} \quad (\text{Eq. 2.18})$$

$$\varphi(\omega) = \arg[Z(\omega)] = \arctan \frac{Z''(\omega)}{Z'(\omega)} \quad (\text{Eq. 2.19})$$

The impedance $Z(\omega)$ is measured by running this experiment at a fixed frequency, $\omega = 2\pi f$, for the AC signal. When this experiment is run at different frequencies, the data can be plotted in the complex plane or a spectrum can be produced. Typical spectra are amplitude or phase versus frequency. If the data is plotted in the complex plane, it is represented as $-Z''$ versus Z' for each frequency.

2.8.5 Electro-active elements

The AC impedance data were analysed by using the software ZView [35]. Data plotted on the complex plane show patterns such as arcs and spikes, as those shown in figure 2.7.

Every arc represents an electroactive element of the sample. The equivalent circuit for each arc is a parallel R C circuit, i.e. a resistor of resistance R in parallel with a capacitor of capacitance C. The resistor value can be obtained from the projection of the arc on the real axis Z' as shown in figure 2.7. The capacitance, C, can be obtained from the frequency at the maximum of the arc, ω , and the corresponding resistance, R, by application of equation 2.20, where $\omega = 2\pi f$ with f being the frequency in Hz.

$$\omega RC = 1 \quad (\text{Eq. 2.20})$$

Alternatively the R and C values can be obtained by circle fit with appropriate software. During this thesis this task was performed with the software Zview [35] which can also model depressed arcs. The product $\tau = RC$ is known as the time constant of the parallel R C circuit.

The time constants of each element are the values that determine at which frequencies the elements appear in the complex plane. The element with the

lowest time constant will appear at the high frequency end of the dataset, by the origin of the complex plane, and then the other elements will appear in order until the element with the largest time constant, that will appear at the low frequency end of the dataset.

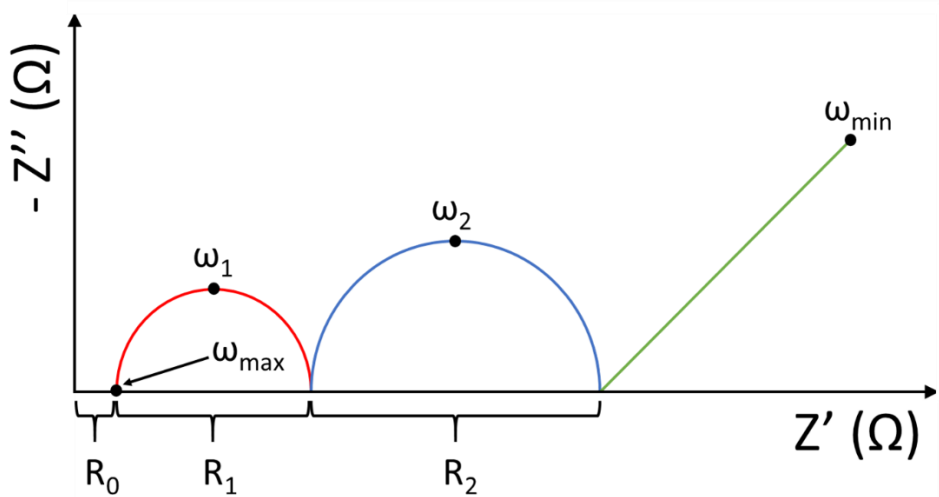


Figure 2.7. Diagram of the complex plane showing generic AC impedance data that has been collected from low frequencies, ω_{\min} , to high frequencies, ω_{\max} . The red and blue arcs correspond to two electroactive elements with time constants R_1C_1 and R_2C_2 respectively. The green spike corresponds to a blocking electrode response. Finally a pure resistor R_0 is also present. The relative values of the time constants are $R_0 < R_1C_1 < R_2C_2$.

The electro-active elements identified in the complex plane plot represent regions of the sample and are known as bulk response, grain boundary response, sample-electrode interface response or blocking electrode response, for citing only those that have arisen during this thesis.

The capacitance of each electroactive element is corrected for sample geometry in order to assign each electroactive element to the corresponding regions in the sample. For samples with grains of thickness l_{bulk} and grain boundaries of thickness l_{gb} , the relationship between the capacitances of the grain and the grain boundary, C_{bulk} and C_{gb} respectively, and their thicknesses can be approximated by the equation 2.21 derived from the “brickwork” model [36].

$$\frac{C_{bulk}}{C_{gb}} = \frac{l_{gb}}{l_{bulk}} \quad (\text{Eq. 2.21})$$

During this thesis the AC impedance data were corrected for the geometry of the sample. Resistance, R , becomes resistivity, ρ , after geometry correction. The capacitance $C = \epsilon_0\epsilon_r A/d$ becomes $C_{corr} = \epsilon_0\epsilon_r$ where ϵ_0 is the vacuum permittivity, ϵ_r is relative permittivity, A is the pellet electrode area and d is the thickness of the pellet. The corrected capacitance, C_{corr} , is used for recognition of the electro-active element by following the data on table 2.2.

Table 2.2. Relative capacitance values for electro-active element assignment [36].

Electroactive element	Corrected capacitance range / F cm^{-1}
Bulk	$10^{-12} - 10^{-11}$
Grain boundary	$10^{-11} - 10^{-8}$
Sample-electrode interface	$10^{-7} - 10^{-5}$

2.9 Density functional theory

Density functional theory, DFT, calculations allow for computational screening of many potential compositions and their relative formation conditions. In many occasions these predictions correlate with laboratory outputs, which allows to select and prioritise the synthetic attempts and therefore accelerate the discovery of new materials. These calculations were performed by Dr Matthew Dyer.

2.10 Solid state nuclear magnetic resonance

Static and magic angle spinning, MAS, solid state nuclear magnetic resonance, NMR, was used during this thesis. The NMR measurements presented in this thesis were carried out by Dr Frédéric Blanc, Mr Michael D. Jones and Ms Mona K. Omir.

2.11 References

1. Weller, M.T., *Inorganic materials chemistry*. 1994: Oxford University Press.
2. Stein, A., S.W. Keller, and T.E. Mallouk, *Turning down the heat: design and mechanism in solid-state synthesis*. *Science*, 1993. **259**(5101): p. 1558-1564.
3. Zhang, D., *Processing of advanced materials using high-energy mechanical milling*. *Progress in Materials Science*, 2004. **49**(3): p. 537-560.
4. Suryanarayana, C., *Mechanical alloying and milling*. *Progress in materials science*, 2001. **46**(1): p. 1-184.
5. Blake, A.J. and W. Clegg, *Crystal structure analysis: principles and practice*. Vol. 13. 2009: Oxford University Press.
6. Smart, L.E. and E.A. Moore, *Solid state chemistry: an introduction*. 2012: CRC press.
7. Müller, U., *Inorganic structural chemistry*. 2007: John Wiley & Sons.
8. Degen, T., M. Sadki, E. Bron, U. König, and G. Nénert, *The highscore suite*. *Powder Diffraction*, 2014. **29**(S2): p. S13-S18.
9. Coelho, A.A., *Topas-Academic*. A Computer Programme for Rietveld Analysis, 2004.
10. Belsky, A., M. Hellenbrandt, V.L. Karen, and P. Luksch, *New developments in the Inorganic Crystal Structure Database (ICSD): accessibility in support of materials research and design*. *Acta Crystallographica Section B: Structural Science*, 2002. **58**(3): p. 364-369.
11. Cromer, D.T. and J.B. Mann, *X-ray scattering factors computed from numerical Hartree–Fock wave functions*. *Acta Crystallographica Section A: Crystal Physics, Diffraction, Theoretical and General Crystallography*, 1968. **24**(2): p. 321-324.
12. Cromer, D.T., *Anomalous dispersion corrections computed from self-consistent field relativistic Dirac–Slater wave functions*. *Acta Crystallographica*, 1965. **18**(1): p. 17-23.
13. Rupp, B. *BR's Macromolecular Crystallography Website* www.ruppweb.org. November 2016].
14. Dreele, R.B.V., M.R. Suchomel, and B.H. Toby. *Argonne National Laboratory, Advanced Photon Source, Compute X-ray Absorption*. <http://11bm.xray.aps.anl.gov/absorb/absorb.php>. August 2016].
15. Smith, R. *Refinement of time-of-flight Profile Parameters in GSAS*.
16. Hull, S., R. Smith, W. David, A. Hannon, J. Mayers, and R. Cywinski, *The POLARIS powder diffractometer at ISIS*. *Physica B: Condensed Matter*, 1992. **180**: p. 1000-1002.
17. Williams, W., R. Ibberson, P. Day, and J. Enderby, *GEM—general materials diffractometer at ISIS*. *Physica B: Condensed Matter*, 1997. **241**: p. 234-236.
18. Pawley, G., *Unit-cell refinement from powder diffraction scans*. *Journal of Applied Crystallography*, 1981. **14**(6): p. 357-361.
19. Rietveld, H., *A profile refinement method for nuclear and magnetic structures*. *Journal of applied Crystallography*, 1969. **2**(2): p. 65-71.
20. McCusker, L., R. Von Dreele, D. Cox, D. Louer, and P. Scardi, *Rietveld refinement guidelines*. *Journal of Applied Crystallography*, 1999. **32**(1): p. 36-50.
21. Young, R., *The Rietveld Method*. IUCr Monographs on Crystallography, Oxford University Press, Oxford, 1993.

22. Young, R. and D. Wiles, *Profile shape functions in Rietveld refinements*. Journal of Applied Crystallography, 1982. **15**(4): p. 430-438.
23. Caglioti, G., A.t. Paoletti, and F. Ricci, *Choice of collimators for a crystal spectrometer for neutron diffraction*. Nuclear Instruments, 1958. **3**(4): p. 223-228.
24. David, W., K. Shankland, L. McCusker, and C. Baerlocher, *Structure determination from powder diffraction data*. 2002: Oxford University Press.
25. Rodríguez-Carvajal, J., *Recent developments of the program FULLPROF*. Commission on powder diffraction (IUCr). Newsletter, 2001. **26**: p. 12-19.
26. Werner, P.-E., L. Eriksson, and M. Westdahl, *TREOR, a semi-exhaustive trial-and-error powder indexing program for all symmetries*. Journal of Applied Crystallography, 1985. **18**(5): p. 367-370.
27. de Wolff, P.d., *A simplified criterion for the reliability of a powder pattern indexing*. Journal of Applied Crystallography, 1968. **1**(2): p. 108-113.
28. Altomare, A., C. Cuocci, C. Giacovazzo, A. Moliterni, R. Rizzi, N. Corriero, and A. Falcicchio, *EXPO2013: a kit of tools for phasing crystal structures from powder data*. Journal of Applied Crystallography, 2013. **46**(4): p. 1231-1235.
29. Slavin, W., *Flames, furnaces, plasmas: how do we choose?* Analytical Chemistry, 1986. **58**(4): p. 589A-[597A].
30. West, A.R., *Basic solid state chemistry*. Vol. 36. 1999: John Wiley & Sons New York.
31. Barsoukov, E. and J.R. Macdonald, *Impedance spectroscopy: theory, experiment, and applications*. 2005: John Wiley & Sons.
32. Suemori, K., M. Yokoyama, and M. Hiramoto, *Electrical shorting of organic photovoltaic films resulting from metal migration*. Journal of Applied Physics, 2006. **99**: p. 036109.
33. Chin, A.K., C. Zipfel, F. Ermanis, L. Marchut, I. Camlibel, M.A. DiGiuseppe, and B.H. Chin, *The migration of gold from the p-contact as a source of dark spot defects in InP/InGaAsP LED's*. IEEE Transactions on Electron Devices, 1983. **30**(4): p. 304-310.
34. Domanski, K., J.-P. Correa-Baena, N. Mine, M.K. Nazeeruddin, A. Abate, M. Saliba, W. Tress, A. Hagfeldt, and M. Grätzel, *Not all that glitters is gold: Metal-migration-induced degradation in perovskite solar cells*. ACS nano, 2016. **10**(6): p. 6306-6314.
35. *Zview software*. Scribner Associates, Inc. <http://www.scribner.com>. 2017].
36. Irvine, J.T., D.C. Sinclair, and A.R. West, *Electroceramics: characterization by impedance spectroscopy*. Advanced Materials, 1990. **2**(3): p. 132-138.

This page is intentionally left blank

Chapter 3

New olivine materials

3.1 Introduction

Olivine materials have been known since antiquity, in particular in the form of beautiful green gemstones that were traded in Egypt and Mesopotamia [1]. There is evidence of olivine materials out of earth, e.g. in Mars, where the evidence has been found by using thermal infrared spectroscopy data collected by the Mars Global Surveyor during its orbits over Mars [2]. It has also been found by infrared spectroscopy in samples retrieved from cometary dust by the Stardust probe [3]. By studying the spectral properties of the 69 μm band of the crystalline olivine it has been identified around evolved stars, light years away from us [4]. Many of the olivine structure materials belong to the large families of minerals known as orthosilicates and orthophosphates. In the earth it is the dominant mineral in the upper mantle that transforms into spinel structure with the pressure found at higher depths [5].

The archetypal material of this family is $(\text{Mg,Fe})_2\text{SiO}_4$. The two end members are fayalite, Fe_2SiO_4 and forsterite, Mg_2SiO_4 , also known in technical literature as Fa and Fo respectively. Compositions in the solid solution can be named by indicating the fraction percent of each end member, e.g. Fa30Fo70, or more simply by mentioning only one, e.g. Fo70 to refer to Fa30Fo70, i.e. $(\text{Fe}_{0.6}\text{Mg}_{1.4})\text{SiO}_4$. The attractive green colour resembling the olive after which is named belongs to Mg rich samples. The order-disorder of these olivine minerals have been studied, e.g. for Fa₅₀ by using neutron diffraction [6]. It was found that there is a cross over temperature, T_{cr} , at which Fe and Mg switch site of preference in the crystal structure.

The olivine crystal structure was briefly mentioned in the introduction chapter and a deeper description is presented here. The structure is formed when the hexagonal closed packed oxide network hosts cations on half of the octahedral sites

and one in eight of the tetrahedral sites. It is based on a distorted hexagonal closed packed oxide network.

The olivine structure has stoichiometry $ABXO_4$, where XO_4 is an oxyanion such as silicate or phosphate. Although the A and B sites are both octahedrally coordinated, the environments are different. The basic motif of the olivine structure is shown in figure 3.1.a. The BO_6 octahedra and the XO_4 tetrahedra are connected by edge sharing. When several units of this motif are linked to each other by corner sharing in the ordered way shown in figure 3.1.b, the olivine framework BPO_4 is formed. This framework can still be completed with unidimensional chains of edge sharing AO_6 octahedra, yielding the common olivine structure. An olivine crystal structure with full occupancy, in both A and B sites, can be seen in figure 3.1.c. If $LiMgPO_4$ is considered, figure 3.1 represents MgO_6 in orange, LiO_6 in green and PO_4 in purple. Oxygen is shown in red. All polyhedra are connected to each other, by both edge and corner sharing, depending on its site in the structure. In summary, each tetrahedron is linked to 5 octahedra of the B site, to 1 of them by edge sharing and to 4 of them by corner sharing. This linkage builds a strong 3D bonding structure which is a valuable property for applications in which the devices can catch fire, e.g. such as in a battery.

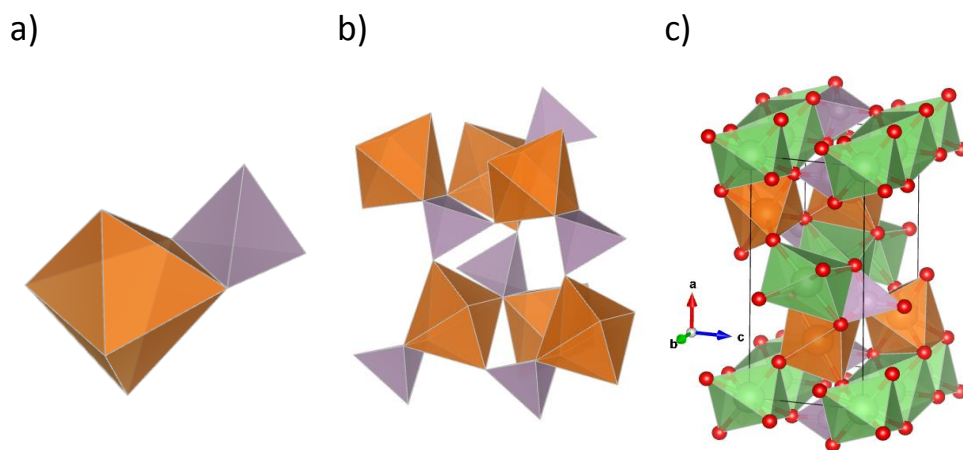


Figure 3.1. a) The basic motif of the olivine structure type showing the B octahedral site in orange and the oxyanion tetrahedral site in purple, both connected by edge sharing. b) Olivine framework made of BPO_4 motifs connected by corner sharing. c) Olivine structure showing full occupancy of the octahedral A site in green. Figures plotted with VESTA [7].

The unit cell is orthorhombic with space group *Pnma*, number 62 in International Tables for Crystallography. Literature also refers to it as *Pbnm*, which is one of the non-standard settings of the same space group. *Pnma* is the short symbol representation of this space group. The extended full symbol is $P2_1/n2_1/m2_1/a$ meaning a primitive cell, with twofold screw axes in the translational directions a, b and c of the unit cell. In addition there are two glide planes perpendicular to the translational directions a and c, the first one with diagonal glide direction and the second one with glide direction a. Finally there is also a reflection plane perpendicular to the translational direction b.

The unit cell contains four formula units in a volume close to 300 \AA^3 . The asymmetric unit is made of 6 atoms, i.e. one less than those in a formula unit ABXO_4 . The structure contains two octahedral metal sites A and B, one tetrahedral site X and three oxygen sites named O1, O2 and O3. All of them are special positions but for one of the oxygens, usually named O3, which is in a general position. That is the site that has its multiplicity doubled with respect to the special positions, i.e. 8 instead of 4. The higher multiplicity of O3 completes the apparently missing atom of the formula unit. The Wyckoff labels for these positions are 4a for the A site, 4c for the remaining special positions and 8d for the general position of O3.

Most of the Li containing olivine materials studied here have an ordered olivine structure, meaning that all Li-ions sit on the octahedral A site, the site that develops in unidimensional channels of edge sharing octahedra. All the other octahedral cations sit on the B site, forming the layers linked by phosphate tetrahedra.

Synthetic olivine materials have been developed for microwave dielectric applications [8], to work as phosphors [9] and to function as catalyst supports [10] among others. In the electrochemical field, materials with the olivine structure have been studied for their use as cathode materials, e.g. LiMnPO_4 , LiFePO_4 , LiCoPO_4 and LiNiPO_4 . For LiCoPO_4 and LiNiPO_4 , with working potentials of 5 V, there is currently no practical electrolyte [11].

The electrical properties of materials depend on composition and crystal structure. The desired properties for a battery cathode material are good electronic and ionic conductivities. For the olivine LiFePO_4 these conductivities are not high, but adequate processing of the raw material have turned it into a functional and competitive cathode [11]. LiFePO_4 was proposed as cathode material in 1997 by

Goodenough et al. [12]. It has been very well studied since then for its application in Li-ion batteries [13-17] and is currently in the market [18].

An electrolyte material has to be a good ionic conductor and an electronic insulator. Therefore olivine materials with acceptable Li-ion conductivity that are electronic insulators can be considered to be tested as potential electrolytes for batteries. Olivine materials have been computationally screened to determine which ones would have better ionic conductivities while having low ionic hopping barriers and negligible electronic conductivity. LiMgPO₄ is one of the potential solid electrolyte materials that have been found during the screening [19]. That is why LiMgPO₄ is the parent material chosen for all the trials of modification and all the new samples discussed here.

In the structure of the olivine LiMgPO₄ the Li-ions sit in edge sharing octahedral sites, forming unidimensional chains that occupy parallel channels in the structure along the b axis of the unit cell. The diffusion pathway to neighbour Li sites of the chain goes through the tetrahedral voids adjacent to each pair of edge sharing Li sites. If the olivine is free of defects, i.e. with all Li sites fully occupied, the diffusion is hindered because there are no available sites where the Li-ion can diffuse to. However, when there is an empty Li site next to a Li-ion, the diffusion is facilitated. That is why the chapter focuses on defect introduction through doping and non-stoichiometry into the olivine structure. The main defect pursued in this study is the Li-vacancy, which is known to affect the Li-ion conductivity through the vacancy mediated mechanism [20].

Isovalent and aliovalent substitutions of olivine materials have been studied by several authors e.g. Mg²⁺, Al³⁺, Zr⁴⁺ and Nb⁵⁺ on the Li and Fe sites, from 5% to 12%, in doped LiFePO₄ [21] or Mg²⁺, Ni²⁺, Al³⁺ and V³⁺, on the Fe site at 5%, in doped LiFePO₄ [22] also Zn²⁺ doped LiMgPO₄ on the Mg site up to 20% and also S doped LiFePO₄ on the O site at about 2% [23]. During this chapter all the efforts have been directed toward the aliovalent substitution with hyper-valent elements with respect to the original elements attempted to be substituted, i.e. Mg and Li. The idea of the aliovalent doping with 3+ hyper valent cations is that every M³⁺ ion substitutes two ions in the structure at the same time: Mg²⁺ and Li⁺ as can be seen in equation 3.1, where □ denotes the vacancy and x is the doping level. This creates

Li-vacancies that improve the Li-ion conductivity by enabling the vacancy mediated mechanism [20].



Depending on the site where the dopant atom sits, different doping scenarios could appear, some of which are mentioned here. For a dopant on the Mg site the vacancy can be created either on the Li site, $[\text{Li}_{1-x}\square_x][\text{Mg}_{1-x}\text{M}_x]\text{PO}_4$ for a M^{3+} ion, or on the Mg site, $\text{Li}[\text{Mg}_{1-2x}\text{M}_x\square_x]\text{PO}_4$ for a M^{4+} ion. For a dopant on the Li site the vacancy can be created again either on the Li site, $[\text{Li}_{1-nx}\square_{(n-1)x}(\text{M}^{n+})_x]\text{MgPO}_4$ or on the Mg site. For a dopant on the P site the vacancy can also be created either on the Li site, $[\text{Li}_{1-x}\square_x]\text{Mg}[\text{P}_{1-x}\text{S}_x]\text{O}_4$, or on the Mg site, $\text{Li}[\text{Mg}_{1-x}\square_x][\text{P}_{1-2x}\text{S}_{2x}]\text{O}_4$. The vacancy on the P site is not likely due to the fact that the P-O bond in the oxyanion is predominantly covalent.

Two main pathways were followed, one led by traditional considerations of ionic radii similarity and another one based on the outcome of DFT calculations. The traditional approach takes into consideration the comparison of the ionic radii in the hosting coordination environment. The DFT calculations are used for quantum mechanical modelling and can be used to predict the relative formation enthalpies for a number of doping scenarios.

This chapter presents the pathway followed for the synthesis, characterisation and property measurements of LiMgPO_4 and a number of new derivatives. The doping strategies tested have been the introduction of In^{3+} , Sc^{3+} , Ga^{3+} and Zr^{4+} , on the Mg site and the introduction of Mg^{2+} on the Li site. Considering the 1976 Shannon radii [24], Mg^{2+} and Zr^{4+} have the same radius when placed in octahedral environments, therefore the substitution of Zr for Mg was tried and the outcome is presented in the corresponding section of the chapter. The rest of the substitutions were selected from DFT calculations or inspired by insights from this chapter. All the chemistry in this chapter makes use of ions with strongly preferred oxidation states that prevent from any redox process that could lead to band filling. In this way the electronic conductivity is avoided. Solid state NMR and AC impedance spectroscopy have been used to evaluate the Li-ion conductivity of the best

samples. The work related to indium doping is published in a paper from 2015 in the journal Chemistry of Materials [25].

3.2 Density functional theory calculations

Periodic density functional theory, DFT, calculations were performed by Dr Matthew S Dyer with the aim of finding a suitable aliovalent substitution for the parent olivine LiMgPO_4 . The framework of the calculations was a 2 by 2 by 2 supercell of LiMgPO_4 which contains 32 formula units. The defect concentration was of 1 dopant atom in every supercell, which yields a fraction of substitution of $1/32 = 3.125\%$.

The relative doping enthalpies to the parent material and potential competing phases were evaluated for a number of different dopant atoms sitting on different sites of the structure. Because there were partially occupied sites in the trial structures, i.e. the Li site, the entropy of mixing was also included to account for temperature effects. The candidate structures were considered as disordered structures. The resulting relative enthalpies are shown in table 3.1.

Table 3.1. Relative doping enthalpies derived from DFT calculations.

Site of doping in LiMgPO_4	Relative doping enthalpy for each dopant
Li^+	$\text{Mg}^{2+} < \text{Ca}^{2+} < \text{Ga}^{3+} < \text{Y}^{3+}$
Mg^{2+}	$\text{In}^{3+} < \text{Sc}^{3+} < \text{Ga}^{3+} < \text{Y}^{3+}$

The most favoured substitutions in each case are the one with In atom on the Mg site and the one with Mg atom on the Li site. All these aliovalent substitutions lead to Li-vacancy introduction in the olivine structure. In principle, the substitutions on the Mg site are preferred because any dopant atom on the Li site would block the postulated Li diffusion pathway along the 1-D channels of the structure [11].

For doping on the Mg site with a M^{3+} cation, the general equation of the composition is $[\text{Li}_{1-x}\square_x][\text{Mg}_{1-x}\text{M}_x]\text{PO}_4$, where x is the doping level. This compositions can be made from solid solutions of LiMgPO_4 and MPO_4 as shown in equation 3.1. For every inclusion of one cation M^{3+} in the structure, the two cations Mg^{2+} and Li^+

are taken out in order to keep the charge balance. This process creates a vacancy in the Li channel, denoted as □, which potentially will increase the Li-ion conductivity.

The doping process to get the series of $[\text{Li}_{1-x}\square_x][\text{Mg}_{1-x}\text{In}_x]\text{PO}_4$ was predicted to be endothermic at low temperatures, i.e. not forming. Calculations showed that at high temperatures the phase would form stabilised by the effect of the entropy of mixing. More details about these calculations are provided in the 2015 publication [25].

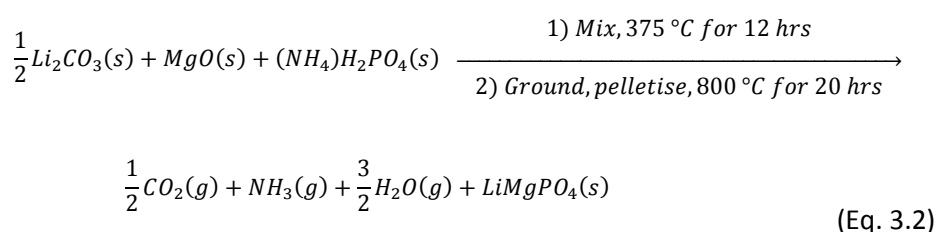
The following sections describe the synthesis of the parent material and the doping attempts with the discussed cations.

3.3 The parent material LiMgPO_4

3.3.1 Synthesis

LiMgPO_4 is the reference material for all the derivatives prepared in this chapter. Its structure is used to build new structural models and its properties used as baseline in all comparisons. For that reason its synthesis and characterisation is described first.

LiMgPO_4 was prepared by using a modified version of a 2012 protocol [26]. The reaction that takes place during the synthesis is shown in equation 3.2.



Stoichiometric amounts of high purity Li_2CO_3 (>99.995 %, Fluka Analytical, used from desiccator), MgO (99.95 %, Alfa Aesar, dried and decarbonated at 950°C), and $(\text{NH}_4)\text{H}_2\text{PO}_4$ (99.999 %, Sigma-Aldrich, dried at 120°C) are dry-mixed in an agate

pestle and mortar. The mixture is subject to a first heat treatment at 375 °C for 12 hours in an alumina crucible, with a heating rate of 0.5 °C/min and cooling rate of 5 °C/min. The resulting solid is thoroughly ground with pestle and mortar and made into a pellet. The pellet is placed into an alumina crucible and fired for 20 hours at 800 °C, with heating rate of 1 °C/min and cooling rate of 2 °C/min.

The initial dry mixing has to be brief because the mixture sticks to the surface of the mortar. One optimisation to this is to grind $(\text{NH}_4)\text{H}_2\text{PO}_4$ separately before the weighing step, so that the pestle pressure can be reduced during the first mixing. A sample scale above 1.5 grams has proven to work properly. On the contrary a sample scale of 0.5 grams produced many impurities. The intermediate grinding is very important in order to get the best homogenisation possible before the high temperature firing at 800 °C in which the final phase is formed.

The diffraction pattern of a small size sample of 0.5 g for which $(\text{NH}_4)\text{H}_2\text{PO}_4$ was not ground separately is shown in figure 3.2. In this case, the extra reflections that can be seen have been matched to the impurities $\text{LiMg}_3\text{P}_3\text{O}_{11}$, $\text{Li}_4\text{P}_2\text{O}_7$, $\text{Mg}_3(\text{PO}_4)_2$, $\text{MgP}_4\text{O}_{11}$ and AlPO_4 , although they could probably be doped versions of the matched phases.

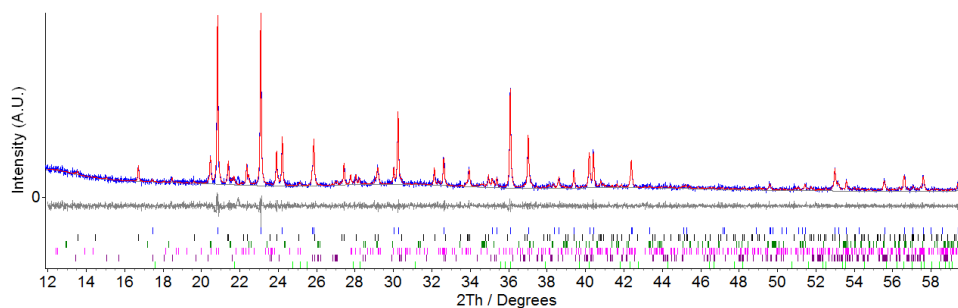


Figure 3.2. $\text{Cu K}\alpha_1$ PXRD pattern of LiMgPO_4 synthesised as described in the text in 0.5 g scale. Multiphase Pawley fit, red, to the data, blue. Background and difference are plotted in grey. Blue tick marks represent the olivine phase. Black, dark green, pink, purple and light green tick marks represent the impurity phases $\text{LiMg}_3\text{P}_3\text{O}_{11}$, $\text{Li}_4\text{P}_2\text{O}_7$, $\text{Mg}_3(\text{PO}_4)_2$, $\text{MgP}_4\text{O}_{11}$ and AlPO_4 respectively, some of which are probably doped versions.

On the other hand, for a sample in scale of 1.5 grams for which $(\text{NH}_4)_2\text{H}_2\text{PO}_4$ was ground separately the result is a high purity sample as shown in figure 3.3. The extra reflection at $2\theta = 32.69^\circ$ belongs to the grease used to stick the powder on the glass slide of the sample holder of the diffractometer. Synchrotron data from this sample will be analysed in the next section.

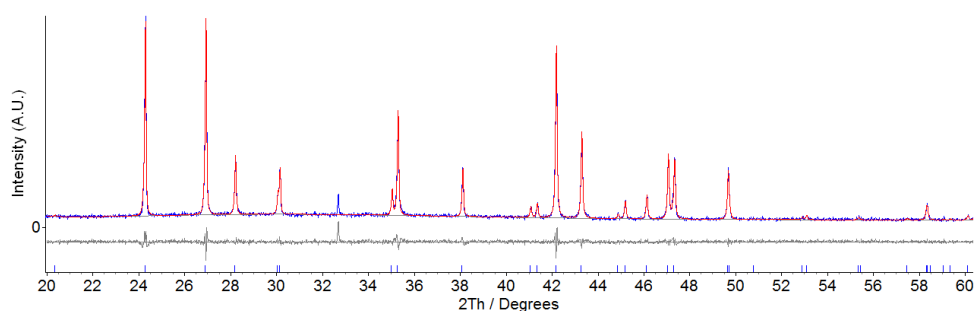


Figure 3.3. $\text{Co K}\alpha_1$ PXRD pattern of a high purity sample of LiMgPO_4 . Pawley fit, red, to the data, blue. Background and difference are plotted in grey. Blue tick marks represent the olivine phase. Reflection at $2\theta = 32.69^\circ$ is not from the sample, belongs to the grease used to prepare the diffraction slide.

3.3.2 Characterisation

A high purity sample of LiMgPO_4 was initially characterised with laboratory PXRD. This sample was prepared for chemical analysis and for high resolution powder X-ray diffraction.

Chemical analysis was performed by ICP-OES. A sample of 14.3 mg was digested in hot concentrated nitric acid 70 % analytical grade. The composition recovered from analysis was $\text{Li}_{0.993(4)}\text{Mg}_{1.000(6)}\text{P}_{1.000(5)}\text{O}_4$. These results have been normalised to phosphorous and oxygen has been added using the nominal value, which is matched within experimental uncertainty. The propagated uncertainty is shown as ± 1 standard deviation ($\sim 68.27\%$ probability).

The high resolution PXRD data was collected with the diffractometer I11 at the synchrotron Diamond Light Source by using the multi-analyser crystal (MAC) detectors at a wavelength of $0.825685(2) \text{ \AA}$. The sample was loaded into a

borosilicate capillary of 0.7 mm diameter. The capillary diameter was chosen based on the X-ray absorption of the sample. These calculations were made by using the web app for X-ray absorption calculations available at the website of the Argonne National Laboratory [27]. The calculated absorption of this sample resulted in a value of $\mu_R = 0.29$, meaning that the X-ray absorption was negligible. Four 30 minutes scans with native step size of 0.001° were added together and re-binned to 0.003° , which is the final dataset analysed here.

The Rietveld refinement of this sample has been performed by following the parameters turn-on sequence introduced in the previous chapter with the software Topas academic version 5 [28]. The Pearson VII peak shape and its initial coefficients have been selected after comparing R_{wp} values against Pseudo-Voigt and TCHZ in a preliminary and restricted Pawley refinement. Starting with the model of Hanic et al. [29], the scale factor and the zero error have been refined along with the simple axial model. The ion P^{5+} is not listed in the scattering tables of International Tables for Crystallography volume C. That is why neutral scattering factors have been used for all atoms. A Chebyshev-type background was added and refined at the same time than the lattice parameters. The number of background coefficients was increased until the number of 30. Such of a high number of coefficients were needed due to the strong capillary background. Before starting the refinement of the scattering model, the absorption correction and the Rietveld models of the impurity phases $LiMg_3P_3O_{11}$ and $Li_4P_2O_7$ were added by using the structural models of Kim et al. [30] and Voronin et al. [31] respectively. At the end of the refinement it was estimated that $LiMg_3P_3O_{11}$ and $Li_4P_2O_7$ were present in weight fractions of 0.553(8) % and 0.137(6) % respectively, with errors shown as 1 e.s.d. The remaining weak peaks were fitted to single profile functions and their position and intensity listed in table 3.4 where a candidate tetragonal phase, found by using TREOR90 [32], has been indicated but not used due to having overlapping reflections with the olivine phase. The tetragonal phase was searched in the ICSD database [33] by using cell dimensions and crystal system but no candidates with sensible chemistry were found. Care has been taken that none of the single profiles fitted are in the same position as any of the Bragg reflections of the refined phases. Their positions were fixed after this refinement step to guarantee no influence during the final stages of the Rietveld refinement. The peak shape for all extra phases and peaks is constrained to be the same as for $LiMgPO_4$. The atomic

coordinates of the general positions and the refinable coordinates of the especial positions are refined next, after which the peak width and the isotropic displacement parameters are refined. Finally all peak shape parameters are refined.

This is a refinement based in X-rays only. Light atoms such as Li or O interact weakly with X-rays due to having few electrons. Because of that during this refinement the occupancies have not been refined and have remained fixed to those of the original model.

Refined crystallographic data and refinement fit factors are presented in table 3.2 and table 3.3 respectively. The refinement graphical output and the refined unit cell showing the olivine structure are shown in figure 3.4.

The refinement fit factors show that R_{wp} is about 5 times R_{exp} . This could mean that the structural model is not complete or there are systematic errors [34]. In the restricted Pawley refinements performed on this dataset for peak shape selection the R_{wp}/R_{exp} ratio was large as well, meaning that a wrong structural model is not the reason for the fit factor values. In this case the peak shape, that could not be improved more, is responsible for the large R_{wp}/R_{exp} ratio. While some peaks are perfectly fit, others remain with a small misfit. The origin of this could be an instrumental or a sample effect.

The processing conditions for this sample and the conductivity measurements will be discussed in next section alongside with the measurements of the In-doped samples.

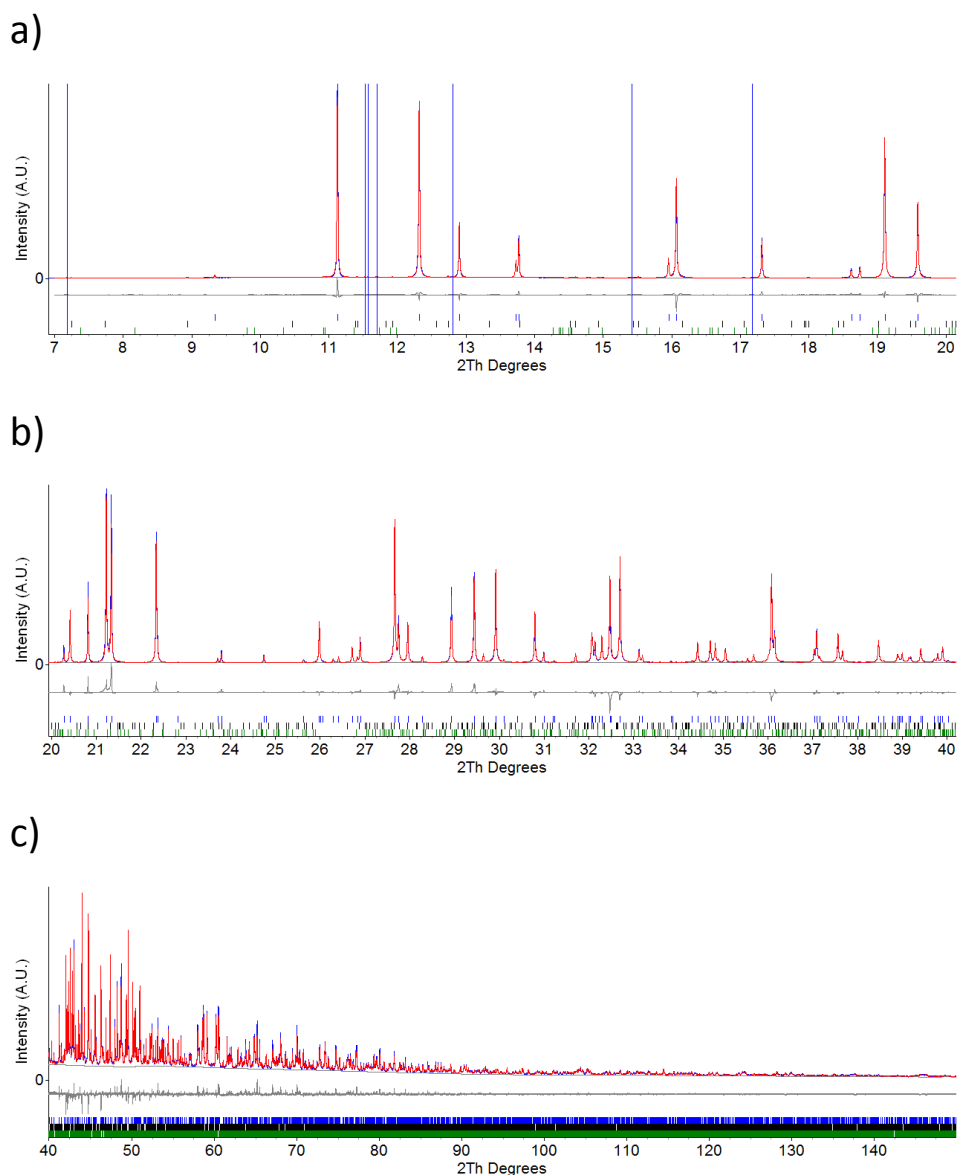


Figure 3.4. Different regions of the PXRD I11 data from a LiMgPO_4 sample and its Rietveld refinement, a), b) and c). Data is in blue, model in red and difference and background in grey. Blue tics represent the olivine phase. Black and green tics represent the impurity phases $\text{LiMg}_3\text{P}_3\text{O}_{11}$ and $\text{Li}_4\text{P}_2\text{O}_7$ respectively. The blue vertical lines on panel a) represent the single profile fits to the individual peaks on table 3.4. The refined olivine structure showing the atoms as 99 % thermal displacement spheres is plotted on d).

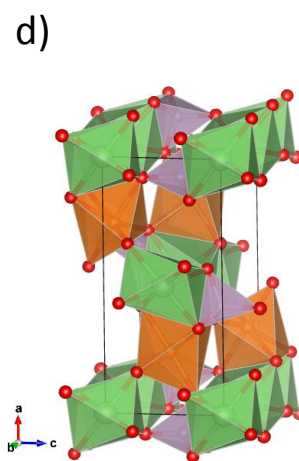


Table 3.2. Crystallographic data of the refined asymmetric unit of LiMgPO_4 in the standard setting of the space group $Pnma$. Errors shown as 1 e.s.d.

Atom	Wyckoff position	X	Y	Z	Occupancy	Biso / \AA^2
Li	4a	0	0	0	1	1.42(4)
Mg	4c	0.27835(3)	0.25	0.98205(7)	1	0.533(9)
P	4c	0.09556(3)	0.25	0.41657(6)	1	0.382(7)
O1	4c	0.10138(7)	0.25	0.74099(13)	1	0.482(13)
O2	4c	0.45281(7)	0.25	0.19990(13)	1	0.423(12)
O3	8d	0.16600(5)	0.04393(7)	0.28088(9)	1	0.422(9)

Table 3.3. Lattice parameters and refinement fit factors of the LiMgPO_4 refinement. Orthorhombic unit cell with space group $Pnma$. Errors shown as 1 e.s.d.

Lattice parameter	Value	Refinement parameter	Value
a	10.138056(15) \AA	R_{wp}	7.3816 %
b	5.905722(8) \AA	R_{exp}	1.4051 %
c	4.689935(7) \AA	$\chi = R_{\text{wp}} / R_{\text{exp}}$	5.2534
volume	280.798(1) \AA^3	χ^2	27.5982

Table 3.4. List of weak peaks with refined position and intensity after single profile fitting. All the indicated peaks index to the tetragonal cell of parameters $a = b = 6.591584 \text{ \AA}$ and $c = 8.200901 \text{ \AA}$. Errors shown as 1 e.s.d.

Position / $^\circ$	Intensity (A.U.)	Indexed by the potential cell
7.183(2)	0.044(8)	Yes
11.528(2)	0.32(3)	Yes
11.574(2)	0.27(3)	Yes
11.704(1)	0.55(3)	Yes
12.809(1)	0.46(4)	No
15.418(1)	0.68(4)	Yes
17.177(2)	0.46(5)	No

3.4 In-doped series

3.4.1 Synthesis

This synthesis is similar to the one discussed for the parent material in the previous section. DFT calculations predicted that the doped compositions needed higher temperature than the parent to form the phase. The initial syntheses tried higher temperature treatments at 900 °C and 1000 °C instead of 800 °C. Regarding the reactants the only difference was the inclusion of In_2O_3 (99.995 %, Alfa Aesar, dried at 220 °C) as dopant precursor in order to complete the stoichiometric amounts indicated by the doping formula $\text{Li}_{1-x}\text{Mg}_{1-x}\text{In}_x\text{PO}_4$.

Experimental techniques such as the type of diffractometers used or how to dissolve samples for ICP were the same than for the parent material unless otherwise stated.

The trial with firing at 900 °C consisted of 3 samples of the series $\text{Li}_{1-x}\text{Mg}_{1-x}\text{In}_x\text{PO}_4$ for $x = 0.05, 0.1$ and 0.15 . These samples were impure as shown in figure 3.5, but the increase in unit cell volume, from $280.81(2) \text{ \AA}^3$ for the parent to $282.45(2) \text{ \AA}^3$ for the $\text{Li}_{0.95}\text{Mg}_{0.95}\text{In}_{0.05}\text{PO}_4$ sample, indicated that the sample was doped. The unit cell volume determination of the doped sample was made without internal standard. The observed impurity is $\text{LiMg}_3\text{P}_3\text{O}_{11}$.

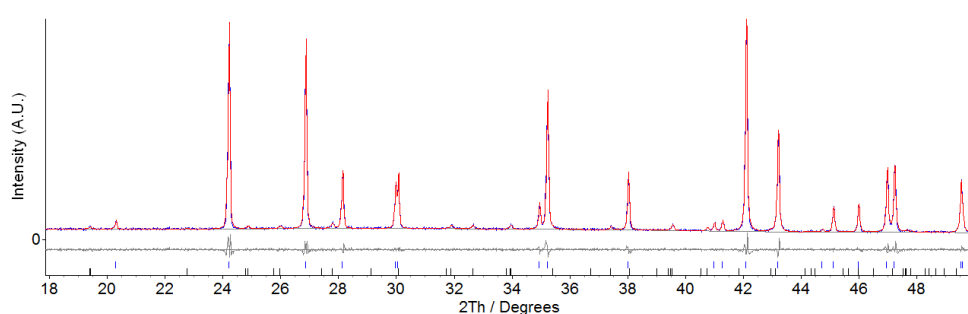


Figure 3.5. $\text{Co K}\alpha_1$ PXR D pattern of $\text{Li}_{0.95}\text{Mg}_{0.95}\text{In}_{0.05}\text{PO}_4$ synthesised as described in the text but with the high temperature firing at 900 °C. Multiphase Pawley fit, red, to the data, blue. Background and difference are plotted in grey. Blue tick marks represent the olivine phase and black tick marks represent the impurity phase $\text{LiMg}_3\text{P}_3\text{O}_{11}$.

Another trial with firing at 1000 °C consisted of three members of the series $\text{Li}_{1-x}\text{Mg}_{1-x}\text{In}_x\text{PO}_4$ for $x = 0.05, 0.1$ and 0.2 . These samples showed a lattice parameter evolution that was evidence of the doping of the material.

The first two samples, for $x = 0.05$ and 0.1 , appeared to be phase pure. The Pawley refinement for the sample with nominal composition $\text{Li}_{0.9}\text{Mg}_{0.9}\text{In}_{0.1}\text{PO}_4$ is shown in figure 3.6. The third sample, for $x = 0.2$, showed many impurity peaks that could not be matched to any known phase of the elements contained in the sample. It was indexed by using TREOR90 [32] to an orthorhombic cell that refined its cell parameters to $a = 13.746(3) \text{ \AA}$, $b = 9.412(2) \text{ \AA}$ and $c = 9.260(2) \text{ \AA}$, i.e. volume = $1198.0(4) \text{ \AA}^3$, with errors as 3 e.s.d. The multiphase Pawley fit for the sample with nominal composition $\text{Li}_{0.8}\text{Mg}_{0.8}\text{In}_{0.2}\text{PO}_4$ is shown in figure 3.7.

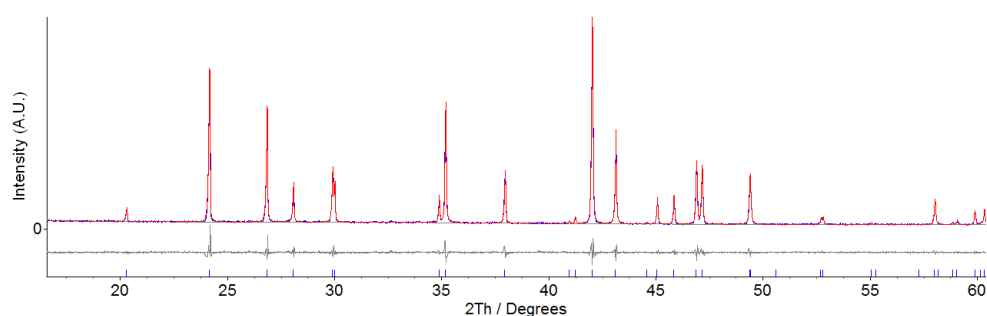


Figure 3.6. Co $K\alpha_1$ PXRD pattern of a high purity sample of $\text{Li}_{0.90}\text{Mg}_{0.90}\text{In}_{0.10}\text{PO}_4$. Pawley fit, red, to the data, blue. Background and difference are plotted in grey. Blue tick marks represent the olivine phase.

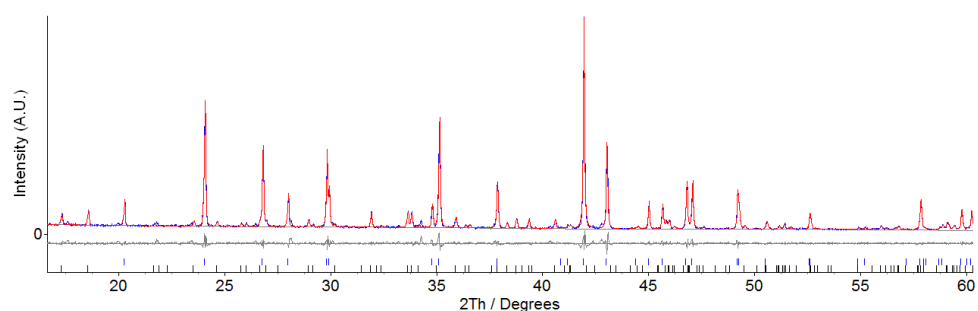


Figure 3.7. Co $K\alpha_1$ PXRD pattern of the sample with nominal composition $\text{Li}_{0.80}\text{Mg}_{0.80}\text{In}_{0.20}\text{PO}_4$. Multiphase Pawley fit, red, to the data, blue. Background and difference are plotted in grey. Blue tick marks represent the olivine phase and black tick marks represent the unknown impurity phase indexed to the orthorhombic unit cell described in the text.

The second evidence to indicate that the doping did happen was the fact that the Rietveld model for In on the Mg site fits the growing intensity with x of the first reflection of the pattern, i.e. (2 0 0).

The comparison of these two syntheses at 900 °C and 1000 °C indicates that the doped compound needs a higher temperature than the parent to be formed in agreement with calculations [25]. From now on the synthesis at 1000 °C was considered the standard procedure for the series $\text{Li}_{1-x}\text{Mg}_{1-x}\text{In}_x\text{PO}_4$.

In order to establish the doping limit and clarify Vegard's law for this system, a new synthesis was planned. The new synthesis included replication of the successful samples made at 1000 °C. The doping levels of the new series of $\text{Li}_{1-x}\text{Mg}_{1-x}\text{In}_x\text{PO}_4$ were $x = 0.05, 0.1, 0.15, 0.17, 0.19, 0.21$. From this set, all the samples from $x = 0.05$ to $x = 0.17$ resulted in phase pure materials with the olivine structure.

The cell parameters of all the samples were obtained with laboratory powder diffraction by using as internal standard the secondary standard LaB_6 . The plot in figure 3.8 shows the relative lattice parameters for these samples. The volume increases linearly from $280.81(2) \text{ \AA}^3$ for $x = 0$ until $285.88(2) \text{ \AA}^3$ for $x = 0.17$, errors shown as 3 e.s.d. The volume increase reaches a plateau for the last two samples with $x = 0.19$ and $x = 0.21$ at the same time that the unknown impurity indexed to the orthorhombic cell of volume = $1198.0(4) \text{ \AA}^3$ appears. This behaviour is known as Vegard's law and the doping limit corresponds to the point where the linear trend of the increasing volume reaches the plateau. Beyond the doping limit impurity phases arise.

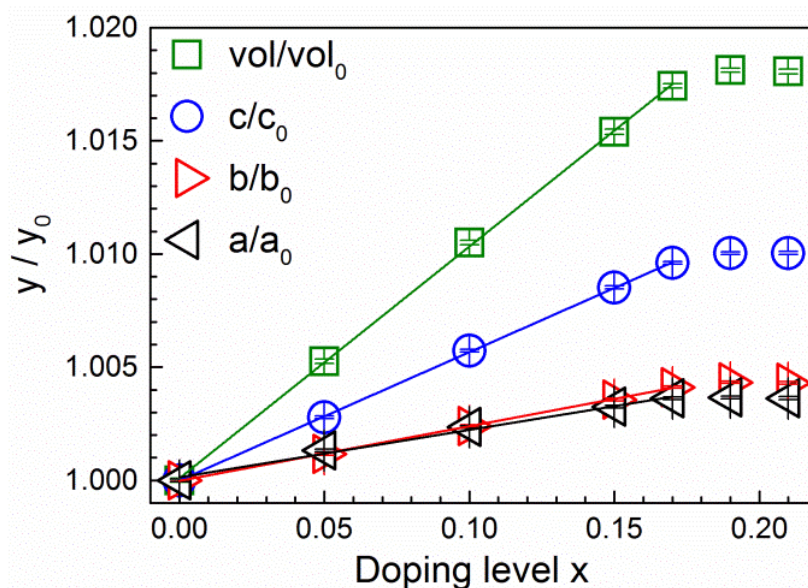


Figure 3.8. Relative cell parameters for the In-doped samples until $x = 0.21$ in $Li_{1-x}Mg_{1-x}In_xPO_4$. Error bars are shown as ± 3 e.s.d. The cell volume for $LiMgPO_4$ is $280.81(2) \text{ \AA}^3$. Reproduced with permission from Chem. Mater., 2015, 27 (6), pp 2074–2091, DOI: 10.1021/cm504518q. Copyright 2015 American Chemical Society.

The powder X ray diffraction data of the series for all samples that appeared to be phase pure are shown in figure 3.9. The reflection marked with the asterisk belongs to the LaB_6 used as internal standard. For the olivine phase, trends arise with respect to the relative intensities and 2θ translation. The reflection (2 0 0) has an intensity that increases with increasing value of x . Reflections (2 0 1) and (1 1 1) swap intensity with increasing x . Finally, the translation of the olivine patterns to the left, i.e. longer d-spacing, with x represents the increase in lattice parameters.

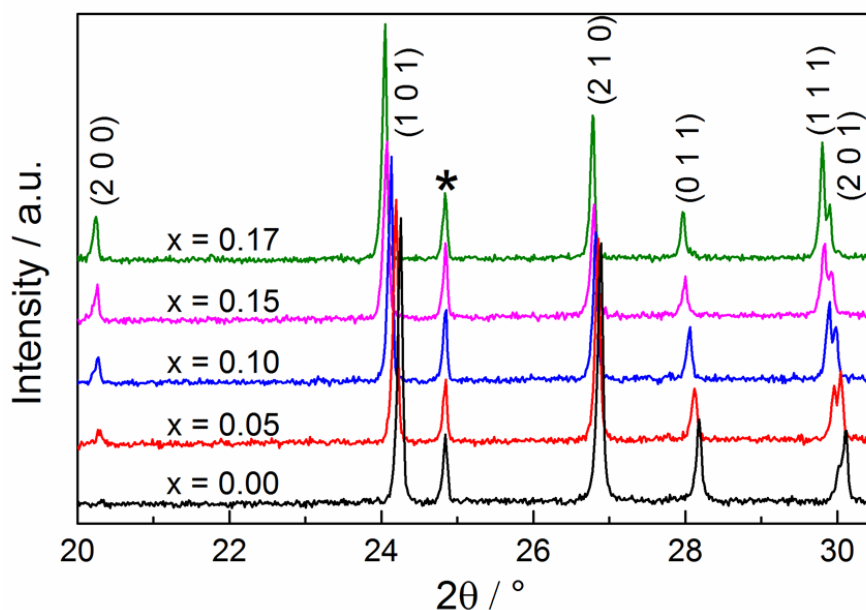


Figure 3.9. Co $K\alpha_1$ powder X-ray diffraction patterns of the phase pure $\text{Li}_{1-x}\text{Mg}_x\text{In}_x\text{PO}_4$ samples as a function of x . The intensities of the reflections (200), (111) and (201) are highly correlated with the value of x . The extra reflection marked with an asterisk is the reflection (100) from the internal standard LaB_6 . Reproduced with permission from *Chem. Mater.*, 2015, 27 (6), pp 2074–2091, DOI: 10.1021/cm504518q. Copyright 2015 American Chemical Society.

In order to perform a detailed structural analysis, large batches (5 – 6 g) of the compositions $\text{Li}_{0.95}\text{Mg}_{0.95}\text{In}_{0.05}\text{PO}_4$, $\text{Li}_{0.90}\text{Mg}_{0.90}\text{In}_{0.10}\text{PO}_4$, $\text{Li}_{0.85}\text{Mg}_{0.85}\text{In}_{0.15}\text{PO}_4$ and $\text{Li}_{0.83}\text{Mg}_{0.83}\text{In}_{0.17}\text{PO}_4$ were prepared for neutron diffraction. These samples were made enriched in ^7Li in order to avoid the high neutron absorption suffered by the isotope ^6Li . The ^7Li enriched samples were prepared using $^7\text{Li}_2\text{CO}_3$ (99% ^7Li atom, Sigma-Aldrich, used from desiccator). $^7\text{Li}_2\text{CO}_3$ was ground to fine powders prior to use.

3.4.2 Chemical analysis

The chemical composition was confirmed by ICP-OES analysis and TEM-EDX. Samples for ICP-OES were prepared by dissolving the powder in hot nitric acid in the same way as for the parent material. The TEM-EDX data were collected by Dr Marco Zanella. The samples for TEM-EDX were prepared by using a Cu grid from a suspension of powder samples in methanol. Data from a sample with $x = 0.1$ is shown in table 3.5 alongside with data for the parent sample discussed in previous section. These two samples were made with natural abundance Li. Another sample with $x = 0.1$, isotopically enriched in ^7Li , was also analysed and its data presented in the same table. The analytical data shown in table 3.5 is in agreement with the nominal compositions within errors. The error shown is 1 standard deviation. Zoomed in regions of the ternary diagrams in Mg-P-In derived from the TEM-EDX measurements of the doped samples in table 3.5 are shown in figure 3.10. TEM-EDX spectra and data are listed in appendix 3.1.

Table 3.5. The chemical composition of three samples determined by ICP-OES and TEM-EDX. The uncertainty is shown as 1 standard deviation. A hyphen indicates lack of data due to technique limitations, e.g. EDX for Li, or instrument reading lower than the limit of detection. Reproduced with permission from Chem. Mater., 2015, 27 (6), pp 2074–2091, DOI: 10.1021/cm504518q. Copyright 2015 American Chemical Society.

Nominal composition	Analysis				
	Technique	Li	Mg	In	P
LiMgPO_4	ICP-OES	0.993(4)	1.000(6)	-	1.000(5)
$\text{Li}_{0.9}\text{Mg}_{0.9}\text{In}_{0.1}\text{PO}_4$	ICP-OES	0.897(7)	0.91(1)	0.0975(4)	1.000(5)
	TEM-EDX	-	0.85(2)	0.096(5)	1.00(3)
$^7\text{Li}_{0.9}\text{Mg}_{0.9}\text{In}_{0.1}\text{PO}_4$	ICP-OES	0.908(9)	0.906(8)	0.0964(6)	1.000(7)
	TEM-EDX	-	0.85(3)	0.088(9)	1.00(4)

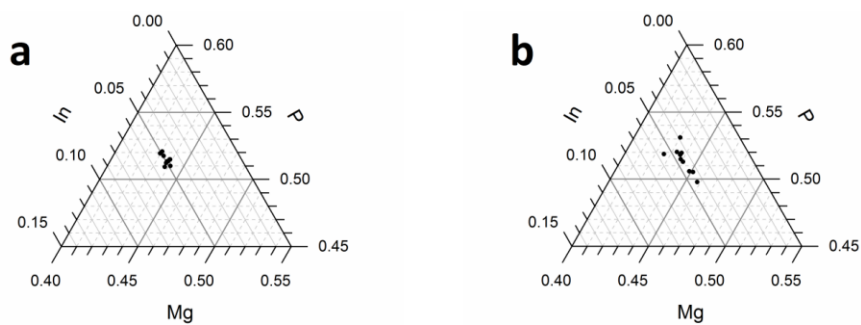


Figure 3.10. Compositional ternary diagrams showing the EDX derived compositions of a) $\text{Li}_{0.9}\text{Mg}_{0.9}\text{In}_{0.1}\text{PO}_4$ and b) ${}^7\text{Li}_{0.9}\text{Mg}_{0.9}\text{In}_{0.1}\text{PO}_4$ obtained from 10 crystallites per sample. Reproduced with permission from Chem. Mater., 2015, 27 (6), pp 2074–2091, DOI: 10.1021/cm504518q. Copyright 2015 American Chemical Society.

3.4.3 Diffraction and refinements

For detailed structural analysis of the In-doped system, neutron powder diffraction data were collected on the samples isotopically enriched in ${}^7\text{Li}$. The neutron diffraction experiments were performed at ISIS, Harwell Oxford (UK) using the diffractometers POLARIS ($x = 0.05, 0.10$) and GEM ($x = 0.15, 0.17$). The neutron diffraction datasets were absorption corrected by using the software Mantid [35]. These four samples were also studied by synchrotron X-ray powder diffraction by using the beam line I11 in Debye-Scherrer geometry with the multi-analyser crystal (MAC) detectors at Diamond Light Source, Oxfordshire (UK).

For neutron diffraction the samples were loaded in vanadium cans. For synchrotron PXRD the samples were loaded into a borosilicate capillary of 0.7 mm diameter. The capillary diameter was chosen based on X-ray absorption calculations performed as explained for the parent material. Assuming a packing fraction of 0.6, the highest absorption resulted for the sample with $x = 0.17$ for which $\mu\text{R} = 0.71$, value that generally allow the absorption to be neglected.

The combined Rietveld refinement of the sample ${}^7\text{Li}_{0.90}\text{Mg}_{0.90}\text{In}_{0.10}\text{PO}_4$ was carried out on synchrotron XRD and NPD data by using the software Topas Academic version 5 [28]. The LiMgPO_4 model from Hanic et al. [29] was used as starting model for developing the indium containing structural model with In^{3+} on the Mg^{2+} site.

The refinement started by setting up a Topas input file with the data filenames, adding the I11 wavelength for that experiment, 0.825685 Å, and the POLARIS difC, difA and t0 diffractometer constants for that period (see chapter 2) from calibration with NBS Si 640b.

The initial peak shape and zero error for the X ray data were taken from a preliminary Pawley refinement, run over a restricted 2θ range. For this dataset Pseudo Voigt gave the best fit after comparing with TCHZ and Pearson VII.

Due to having a three column data file, i.e. .xye, the weighing method was changed from the default 1/I to 1/σ². The parent olivine structure was introduced in the structure section and adapted to contain the nominal composition ⁷Li_{0.90}Mg_{0.90}In_{0.10}PO₄, i.e. the Mg site was duplicated and its occupancies partitioned for In and Mg in stoichiometric ratios through a compositional constraint for the Mg site so that both elements add up to 1. The constraint was extended to the Li site so that the vacancy level is actually the same as the occupancy of indium, i.e. vacancy fraction plus Li occupancy add up to 1.

The cell parameters were changed to those from the preliminary Pawley fit, the initial B_{iso} values were used from the previous LiMgPO₄ I11 refinement discussed previously in this chapter and the scattering factors were set to neutral for all atoms for the same reason as it was done for the parent sample, but noting that this sample is ⁷Li enriched and therefore its scattering factor was chosen instead of the one for natural abundance Li. The initial axial divergence was taken from the Pawley fit.

During the first stage of refinement X-ray data was fitted alone. In the first run, only I11 scale and zero error were refined. During the second cycle lattice parameters and a constant background were refined. The 2θ range was then set to refine from 7 °. Subsequent cycles were used to increase the number of coefficients of the background up to a number of 24 that were needed by visual inspection. X-ray absorption correction was introduced before starting with the structure refinement. It was double checked that no absorption correction would be applied to the neutron data during the refinement because these datasets were previously corrected for absorption.

In a second stage of the refinement, the lattice parameters were fixed and the neutron histograms added to the refinement at the same time as the X-ray histogram is switched off. Polaris banks 3, 4 and 5 are added and difA refined, which is sample dependent. It is the t^2 contribution to the TOF vs d-spacing relationship (see chapter 2). The banks still show TOF misfit and that is why difC is refined. difC is the constant that linearly relates TOF with d-spacing.

At this stage X-rays are included again in the refinement to refine all 4 histograms at the same time. The lattice parameters are left to refine again. For the refinement of the crystal structure, atomic coordinates are refined first, then B_{iso} factors are refined. The following cycle is used to refine occupancy of Indium which is constrained with Li and Mg. The indium occupancy refines to 0.0948(7), with error as 3 e.s.d. The occupancy is fixed and the next cycle is used to refine B_{aniso} factors also known as anisotropic displacement parameters, ADPs. In the *Pnma* space group not all the B_{aniso} components can be refined, because the symmetry imposes the restriction of $U_{12} = U_{23} = 0$ for all atoms on a 4c site. For this particular case Topas failed to keep them fixed automatically and that is why they were fixed manually before running the last cycle of the refinement. Finally the In occupancy is refined again to yield a value of 0.0924(7) with error as 3 e.s.d.

A set of weak peaks was visible in synchrotron X-ray data for all the samples at 2θ angles below 30° . A second set of weak peaks was observed for samples $x = 0.10$, 0.15 and 0.17. These weak peaks were not observed in laboratory diffractometer data. The first set of peaks was assigned to $LiMg_3P_3O_{11}$ and included as a Rietveld phase by using the model from Kim et al. [30] which weight fraction refined to 2.02(5) % with error as 1 e.s.d. The second set of peaks was indexed by using TREOR90 [32] from peak positions extracted with Fullprof [36] to an orthorhombic cell of refined dimensions $a = 18.922(3) \text{ \AA}$, $b = 9.0713(9) \text{ \AA}$ and $c = 8.3541(12) \text{ \AA}$, volume = $1434.0(3) \text{ \AA}^3$ with errors shown as 1 e.s.d. The space group used for fitting these peaks was *Pmna*, # 53. The indexed phase was inserted as a Pawley phase in the X-ray histogram only and it was restricted to $2\theta < 20^\circ$, because it was barely visible only in synchrotron data at low angles. Care was taken about the overlapping of indexed peaks with the olivine phase reflections.

The constraints used in this refinement consider an ordered model with all Li and vacancies on the A site of the olivine and all Mg and In on the B site, i.e. $\text{Li}_{1-x}\text{Mg}_{1-x}\text{In}_x\text{PO}_4$. Also a model that allowed Mg to interchange with vacancies of the A site was tested showing that this type of vacancy-Mg anti-site defects were not present, i.e. the model $[\text{Li}_{1-x}\text{Mg}_y][\text{Mg}_{1-x-y}\text{In}_x]\text{PO}_4$ refined $y = 0$ with no changes for x within errors.

The graphical outputs of the refinement and the resulting crystal structure showing the anisotropic displacement parameters as 99 % probability and the fraction of vacancies and dopant occupancy on each site are plotted in figure 3.11. The refined structural parameters and refinement fit factors are shown in tables 3.6, 3.7 and 3.8.

The high value of the goodness of fit χ is attributed to the models used for the peak shape and the background. The first was observed during the preliminary Pawley fits for selection of the peak shape and the second by visual inspection during the optimisation of the background.

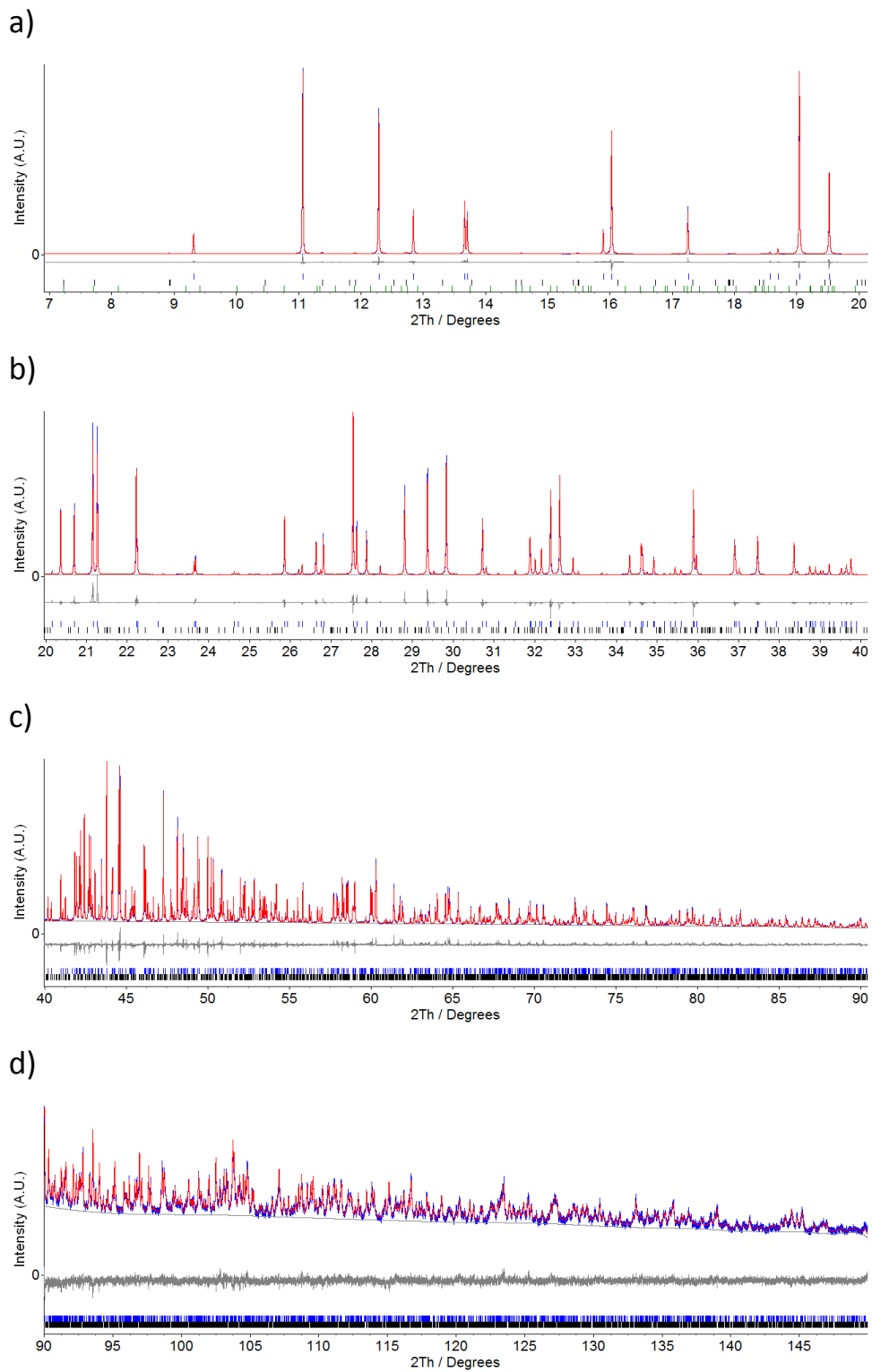


Figure 3.11. Combined Rietveld refinement of the sample ${}^7\text{Li}_{0.90}\text{Mg}_{0.90}\text{In}_{0.10}\text{PO}_4$ against neutron powder diffraction data from POLARIS, and PXRD I11 MAC data. Panels a) to d) show different regions of the X-ray histogram. Data is in blue, model in red and difference and background in grey. Blue, black and green tick marks represent the olivine phase, $\text{LiMg}_3\text{P}_3\text{O}_{11}$ and the indexed phase respectively.

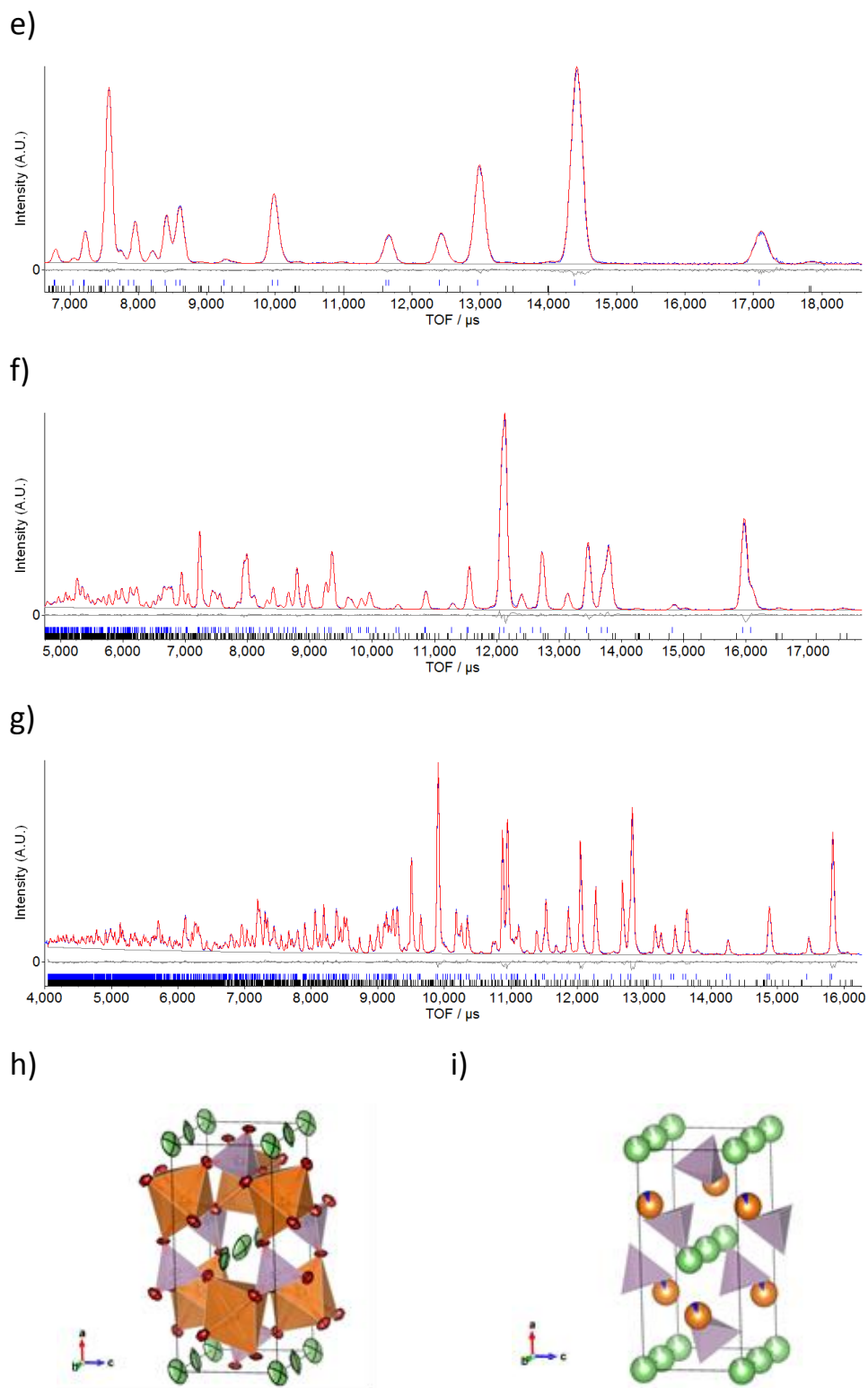


Figure 3.11. (Cont.) Panels e) to g) show the POLARIS banks 3 to 5 respectively. The refined olivine structure showing the atoms as 99 % thermal displacement ellipsoids is plotted on panel h). Abridged structure model with occupancies of the Li and Mg site represented with pie-charts is shown on panel i). The atom colours are green, orange, blue, purple and red for Li, Mg, In, P and O respectively.

Table 3.6. Crystallographic data of the refined asymmetric unit of ${}^7\text{Li}_{0.90}\text{Mg}_{0.90}\text{In}_{0.10}\text{PO}_4$ in the standard setting of the space group *Pnma*. Errors shown as 1 e.s.d.

Atom	Wyckoff position	X	Y	Z	Occupancy	Biso / Å ²
Li	4a	0	0	0	0.9076(2)	1.33(4)
Mg	4c	0.27797(2)	0.25	0.97875(4)	0.9076(2)	0.517(4)
In					0.0924(2)	
P	4c	0.09527(2)	0.25	0.41535(5)	1	0.400(4)
O1	4c	0.10346(5)	0.25	0.73813(10)	1	0.634(11)
O2	4c	0.45292(5)	0.25	0.19605(10)	1	0.493(10)
O3	8d	0.16602(4)	0.04484(6)	0.27858(7)	1	0.487(7)

Table 3.7. Anisotropic displacement parameters of the refined asymmetric unit of ${}^7\text{Li}_{0.90}\text{Mg}_{0.90}\text{In}_{0.10}\text{PO}_4$ in the standard setting of the space group *Pnma*. Errors shown as 1 e.s.d. The space group imposes the symmetry restriction of $U_{12} = U_{23} = 0$ for all atoms on a 4c site.

Atom	$U_{11} / \text{Å}^2$	$U_{22} / \text{Å}^2$	$U_{33} / \text{Å}^2$	$U_{12} / \text{Å}^2$	$U_{13} / \text{Å}^2$	$U_{23} / \text{Å}^2$
Li	0.0240(10)	0.0319(11)	0.0094(9)	0.0028(8)	-0.0059(8)	-0.0101(8)
Mg/In	0.00502(10)	0.00790(11)	0.00641(11)	0	0.00019(8)	0
P	0.00475(10)	0.00763(11)	0.00609(11)	0	-0.00046(9)	0
O1	0.0070(3)	0.0128(3)	0.0060(3)	0	-0.0017(2)	0
O2	0.0026(2)	0.0132(3)	0.0076(3)	0	0.00033(2)	0
O3	0.00683(18)	0.00651(17)	0.00828(19)	0.00154(16)	0.00174(15)	0.00053(15)

Table 3.8. Lattice parameters and refinement fit factors of the ${}^7\text{Li}_{0.90}\text{Mg}_{0.90}\text{In}_{0.10}\text{PO}_4$ refinement. Orthorhombic unit cell with space group *Pnma*. Errors shown as 1 e.s.d.

Lattice parameter	Value	Refinement parameter	Value
a	10.162488(7) Å	R_{wp}	5.4981 %
b	5.920588(4) Å	R_{exp}	1.2617 %
c	4.717274(3) Å	$\chi = R_{\text{wp}} / R_{\text{exp}}$	4.3575
volume	283.828(0) Å ³	χ^2	18.99

This sample, ${}^7\text{Li}_{0.9}\text{Mg}_{0.9}\text{In}_{0.1}\text{PO}_4$, was subject to variable temperature synchrotron PXRD from room temperature until 800 °C. The lattice parameters at each temperature were determined from Pawley fits. The relative lattice parameters are shown in figure 3.12.a, showing a linear increase in their values. The ratios a/b , a/c and b/c at each temperature are shown in figure 3.12.b, showing constant values for each ratio at all temperatures. These outcomes are in agreement with an isotropic expansion of the unit cell with temperature along with the retention of the space group $Pnma$.

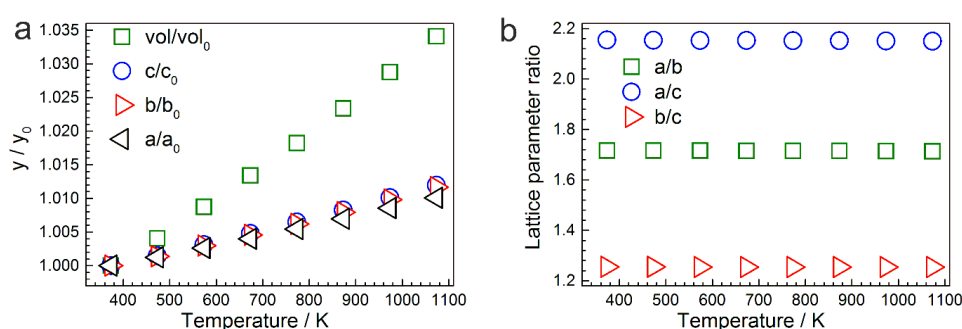


Figure 3.12. (a) Normalised lattice parameters for ${}^7\text{Li}_{0.9}\text{Mg}_{0.9}\text{In}_{0.1}\text{PO}_4$ as a function of temperature. (b) Lattice parameter ratios for ${}^7\text{Li}_{0.9}\text{Mg}_{0.9}\text{In}_{0.1}\text{PO}_4$ as a function of temperature, showing isotropic expansion of the unit cell on heating. Data for both plots were derived from Pawley fits to synchrotron PXRD data (I11 with PSD detector). Reproduced with permission from Chem. Mater., 2015, 27 (6), pp 2074–2091, DOI: 10.1021/cm504518q. Copyright 2015 American Chemical Society.

All the refinements presented in this thesis have been performed by the PhD candidate. The Rietveld refinements of all the samples of this family were presented in the 2015 publication [25] in which the Rietveld refinements were performed by Dr Michael Pitcher. In the article, a number of defect models are discussed and finally the model with all In on Mg site and a small fraction between 0 – 2 % of Li-Mg anti-site defects was chosen as the best, i.e. $[\text{Li}_{1-x-y}\square_x\text{Mg}_y][\text{Mg}_{1-x-y}\text{In}_x\text{Li}_y]\text{PO}_4$, where x is the doping level, y the fraction of Li-Mg anti-site defects and \square represents the vacancy. The refined occupancies of indium on Mg site derived from those refinements is presented in figure 3.13. This plot shows that the refinements systematically underestimate the indium occupancy.

Due to the fact that the occupancy factors are highly correlated with several refined parameters, such as the thermal displacement parameters [37], the deviation observed in this plot can be considered a common systematic error in this type of refinements.

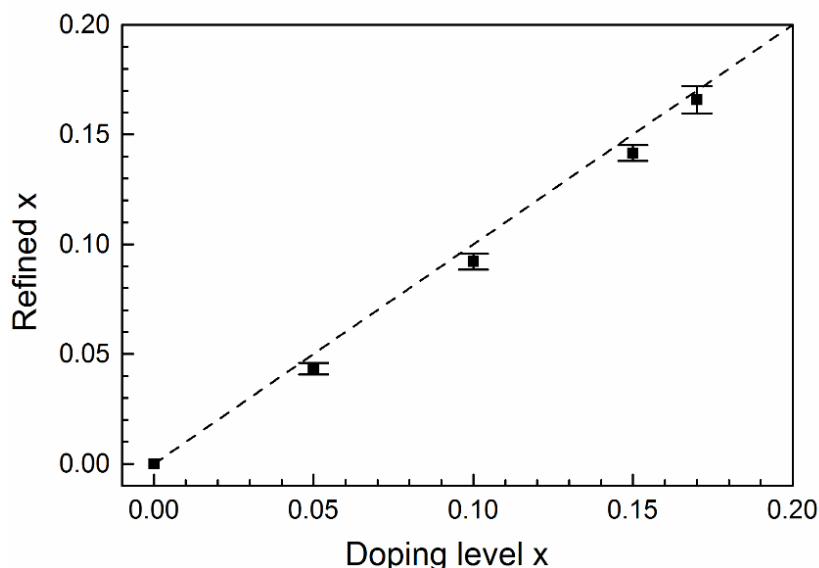


Figure 3.13. Refined In occupancy from synchrotron XRD and NPD combined refinements ($x = 0.05, 0.10, 0.15$) and from synchrotron XRD ($x = 0.17$) with the dashed line indicating the nominal stoichiometry. Error bars shown as ± 3 e.s.d. Reproduced with permission from Chem. Mater., 2015, 27 (6), pp 2074–2091, DOI: 10.1021/cm504518q. Copyright 2015 American Chemical Society.

3.4.4 Densification

For AC impedance measurements, high relative density pellets are needed. The processing conditions have been optimised from sintering the raw powder as synthesised, which gave relative densities lower than 90 %, to the following procedure that finally achieved relative densities above 90 %.

Ball milling is a critical step without which, high density cannot be achieved for this system. This was established by trial and error. Although the particle size of these materials were not measured before and after ball milling, the increase in relative density with ball milling is attributed to the reduction of particle size, which enable

denser particle packing and higher surface contact between grains. The ball milled powder enhances the sintering and the resulting relative density.

The bulk powders as synthesised were ball-milled in ethanol. Samples were loaded in 45 mL zirconia pots with 3 x 10 mm diameter zirconia balls. A Fritsch Pulverisette 7 planetary mill was used. The working milling time ranged from 45 minutes to 2.5 hours when milling samples in the range 0.5 – 2.8 grams. The mill speed was set at 350 rpm. Resting periods were set at regular intervals of 10 – 15 minutes. Finally, the slurry was dried under stirring in a crystallising dish at 60 – 70 °C. To determine that there was no zirconia contamination of the samples from the zirconia milling media, the final sintered pellets were studied by X-ray diffraction.

The resulting fine powder was recovered and pressed into pellets of 1 – 2 mm thickness by using a uniaxial press under a pressure of 60 MPa. The template used for making the pellets was a pellet die set of 13 mm of diameter. The formed pellets were then subject to cold isostatic pressing by using a hydrostatic pressure of 207 MPa.

All pellets were sintered loaded in alumina crucibles. The LiMgPO_4 pellets were placed directly in contact with alumina. For the In-doped samples a previously sintered buffer pellet of the same composition was used. The sintering temperature treatment consisted of dwelling the samples at 1000 °C for 5 hours with symmetric heating/cooling rates of 5 °C/min.

The density of each pellet was calculated from its mass and from its volume derived from calliper measurements. The relative density was calculated from the ratio between the pellet density and the crystallographic density determined in Rietveld refinements. All the relative densities were above 90 %.

X-ray diffraction patterns collected from each side of all pellets confirmed the phase purity of all processed samples.

3.4.5 Conductivity measurements

All the data shown in this section was collected and analysed by the PhD candidate, although guidance from Dr Ming Li, especially in the use and interpretation of modulus spectroscopic plots, was very useful.

All the phase pure compositions of the series $\text{Li}_{1-x}\text{Mg}_{1-x}\text{In}_x\text{PO}_4$ were studied by AC impedance spectroscopy, i.e. samples for $x = 0, 0.05, 0.10, 0.15$ and 0.17 . Dense pellets above 90 % relative density were obtained as explained in the previous section.

The electrodes needed for AC impedance measurements were mounted by painting both faces of the pellet with gold paste. Gold mesh and wire were added during this stage and used to provide wiring to the sample. After firing it at $600\text{ }^\circ\text{C}$ for 1 h, the sample was ready for AC impedance measurements. These measurements were performed under dry air.

All the plots presented in this section have been corrected for sample geometry. For all samples studied in this section there are temperatures at which the AC impedance response in the complex plane is of the same kind as the one shown in figure 3.14 for $\text{Li}_{85}\text{Mg}_{85}\text{In}_{15}\text{PO}_4$ at $249\text{ }^\circ\text{C}$. The main features are a single depressed arc at high frequencies and a spike at low frequencies. The data showed no more arcs at the high frequency end.

When these samples are measured at a lower temperature the spike due to electrode response is lost. If the temperature is lowered even more, the arc is partially lost as can be seen in figure 3.15 for the same sample at $97\text{ }^\circ\text{C}$. Below this temperature the fraction of arc seen in the data is too small for giving a satisfactory fit when analysing the data.

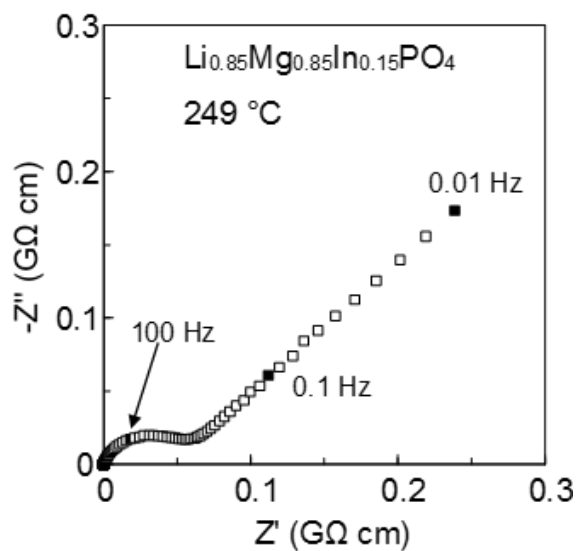


Figure 3.14. Common impedance complex plane plot for the In-doped samples of the series $\text{Li}_{1-x}\text{Mg}_{1-x}\text{In}_x\text{PO}_4$. The data corresponds to the sample for $x = 0.15$ at $249\text{ }^\circ\text{C}$.

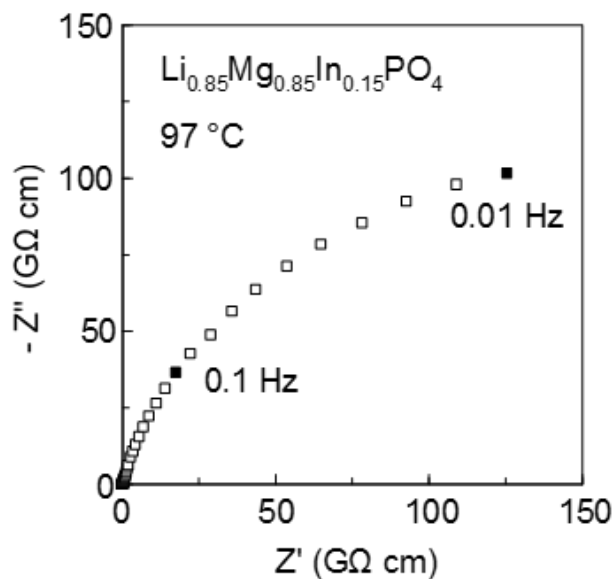


Figure 3.15. Common impedance complex plane plot for the In-doped samples of the series $\text{Li}_{1-x}\text{Mg}_{1-x}\text{In}_x\text{PO}_4$. The data corresponds to the sample for $x = 0.15$ at $97\text{ }^\circ\text{C}$.

The initial analysis of this system focused on the single arc shown in the complex plane, which was studied by single circle fit and therefore the whole dataset was not fitted to an equivalent circuit model. This arc was fitted to a depressed arc model by using the Zview software [38]. From this fit, the two parameters that are discussed here are R and C. R is the resistance associated with the arc, which corresponds to the projection of the arc on the real axis, Z' , of the Nyquist plot. C is the capacitance associated with the same arc.

The capacitance derived from circle fit is corrected for sample geometry as shown in equation 3.3. The geometry corrected value of the capacitance, C_{corr} , is generally used for classification of the type of electro-active element to which the arc corresponds.

$$C_{corr} = C \times \text{thickness} / \text{area} \quad (\text{Eq. 3.3})$$

Once the capacitance, C, of the electroactive element of the sample is known, the relative permittivity for that element, ϵ_r , can be calculated by using the capacitor equation shown in equation 3.4.

$$C = \epsilon_0 \times \epsilon_r \times \text{area} / \text{thickness} \quad (\text{Eq. 3.4})$$

Where ϵ_0 is the vacuum permittivity, $\sim 8.8542 \times 10^{-14} \text{ F cm}^{-1}$. After solving for ϵ_r the equation 3.5 is obtained.

$$\epsilon_r = C \times \text{thickness} / (\text{area} \times \epsilon_0) = C_{corr} / \epsilon_0 \quad (\text{Eq. 3.5})$$

Although the arc shown in figure 3.14, with resistivity $\rho = 54.0 \text{ M}\Omega \text{ cm}$, could be thought of as being associated with the bulk, there are two reasons to assign it to the grain boundary. The first reason is that the corrected capacitance has a value of $C_{corr} = 5.2 \times 10^{-11} \text{ F cm}^{-1}$ which is in the range that corresponds to the grain boundary [39]. The second reason is that the derived relative permittivity from a fitted arc to the experimental data is ~ 590 , i.e. two orders of magnitude higher than the value published for LiMgPO_4 of 6.6 [40]. This single arc is therefore considered to be associated with the grain boundary of the olivine phase. A close inspection of the high frequency region of the data in the complex plane does not reveal any other electro-active element. This means that the bulk response cannot

be studied from the Nyquist plot for this material. For the impedance data shown in figure 3.15 the resistivity is $\rho = 286 \text{ G}\Omega \text{ cm}$ and the corrected capacitance is $C_{\text{corr}} = 6.7 \times 10^{-11} \text{ F cm}^{-1}$.

In order to study the bulk conductivity of these olivine materials the attention is focused on the spectroscopic plots of the imaginary part of the electric modulus. It is known that when the grain is much more conducting than the grain boundary, its response in the impedance complex plane plots could be hidden by the grain boundary arc [41]. This is the situation in figure 3.14 where the much smaller arc of the conducting element, located at the origin of the plot, is fully covered by the comparatively much larger arc of the resistive element. The small arc cannot be distinguished in the impedance complex plane plot because it is 2 – 4 orders of magnitude smaller than the large arc, i.e. a zoom of the origin region of the impedance plot only shows a nearly vertical line that corresponds to the high frequency end of the depressed arc observed in figure 3.14. When this situation arises, the spectroscopic plot of the imaginary component of the electric modulus is useful to uncover the response associated with the bulk [41].

The electric modulus is represented by M , its real part by M' and its imaginary part as M'' . The electric modulus is the inverse of the complex dielectric constant, $\epsilon = \epsilon' + i \epsilon''$ with i being the imaginary unit, and is related with the impedance through the empty cell capacitance, C_c , i.e. $M = M' + iM'' = \epsilon^{-1} = i\omega C_c Z$ [42]. The electric modulus is dominated by the electro-active element of the system with smallest capacitance while the impedance is dominated by the element with the largest impedance [41].

The same AC impedance dataset used for generating figure 3.14 can be used for plotting the spectroscopic plot of the imaginary part of the electric modulus, M'' , which is shown in Figure 3.16. The maximum of the peak shown in the spectra of M'' at about 100 Hz is related to the maximum of the arc seen in the complex plane in figure 3.14 and is assigned to the grain boundary. The incline shown by M'' at high frequencies in figure 3.16 belongs to a partially visible peak that is brought into the measured frequency range at lower temperatures, which is assigned to the bulk response.

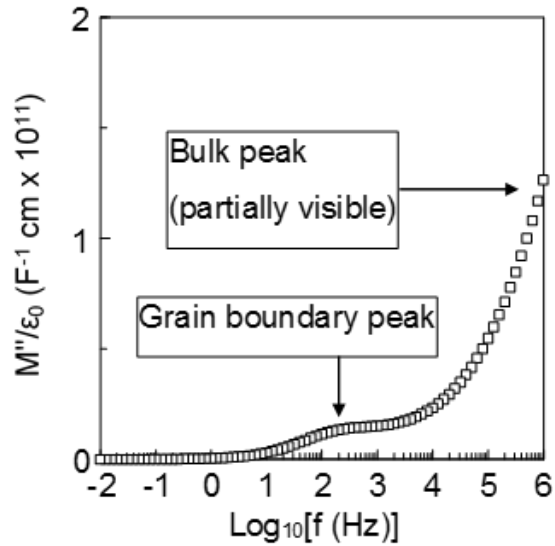


Figure 3.16. Spectroscopic plot of the imaginary component of the electric modulus, M'' , at 249 °C for $\text{Li}_{0.85}\text{Mg}_{0.85}\text{In}_{0.15}\text{PO}_4$.

Varying the temperature of the sample causes the two peaks described for the spectrum of the imaginary part of the electric modulus, M'' , to shift to higher frequencies at higher temperatures and conversely for lower temperatures. This behaviour is shown in figure 3.17.

The most conducting element that appears at higher frequencies, assigned to the bulk, is the large broad peak which maximum is only visible at low temperatures between 25 and 97 °C in figure 3.17. At higher temperatures, the conducting element is missing from the spectrum, with the maximum of the peak laying at higher frequencies than the instrument can reach.

The maximum of the small peak of the resistive element, i.e. the grain boundary, is missing beyond the low frequency end of the spectrum for the datasets collected at 25 and 50 °C. The maximum of this weak broad peak is only visible at high temperatures, when it has entered the frequency range observable with the impedance spectrometer as shown in figure 3.17.

From the frequency at which the maximum of these peaks happens, f_{\max} , the conductivity of the electro-active element can be calculated. The relationship between the resistivity, ρ , or conductivity, σ , and f_{\max} is defined in equation 3.6.

$$f_{\max} = 1/(2\pi\rho\varepsilon_0\varepsilon_r) = \sigma/(2\pi\varepsilon) \quad (\text{Eq. 3.6})$$

Where ε_0 and ε_r are the vacuum permittivity and the relative permittivity respectively while ε is the product of both, i.e. the permittivity of the region of the sample to which the electro-active element corresponds.

From equation 3.6 it is seen that f_{\max} is proportional to the conductivity and proportional to the inverse of the permittivity, i.e. highly conducting elements with low permittivity will show the M'' peak shifted to very high frequencies.

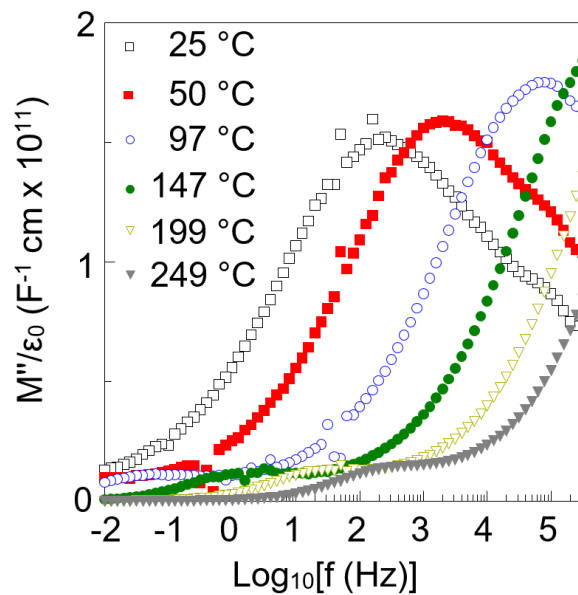


Figure 3.17. Spectroscopic plot of the imaginary component of the electric modulus, M'' , at a number of temperatures for $\text{Li}_{0.85}\text{Mg}_{0.85}\text{In}_{0.15}\text{PO}_4$.

So far the grain boundary has been assigned to the arc in figures 3.14 and 3.15 and to the weak peak in figures 3.16 and 3.17. For the purposes of determining its conductivity at each temperature, circle fits to the arc in the Nyquist plots will be

used. The resistance, R , from the fit is converted to resistivity, ρ , by using the pellet dimensions and finally translated to conductivity, σ . As already seen, this measurement will be possible where the arc is visible, i.e. from high temperatures down to about 100 °C.

On the other hand the bulk has not been detected in the Nyquist plots and finally has been assigned to the intense peak in figure 3.17. As it can be seen in figure 3.17, the maximum of the peak can be read only from low temperatures up to about 100 °C, depending on the conductivity of the sample.

The determination of the bulk conductivity by using equation 3.6 needs as input the relative permittivity of the material. The ϵ_r values were obtained from the capacitance spectroscopic plots at room temperature, shown in figure 3.18 for all samples. The ϵ_r values were derived from the measurement at 500 kHz by application of equation 3.5 and were in the range from ~ 7 for LiMgPO_4 to 10.7 for $\text{Li}_{0.83}\text{Mg}_{0.83}\text{In}_{0.17}\text{PO}_4$, see table 3.9. These ϵ_r values compare well with the literature value of 6.6 for LiMgPO_4 [40] and increase slightly with indium doping.

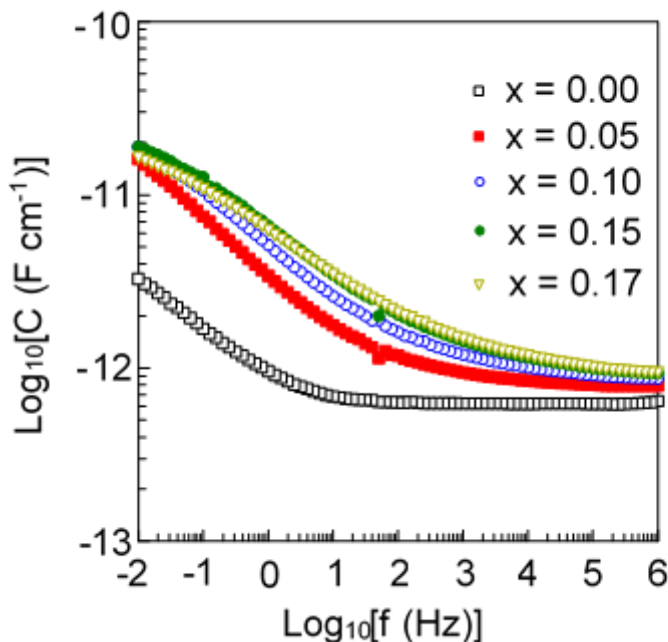


Figure 3.18. Capacitance spectroscopic plots at room temperature for all the samples of the series $\text{Li}_{1-x}\text{Mg}_{1-x}\text{In}_x\text{PO}_4$.

The conductivity data for the grain boundary and the bulk, obtained as explained above for each temperature, are used for building an Arrhenius-type plot which is shown in figure 3.19. The activation energies of the bulk and the grain boundary are listed in tables 3.9 and 3.10 respectively.

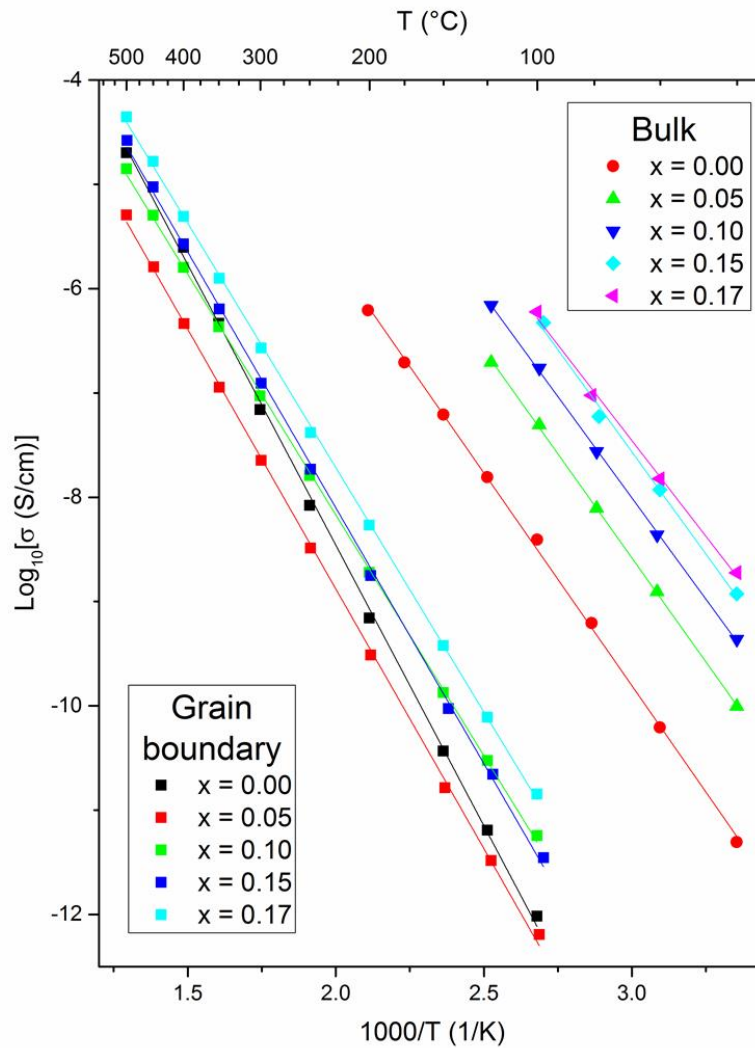


Figure 3.19. Arrhenius-type plots for both the bulk and grain boundary responses for all compositions of the series $\text{Li}_{1-x}\text{Mg}_{1-x}\text{In}_x\text{PO}_4$.

From the linear fits to the Arrhenius plot, the activation energy for each electroactive element of each sample can be calculated and their values are shown in tables 3.9 and 3.10. For all samples, the activation energy for the bulk, $E_{a, \text{bulk}}$, is in the range from 0.7 to 0.8 eV while the activation energy for the grain boundary, $E_{a, \text{gb}}$, is in the range from 0.9 to 1.1 eV.

The bulk conductivities, σ_{bulk} , at room temperature are $\sim 5 \times 10^{-12} \text{ S cm}^{-1}$ for LiMgPO_4 and $\sim 2 \times 10^{-9} \text{ S cm}^{-1}$ for $\text{Li}_{0.83}\text{Mg}_{0.83}\text{In}_{0.17}\text{PO}_4$. The rest of the conductivities for the bulk are of these samples are shown in table 3.9.

The grain boundary conductivities, σ_{gb} , at about 100 °C are in the range from $6 \times 10^{-13} \text{ S cm}^{-1}$ to $2 \times 10^{-11} \text{ S cm}^{-1}$ as can be seen in table 3.10. These conductivities cannot be measured with this method below 100 °C for the reasons already outlined.

The total conductivity, $\sigma_{\text{total}} = 1/\rho_{\text{total}}$, of these samples can be calculated from measured data at 100 °C by adding up both components of the resistivity, i.e. $\rho_{\text{total}} = \rho_{\text{bulk}} + \rho_{\text{gb}}$. For higher or lower temperatures than 100 °C, not all samples have measured data for both components due to the limitations explained in this section. Therefore, for temperatures other than 100 °C, the total conductivity could be calculated by using extrapolations of the measured data under the assumption that the trend would continue to behave linearly in the Arrhenius plot. Under the same assumption, the total conductivity for these samples can be approximated by the grain boundary conductivity, having this estimation an error lower than 1 %, i.e. $\sigma_{\text{total}} \sim \sigma_{\text{gb}}$ because at any given temperature between room temperature and 500 °C both elements, grain boundary and bulk, either from data or extrapolations are separated more than two orders of magnitude in the Arrhenius plot.

Table 3.9. Relative permittivity, ϵ_r , at 25 °C measured at 500 kHz, bulk conductivity, σ_{bulk} , at 25 °C and activation energy for bulk, $E_{a, \text{bulk}}$, for all samples of the series $\text{Li}_{1-x}\text{Mg}_{1-x}\text{In}_x\text{PO}_4$. $E_{a, \text{bulk}}$ errors shown as 1 s.d.

Composition	ϵ_r (500 kHz, 25 °C)	σ_{bulk} (25 °C)	$E_{a, \text{bulk}}$
x = 0.00	7.0	$4.93 \times 10^{-12} \text{ S cm}^{-1}$	0.809(9) eV
x = 0.05	8.9	$9.86 \times 10^{-11} \text{ S cm}^{-1}$	0.791(7) eV
x = 0.10	9.9	$4.36 \times 10^{-10} \text{ S cm}^{-1}$	0.770(8) eV
x = 0.15	10.7	$1.18 \times 10^{-9} \text{ S cm}^{-1}$	0.78(3) eV
x = 0.17	10.7	$1.89 \times 10^{-9} \text{ S cm}^{-1}$	0.73(3) eV

Table 3.10. Grain boundary conductivity, σ_{gb} , at the indicated temperature and E_a for grain boundary, $E_{a, \text{gb}}$, for all samples of the series $\text{Li}_{1-x}\text{Mg}_{1-x}\text{In}_x\text{PO}_4$. $E_{a, \text{gb}}$ errors shown as 1 s.d.

Composition	Temperature	σ_{gb} (Temperature)	$E_{a, \text{gb}}$
x = 0.00	100 °C	$9.63 \times 10^{-13} \text{ S cm}^{-1}$	1.066(11) eV
x = 0.05	99 °C	$6.40 \times 10^{-13} \text{ S cm}^{-1}$	0.987(8) eV
x = 0.10	100 °C	$5.70 \times 10^{-12} \text{ S cm}^{-1}$	0.915(5) eV
x = 0.15	97 °C	$3.50 \times 10^{-12} \text{ S cm}^{-1}$	0.972(8) eV
x = 0.17	100 °C	$1.43 \times 10^{-11} \text{ S cm}^{-1}$	0.929(5) eV

The AC impedance measurements were also carried out in flow of Ar and O₂ at different temperatures. This test was used to discard any contribution to the measured electrical conductivities other than from Li-ions, i.e. if other species such as electrons or electron holes contribute to the conductivity, it is expected a dependence of the conductivity with oxygen partial pressure, pO₂.

The result of these measurements in Ar and O₂ was that the conductivities of both electro-active elements, grain boundary and bulk, were shown to be independent on the pO₂, as can be seen in figures 3.20.a and 3.20.b respectively. This fact, along with the low frequency spike in the impedance complex plane plot, indicates that the measured conductivity is associated with Li-ions and has no electronic component.

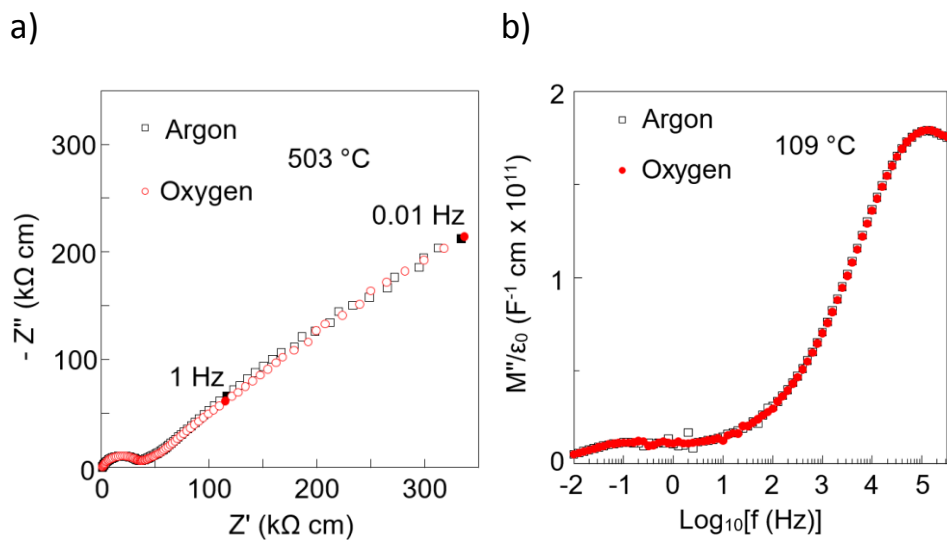


Figure 3.20. a) Impedance complex plane plots for $\text{Li}_{0.85}\text{Mg}_{0.85}\text{In}_{0.15}\text{PO}_4$ at $503\text{ }^\circ\text{C}$ under flowing Ar and O_2 . b) M'' plots at $109\text{ }^\circ\text{C}$ under flowing Ar and O_2 .

The most interesting result of the conductivity study is that, after vacancy introduction in the Li channels, the bulk Li-ion conductivity has been improved more than 100 times at room temperature, as can be seen in table 3.9.

3.4.6 NMR

The samples LiMgPO_4 and $\text{Li}_{0.9}\text{Mg}_{0.9}\text{In}_{0.1}\text{PO}_4$ were subject to NMR measurements. The ^7Li static NMR spectra for the parent and the doped samples collected at a field of 9.4 Tesla showed a line shape that compares well with simulations at room temperature as shown in figure 3.21. At high temperatures it is observed that the line width narrows because the Li-Li dipolar interaction averages due to the increased mobility.

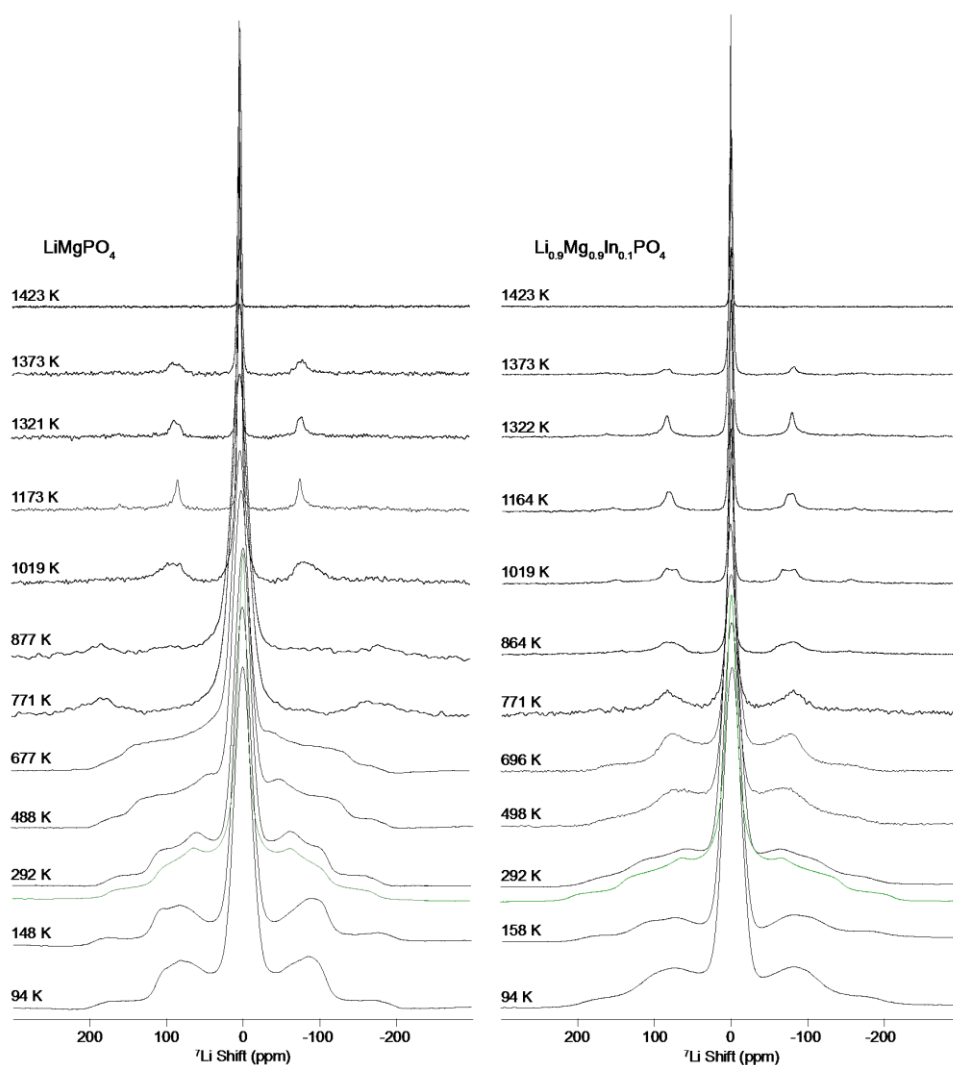


Figure 3.21. Static ^7Li Solid-state NMR spectra at 9.4 T for the samples LiMgPO_4 and $\text{Li}_{0.9}\text{Mg}_{0.9}\text{In}_{0.1}\text{PO}_4$ at a range of temperatures. The green line shapes below the spectra at 292 K is from a simulation. Reproduced with permission from Chem. Mater., 2015, 27 (6), pp 2074–2091, DOI: 10.1021/cm504518q. Copyright 2015 American Chemical Society.

When the central transition line width of the spectra on figure 3.21 is plotted against temperature for both samples, it can be seen that the motional narrowing happens at lower temperatures for the doped sample than for the parent sample, as can be seen in figure 3.22, which indicates that the Li-ion mobility is higher in the doped sample. The motional narrowing for the doped sample starts at 470 K, however the motional narrowing for the parent sample starts at 750 K, i.e. 280 K above.

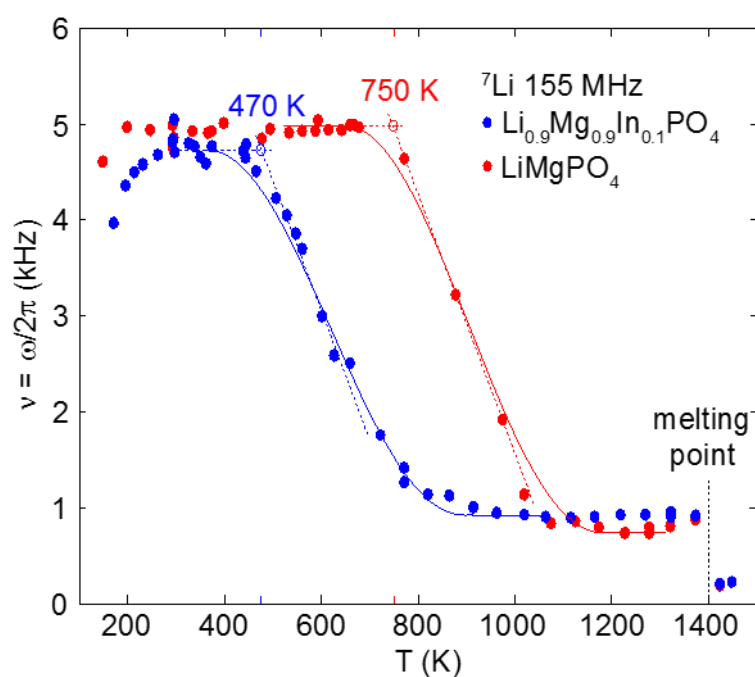


Figure 3.22. Static ${}^7\text{Li}$ solid-state NMR central transition line width versus temperature for the samples LiMgPO_4 and $\text{Li}_{0.9}\text{Mg}_{0.9}\text{In}_{0.1}\text{PO}_4$. Reproduced with permission from Chem. Mater., 2015, 27 (6), pp 2074–2091, DOI: 10.1021/cm504518q. Copyright 2015 American Chemical Society.

The NMR measurements were carried out by Dr Frédéric Blanc, Mr Michael D. Jones and Ms Mona K. Omir. Experimental details and data analysis are published in the 2015 paper [25].

3.5 Sc-doped series

3.5.1 Synthesis

The synthesis used for this aliovalent substitution is identical to the one used for the indium doped series. The precursor is subject to a pre-treatment at 375 °C for 12 hours, followed by re-grinding and pelletising. The pellet is then fired at 1000 °C for 20 hours. The reactant Sc_2O_3 (99.9 %, Alfa Aesar, dried at 220 °C) was used as Sc precursor for this series with doping formula $\text{Li}_{1-x}\text{Mg}_{1-x}\text{Sc}_x\text{PO}_4$.

Initially 3 members of the series were synthesised for $x = 0.05, 0.1$ and 0.20 . The secondary phase $\text{Li}_3\text{Sc}_2(\text{PO}_4)_3$, appeared in all three Sc-doped samples as shown in figure 3.23, although the sample with $x = 0.05$ was almost phase pure. The lattice parameters from the olivine phase in these three samples are plotted in figure 3.24. The secondary standard LaB_6 was used as internal standard for this determination. These three samples show a linear trend for which a plateau has not been reached at $x = 0.20$. At the same time the gradients observed from $x = 0$ to $x = 0.05$ and from $x = 0.05$ to $x = 0.20$ are different.

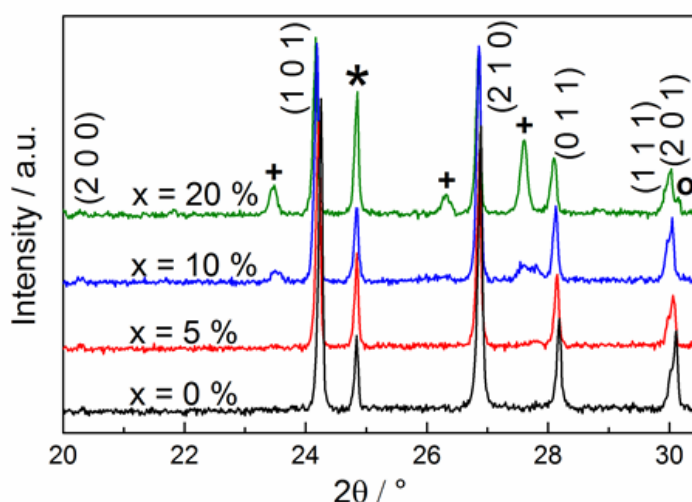


Figure 3.23. $\text{Co K}\alpha_1$ PXRD patterns of $\text{Li}_{1-x}\text{Mg}_{1-x}\text{Sc}_x\text{PO}_4$ series as a function of Sc doping level x . The (100) reflection from the LaB_6 internal standard is marked with an asterisk. The peaks marked with + are from the impurity phase $\text{Li}_3\text{Sc}_2(\text{PO}_4)_3$. The peak marked with o has not been identified.

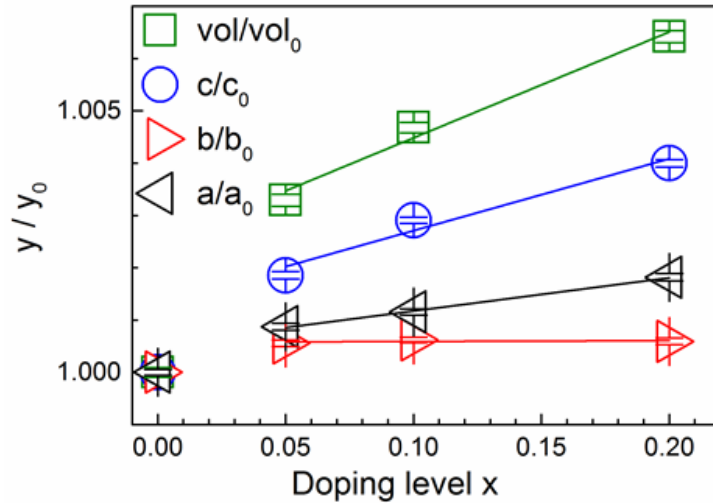


Figure 3.24. Relative cell parameters for the Sc-doped series, $\text{Li}_{1-x}\text{Mg}_{1-x}\text{Sc}_x\text{PO}_4$. The straight lines are guide to the eyes. Error bars shown as ± 3 e.s.d.

Initially it was thought that two different processes were happening in the olivine structure, one from $x = 0$ to a limit of about $x = 0.05$ and a second one from $x = 0.05$. The former was expected to be the Sc substitution for Li and Mg, shown in equation 3.7, while the latter could be the Sc substitution for 3 x Li atoms after reaching the limit of the first substitution, i.e. $[\text{Li}_{1-\text{limit}-3x}\square_{\text{limit}}\text{Sc}_x][\text{Mg}_{1-\text{limit}}\text{Sc}_{\text{limit}}]\text{PO}_4$. The latter could be possible due to the similar ionic radii of Li and Sc from the 1976 Shannon tables [24].



To investigate this further a series of new samples was prepared for doping levels of $x = 0.01, 0.02, 0.03, 0.04, 0.30$ and 0.40 . The PXRD patterns for $\text{Li}_{0.96}\text{Mg}_{0.96}\text{Sc}_{0.04}\text{PO}_4$ and $\text{Li}_{0.70}\text{Mg}_{0.70}\text{Sc}_{0.30}\text{PO}_4$ are shown in figures 3.25 and 3.26 respectively. The lattice parameters determined for the new samples, again with the aid of the same internal standard, are shown in figure 3.27.

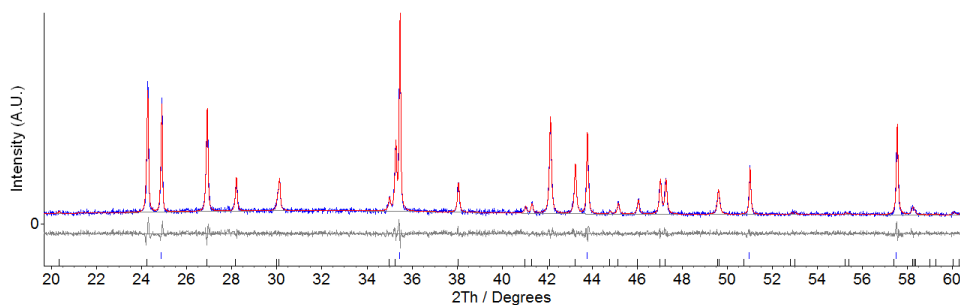


Figure 3.25. Co $K\alpha_1$ PXR D pattern of $\text{Li}_{0.96}\text{Mg}_{0.96}\text{Sc}_{0.04}\text{PO}_4$. Multiphase Pawley fit, red, to the data, blue. Background and difference are plotted in grey. Blue tick marks represent LaB_6 used as internal standard and black tick marks represent the olivine phase.

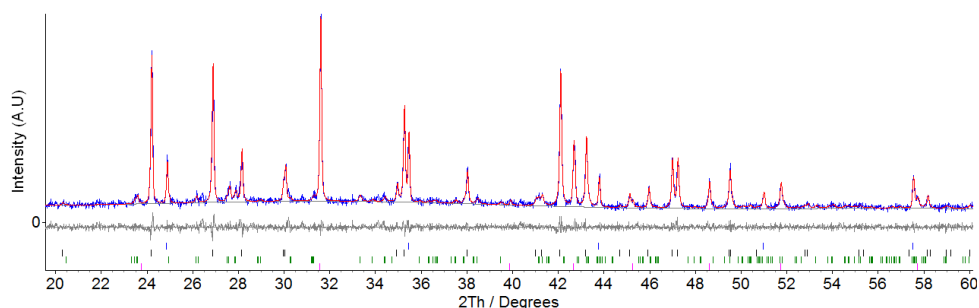
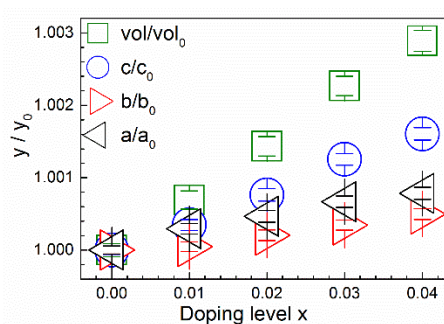


Figure 3.26. Co $K\alpha_1$ PXR D pattern of $\text{Li}_{0.70}\text{Mg}_{0.70}\text{Sc}_{0.30}\text{PO}_4$. Multiphase Pawley fit, red, to the data, blue. Background and difference are plotted in grey. Blue tick marks represent LaB_6 used as internal standard, black tick marks represent the olivine phase, green and pink tick marks represent the impurity phases $\text{Li}_3\text{Sc}_2(\text{PO}_4)_3$ and ScPO_4 respectively.

a)



b)

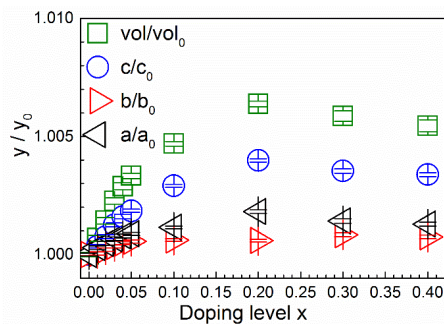


Figure 3.27. Relative cell parameters for the Sc-doped series, $\text{Li}_{1-x}\text{Mg}_{1-x}\text{Sc}_x\text{PO}_4$, a) detail for the samples from $x = 0$ to $x = 0.04$ and b) data for all the samples. Error bars shown as ± 3 e.s.d.

The powder diffraction patterns of this series show that the doping limit is at $x = 0.04$. The impurity phase $\text{Li}_3\text{Sc}_2(\text{PO}_4)_3$ is present from $x = 0.05$ to $x = 0.40$, while ScPO_4 , $I4_1/amd$ is present from $x = 0.20$ to $x = 0.40$. The olivine unit cell volume varies linearly with three different slopes along the doping range. Firstly from $x = 0$ to $x = 0.04$ the highest slope is observed. It represents the doping that produces phase pure samples. Secondly from $x = 0.05$ until $x = 0.20$ the slope shows a lower value. Finally between $x = 0.20$ and $x = 0.40$ the slope becomes negative.

With the aim of clarifying what happens after $x = 0.20$, the cell volume was measured for the impurity phase $\text{Li}_3\text{Sc}_2(\text{PO}_4)_3$ in the same patterns with internal standard and the result is shown in figure 3.28. Although the e.s.d. is relatively large, the trend is linearly distributed with two slopes. The slopes have the same slope signs than for the olivine phase at each side of $x = 0.20$, i.e. positive for $x < 0.20$ and negative for $x > 0.20$. This could indicate that this impurity phase is being doped as well.

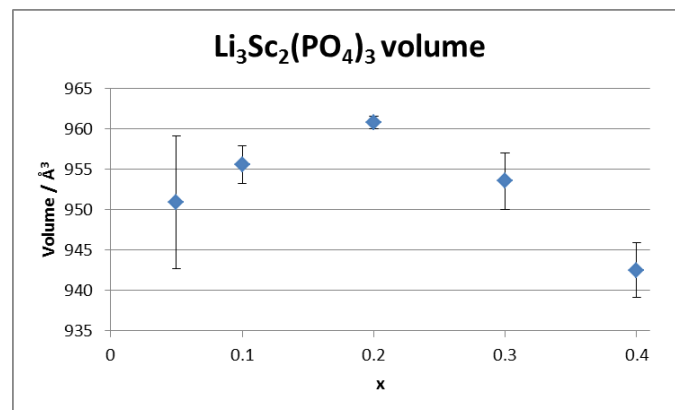


Figure 3.28. Relative cell parameters for the impurity phase $\text{Li}_3\text{Sc}_2(\text{PO}_4)_3$. The straight lines are guide to the eyes. Error bars shown as ± 3 e.s.d.

In conclusion the only process that is clear is the first one that produces phase pure samples from $x = 0$ to $x = 0.04$ for the series $\text{Li}_{1-x}\text{Mg}_{1-x}\text{Sc}_x\text{PO}_4$. Clarification of the second process would need further work in order to find out which compositions would produce phase pure samples with those lattice parameters. The third process could be a reversion of the second one, due to competition between phases. The sample for $x = 0.04$ was not studied by AC impedance spectroscopy because the priority was focused on synthetic work of other new systems.

3.6 Ga-doped series

3.6.1 Synthesis

The aim of this aliovalent substitution is to substitute Ga with Mg and Li. The synthesis conditions were the same as for the indium and scandium doped series. The reactant Ga₂O₃ (99.999 %, Alfa Aesar, dried at 220 °C) was used as dopant precursor for the synthesis of these samples of Li_{1-x}Mg_{1-x}Ga_xPO₄.

The substitution was tried at doping levels of $x = 0.05, 0.10$ and 0.20 . The Ga-doped samples showed the secondary phase GaPO₄ for $x = 0.05$ and 0.10 while the sample for $x = 0.20$ melted. The lattice parameters of the non-melted samples were studied with the aid of the secondary standard LaB₆ as internal standard. For the olivine phase a cell shrinkage consistent with the lattice parameters a , b , and c was observed. While for the parent olivine the measured cell volume was of 280.81(2) Å³, the two samples for $x = 0.05$ and 0.10 showed a final cell volume of 280.59(2) and 280.56(3) Å³ respectively, errors shown as 3 e.s.d. This unit cell behavior suggests that some type of modification is happening to the olivine phase and that a lower doping level or a different doping model would be possible.

When the PXRD pattern of the sample Li_{0.9}Mg_{0.9}Ga_{0.1}PO₄ is studied by using multiphase Pawley fits, it is found that the fit to the olivine phase shows a mismatch for its most intense reflection, (101) at $2\theta \approx 24.2^\circ$, as shown in figure 3.29. This mismatch disappears when a monoclinic cell, found by exploring the maximal subgroup graph from $Pnma$ to $P\bar{1}$, with space group $P2_1/m$, # 11, is used as seen in figure 3.30. Due to the overlapping of the most intense reflection of the olivine, (101), with a reflection of the impurity phase GaPO₄, (010), the phase GaPO₄ has been kept fixed with a Rietveld model in both refinements. The internal standard LaB₆ and the olivine model have been refined with Pawley fits. In this comparison R_{wp} improves from 9.0603 % for the olivine orthorhombic unit cell to 8.7578 % for the olivine monoclinic unit cell. The monoclinic unit cell refined its lattice parameters to $a = 10.1323(11)$, $b = 5.9015(4)$, $c = 4.6903(7)$ and $\beta = 90.03(2)$, i.e. volume = 280.46(6), with error shown as 3 e.s.d.

In conclusion, a non-common monoclinic distortion of the olivine structure has been found during the work on this series. In further work this phase could be isolated and studied with high resolution powder X-ray diffraction.

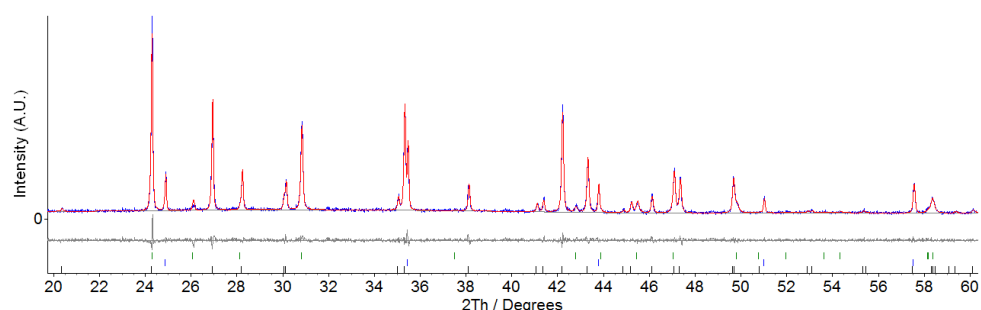


Figure 3.29. Co $K\alpha_1$ PXR D pattern of $\text{Li}_{0.9}\text{Mg}_{0.9}\text{Ga}_{0.1}\text{PO}_4$. Multiphase Rietveld/Pawley fit, red, to the data, blue. Background and difference are plotted in grey. Green tick marks represent the impurity phase GaPO_4 for which a Rietveld model has been used. Blue and black tick marks represent LaB_6 used as internal standard and the olivine phase respectively, for which Pawley fits have been used. The space group of the olivine fit was $Pnma$. The multiphase fit produced a fit factor $R_{wp} = 9.06\%$.

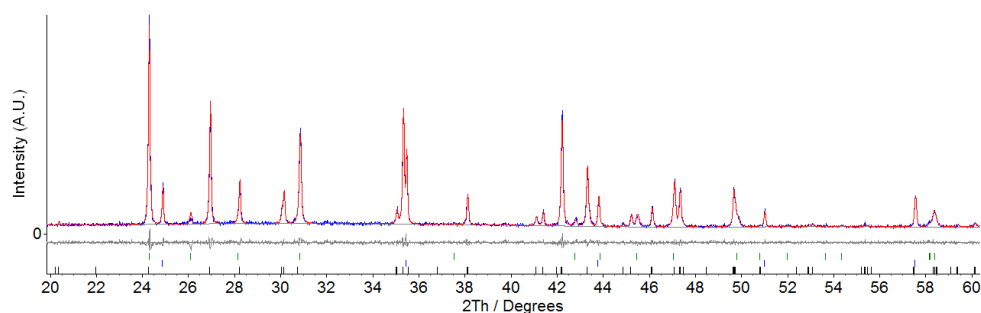


Figure 3.30. Co $K\alpha_1$ PXR D pattern of $\text{Li}_{0.9}\text{Mg}_{0.9}\text{Ga}_{0.1}\text{PO}_4$. Multiphase Rietveld/Pawley fit, red, to the data, blue. Background and difference are plotted in grey. Green tick marks represent the impurity phase GaPO_4 for which a Rietveld model has been used. Blue and black tick marks represent LaB_6 used as internal standard and the olivine phase respectively, for which Pawley fits have been used. The space group of the olivine fit was $P2_1/m$. The refined lattice parameters of the monoclinic unit cell are listed in the main text. The multiphase fit produced a fit factor $R_{wp} = 8.76\%$.

3.7 In, Ga co-doping series

3.7.1 Synthesis

These co-doping experiments used the same preparation conditions and reactants previously used for the indium and gallium doped series. The aim of this series is the extension of the Li vacancy fraction in the olivine structure.

When the indium doped series was presented, it was shown that the higher vacancy fraction achieved for the olivine structure was $x = 0.17$ for the composition $\text{Li}_{0.83}\text{Mg}_{0.83}\text{In}_{0.17}\text{PO}_4$. The cell volume for this sample is almost in the plateau that appears after Vegard's law for the In-doped series. It was thought that this limit could have been imposed by a natural upper limit of the unit cell size.

In the Ga-doped series section it was shown that the dopant gallium reduces the olivine cell size with respect to the parent material. Since indium increases the cell volume and gallium reduces it, it was thought that perhaps it was possible to keep the cell volume within the limits explored in the In-doped series section, i.e. to combine indium and gallium dopants, which have revealed themselves to act as antagonist with respect to the unit cell size control of the olivine, to extend the Li vacancy fraction introduced in the structure.

In order to test this approach, the composition $\text{Li}_{0.85}\text{Mg}_{0.85}\text{In}_{0.15}\text{PO}_4$ was used as a sample close to the doping limit. Then the substitution of Ga for Li and Mg was tried on this composition in order to form the series $\text{Li}_{0.85-x}(\text{Mg}_{0.85-x}\text{In}_{0.15}\text{Ga}_x)\text{PO}_4$. Samples for $x = 0.02, 0.05$ and 0.10 were synthesized and their unit cell volume studied from PXRD with the secondary standard LaB_6 . As shown in figure 3.31, initially the cell volume goes down, then after $x = 0.02$ it starts going up. In addition, the impurity GaPO_4 *P3₁21* with the Berlinite structure type appeared in all samples. The PXRD pattern for the sample with $x = 0.1$ is shown in figure 3.32.

In conclusion, all samples were impure and the unit cell volume for this set of samples did not reach the maximum unit cell volume achieved for the In-doped series.

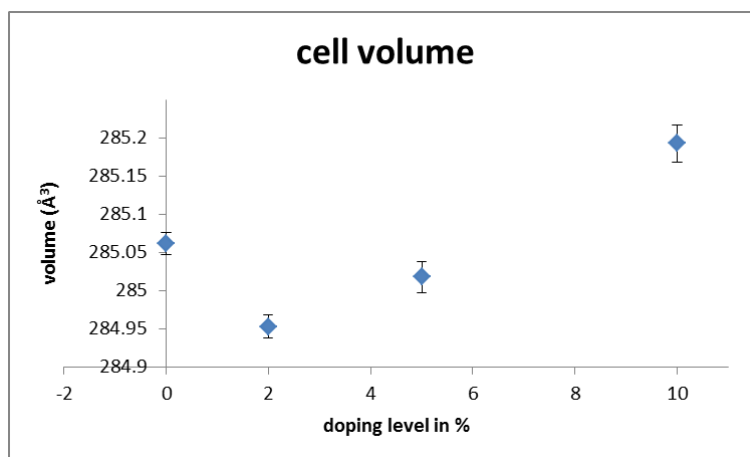


Figure 3.31. Cell volume for the In, Ga co-doping experiment for the series $\text{Li}_{0.85-x}(\text{Mg}_{0.85-x}\text{In}_{0.15}\text{Ga}_x)\text{PO}_4$ with $x = 0, 0.02, 0.05$ and 0.10 . Error bars shown as ± 3 e.s.d.

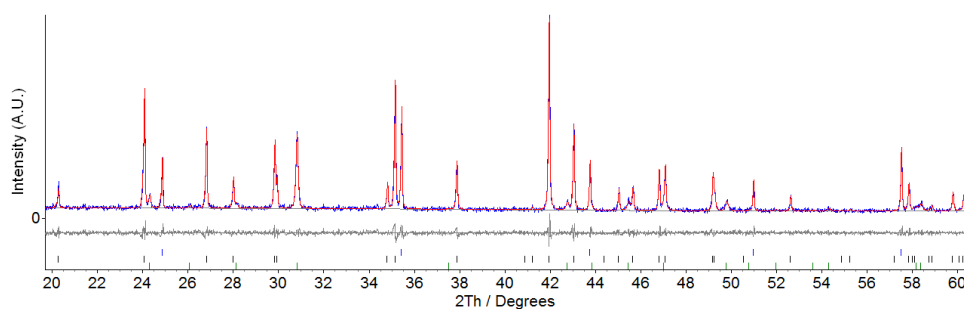


Figure 3.32. $\text{Co K}\alpha_1$ PXRD pattern of $\text{Li}_{0.85-x}(\text{Mg}_{0.85-x}\text{In}_{0.15}\text{Ga}_x)\text{PO}_4$ for $x = 0.1$. Multiphase Pawley fit, red, to the data, blue. Background and difference are plotted in grey. Blue tick marks represent LaB_6 used as internal standard, black tick marks represent the olivine phase and green tick marks represent the impurity phase GaPO_4 with space group $P3_121$ and the Berlinite structure type.

3.8 In, Li co-doping series

3.8.1 Synthesis

The work around the olivine structure presented so far highlights the sensitivity of the structure to the dopants tried in this chapter. At this point there was a question

that had not been answered. Would it be possible to extend the dimensionality of the Li diffusion pathways? i.e. would it be possible to create a gateway to communicate the 1D Li-channels?

In order to test this, the strategy was to start with the composition $\text{Li}_{0.85}\text{Mg}_{0.85}\text{In}_{0.15}\text{PO}_4$ and try the substitution of 2 Li atoms for Mg, with the idea of placing a Li atom or a vacancy on Mg site and the remaining Li atom in the available vacancies for that composition. This approach makes the series $\text{Li}_{0.85+x}(\text{Mg}_{0.85-x}\text{In}_{0.15}\text{Li}_x)\text{PO}_4$ that was synthesised for $x = 0.02, 0.05$ and 0.10 . The unit cell volume was determined from PXRD with the aid of the secondary standard LaB_6 . The result is plotted in figure 3.33 where it can be seen that two processes are present. Initially the cell volume goes down at a linear low rate, then after $x = 0.10$ it falls down at a higher rate. Not much detail can be extracted due to the size of the dataset.

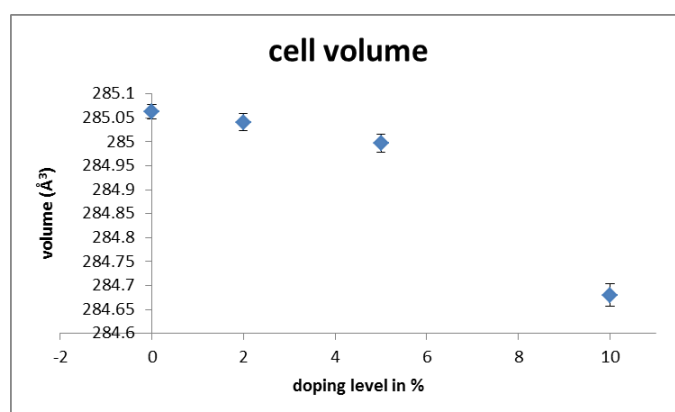


Figure 3.33. Cell volume for the In, Li co-doping experiment for the series $\text{Li}_{0.85+x}(\text{Mg}_{0.85-x}\text{In}_{0.15}\text{Li}_x)\text{PO}_4$ with $x = 0, 0.02, 0.05$ and 0.10 . Error bars shown as ± 3 e.s.d.

The sample for $x = 0.05$ appeared to be phase pure in laboratory PXRD as can be seen in figure 3.34. The appearance of the impurity $\text{Li}_3\text{In}_2\text{P}_3\text{O}_{12}$ $P2_1/n$ in the sample for $x = 0.1$ can be seen in figure 3.35. The presence of an extra In-containing phase could explain the fall in volume of the olivine phase, e.g. due to the production of a sample of the In-doped series with lower doping level than $x = 0.15$, which is the base composition for this co-doping series.

In conclusion, the apparent linear trend observed for the unit cell volume between $x = 0$ and $x = 0.05$ in figure 3.33 could indicate that some type of defect was introduced in the olivine structure. More work would be needed to establish if the gateway was actually created between the Li channels. The sample for $x = 0.05$ was not studied further because the priority was focused on synthetic work of other new systems.

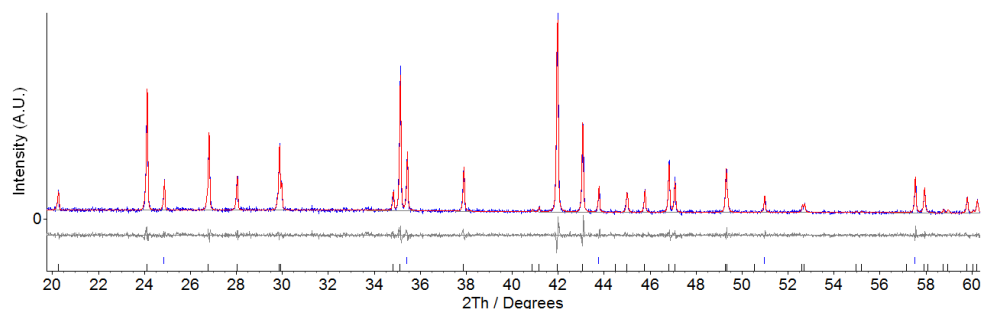


Figure 3.34. Co $K\alpha_1$ PXRD pattern of $\text{Li}_{0.85+x}(\text{Mg}_{0.85-x}\text{In}_{0.15}\text{Li}_x)\text{PO}_4$ for $x = 0.05$. Multiphase Pawley fit, red, to the data, blue. Background and difference are plotted in grey. Blue and black tick marks represent the internal standard LaB_6 and the olivine phase respectively.

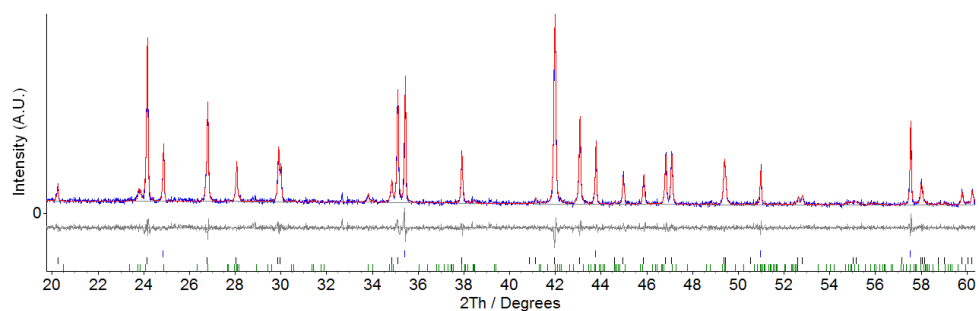


Figure 3.35. Co $K\alpha_1$ PXRD pattern of $\text{Li}_{0.85+x}(\text{Mg}_{0.85-x}\text{In}_{0.15}\text{Li}_x)\text{PO}_4$ for $x = 0.1$. Multiphase Pawley fit, red, to the data, blue. Background and difference are plotted in grey. Blue tick marks represent the internal standard LaB_6 . Black and green tick marks represent the olivine phase and the impurity phase $\text{Li}_3\text{In}_2\text{P}_3\text{O}_{12}$ $P12_1/n1$ respectively. The reflection at $2\theta = 32.69^\circ$ is not from the sample, belongs to the grease used to prepare the PXRD slide.

3.9 Zr-doping trials.

3.9.1 Synthesis

Initially the attempt was to achieve the substitution of Zr^{4+} for Mg^{2+} in $LiMgPO_4$. This is an ambitious substitution because the net charge difference is $2e^-$ instead of one. However it was tried due to the fact that the cations Zr^{4+} and Mg^{2+} have similar 1976 Shannon ionic radii [24] for octahedral coordination. The idea was to create 2 x Li-vacancies for each Zr atom introduced on the Mg-site in order to create the series $Li_{1-2x}Mg_{1-x}Zr_xPO_4$.

The initial synthesis was analogous to the one used for $LiMgPO_4$ with the addition of the reactant ZrO_2 (99 %, ~ 3 % HfO_2 , from Fluka Chemika, dried at 220 °C). Samples of $Li_{1-2x}Mg_{1-x}Zr_xPO_4$ were synthesised for $x = 0, 0.05, 0.10, 0.15, 0.20, 0.25, 0.30$ and 0.35 . Samples for $x = 0, 0.05, 0.1$ and 0.2 were synthesised with $(NH_4)_2HPO_4$ instead of $(NH_4)H_2PO_4$. After grinding the stoichiometric amounts of reactants with pestle and mortar, the mixture was held at 375 °C for 12 hours, with heating at 0.5 °C/min and cooling at 5 °C/min. The resulting solid was re-ground and fired at 800 °C for 20 hours, with heating rate of 1 °C/min and cooling rate of 2 °C/min. A final grind yielded white powders, all of which produced PXRD patterns with the secondary phase $MgZr_4(PO_4)_6$. Samples for $x = 0, 0.05, 0.1$ and 0.2 were re-fired at 850 °C. Samples for $x = 0.15$ and 0.25 were re-fired at 900 °C and then at 950 °C but the $MgZr_4(PO_4)_6$ impurity was not removed from the doped samples. A Rietveld refinement for a sample with $x = 0.05$ that was re-fired at 900 °C and at 950 °C is shown in figure 3.36. It was observed that the weight fraction of the secondary phase is nearly proportional to the doping level until $x = 0.2$ and it is plotted in figure 3.37.

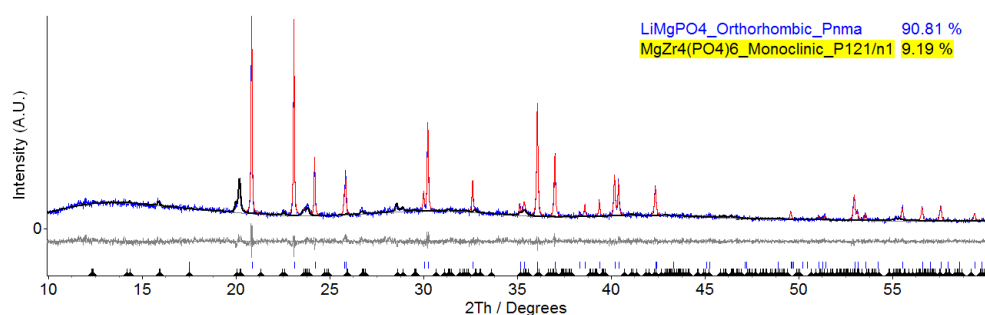


Figure 3.36. Cu $K\alpha_1$ PXRD pattern of a sample of nominal composition $\text{Li}_{0.90}\text{Mg}_{0.95}\text{Zr}_{0.05}\text{PO}_4$. Multiphase Rietveld fit, red, to the data, blue. The difference is plotted in grey. Blue tick marks represent the olivine phase LiMgPO_4 . Black tick marks represent the impurity phase $\text{MgZr}_4(\text{PO}_4)_6$. The diffraction pattern of the impurity phase appears highlighted in black over the data. The weight fractions per cent of each phase determined by the refinement appear on the upper-right corner of the plot.

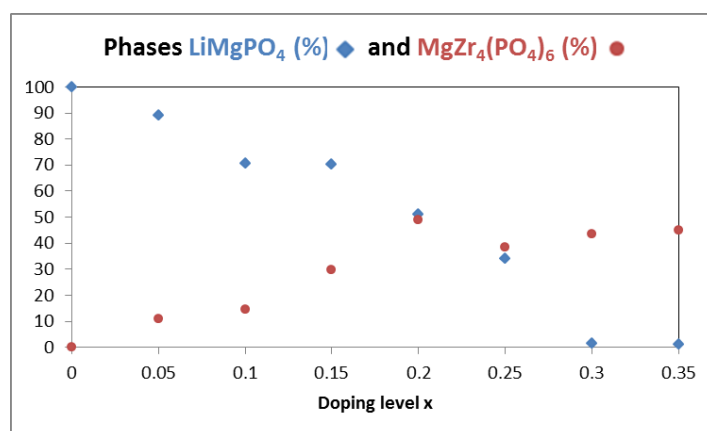


Figure 3.37. Weight fraction per cent for LiMgPO_4 and $\text{MgZr}_4(\text{PO}_4)_6$ for the series of $\text{Li}_{1-2x}\text{Mg}_{1-x}\text{Zr}_x\text{PO}_4$ with $x = 0, 0.05, 0.10, 0.15, 0.20, 0.25, 0.30$ and 0.35 , synthesised as explained in the text.

In order to avoid the secondary phase, ball milling was attempted instead of grinding with pestle and mortar. Precursors for the samples $\text{Li}_{0.90}\text{Mg}_{0.95}\text{Zr}_{0.05}\text{PO}_4$ and $\text{Li}_{0.80}\text{Mg}_{0.9}\text{Zr}_{0.1}\text{PO}_4$ were ball milled with ethanol using zirconia milling media. After the same heat treatment at $800\text{ }^\circ\text{C}$ as for the samples prepared with pestle and

mortar, the results were the same. The secondary phase $\text{MgZr}_4(\text{PO}_4)_6$ was present in similar weight ratios as for the previous samples of the same compositions.

In order to eliminate the impurity, the next attempt was to fire the full series of the samples made with pestle and mortar at higher temperatures. This was done in steps of 100 °C. For these higher temperature firings, the heating and cooling rates were of 2 °C/min and 5 °C/min respectively. The samples were held for 20 hours at each temperature, i.e. at 900 °C, at 1000 °C and at 1100 °C, with intermediate reground and PXRD data collection for each sample. At 1100 °C all samples for x from 0.05 to 0.25 melted.

The overall result of these re-firings was the same as for the samples discussed above, i.e. the samples were still impure. The weight fraction of both phases derived from Rietveld refinements are shown in figure 3.38 for each sample for all the reaction temperatures. In figure 3.38.b it can be seen that the linearity of the weight fraction of $\text{MgZr}_4(\text{PO}_4)_6$ improved slightly as the reaction temperature increased. The lattice parameters of the two phases were refined without internal standard. For all the samples in the series, the cell volume of both phases increased with increasing doping level and these data are plotted in figure 3.39.

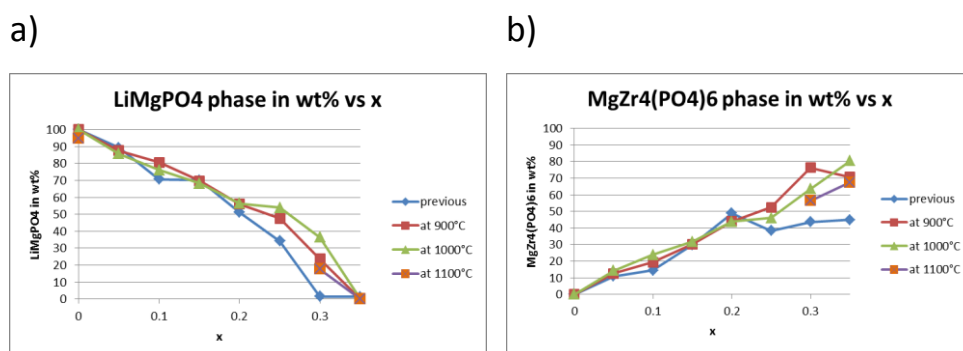
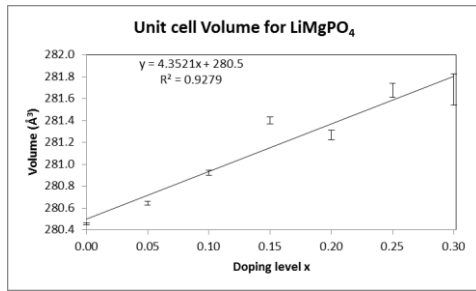


Figure 3.38. Weight fraction per cent for a) LiMgPO_4 and b) $\text{MgZr}_4(\text{PO}_4)_6$ for the series of $\text{Li}_{1-2x}\text{Mg}_{1-x}\text{Zr}_x\text{PO}_4$ with $x = 0, 0.05, 0.10, 0.15, 0.20, 0.25, 0.30$ and 0.35 , synthesised as explained in the text and re-fired at 900 °C, 1000 °C and 1100 °C.

a)



b)

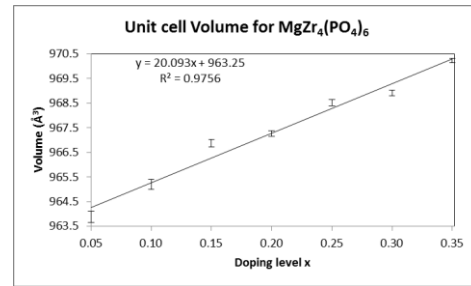
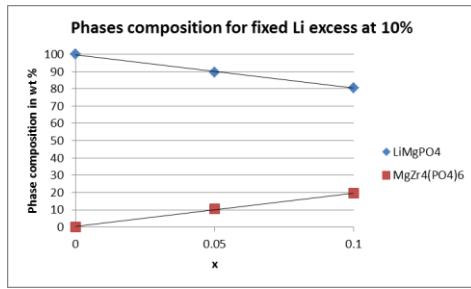


Figure 3.39. Cell volume for a) LiMgPO₄ and b) MgZr₄(PO₄)₆ for the series of Li_{1-2x}Mg_{1-x}Zr_xPO₄ with x = 0, 0.05, 0.10, 0.15, 0.20, 0.25, 0.30 and 0.35, synthesised as explained in the text and re-fired at 900 °C and 1000 °C.

This exploratory work continued by trying lithium excess in the synthesis at 800 °C, because some authors do this to compensate the loss of lithium during the annealing of the samples [43]. Two approaches were taken for this. Firstly, the effects on different doping levels, x = 0, 0.5 and 0.1, were tested for a fixed Li excess of 10 %. Secondly, the effects of different amounts of Li excess, 5 %, 10 %, 15 % and 20 %, were tested for a fixed doping level of x = 0.05.

For increasing doping levels, all the trends were the same as for the samples prepared with no lithium excess, i.e. linear dependence of the secondary phase fraction with x and expansion of the unit cell for both phases. For increasing Li excess levels, the secondary phase decreases slightly until the reactant ZrO₂ appears at 20% of Li excess. The feature to highlight from this experiment is that the lattice parameters shrink for both phases for increasing levels of Li excess. The phase fractions in weight per cent for both series are shown in figure 3.40.

a)



b)

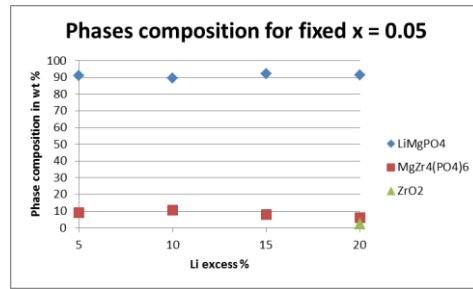


Figure 3.40. Phase fractions in weight per cent for a) samples of $\text{Li}_{1-2x}\text{Mg}_{1-x}\text{Zr}_x\text{PO}_4$ for $x = 0, 0.05$ and 0.1 at a fixed Li excess of 10 %; and b) for $\text{Li}_{0.90}\text{Mg}_{0.95}\text{Zr}_{0.05}\text{PO}_4$ with Li excess of 5, 10, 15 and 20 %.

The last attempt made with the element Zr was to try the substitution of Zr^{4+} for Li^+ to make samples of the series $\text{Li}_{1-x}\text{Zr}_{x/4}\text{MgPO}_4$. Only one sample for $x = 0.1$ was made, i.e. $\text{Li}_{0.9}\text{Zr}_{0.025}\text{MgPO}_4$. The final firing for this sample was at $1000\text{ }^\circ\text{C}$. The result was again the same as for the previous attempts with Zr, i.e. $\text{MgZr}_4(\text{PO}_4)_6$ was observed as secondary phase.

The work on the Zr-doping trials has served to understand this system. The general trend along all this section, but for the Li excess attempt, has been expansion of the unit cell of the two observed phases with increasing doping level. In order to explain this, equation 3.8 shows how the nominal composition of a Zr-doped sample can be decomposed and balanced into other observable phases.

$$\begin{aligned}
 \text{Li}_{0.90}\text{Mg}_{0.95}\text{Zr}_{0.05}\text{PO}_4 &= \\
 &= \text{Li}_{0.9}\text{Mg}_{0.9}(\text{PO}_4)_{0.9} + \text{Mg}_{0.0125}\text{Zr}_{0.05}(\text{PO}_4)_{0.075} + \text{Mg}_{0.0375}(\text{PO}_4)_{0.025} = \quad (\text{Eq. 3.8}) \\
 &= 0.9 \text{LiMgPO}_4 + 0.0125 [\text{MgZr}_4(\text{PO}_4)_6 + \text{Mg}_3(\text{PO}_4)_2]
 \end{aligned}$$

From the phases in equation 3.8, the non-observed phase in these reactions is $\text{Mg}_3(\text{PO}_4)_2$. If it is not seen in the diffraction patterns, it has to be present either as an amorphous phase or as a solid solution with at least one of the observed phases. For each sample of $\text{Li}_{1-2x}\text{Mg}_{1-x}\text{Zr}_x\text{PO}_4$, the produced amounts of $\text{MgZr}_4(\text{PO}_4)_6$ and $\text{Mg}_3(\text{PO}_4)_2$ increase with x . The expansion of the unit cell parameters of both phases,

shown in figure 3.39, leads to think that $\text{Mg}_3(\text{PO}_4)_2$ makes solid solution with the other two phases yielding the products $\text{Li}_{1-2y}\text{Mg}_{1+y}(\text{PO}_4)$ and $\text{Mg}_{1+2z}\text{Zr}_{4-z}(\text{PO}_4)_6$. These solid solutions would introduce defects in the parent phases, e.g. for the olivine phase each Mg^{2+} would substitute $2 \times \text{Li}^+$ resulting in a Li-site vacancy and a Mg^{2+} sitting on the Li site, i.e. $[\text{Li}_{1-2x}\square_x\text{Mg}_x]\text{MgPO}_4$.

In conclusion this section has shown that, under the discussed experimental approaches, Zr cannot be doped into LiMgPO_4 to produce phase pure samples of the series $\text{Li}_{1-2x}\text{Mg}_{1-x}\text{Zr}_x\text{PO}_4$. On the other hand, if the argument developed above is right, it could be possible to make the solid solution between the parent olivine and the magnesium phosphate phases, to yield a new lithium containing compound with Li-vacancies, of interest as potential Li-ion conductor. This new direction is discussed in the next section.

3.10 Mg-doped series

3.10.1 Synthesis

The evidence that the aliovalent substitution of Mg^{2+} for Li^+ to get the series $\text{Li}_{1-2x}\text{Mg}_{1+x}\text{PO}_4$ could be possible was presented at the end of the previous section. Representing the vacancy as \square , this series can also be written as $[\text{Li}_{1-2x}\square_x\text{Mg}_x]\text{MgPO}_4$. This substitution was also predicted by calculations to have a relatively low formation enthalpy as shown in table 3.1. The attempts for making phase pure samples of this series followed again a conventional solid state route with the same reactants as for the parent material.

A set of samples of the series $\text{Li}_{1-2x}\text{Mg}_{1+x}\text{PO}_4$ with $x = 0.025, 0.05, 0.075, 0.1, 0.15, 0.2$ and 0.25 was prepared. The synthesis was made in the same way as for the parent material, initial treatment at $375\text{ }^\circ\text{C}$ and high temperature step at $1000\text{ }^\circ\text{C}$ for 20 hours. The diffraction patterns revealed impurity peaks for all samples. After re-ground and re-firing at $1000\text{ }^\circ\text{C}$ for 11 hours followed by quenching to room temperature, only the composition with $x = 0.025$ resulted phase pure. The rest of the samples were subject to a new re-grind and re-firing at $1050\text{ }^\circ\text{C}$ for 10 h. After that, the samples of the series resulted phase pure up to $x = 0.1$. A further firing at

1080 °C for 10 hours to the multiphasic samples did not remove the extra peaks. The internal standard LaB_6 was used for the determination of the lattice parameters. There is a clear trend in unit cell volume that can be seen in figure 3.41. The diffraction patterns of the series from $x = 0$ to $x = 0.25$ are shown in figure 3.42.

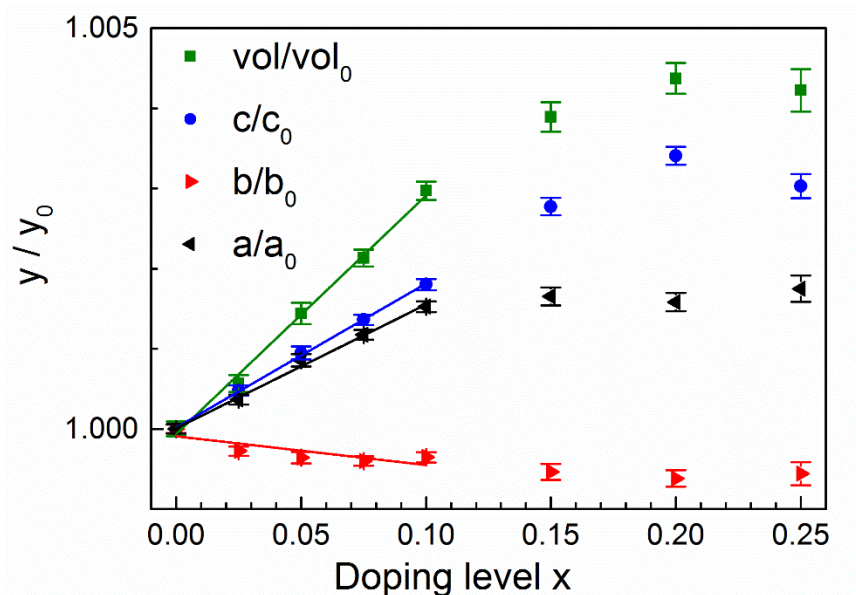


Figure 3.41. Cell volume of the olivine phase for the series $\text{Li}_{1-2x}\text{Mg}_{1+x}\text{PO}_4$ with $x = 0.025, 0.05, 0.075, 0.1, 0.15, 0.2$ and 0.25 . The straight lines are guide to the eyes. Error bars shown as ± 3 e.s.d.

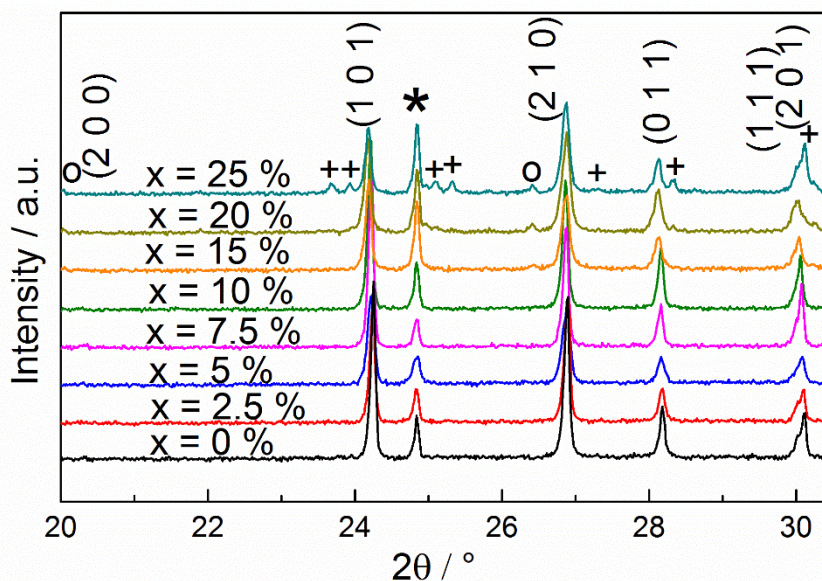


Figure 3.42. PXRD patterns for the series $\text{Li}_{1-2x}\text{Mg}_{1+x}\text{PO}_4$ with $x = 0.025, 0.05, 0.075, 0.1, 0.15, 0.2$ and 0.25 . The (100) reflection from the LaB_6 internal standard is marked with an asterisk. The peaks marked with + are from the impurity phase $\text{Mg}_3(\text{PO}_4)_2$ $P12_1/n1$. The peak marked with o has not been identified.

3.10.2 Densification

A sample of composition $\text{Li}_{0.8}\text{Mg}_{1.1}\text{PO}_4$ was selected for AC impedance spectroscopy. In order to densify the material for measurements, the powder was initially ground with pestle and mortar. Then it was shaped into a 13 mm diameter pellet with the uniaxial press by applying a load of 1000 Kg. The formed pellet was then subject to cold isostatic pressing. Finally the pellet was sintered at 1000 °C for 5 hours inside an alumina crucible, by using a box furnace with heating and cooling rates of 5 °C/min. The relative density achieved with this method was 72.4 %. This pellet will be referred as sample 1. The density of this pellet is relatively low and therefore further optimisation was pursued.

In order to increase the relative density reached with sample 1, a second sample of the same composition, $\text{Li}_{0.8}\text{Mg}_{1.1}\text{PO}_4$, was ball-milled in ethanol in the same way as the powders of the In-doped system. These powders were then made a pellet, cold isostatic pressed and sintered in the same way as for sample 1. The final relative density was 84.3 %. This pellet will be referred as sample 2.

3.10.3 Conductivity measurements

The conductivity of the two pellets sintered in the previous section was studied. The pellet of composition $\text{Li}_{0.8}\text{Mg}_{1.1}\text{PO}_4$ with relative density 72.4 %, sample 1, was subject to AC impedance measurements. Gold paste was used for painting the electrodes on the sides of the pellet. Gold mesh and wire were used for attaching the connections to the electrodes. The gold paste was dried at 200 °C for 1 hour and finally fired at 600 °C for 1 hour.

The pellet with relative density 72.4 % was measured in ambient air. The AC impedance complex plane plot from data collected at 600 °C is shown in figure 3.43.

The main feature is an arc from 1 MHz to 1 kHz. This arc was measured by circle fit with the software Zview [38] presenting a $\rho = 3.5 \text{ M}\Omega \text{ cm}$ and a corrected capacitance of $2.2 \times 10^{-12} \text{ F cm}^{-1}$, and therefore was assigned to the bulk [39]. At 400 °C the corrected capacitance was of $1.4 \times 10^{-12} \text{ F cm}^{-1}$ and the Li-ion conductivity was of $4.18 \times 10^{-10} \text{ S cm}^{-1}$ with an activation energy $E_a = 1.66(3) \text{ eV}$ in the range from 400 to 600 °C, with the E_a error shown as 1σ .

There is a second feature which consists in a very depressed arc between 100 Hz and 0.1 Hz. This arc was measured by circle fit in the same way as the previous one. The corrected capacitance was of $3.7 \times 10^{-8} \text{ F cm}^{-1}$, and therefore was assigned to the grain boundary. It presented a $\rho = 2.1 \text{ M}\Omega \text{ cm}$. This element was not measured at lower temperatures because it was too small for allowing circle fit with Zview.

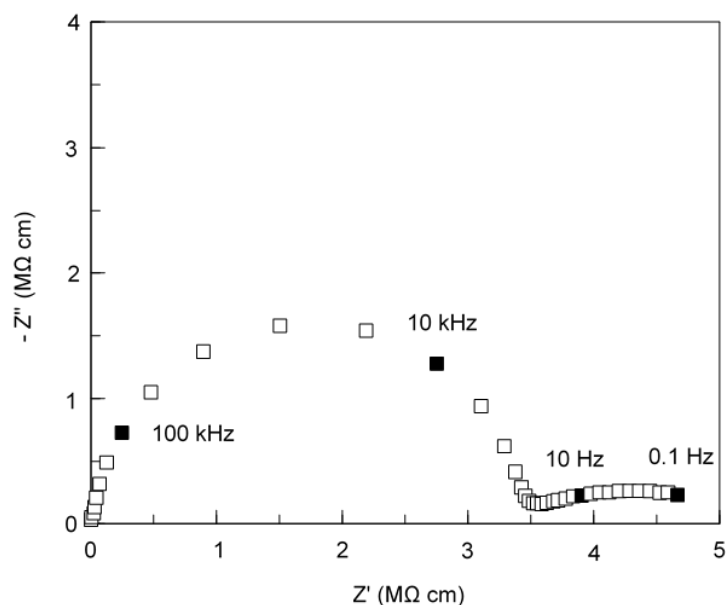


Figure 3.43. AC impedance complex plane plot at 600 °C for the sample of composition $\text{Li}_{0.8}\text{Mg}_{1.1}\text{PO}_4$ with relative density 72.4 %.

The conductivity of sample 2 was also studied by AC impedance spectroscopy. This pellet had the same composition as sample 1, $\text{Li}_{0.8}\text{Mg}_{1.1}\text{PO}_4$, but a higher relative density of 84.3 %. Gold electrodes were mounted on the pellet in the same way as for sample 1.

Sample 2 was measured in dry air. The AC impedance complex plane plots from data collected at 299 °C and 500 °C are shown in figure 3.44.

The Nyquist plot from the data collected at 500 °C, figure 3.44.b, presents the same features as the one shown for sample 1 in figure 3.43. The arc from 1 MHz to 100 Hz was measured by circle fit with the software Zview [38] presenting a $\rho = 8.55$ MΩ cm and a corrected capacitance of 6.69×10^{-12} F cm^{-1} , and therefore was assigned to the bulk [39]. The very depressed arc between 10 Hz and 0.1 Hz was also measured by circle fit presenting a $\rho = 8.61$ MΩ cm and a corrected capacitance of 2.44×10^{-8} F cm^{-1} , and therefore was assigned to the grain boundary [39].

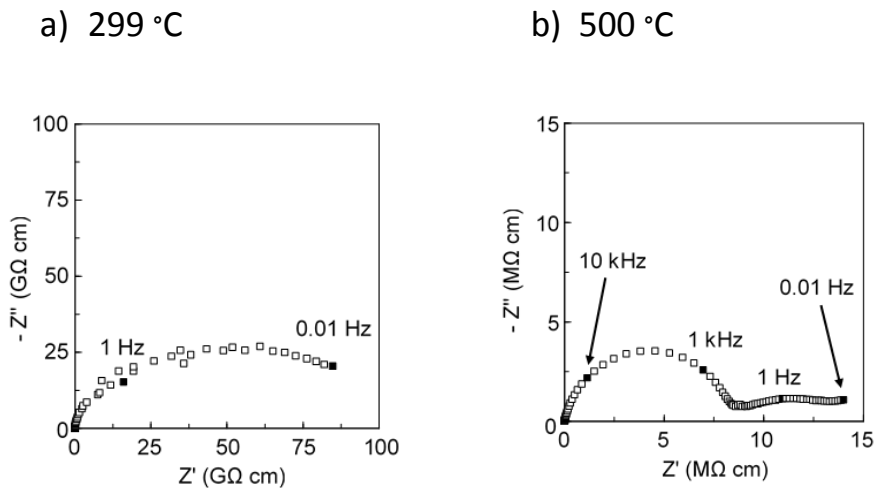


Figure 3.44. AC impedance complex plane plots at 299 °C a) and at 500 °C b) for the sample of composition $\text{Li}_{0.8}\text{Mg}_{1.1}\text{PO}_4$ with relative density 84.3 %.

When the temperature is lowered, the very depressed arc that corresponds to the grain boundary tends to disappear. A broad arc that mainly contains the bulk component is what remains at 299 °C as can be seen in figure 3.44.a and this was the lowest temperature at which the bulk arc was measured. The lowest temperature at which the grain boundary could be measured was 399 °C.

For the Nyquist plot from the data collected at 299 °C, figure 3.44.a, only the bulk component could be measured. The region of the arc from 1 MHz to about 1 Hz was fitted to a circle with the software Zview [38] presenting a $\rho = 69.4$ GΩ cm and a corrected capacitance of 1.04×10^{-11} F cm^{-1} , and therefore was assigned to the bulk [39].

The activation energies for sample 2 were $E_{a,\text{bulk}} = 1.72(4)$ eV in the range from 299 to 500 °C and $E_{a,\text{gb}} = 2.24(12)$ eV in the range from 399 to 500 °C. The E_a errors are shown as 1σ .

The Arrhenius plot for these two samples of $\text{Li}_{0.8}\text{Mg}_{1.1}\text{PO}_4$ is shown in figure 3.45. Due to having a lower Li-ion conductivity than the parent material, no other compositions of the same family were probed for Li-ion conductivity. For the same reason, the densification of this material was not optimised further.

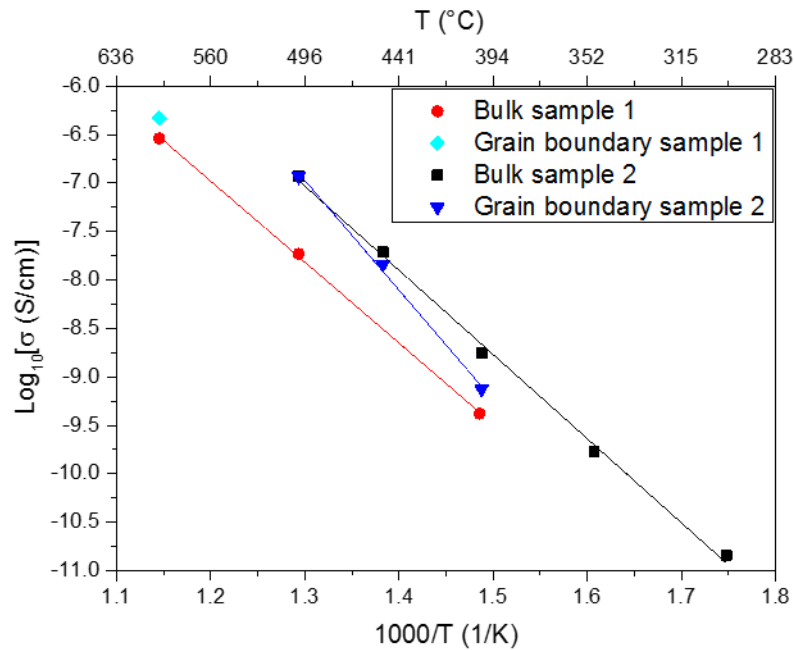


Figure 3.45. Arrhenius-type plot for both, the bulk and grain boundary, responses for the samples of composition $\text{Li}_{0.8}\text{Mg}_{1.1}\text{PO}_4$ with relative densities 72.4 % (sample 1) and 84.3 % (sample 2).

The Li-ion conductivity of this material is 2 – 3 orders of magnitude lower than for the parent material at 400 °C. The linear extrapolation to room temperature gives a bulk conductivity of about $10^{-25} \text{ S cm}^{-1}$, which is many orders of magnitude lower than for the parent material, although this estimation has to be dealt with care because it is not a measurement but an extrapolation under the assumption that the behaviour will still be linear until room temperature. In addition, the activation energy measured by AC impedance spectroscopy is also higher, meaning that the long range Li transport in this material is less easy. This can be explained structurally by taking into account that the Li-vacancy and the Mg atom sit on the same crystallographic site, which is shown by the formula of the series: $[\text{Li}_{1-2x}\square_x\text{Mg}_x]\text{MgPO}_4$. It is thought that the Li transport in olivine materials occurs by the hopping mechanism along the channels where the Li atoms sit [44]. The material of composition $\text{Li}_{0.8}\text{Mg}_{1.1}\text{PO}_4$ would have in the conduction channels sets of Li atoms and vacancies locked between two Mg atoms. This picture shows that even if within those segments the Li-mobility is easier due to the vacancy, overcoming the Mg atoms to pass to the next segment would have a high energy

cost that is translated in the observed higher activation energy and lower bulk ionic conductivity.

In conclusion, a new series of materials with the non-stoichiometric composition $\text{Li}_{1-2x}\text{Mg}_{1+x}\text{PO}_4$ has been developed. The higher doping limit that achieved a phase pure sample was $x = 0.1$. The Li-ion conductivity of $\text{Li}_{0.8}\text{Mg}_{1.1}\text{PO}_4$ was 2 – 3 orders of magnitude lower than for LiMgPO_4 at 400 °C. The activation energy was also higher. These electrical properties with respect to the parent material are in agreement with having Mg on Li sites blocking the Li channels, i.e. the diffusion pathways.

3.11 Summary and Conclusions

The aim of the work presented in this chapter is to find new Li-ion conductor materials through structural modification of the olivine LiMgPO_4 to be probed as potential solid electrolytes by measurements of their conductivity properties. This task was addressed by initial computational screening of the most suitable dopants along with the comparison of the 1976 Shannon radii [24]. This was followed by the synthesis and characterisation of the parent material LiMgPO_4 and some of its doped derivatives which led to the discovery of new compositions of single phase materials. Finally, the features revealed by the new phases inspired a few more trials. The most promising of these new phases was probed for Li-ion conductivity with AC impedance spectroscopy and NMR spectroscopy indicating an improvement in Li-ion conductivity. All the reactions have followed a ceramic synthesis by the standard solid state route, i.e. mixing powder precursors and heating at high temperatures. These samples have been synthesised by using a range of temperatures from 800 to 1100 °C.

Using DFT calculations, the doping enthalpy was ranked for a number of atoms. The top three favoured substitutions were In, Sc and Ga on the Mg site. For the Li site the top one was Mg. The ambitious Zr substitution was selected from ionic radius similarity with Mg. After completing and optimising the syntheses of all the series it was found that for In, Sc and Ga the extent of the substitution followed the DFT relative doping enthalpies derived rank. The contribution of the entropy of mixing used in DFT calculations has also predicted well the need to increase the

temperature, above the one used for the parent material, to stabilise the new phases. The new phases are stable once formed and do not fall apart on slow cooling. The Zr trial was unsuccessful, but the lattice parameters trend for the olivine phase showed evidence that the solid solution of LiMgPO_4 with $\text{Mg}_3(\text{PO}_4)_2$ retaining the olivine structure was possible, i.e. substitution of Mg on the Li site, in agreement with the DFT screening. The latter solid solution was successfully synthesised as well. Observations derived from the new samples led to try co-doping strategies in order to beat the highest level of Li-vacancies achieved until that time and to pursue the extension of the Li pathway dimensionality in the olivine structure.

The best dopant was indium, for which a substitution of 17 % of Li and Mg was achieved. Samples of the series $\text{Li}_{1-x}\text{Mg}_{1-x}\text{In}_x\text{PO}_4$ were analysed by ICP-OES and TEM-EDX and agreement with the nominal compositions was found. Combined Rietveld refinements on high resolution powder X-ray and neutron diffraction patterns accounted for the Li-vacancies and confirmed the In occupancy on Mg site. NMR showed increased hopping rate and mobility of the Li-ions at high temperature. After optimisation of the processing conditions, relative densities above 90 % were achieved and AC impedance measurements revealed an improved Li-ion conductivity above two orders of magnitude at room temperature. This result shows the value of this synthetic approach and offers insight on the correlation between the vacancies introduced and the Li-ion conductivity. Extensive analysis of this system with important contributions by other authors is presented elsewhere [25].

The second best dopant was scandium, for which a substitution of 4 % of Li and Mg was achieved. Samples of the series $\text{Li}_{1-x}\text{Mg}_{1-x}\text{Sc}_x\text{PO}_4$, revealed that a second process is likely to happen in the olivine structure above $x = 0.04$. To clarify the details more research on this system would be needed. The third best dopant was gallium. Samples of the series $\text{Li}_{1-x}\text{Mg}_{1-x}\text{Ga}_x\text{PO}_4$ showed that for low doping levels the olivine cell shrinks. Taking advantage of this discovery, the co-doping with In and Ga was attempted in order to control the unit cell size. The effect on the unit cell was quite modest for the series $\text{Li}_{0.85-x}(\text{Mg}_{0.85-x}\text{In}_{0.15}\text{Ga}_x)\text{PO}_4$ and the vacancy level reached with the indium system was not hit. Another co-doping attempt had the intention of creating gateways between the lithium channels, i.e. creating a Li site between the channels. This was attempted based on ionic radii similarity with the test series

being $\text{Li}_{0.85+x}(\text{Mg}_{0.85-x}\text{In}_{0.15}\text{Li}_x)\text{PO}_4$. More research is needed to establish if this is possible. Finally, after unsuccessful trials with the series $\text{Li}_{1-2x}\text{Mg}_{1-x}\text{Zr}_x\text{PO}_4$, the substitution of Mg for Li was also explored. In agreement with the evidence obtained during the Zr-doping trials and the calculations, it was possible. Samples of the series $\text{Li}_{1-2x}\text{Mg}_{1+x}\text{PO}_4$ are phase pure until $x = 0.1$. Li-vacancies introduced in this system have a limitation concerning the Li-ion conductivity, i.e. since the extra Mg sits in the Li channels, the diffusion pathway is blocked.

In conclusion, the ranking of substitutions derived from computational screening proved to be correct when compared with synthetic work. The calculated order in relative doping enthalpies translated into maximum vacancy fraction. The mixing entropy term correctly predicted the need of higher temperatures to stabilise the doped structures for all cases. The most successful substitution discovered during this work was In for Mg. In particular, the increased conductivity for this system has been found in short range by NMR and in long range by AC impedance. The other compositions explored still remain as interesting systems for further study.

3.12 Appendix 3.1: TEM-EDX spectra of Olivine samples.

3.12.1 Sample of nominal composition $\text{Li}_{0.9}\text{Mg}_{0.9}\text{In}_{0.1}\text{PO}_4$

This section presents the TEM-EDX measurements for the sample $\text{Li}_{0.9}\text{Mg}_{0.9}\text{In}_{0.1}\text{PO}_4$. Figures 3.46 and 3.47 show the first two spectra of the ten measurements shown in table 3.11.

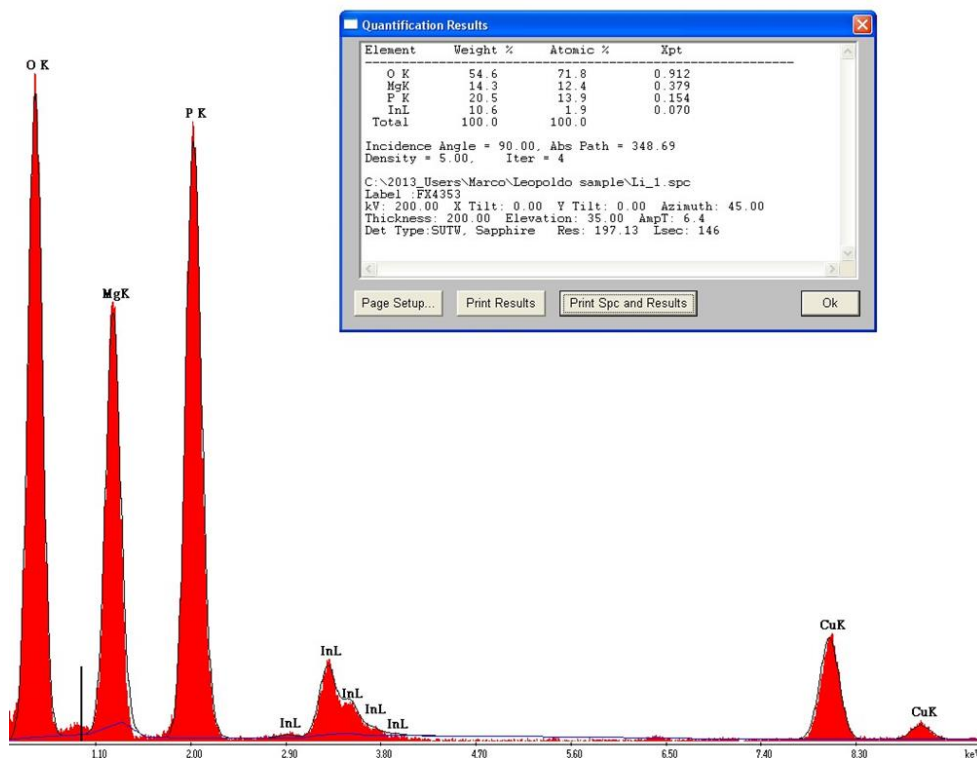


Figure 3.46. TEM-EDX spectrum for measurement 1 of sample $\text{Li}_{0.9}\text{Mg}_{0.9}\text{In}_{0.1}\text{PO}_4$.

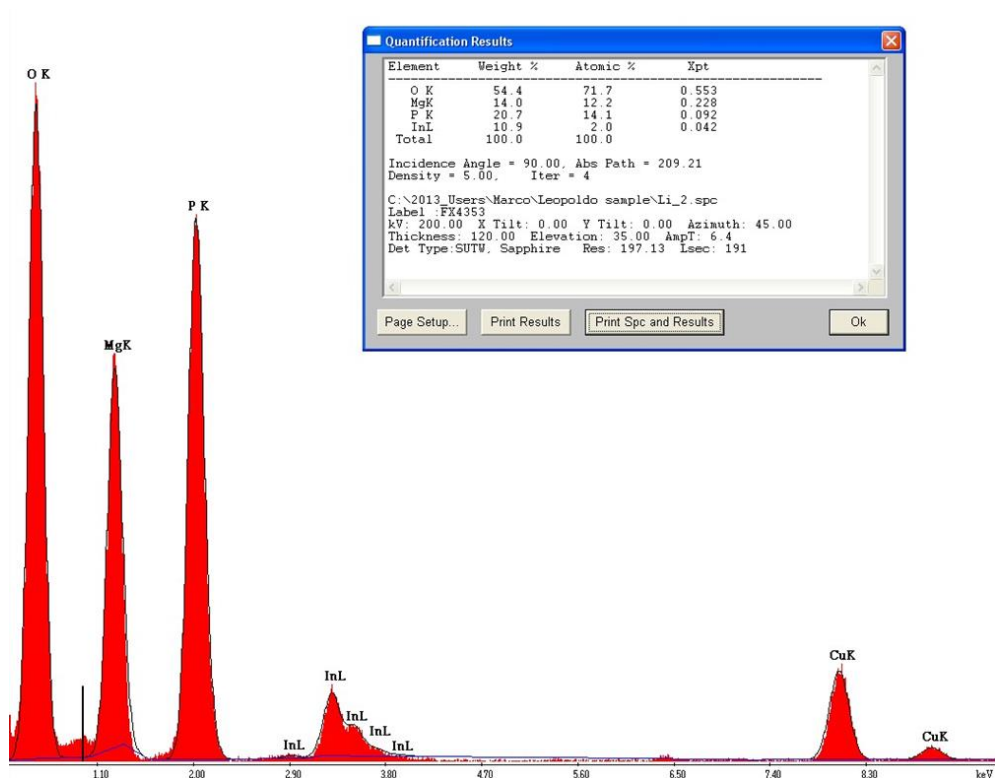


Figure 3.47. TEM-EDX spectrum for measurement 2 of sample $\text{Li}_{0.9}\text{Mg}_{0.9}\text{In}_{0.1}\text{PO}_4$.

Table 3.11. Atom % quantification produced by the instrument as extracted from the TEM-EDX spectra for the sample $\text{Li}_{0.9}\text{Mg}_{0.9}\text{In}_{0.1}\text{PO}_4$.

Measurement number	O	Mg	P	In
1	71.8	12.4	13.9	1.9
2	71.7	12.2	14.1	2
3	71.2	12.6	14.1	2.1
4	71.9	12.3	13.8	2
5	71.7	12.5	13.8	2
6	71.6	12.5	14	2
7	71.5	12.3	14.2	2.1
8	71.9	12.3	13.8	1.9
9	71.3	12.6	14	2.2
10	70.6	12.7	14.5	2.1

The EDX quantification was corrected with correction factors for each element. The correction factors for this sample were 1.07, 1.12 and 0.74 for Mg, P and In respectively. For each element, the final value was calculated by application of equation 3.9.

$$\text{Final value} = \text{Measured value} \times \text{Correction factor} \quad (\text{Eq. 3.9})$$

After application of the correction factors the new table 3.12 was produced.

Table 3.12. Relative atom quantification after application of the correction factors for the sample $\text{Li}_{0.9}\text{Mg}_{0.9}\text{In}_{0.1}\text{PO}_4$.

Measurement number	O	Mg	P	In
1	71.8	13.268	15.568	1.406
2	71.7	13.054	15.792	1.48
3	71.2	13.482	15.792	1.554
4	71.9	13.161	15.456	1.48
5	71.7	13.375	15.456	1.48
6	71.6	13.375	15.68	1.48
7	71.5	13.161	15.904	1.554
8	71.9	13.161	15.456	1.406
9	71.3	13.482	15.68	1.628
10	70.6	13.589	16.24	1.554

Finally this table was normalised so that every row adds up to 100 and the relevant three columns were plotted to form the ternary diagram shown in figure 3.10.a.

3.12.2 Sample of nominal composition ${}^7\text{Li}_{0.9}\text{Mg}_{0.9}\text{In}_{0.1}\text{PO}_4$

This section presents the TEM-EDX measurements for the sample ${}^7\text{Li}_{0.9}\text{Mg}_{0.9}\text{In}_{0.1}\text{PO}_4$. Figures 3.48 and 3.49 show the first two spectra of the ten measurements shown in table 3.13.

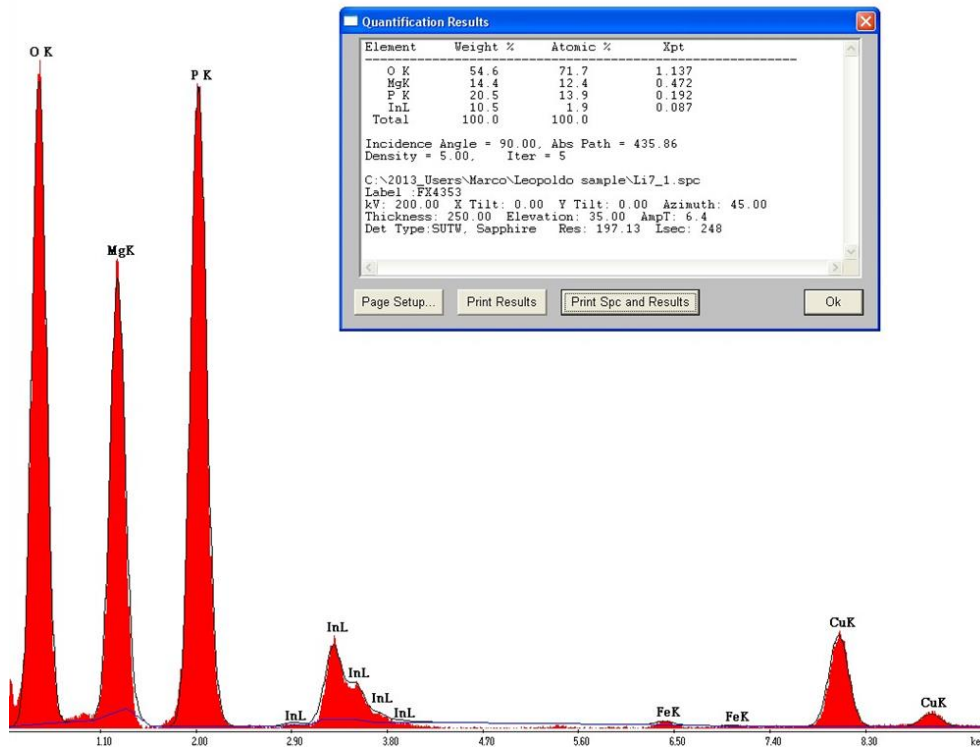


Figure 3.48. TEM-EDX spectrum for measurement 1 of sample ${}^7\text{Li}_{0.9}\text{Mg}_{0.9}\text{In}_{0.1}\text{PO}_4$.

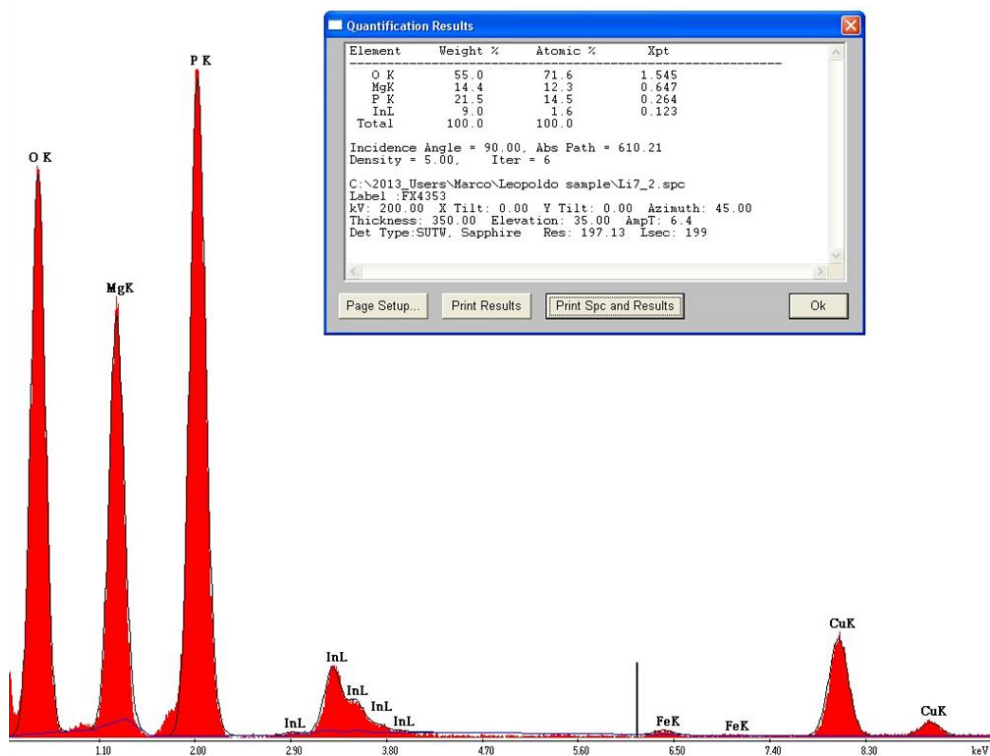


Figure 3.49. TEM-EDX spectrum for measurement 2 of sample ${}^7\text{Li}_{0.9}\text{Mg}_{0.9}\text{In}_{0.1}\text{PO}_4$.

Table 3.13. Atom % quantification produced by the instrument as extracted from the TEM-EDX spectra for the sample ${}^7\text{Li}_{0.9}\text{Mg}_{0.9}\text{In}_{0.1}\text{PO}_4$.

Measurement number	O	Mg	P	In
1	71.7	12.4	13.9	1.9
2	71.6	12.3	14.5	1.6
3	71.8	12.9	13.4	1.8
4	71.4	12.2	14.2	2.3
5	71.3	13	13.9	1.8
6	71.7	12.3	14.1	1.9
7	71.2	13	14	1.9
8	71	12.7	14.4	1.9
9	71.5	12.5	14.2	1.8
10	71.6	12.6	14	1.9

The EDX quantification was corrected in the same way as for the previous sample. The correction factors for this sample were the same as for the previous sample, i.e. 1.07, 1.12 and 0.74 for Mg, P and In respectively. After application of the correction factors the new table 3.14 was produced.

Table 3.14. Relative atom quantification after application of the correction factors for the sample ${}^7\text{Li}_{0.9}\text{Mg}_{0.9}\text{In}_{0.1}\text{PO}_4$.

Measurement number	O	Mg	P	In
1	70.36318	13.00249	15.25646	1.377864
2	70.09825	12.86699	15.87721	1.15755
3	70.25646	13.62008	14.80911	1.314348
4	70.1053	12.72816	15.50702	1.659516
5	69.9444	13.56941	15.18681	1.299385
6	70.22431	12.90813	15.48858	1.378986
7	69.75882	13.57126	15.29816	1.371761
8	69.79024	13.19026	15.65476	1.364744
9	69.96301	13.1242	15.60577	1.307023
10	69.78491	13.32635	15.49897	1.389768

Finally this table was normalised so that every row adds up to 100 and the relevant three columns were plotted to form the ternary diagram shown in figure 3.10.b.

3.13 References

1. Moorey, P.R.S., *Ancient Mesopotamian materials and industries: the archaeological evidence*. 1999: Eisenbrauns.
2. Hoefen, T.M., R.N. Clark, J.L. Bandfield, M.D. Smith, J.C. Pearl, and P.R. Christensen, *Discovery of Olivine in the Nili Fossae Region of Mars*. *Science*, 2003. **302**(5645): p. 627-630.
3. Keller, L.P., S.a. Bajt, G.A. Baratta, J. Borg, J.P. Bradley, D.E. Brownlee, H. Busemann, J.R. Brucato, M. Burchell, and L. Colangeli, *Infrared spectroscopy of comet 81P/Wild 2 samples returned by Stardust*. *Science*, 2006. **314**(5806): p. 1728-1731.
4. Blommaert, J., B.L. de Vries, L. Waters, C. Waelkens, M. Min, H. Van Winckel, F. Molster, L. Decin, M. Groenewegen, and M. Barlow, *Herschel/PACS observations of the 69 μm band of crystalline olivine around evolved stars*. *Astronomy & Astrophysics*, 2014. **565**: p. A109.
5. Burns, R.G. and C.-M. Sung, *The effect of crystal field stabilization on the olivine \rightarrow spinel transition in the system $\text{Mg}_2\text{SiO}_4\text{-Fe}_2\text{SiO}_4$* . *Physics and Chemistry of Minerals*, 1978. **2**(4): p. 349-364.
6. Redfern, S.A.T., G. Artioli, R. Rinaldi, C.M.B. Henderson, K.S. Knight, and B.J. Wood, *Octahedral cation ordering in olivine at high temperature. II: an in situ neutron powder diffraction study on synthetic MgFeSiO_4 (Fa50)*. *Physics and Chemistry of Minerals*, 2000. **27**(9): p. 630-637.
7. Momma, K. and F. Izumi, *VESTA 3 for three-dimensional visualization of crystal, volumetric and morphology data*. *Journal of Applied Crystallography*, 2011. **44**(6): p. 1272-1276.
8. Thomas, D., P. Abhilash, and M.T. Sebastian, *Casting and characterization of LiMgPO_4 glass free LTCC tape for microwave applications*. *Journal of the European Ceramic Society*, 2013. **33**(1): p. 87-93.
9. Kalaji, A., M. Mikami, and A.K. Cheetham, *Ce^{3+} -activated $\gamma\text{-Ca}_2\text{SiO}_4$ and other olivine-type ABXO_4 phosphors for solid-state lighting*. *Chemistry of Materials*, 2014. **26**(13): p. 3966-3975.
10. Świerczyński, D., S. Libs, C. Courson, and A. Kiennemann, *Steam reforming of tar from a biomass gasification process over Ni/olivine catalyst using toluene as a model compound*. *Applied Catalysis B: Environmental*, 2007. **74**(3): p. 211-222.
11. Zaghbi, K., A. Guerfi, P. Hovington, A. Vijn, M. Trudeau, A. Mauger, J.B. Goodenough, and C.M. Julien, *Review and analysis of nanostructured olivine-based lithium rechargeable batteries: Status and trends*. *Journal of Power Sources*, 2013. **232**: p. 357-369.
12. Padhi, A.K., K. Nanjundaswamy, and J. Goodenough, *Phospho-olivines as positive-electrode materials for rechargeable lithium batteries*. *Journal of the electrochemical society*, 1997. **144**(4): p. 1188-1194.
13. Malik, R., A. Abdellahi, and G. Ceder, *A critical review of the Li insertion mechanisms in LiFePO_4 electrodes*. *Journal of The Electrochemical Society*, 2013. **160**(5): p. A3179-A3197.
14. Shi, S., L. Liu, C. Ouyang, D.-s. Wang, Z. Wang, L. Chen, and X. Huang, *Enhancement of electronic conductivity of LiFePO_4 by Cr doping and its identification by first-principles calculations*. *Physical Review B*, 2003. **68**(19): p. 195108.

15. Wang, Y., Y. Wang, E. Hosono, K. Wang, and H. Zhou, *The design of a LiFePO₄/carbon nanocomposite with a core-shell structure and its synthesis by an in situ polymerization restriction method*. *Angewandte Chemie International Edition*, 2008. **47**(39): p. 7461-7465.
16. Jugović, D. and D. Uskoković, *A review of recent developments in the synthesis procedures of lithium iron phosphate powders*. *Journal of Power Sources*, 2009. **190**(2): p. 538-544.
17. Yamada, A., S.-C. Chung, and K. Hinokuma, *Optimized LiFePO₄ for lithium battery cathodes*. *Journal of the electrochemical society*, 2001. **148**(3): p. A224-A229.
18. Porcher, W., P. Moreau, B. Lestriez, S. Jouanneau, F. Le Cras, and D. Guyomard, *Stability of LiFePO₄ in water and consequence on the Li battery behaviour*. *Ionics*, 2008. **14**(6): p. 583-587.
19. Jalem, R., T. Aoyama, M. Nakayama, and M. Nogami, *Multivariate Method-Assisted Ab Initio Study of Olivine-Type LiMXO₄ (Main Group M²⁺-X⁵⁺ and M³⁺-X⁴⁺) Compositions as Potential Solid Electrolytes*. *Chemistry of Materials*, 2012. **24**(7): p. 1357-1364.
20. Park, M., X. Zhang, M. Chung, G.B. Less, and A.M. Sastry, *A review of conduction phenomena in Li-ion batteries*. *Journal of Power Sources*, 2010. **195**(24): p. 7904-7929.
21. Meethong, N., Y.H. Kao, S.A. Speakman, and Y.M. Chiang, *Aliovalent substitutions in olivine lithium iron phosphate and impact on structure and properties*. *Advanced functional materials*, 2009. **19**(7): p. 1060-1070.
22. Yang, M.-R. and W.-H. Ke, *The doping effect on the electrochemical properties of LiFe_{0.95}M_{0.05}PO₄ (M= Mg²⁺, Ni²⁺, Al³⁺, or V³⁺) as cathode materials for lithium-ion cells*. *Journal of the Electrochemical Society*, 2008. **155**(10): p. A729-A732.
23. Lee, S.-B., S.-H. Cho, V. Aravindan, H.-S. Kim, and Y.-S. Lee, *Improved cycle performance of sulfur-doped LiFePO₄ material at high temperatures*. *Bulletin of the Korean Chemical Society*, 2009. **30**(10): p. 2223-2226.
24. Shannon, R.t., *Revised effective ionic radii and systematic studies of interatomic distances in halides and chalcogenides*. *Acta Crystallographica Section A: Crystal Physics, Diffraction, Theoretical and General Crystallography*, 1976. **32**(5): p. 751-767.
25. Enciso-Maldonado, L., M.S. Dyer, M.D. Jones, M. Li, J.L. Payne, M.J. Pitcher, M.K. Omir, J.B. Claridge, F. Blanc, and M.J. Rosseinsky, *Computational Identification and Experimental Realization of Lithium Vacancy Introduction into the Olivine LiMgPO₄*. *Chemistry of Materials*, 2015. **27**(6): p. 2074-2091.
26. Minakshi, M., P. Singh, D. Ralph, D. Appadoo, M. Blackford, and M. Ionescu, *Structural characteristics of olivine Li(Mg_{0.5}Ni_{0.5})PO₄ via TEM analysis*. *Ionics*, 2012. **18**(6): p. 583-590.
27. Dreele, R.B.V., M.R. Suchomel, and B.H. Toby. *Argonne National Laboratory, Advanced Photon Source, Compute X-ray Absorption*. <http://11bm.xray.aps.anl.gov/absorb/absorb.php>. August 2016].
28. Coelho, A.A., *Topas-Academic*. A Computer Programme for Rietveld Analysis, 2004.
29. Hanic, F., M. Handlović, K. Burdova, and J. Majling, *Crystal structure of lithium magnesium phosphate, LiMgPO₄: crystal chemistry of the olivine-type compounds*. *Journal of crystallographic and spectroscopic research*, 1982. **12**(2): p. 99-127.

30. Kim, S.-C., M.-S. Lee, J. Kang, Y.-I. Kim, and S.-J. Kim, *Crystal structure and ion conductivity of a new mixed-anion phosphate $\text{LiMg}_3(\text{PO}_4)\text{P}_2\text{O}_7$* . Journal of Solid State Chemistry, 2015. **225**: p. 335-339.
31. Voronin, V., E. Sherstobitova, V. Blatov, and G.S. Shekhtman, *Lithium-cation conductivity and crystal structure of lithium diphosphate*. Journal of Solid State Chemistry, 2014. **211**: p. 170-175.
32. Werner, P.-E., L. Eriksson, and M. Westdahl, *TREOR, a semi-exhaustive trial-and-error powder indexing program for all symmetries*. Journal of Applied Crystallography, 1985. **18**(5): p. 367-370.
33. Belsky, A., M. Hellenbrandt, V.L. Karen, and P. Luksch, *New developments in the Inorganic Crystal Structure Database (ICSD): accessibility in support of materials research and design*. Acta Crystallographica Section B: Structural Science, 2002. **58**(3): p. 364-369.
34. Toby, B.H., *R factors in Rietveld analysis: How good is good enough?* Powder diffraction, 2006. **21**(01): p. 67-70.
35. Taylor, J., O. Arnold, J. Bilheaux, A. Buts, S. Campbell, M. Doucet, ..., and J. Zikovsky, *Mantid, A high performance framework for reduction and analysis of neutron scattering data*. Bulletin of the American Physical Society, 2012. **57**.
36. Rodríguez-Carvajal, J., *Recent developments of the program FULLPROF*. Commission on powder diffraction (IUCr). Newsletter, 2001. **26**: p. 12-19.
37. McCusker, L., R. Von Dreele, D. Cox, D. Louer, and P. Scardi, *Rietveld refinement guidelines*. Journal of Applied Crystallography, 1999. **32**(1): p. 36-50.
38. *Zview software*. Scribner Associates, Inc. <http://www.scribner.com>. 2017].
39. Irvine, J.T., D.C. Sinclair, and A.R. West, *Electroceramics: characterization by impedance spectroscopy*. Advanced Materials, 1990. **2**(3): p. 132-138.
40. Thomas, D. and M.T. Sebastian, *Temperature-Compensated LiMgPO_4 : A New Glass-Free Low-Temperature Cofired Ceramic*. Journal of the American Ceramic Society, 2010. **93**(11): p. 3828-3831.
41. Li, M. and D.C. Sinclair, *Transformation from insulating p-type to semiconducting n-type conduction in $\text{CaCu}_3\text{Ti}_4\text{O}_{12}$ -related $\text{Na}(\text{Cu}_{5/2}\text{Ti}_{1/2})\text{Ti}_4\text{O}_{12}$ ceramics*. Journal of Applied Physics, 2013. **114**(3): p. 034106.
42. Barsoukov, E. and J.R. Macdonald, *Impedance spectroscopy: theory, experiment, and applications*. 2005: John Wiley & Sons.
43. Li, Y., J.-T. Han, C.-A. Wang, H. Xie, and J.B. Goodenough, *Optimizing Li^+ conductivity in a garnet framework*. Journal of Materials Chemistry, 2012. **22**(30): p. 15357-15361.
44. Nishimura, S.-i., G. Kobayashi, K. Ohoyama, R. Kanno, M. Yashima, and A. Yamada, *Experimental visualization of lithium diffusion in Li_xFePO_4* . Nature materials, 2008. **7**(9): p. 707-711.

Chapter 4

New olivine cathode materials

4.1 Introduction

LiCoO_2 has been one of the preferred cathodes used since 1991 (Sony Corporation) in Li-ion secondary batteries due to its high capacity, i.e. high energy density [1]. However for the established technology there is some risk of the battery catching fire [2]. When the battery catches fire, the liquid organic electrolyte provides the fuel, while the oxygen for the combustion can be provided by delithiated cathodes when the temperature increases.

As it was described in chapter one, the main failure mechanisms that lead to fire in a battery are short, due to e.g. dendrite formation, and temperature increase, due to e.g. over abuse. The fire risk was also explained in detail in chapter one. Within the series of events that lead to a battery fire, there is one that provides oxygen from inside of the battery which is related to the cathode. It happens after thermal decomposition/disproportionation of the cathode in a series of reactions shown in chapter one for LiCoO_2 . It was also discussed that the onset temperature for self-sustained thermal runaway of LiCoO_2 was 150 °C while for LiFePO_4 it was 310 °C. This shows that new cathode materials with higher thermal stability can help to reduce the risk of the battery catching fire. Therefore safety and environmental concerns have led to the search for new materials.

LiFePO_4 , published by Goodenough et al. in 1997 [3], has proven to show an improved safety profile due to its crystal chemistry and the nature of the bonding providing high structural stability [4], which makes it an ideal material for applications such as batteries for large systems and transportation. In addition Fe is cheaper and less toxic than Co.

Many methods have been used to synthesise this material, from conventional solid state ceramic route to sol gel or hydrothermal methods [5]. Diffraction studies have

shown that this material possess the ordered olivine structure, $ABXO_4$, with the Li atom preferring the A site and the Fe atom preferring the B site. However a small fraction of Li-Fe anti-site defects, less than 4 %, have been introduced reversibly after annealing at high temperatures, such as 900 °C [6], that are close to the melting point of the material which is approximately at 1000 °C [7]. These anti-site defects can be eliminated on annealing at lower temperatures such as 600 °C [6]. When $LiFePO_4$ is delithiated it retains the BXO_4 original olivine topology with a unit cell volume fall of 8.6 % [8].

However, if $LiFePO_4$ is used as produced for making a cathode and build a battery, the result will be an impaired charge-discharge rate capability, i.e. the maximum charge/discharge rate of the battery will be much lower than for a battery made with other cathode materials. The underlying reason is the small Li-ion diffusion coefficient for this material, 10^{-14} to 10^{-15} $cm^2 s^{-1}$ along with its low electronic conductivity, $< 10^{-9}$ $S cm^{-1}$ [9]. This initially places $LiFePO_4$ in a clear disadvantage with respect to materials such as $LiCoO_2$ or $LiMn_2O_4$.

In order to enhance the performance of this material in cathode applications, large amounts of research have been carried out resulting in important improvements for its application as cathode material in Li-ion batteries. After the discovery that carbon coating highly improved the electronic conductivity by Ravet et al. [10], the improvements have continued since then with particle size reduction and core-shell structures that have tried conductive surface coatings such as silver [11]. Doping has also been studied with cations such as V^{5+} , Ti^{4+} , Cr^{3+} or Al^{3+} although the improvements in conductivity led to controversy with respect to its origin [12].

Therefore, since the electronic conductivity can be improved by carbon coating, it seems that there is still room for finding a modification through defect introduction that could lead to a much better ionic conductivities in the material as produced. With this aim and after the success of indium doping in the isostructural material $LiMgPO_4$ shown in the previous chapter, the In-doping of $LiFePO_4$ is tried in this chapter. If an improvement in ionic conductivity of the same order as for $LiMgPO_4$ is achieved, larger than 100-fold, this could lead to immediate advantages in the process of $LiFePO_4$ battery fabrication.

The second potential advantage could be the possibility of cell voltage modification. As it was described in chapter one, the cell potential depends on the difference in

chemical potential of Li in the anode and in the cathode. The chemical potentials are determined by the energy used in electron and Li^+ transfer. As explained in chapter one, a fraction of the oxygen of the cathode is believed to participate in the electron transfer. The participation of oxygen in electron transfer not only depends on the state of charge but also on the presence of no transition metals in the structure. Therefore doping with no transition metals is a way of increasing the participation of oxygen in the electron transfer, creating a more oxidising environment which increases the Li^+ intercalation voltage.

If the voltage of the cell can be increased with doping up to the level that equalises the value in LiCoO_2 , this would also be important due to the possibility of building LiFePO_4 cells that mimic the charge/discharge galvanostatic profiles of LiCoO_2 cells. The advantage is a huge leap in technological retro-compatibility of the new LiFePO_4 cells that would work straightforward in hardware designed for the older technology.

With this target in mind, this chapter presents how a method for synthesis of LiFePO_4 has been set up and then how the synthetic conditions have been optimised to explore the possibility of In-doping to finally find out the doping limit. Then the task of making large batches for neutron powder diffraction is described. The study is completed with chemical analysis with ICP-OES and detailed Rietveld refinements with combined X-ray powder synchrotron and neutron diffraction. Diffraction data of the doped sample at $200\text{ }^\circ\text{C}$ is also studied in a Rietveld combined refinement. Data from cathode testing is also shown. Finally, beyond the doping limit a new phase has been found and its structure solved.

4.2 Parent LiFePO₄

4.2.1 Finding a suitable reaction and setup

The synthesis was adapted from those in literature by Kim et al. [13] and by Hong et al. [14]. The first attempt of synthesis in an argon gas flow sealed tube furnace showed Fe₃O₄ as impurity. To overcome this limitation iron granules were used upstream in order to trap the traces of oxygen remaining in the argon flow. This method produced phase pure samples of LiFePO₄ and at the same time showed how critical this setup is.

For exploratory synthesis and small scale samples a hinge furnace with a silica tube and Swagelok fitting-type end caps was used. Argon was flowed directly from a bottle and iron granules were placed upstream to function as oxygen getters. For large scale synthesis a large tube furnace was used with a working alumina tube and stainless steel end caps with rubber seals. Again the argon gas and iron granules were used in the same way as for small scale synthesis.

The synthesis followed a conventional solid state route from Fe(II) oxalate which is explained in detail in the next section. Ball milling in ethanol was proven to be successful as mixing procedure and followed by slurry drying below 70 °C produced appropriate precursors.

Once the setup was working and producing phase pure samples, the temperature profile was tuned so that each furnace was able to be loaded and yield a new batch in 24 hours. Finally the firing temperature was optimised before the synthesis of the large scale samples. The synthesis was tested at 600 °C, 650 °C and 700 °C. The diffraction patterns were similar for all three samples. Because of that the middle temperature was chosen for the scaled up sample. The final detailed conditions are presented in next section. The precursors were prepared in large batches, target amounts of 4 – 5 grams, or in small batches, target amounts 0.5 – 0.75 grams.

4.2.2 Optimised synthesis of the parent LiFePO₄

Stoichiometric amounts of the high purity reactants Li₂CO₃ (Sigma-Aldrich, 99.997 %, used from desiccator), FeC₂O₄·2H₂O (Alfa-Aesar, 99.99 %, used from desiccator) and (NH₄)H₂PO₄ (Sigma-Aldrich, 99.999 %, used as received after pestle and mortar ground to reduce the size of the crystals) are ball milled in ethanol using zirconia milling media in a planetary mill. The slurry is dried under stirring in a crystallising dish at 60-70 °C. The resulting dried mixture is homogenised and most of it is made a pellet using a 32 mm diameter pellet die and a load lower than 100 Kg. For small scale samples lower diameter and loads were used. The remainder is used for one or several sacrificial buffer pellets to be placed between the main pellet and the alumina crucible. The crucible containing the preparation is placed in a temperature calibrated and leak tested tube furnace with Ar flow of 1 bubble/second and Fe granules upstream to reduce the traces of O₂. The temperature program consist of: dwell for 4 hours at room temperature for purge, then heating up at 2 °C/min to 350 °C and dwell for 3 hours, then heating up at 2 °C/min to 650 °C and dwell for 6 hours, and finally cooling down at 10 °C/min to room temperature.

The resulting main pellet should exhibit a homogeneous colour/texture all around. If any surface inhomogeneity was seen, it was removed before any further experiment with the material. Only homogeneous pellets were powdered for further structural or electrochemical characterisation.

The Fe granules used as oxygen getter should not be fully oxidised, showing that the oxygen content was low enough for a successful synthesis. During the successful syntheses of this chapter, normally the upper fraction of the iron granules lost its shiny metal aspect, while the lower fraction remained shiny.

4.2.3 Diffraction and refinements

4.2.3.1 Ordered model at room temperature for LiFePO₄

Laboratory PXRD was used for evaluation of the synthesis procedure until high phase purity was achieved in both, small scale and large scale samples for neutron diffraction. Once the large sample was made, ICP-OES analysis, FTIR spectrum and neutron and synchrotron diffraction data were collected on it. The powder diffractometers were GEM at ISIS Neutron Source and I11 at Diamond Light Source, both at Harwell campus, Oxford, UK.

For synchrotron X-ray diffraction at beam line I11, the sample was loaded in a borosilicate capillary of 0.5 mm diameter. For this capillary size, the absorption was evaluated in the same way as for LiMgPO₄ and resulted a value of $\mu_R = 1.27$ when assuming a packing fraction of 0.6 for this composition. The data was collected in Debye-Scherrer geometry with the position sensitive detector, PSD, for 11 seconds and finally with the MAC detectors 4 scans of 30 minutes each were collected. The final MAC dataset used in the combined refinement presented here was built by summing the original 4 datasets and re-binning the data to a step size of 0.005 °.

For neutron diffraction data the sample was loaded in an 8 mm diameter vanadium can and placed in the GEM sample changer along with other samples. The data collection lasted in the order of 1-2 hours, until the beam current in μA integrated up to 240 $\mu\text{A}\text{hour}$. The final dataset was absorption corrected by using the software Mantid [15].

The combined refinement was made with the software Topas academic version 5 [16]. The Topas input file was setup with the filenames of the datasets, I11 wavelength for MAC detectors, $\lambda = 0.826185(5) \text{ \AA}$ with error as 1 e.s.d., and GEM diffractometer constants, difC, difA and t0 from Y₂O₃ and Si calibration. The X-ray peak shape, initial cell parameters, axial divergence and zero error were selected by preliminary Pawley fits over a restricted 2 θ range. Pearson VII is the peak shape chosen after comparing with Pseudo-Voigt and TCHZ. The weighing method for X-rays was set to $1/\sigma^2$. The crystal structure from Yakubovich et al. [17] is used as starting model for the Rietveld refinement. The initial B_{iso} are set to 0.5 \AA^2 .

The scattering factors are set to neutral for the same reason as in chapter 3. The 2θ range is set to refine from 8° to the end of the histogram, i.e. 150° . The number of coefficients of the Chebyshev-type background were increased up to 24 in order to achieve a good fit. Finally X-ray absorption correction was added.

To add the neutron histograms, the lattice parameters are fixed to keep the correspondence with the highest resolution scattering dataset, i.e. the MAC I11 dataset. The lowest angle GEM bank used is number 3 due to being the higher one that includes the reflection (200), i.e. the longest d-spacing reflection for the starting model. GEM banks 4, 5 and 6 are included too. difA, the t^2 contribution to the TOF vs d-spacing relationship, is refined for all banks. The small remaining misfit almost vanishes by refining difC for all banks, the coefficients that linearly relates the TOF with d-spacing.

Now the structure is refined starting with the lattice parameters and following with the refinable atomic positions. All the individual B_{iso} for each atom of the asymmetric unit are refined at the same time. Then atomic positions are refined again with negligible change. Finally the anisotropic displacement parameters, ADPs, are refined taking care of the symmetry restriction that imposes $U_{12} = U_{23} = 0$ for all atoms in 4c site, i.e. for Fe, P, O1 and O2. Final fit factors and structural parameters are shown in table 4.2 along with the data for the doped samples. The refined model is basically the same as found in literature. The graphical output of the refinement for each histogram is shown in figure 4.1. A projection of the resulting structural model showing the atoms as 99 % of thermal displacement ellipsoids is shown in figure 4.8 for comparison with the doped material. The refined structural parameters and refinement factors are shown in table 4.2 for comparison with the doped samples.

4.2.3.2 Testing the model: cation occupancy and Li-Fe anti site defects

The robustness of the fit is tested by refining simultaneously the occupancies of Li, Fe and P in the model with B_{iso} . The refinement yields an output of $Li_{1.008(8)}Fe_{0.979(2)}P_{0.976(2)}O_4$, with errors shown as 3 e.s.d., which is stoichiometric in Li and 2 % deficient in Fe and P. In general the e.s.d. is much smaller than the experimental error, especially for high resolution data [18], which would suggest that the test is successful and within reasonable limits. In addition, no impurities were visible in these histograms.

In order to study the fraction of Li-Fe anti-site defects discussed by some authors [6], a new model with compositional constraint is built on the best model with B_{iso} values, i.e. $[Li_{1-x}Fe_x][Fe_{1-x}Li_x]PO_4$. In the latter formula, x is the fraction of anti-site defects. After refining x, B_{iso} were refined and finally x was refined again. The final output was a value for the anti-site parameter of $x = 0.0050(6)$ with the error shown as 3 e.s.d. This indicates that the fraction of anti-site defects is about 0.5 %. Considering again that e.s.d. values largely under-estimate the experimental errors [18] this sample could also be considered to have a conventional ordered olivine structure. In any case the temperature used for the synthesis of this sample, 650 °C, is very close to the annealing temperature which is recognised to reverse the anti-site disorder, i.e. 600 °C [6].

Finally, comparing the fit factor from the stoichiometric and fully ordered model with no anti-site defects, $R_{wp} = 4.56$ %, with the fit factor from the slightly disordered model with a small fraction of anti-site defects, $R_{wp} = 4.54$, it could be stated that a small fraction of defects between 0 and 0.5 % is possible in this sample.

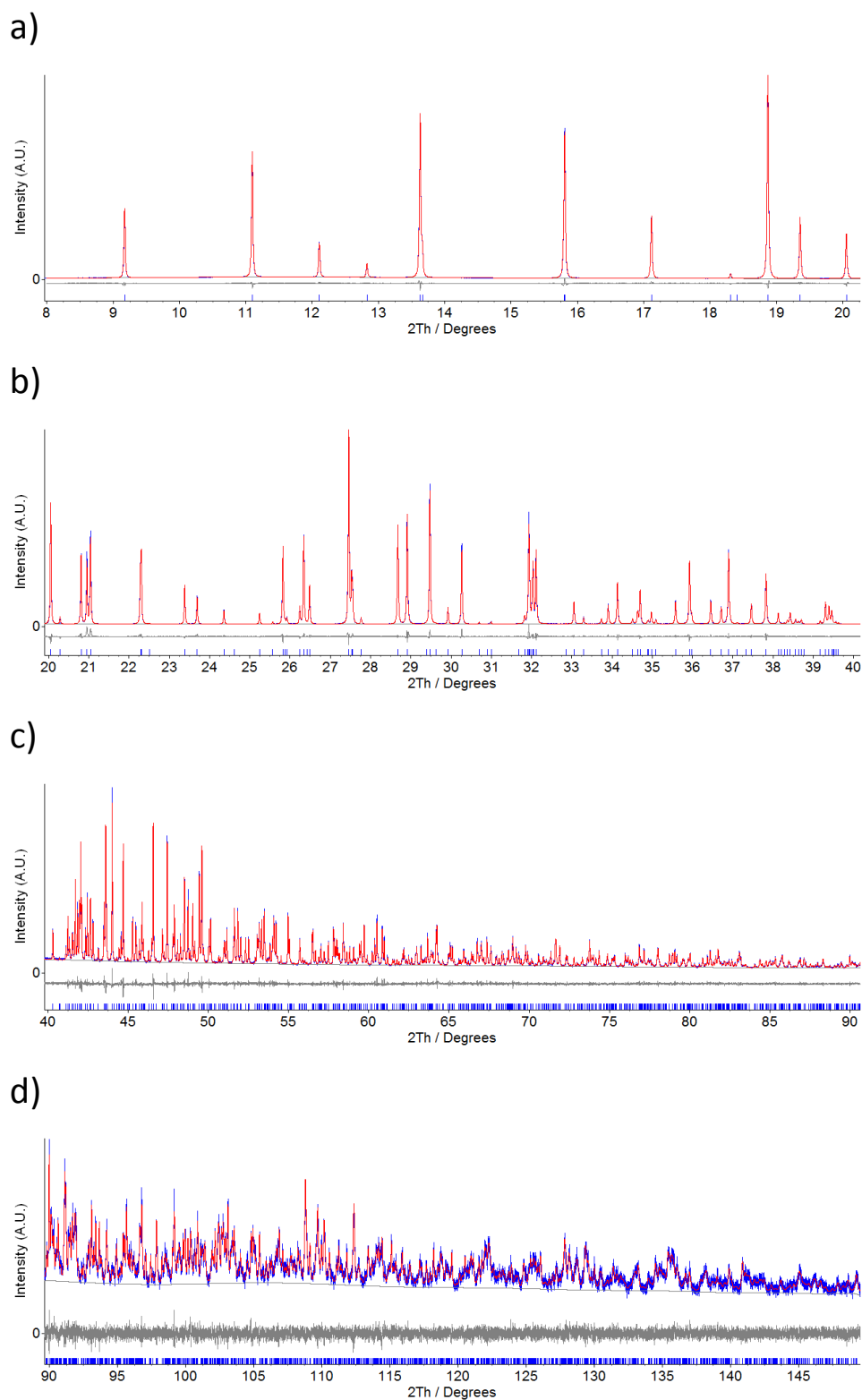
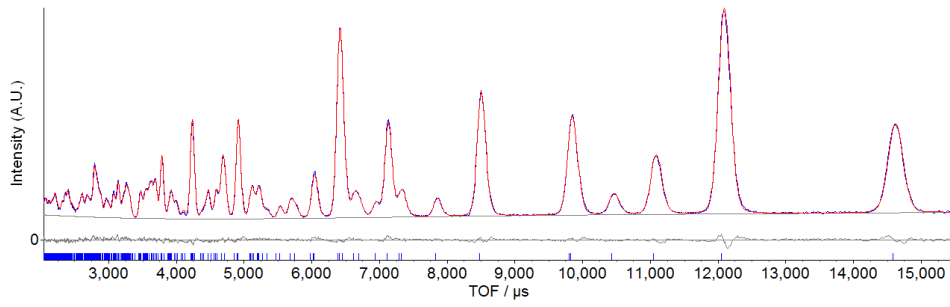
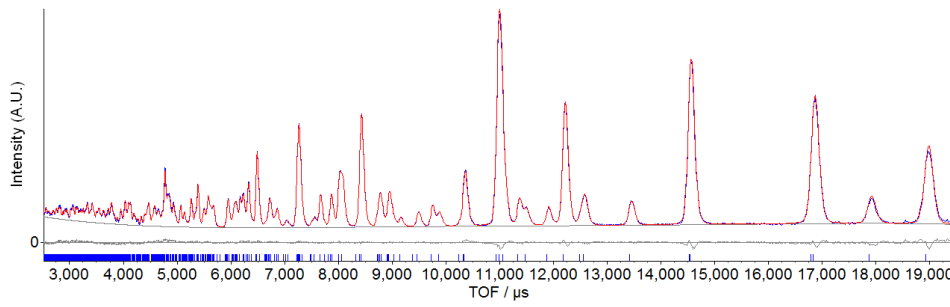


Figure 4.1. Combined Rietveld refinement of the sample LiFePO_4 against neutron powder diffraction data from GEM, and PXRD I11 MAC data. Data is in blue, model in red and difference and background in grey. Blue tick marks represent the olivine phase. The X-ray histogram has been split in four parts shown along panels a, b, c and d to present the refinement in more detail.

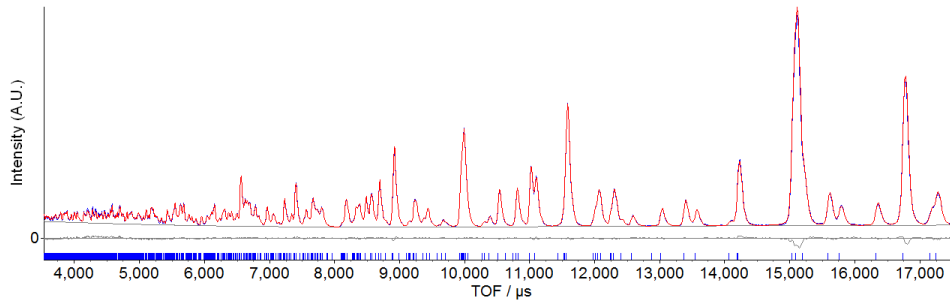
e)



f)



g)



h)

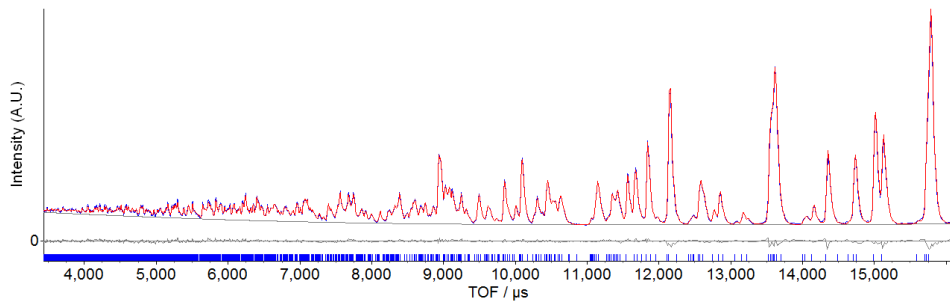


Figure 4.1. (Cont.) Histograms from GEM banks 3, 4, 5 and 6 are shown in panels e, f, g and h respectively. Data is in blue, model in red and difference and background in grey. Blue tick marks represent the olivine phase.

4.3 In-doped series

4.3.1 Finding the right temperature for the synthesis

The work in chapter 3 revealed the importance of increasing the temperature above that used for the parent material in order to achieve successful defect introduction. In this section this strategy is used for developing phase pure materials of the series $\text{Li}_{1-x}\text{Fe}_{1-x}\text{In}_x\text{PO}_4$.

After defining a successful synthesis for the parent material at 650 °C, the search for the temperature to introduce indium in the olivine structure starts at 700 °C and 800 °C for the composition $\text{Li}_{0.9}\text{Fe}_{0.9}\text{In}_{0.1}\text{PO}_4$. The synthesis at 650 °C was not attempted for the doped sample because the role of the entropy of mixing was anticipated. It was thought that the synthesis at 650 °C would have been unsuccessful, i.e. resulting in a polyphasic sample.

As it can be seen in figure 4.2, the samples made at 700 °C and 800 °C produced the olivine with an extra phase that has been assigned to $\text{LiFeIn}(\text{PO}_4)_2$ identified for first time in this thesis. Its structure solution is described later on in this chapter. As it can be seen in the same figure 4.2, the level of the impurity decreases considerably from 700 °C to 800 °C. In a further attempt in search for phase purity the sample made at 700 °C was re-fired at 850 °C and it looked almost phase pure, with a barely-visible extra reflection at $2\theta = 32^\circ$, as can be seen in the same figure 4.2. After these trials, it was considered that 850 °C was the appropriate synthetic temperature for these samples.

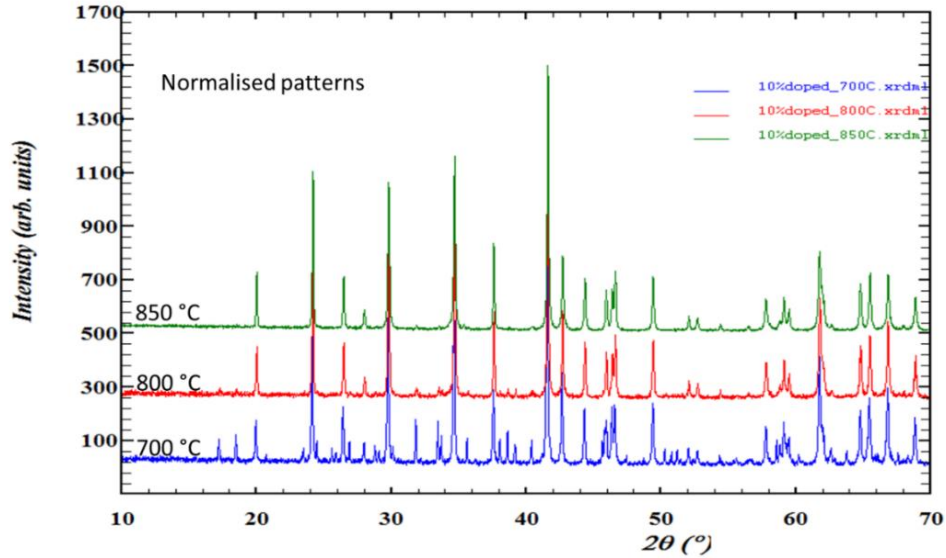


Figure 4.2. Co $K\alpha_1$ PXR D patterns of samples of nominal composition $\text{Li}_{0.90}\text{Fe}_{0.90}\text{In}_{0.10}\text{PO}_4$ after heat treatments at 700 °C, 800 °C and 850 °C. Samples prepared at 700 °C and 800 °C were made from fresh precursor while the sample at 850 °C is a re-firing of the sample shown at 700 °C. The impurity peaks that vanish with increased temperature were assigned to the new phase $\text{LiFeIn}(\text{PO}_4)_2$. The sample at 850 °C still has the extra reflection at $2\theta = 32^\circ$.

The olivine cell volume for the parent phase derived from the combined refinement in the previous section was 291.043(0). The sample made at 700 °C and re-fired at 850 °C has a cell volume of 292.615(6) \AA^3 , error as 1 e.s.d., which indicates that the cell has changed and the doping has been successful. A Pawley refinement to the olivine phase on this sample is shown in figure 4.3.

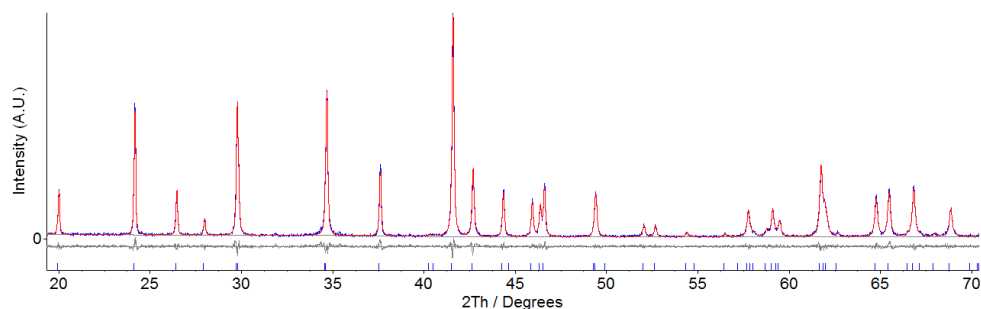


Figure 4.3. Co $K\alpha_1$ PXRD pattern of a sample of nominal composition $\text{Li}_{0.90}\text{Fe}_{0.90}\text{In}_{0.10}\text{PO}_4$. Pawley fit, red, to the data, blue. Background and difference are plotted in grey. Blue tick marks represent the olivine phase. This sample contains a small fraction of the impurity $\text{LiFeIn}(\text{PO}_4)_2$ discovered and solved during this thesis, barely-visible as an extra reflection at $2\theta = 32^\circ$.

From the beginning the pellet homogeneity was a problem for the doped series. The 2 step cycle, i.e. first step at 350°C and second step at 850°C showed inhomogeneous pellets. This inhomogeneity consisted of black inclusions that in some cases went all the way through the pellet. However the pellet was homogeneous when the second step was at 800°C . This led to the design of the three steps cycle that is presented as the standard method for the synthesis of this series in the next section.

The scaling up of these samples for neutron diffraction used the same setup described for the parent material but the temperature profile designed for this series. The compositions selected for scaling up were $\text{Li}_{0.96}\text{Fe}_{0.96}\text{In}_{0.04}\text{PO}_4$ and $\text{Li}_{0.92}\text{Fe}_{0.92}\text{In}_{0.08}\text{PO}_4$.

4.3.2 Optimised Synthesis of the In-doped series

The synthesis is very similar to that for the parent material. The major changes are in the inclusion of the new reactant In_2O_3 and the new temperature profile.

Stoichiometric amounts of the high purity reactants Li_2CO_3 , $\text{FeC}_2\text{O}_4 \cdot 2\text{H}_2\text{O}$, In_2O_3 (Alfa-Aesar, 99.995 %, dried at 200°C) and $(\text{NH}_4)_2\text{H}_2\text{PO}_4$ are ball milled in ethanol using zirconia milling media in a planetary mill. The resulting slurry is dried under

stirring in a crystallising dish at about 60-70 °C. The resulting dried mixture is homogenised and most of it is made a pellet using a 32 mm diameter pellet die and load lower than 100 Kg. For small scale samples lower diameter and loads were used. The remainder is used for one or several sacrificial buffer pellets to be placed between the main pellet and the alumina crucible. The crucible containing the preparation is placed in a temperature calibrated and leak tested tube furnace with Ar flow of 1 bubble/second and Fe granules to reduce the traces of O₂. The temperature program consists of: dwell for 4 hours at room temperature for purge, then heating up at 2 °C/min to 350 °C and dwell for 3 hours, then heating at 2 °C/min to 800 °C and dwell for 3 hours, then heating up at 2 °C/min to 850 °C and dwell for 6 hours, and finally cooling down at 10 °C/min to room temperature.

As for the parent material, the resulting main pellet should exhibit a homogeneous colour/texture all around. If any surface inhomogeneity was seen, it was removed before any further experiment with the material. Only homogeneous pellets were powdered for further structural or electrochemical characterisation.

The Fe granules used as oxygen getter should not be fully oxidised, showing that the oxygen content was low enough for a successful synthesis. Again, as for the parent material, normally the upper fraction of the iron granules lost its shiny metal aspect, while the lower fraction remained shiny.

Following this procedure a set of samples for the series $\text{Li}_{1-x}\text{Fe}_{1-x}\text{In}_x\text{PO}_4$ was synthesised. Apart from the large batches for neutron diffraction with $x = 0.04$ and 0.08 , 4 – 5 grams of each, also small scale samples were prepared for $x = 0.02, 0.06, 0.07, 0.09, 0.10$ and 0.15 , precursor for 0.5 – 0.75 grams of each sample. LaB_6 was used as internal standard in PXRD patterns collected up to high angles, $2\theta = 130^\circ$, on the laboratory diffractometer to obtain the lattice parameters of the olivine phase by using Rietveld fits to both phases. A Pawley fit to a high purity sample of $\text{Li}_{0.92}\text{Fe}_{0.92}\text{In}_{0.08}\text{PO}_4$ with added LaB_6 is shown in figure 4.4.

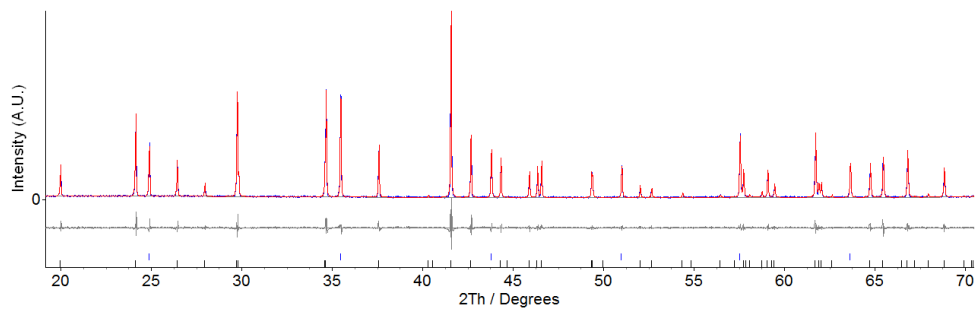


Figure 4.4. Co $K\alpha_1$ PXR D pattern of a high purity sample of nominal composition $\text{Li}_{0.92}\text{Fe}_{0.92}\text{In}_{0.08}\text{PO}_4$. Multiphase Pawley fit, red, to the data, blue. Background and difference are plotted in grey. Blue tick marks represent the internal standard LaB_6 and black tick marks represent the olivine phase.

The highest nominal doping level for which a sample can be made phase pure under these synthetic conditions is $x = 0.09$. A Pawley fit of a high purity sample of $\text{Li}_{0.91}\text{Fe}_{0.91}\text{In}_{0.09}\text{PO}_4$ is shown in figure 4.5. The resulting lattice parameters for the whole series are shown in figure 4.6. Samples with x in the range 0 to 0.09 follow Vegard's law. After $x = 0.09$ a plateau is reached along with the appearance of the impurity $\text{LiFeIn}(\text{PO}_4)_2$ which is described for first time in this thesis.

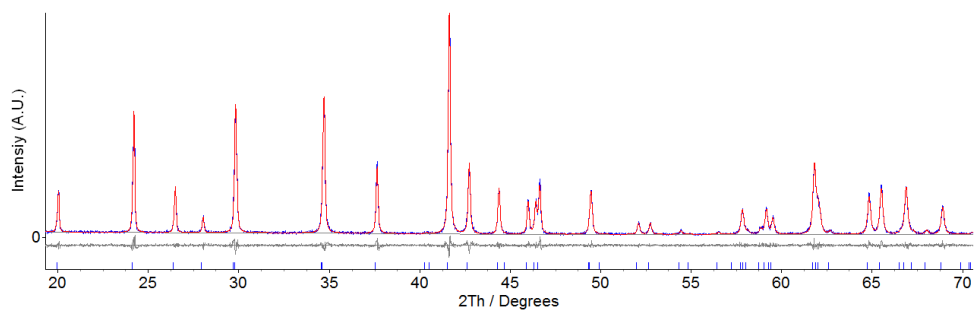


Figure 4.5. Co $K\alpha_1$ PXR D pattern of a high purity sample of nominal composition $\text{Li}_{0.91}\text{Fe}_{0.91}\text{In}_{0.09}\text{PO}_4$. Pawley fit, red, to the data, blue. Background and difference are plotted in grey. Blue tick marks represent the olivine phase.

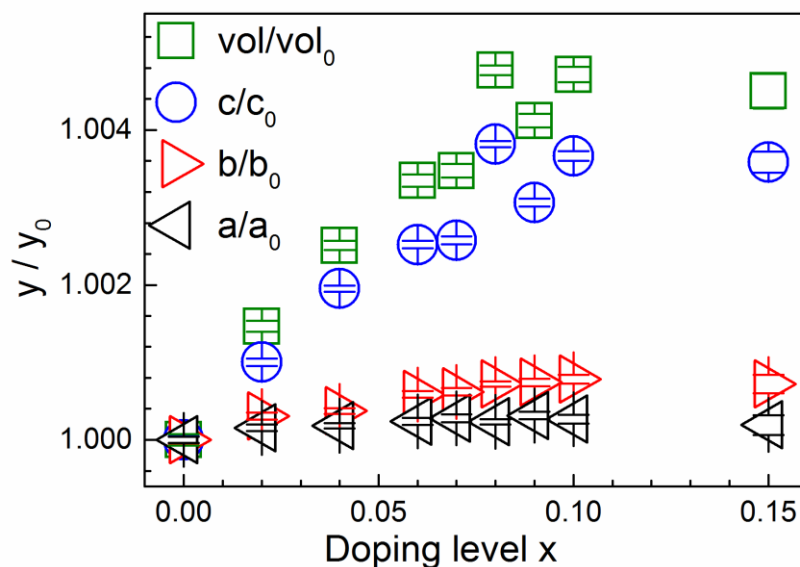


Figure 4.6. Relative cell parameters for the whole In-doped series, $\text{Li}_{1-x}\text{Fe}_{1-x}\text{In}_x\text{PO}_4$. Error bars shown as ± 3 e.s.d. This data was derived from fits to laboratory diffractometer data collected with Co $\text{K}\alpha_1$ radiation in Bragg-Brentano geometry up to high angles, $2\theta = 130^\circ$. The internal standard LaB_6 was used in this determination.

4.3.3 Diffraction and refinements

4.3.3.1 Ordered model at room temperature for $\text{Li}_{0.92}\text{Fe}_{0.92}\text{In}_{0.08}\text{PO}_4$

Laboratory PXRD was used again for optimising the synthesis procedure until high phase purity was achieved, which led to the search of the doping limit and the discovery of the new phase in the plateau after Vegard's law. Large scale samples, 4 – 5 grams each, of $\text{Li}_{1-x}\text{Fe}_{1-x}\text{In}_x\text{PO}_4$ for $x = 0.04$ and 0.08 were prepared. ICP-OES analysis, FTIR spectra and neutron and synchrotron diffraction data were collected on them. The powder diffractometers were GEM at ISIS Neutron Source and I11 at Diamond Light Source, both at Harwell campus, Oxford, UK.

For synchrotron X-ray diffraction at beam line I11, the two samples were loaded in borosilicate capillaries of 0.5 mm diameter. Absorption was evaluated as explained in the section for the parent material and was of $\mu\text{R} = 1.33$ when assuming a packing fraction of 0.6. For the sample with $x = 0.08$, the data were initially collected in

Debye-Scherrer geometry with the position sensitive detector, PSD, for 10 seconds. Finally with the MAC detectors 1 scan of 60 minutes was collected. The final MAC dataset used in the combined refinement presented here for the $x = 0.08$ sample was built by re-binning the original data, at 0.001° , to a step size of 0.005° .

For neutron diffraction data the samples were loaded in an 8 mm diameter vanadium can and placed in the GEM sample changer along with other samples. The data collection lasted in the order of 1-2 hours, until the beam current in μA integrated up to $240 \mu\text{Ahour}$. The final datasets were absorption corrected by using the software Mantid [15].

The combined refinement was made with the software Topas academic version 5 [16]. The Topas input file for the sample with $x = 0.08$ was setup by editing the one used in the parent material for the final ordered model with B_{iso} . The new filenames of the datasets were added, the λ wavelength for the MAC detectors was the same, and the GEM diffractometer constants were as well the same. The X-ray peak shape, initial cell parameters, axial divergence and zero error were preliminary refined in a Pawley fit over a restricted 2θ range. Pearson VII was the peak shape kept after comparison with Pseudo-Voigt, TCHZ and Stephens orthorhombic. The weighing method for X-rays was kept to $1/\sigma^2$. The refined crystal structure derived from that of Yakubovich et al. [17] was used as starting model for the Rietveld refinement. The initial B_{iso} were kept as the refined values for the parent sample. The scattering factors were kept as neutral for the same reason as before. The 2θ range is set to refine from 7° to the end of the histogram, i.e. 150° . The number of coefficients of the Chebyshev-type background were initially kept to 24 but finally increased to 36 in order to achieve a good fit.

Although in neutron data no impurities can be seen, in synchrotron data a set of very weak peaks can be observed. This impurity phase cannot be matched to any of the entries of the PDF2. After indexing, no sensible matches were found in the ICSD [19] for similar unit cell dimensions and related compositions. Finally the structure was solved, as explained later in this chapter, and resulted to be $\text{LiFeIn}(\text{PO}_4)_2$. This impurity phase is introduced as a second Rietveld phase.

The neutron histograms are refined from the beginning with initial settings from the parent material. The lowest angle GEM bank used is again number 3 due to the same reason as for the parent, i.e. being the higher one that includes the reflection

(200). The diffractometer constants difA and difC are refined for all banks from the best values for the parent material. The olivine model was modified to fit the nominal composition with indium on the Fe site and lower occupancy of Li in accordance with the vacancies on the Li site. X-ray absorption correction was updated for the nominal composition.

The doped structure is refined starting with the lattice parameters and following with the refinable atomic positions. All the individual B_{iso} for each atom of the asymmetric unit are refined at the same time. Then atomic positions are refined again with almost no change.

Now the anisotropic displacement parameters, ADPs, are refined and fixed. For the ADPs refinement the symmetry restriction that imposes $U_{12} = U_{23} = 0$ have been used for all atoms in 4c site, i.e. for Fe, In, P, O1 and O2. Finally the In occupancy is refined with the compositional constraint of $Li_{1-x}Fe_{1-x}In_xPO_4$, giving a refined $x = 0.066(2)$, 3 e.s.d., which is below the nominal composition, in agreement with the impurity found. If the In occupancy is refined with the B_{iso} fixed, the same constrained model yields a refined $x = 0.065(2)$, 3 e.s.d., again in agreement with the previous result. The impurity phase $LiFeIn(PO_4)_2$ represents a weight fraction of 1.05(7) % with error as 3 e.s.d.

The robustness of the fit is tested by refining simultaneously the occupancies of Li, Fe, In and P in the model with B_{iso} . The refinement yields an output of $Li_{0.942(10)}Fe_{0.947(5)}In_{0.052(3)}P_{0.974(3)}O_4$, with errors shown as 3 e.s.d., which approximately keeps the compositional restriction without imposing it, which is evidence of the quality of the refinement and the model. The elements for which the occupancy was freely refined, i.e. Li, Fe, In and P, have a good scattering contrast in both radiation beams as can be seen in table 4.1.

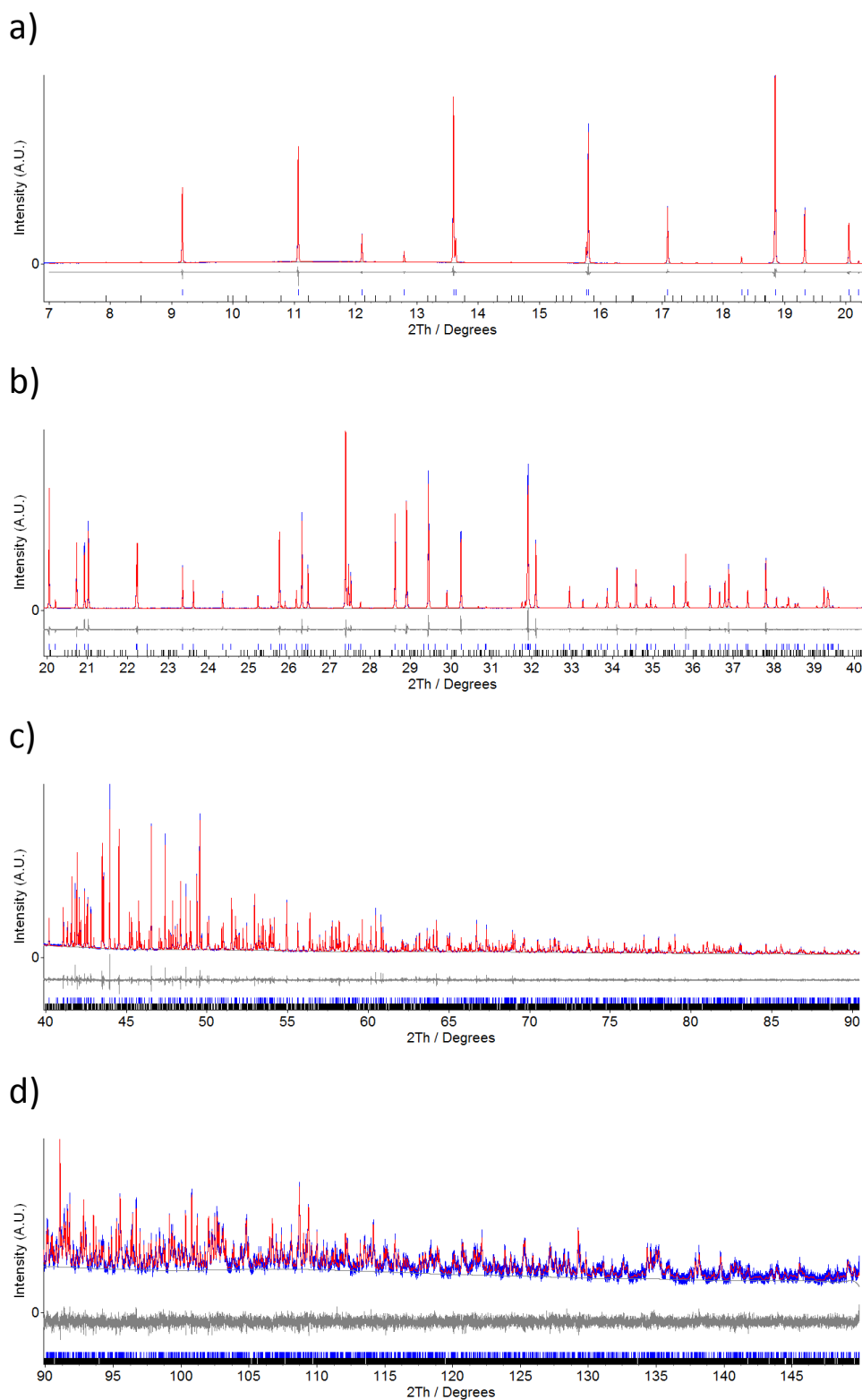
Finally, placing either In or Fe on the Li site in the latter refinement and starting with an occupancy of 0, the refinement yields only Li on the Li site with similar value as before within the errors, e.g. $[Li_{0.941(12)}Fe_{0.0003(13)}][Fe_{0.947(5)}In_{0.052(3)}]P_{0.974(3)}O_4$, error shown as 3 e.s.d.

In conclusion, the model can be considered stoichiometric and fully ordered with no anti-site defects. The graphical outputs of the refinement with ADPs are shown in figure 4.7 for every histogram. A projection of the resulting structural model

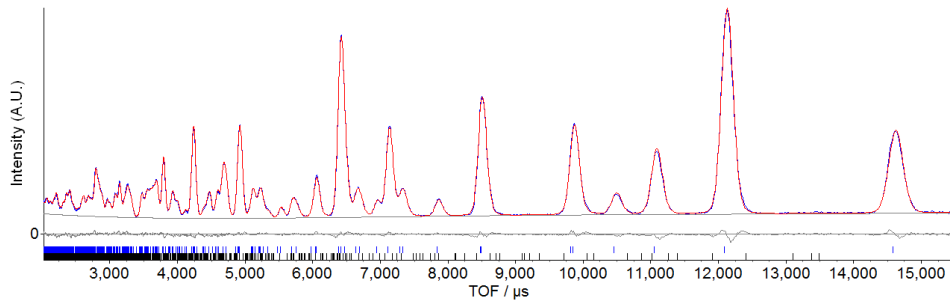
showing the atoms as 99 % of thermal displacement ellipsoids is shown in figure 4.8 for comparison with other samples of the series. The refined structural parameters and refinement factors are shown in table 4.2.

Table 4.1. Selected scattering constants for the elements in the samples. Only natural abundance Li was used for the samples of this chapter.

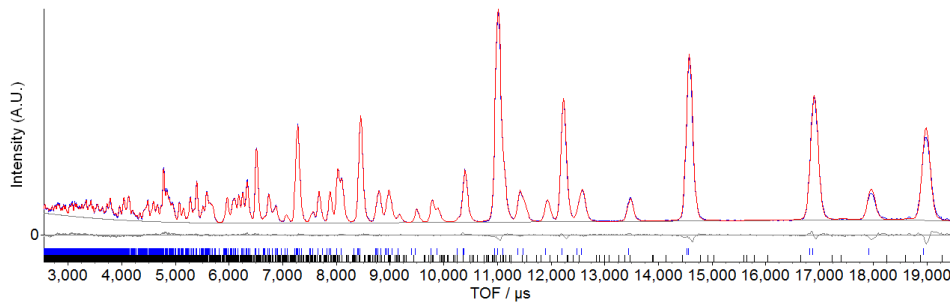
Element	Number of electrons	Neutron coherent scattering length / fm
Li	3	-1.90
Fe	26	9.45
In	49	4.065-0.0539i
P	15	5.13
O	8	5.803



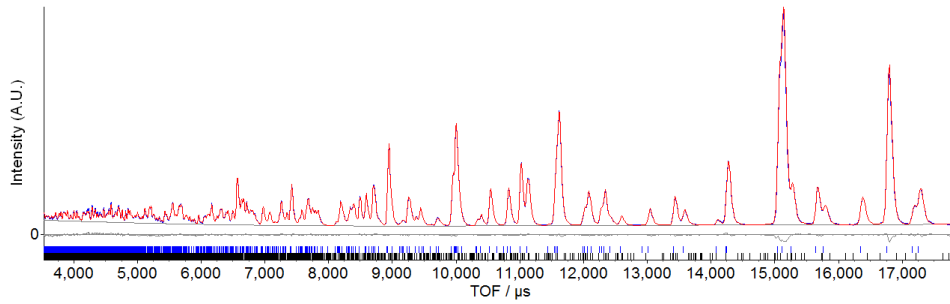
e)



f)



g)



h)

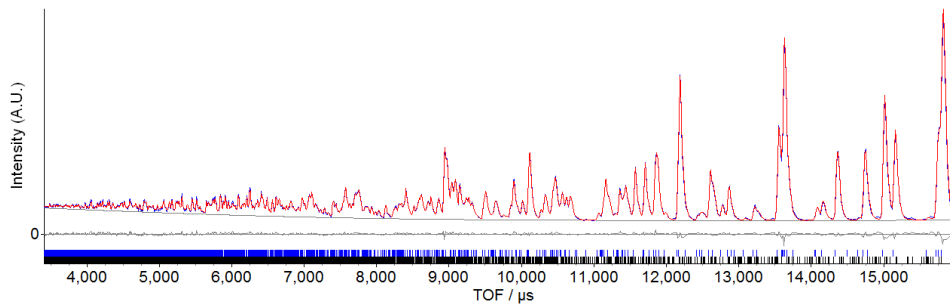


Figure 4.7. (Cont.) Histograms from GEM banks 3, 4, 5 and 6 are shown in panels e, f, g and h respectively. Data is in blue, model in red and difference and background in grey. Blue tick marks represent the olivine phase.

4.3.3.2 Ordered model at room temperature for $\text{Li}_{0.96}\text{Fe}_{0.96}\text{In}_{0.04}\text{PO}_4$

For the sample with $x = 0.04$ another combined refinement was performed. The procedure was similar to the previous one. The input file was setup by editing the one with nominal composition and B_{iso} used for $\text{Li}_{0.92}\text{Fe}_{0.92}\text{In}_{0.08}\text{PO}_4$. The new filenames of the datasets were added, the 111 wavelength for the PSD detector was input, and the GEM diffractometer constants were the same. The X-ray peak shape, initial cell parameters, axial divergence and zero error were preliminary refined in a Pawley fit over a restricted 2θ range. TCHZ was the peak shape kept after comparison with Pseudo-Voigt, Pearson VII and Stephens orthorhombic. The weighing method for X-rays was kept to $1/\sigma^2$. The refined crystal structure from the sample with $x = 0.8$ was used as starting model for the Rietveld refinement. The scattering factors were kept as neutral. The 2θ range is set to refine from 8° to the end of the histogram, i.e. 92° . The number of coefficients of the Chebyshev-type background were initially 18 and finally 24.

For the refinement of the neutron histograms, the lowest angle GEM bank used is again number 3. The diffractometer constants difA and difC are refined for all banks. The olivine model was modified to fit the new nominal composition of $x = 0.04$. X-ray absorption correction was updated for the new nominal composition.

This sample appears as fully phase pure in the synchrotron data. The nominal doped structure is refined starting with the lattice parameters and following with the refinable atomic positions. All the individual B_{iso} for each atom of the asymmetric unit are refined at the same time. Then atomic positions are refined again.

Now the anisotropic displacement parameters, ADPs, are refined and fixed. For the ADPs refinement the symmetry restriction that imposes $U_{12} = U_{23} = 0$ have been used for all atoms in 4c site, i.e. for Fe, In, P, O1 and O2. Finally the In occupancy is refined with the compositional constraint of $\text{Li}_{1-x}\text{Fe}_{1-x}\text{In}_x\text{PO}_4$, giving a refined $x = 0.031(2)$, error as 3 e.s.d., which is below the nominal composition. If the In occupancy is refined with the B_{iso} fixed, the same constrained model yields a refined $x = 0.031(2)$, which is again the same result. A projection of the resulting structural model showing the atoms as 99 % of thermal displacement ellipsoids is shown in

figure 4.8 for comparison with other samples of the series. The refined structural parameters and refinement factors are shown in table 4.2.

4.3.3.3 Variable temperature diffraction for $\text{Li}_{0.92}\text{Fe}_{0.92}\text{In}_{0.08}\text{PO}_4$

For the sample with $x = 0.08$ another combined refinement was made with data collected at 200 °C. The input file was setup by editing the one for the same sample at room temperature, therefore nominal composition and B_{iso} were initially set at the values for the refinement at room temperature. The new filenames of the datasets were added, the I11 wavelength for the MAC detector was the same, and the GEM diffractometer constants were also the same. The X-ray peak shape, initial cell parameters for main and impurity phase, axial divergence and zero error were preliminary refined in a Pawley fit over a restricted 2θ range. TCHZ was the peak shape kept after comparison with Pseudo-Voigt, Pearson VII and Stephens orthorhombic. The weighing method for X-rays was kept to $1/\sigma^2$. The refined crystal structure from the sample with $x = 0.8$ was used as starting model for the Rietveld refinement. The scattering factors were kept as neutral. The X-ray 2θ range was set to refine from 7 ° to the end of the histogram, i.e. 150 °. The number of coefficients of the Chebyshev-type background were kept to 36 in the same way as for the refinement at room temperature.

For the refinement of the neutron histograms, the lowest angle GEM bank used is again number 3. The diffractometer constants difA and difC are refined for all banks. X-ray absorption correction was kept the same.

The nominal doped structure is refined starting with the lattice parameters and following with the refinable atomic positions. All the individual B_{iso} for each atom of the asymmetric unit are refined at the same time. Then atomic positions are refined again. For the small impurity present in this sample, i.e. $\text{LiFeIn}(\text{PO}_4)_2$, only lattice parameters were refined.

The anisotropic displacement parameters, ADPs, are refined and fixed in the same way as in the previous refinements. Finally the In occupancy is refined with the compositional constraint of $\text{Li}_{1-x}\text{Fe}_{1-x}\text{In}_x\text{PO}_4$, giving a refined $x = 0.068(3)$, error as 3 e.s.d., which is below the nominal composition. A projection of the resulting

structural model showing the atoms as 99 % of thermal displacement ellipsoids is shown in figure 4.8 for comparison. The refined structural parameters and refinement factors are shown in table 4.2.

It is worth noting that the X-ray pattern shows an asymmetric broadening towards the shorter d-spacing side, i.e. towards higher 2θ angles, for a fraction of single reflections. This broadening is not seen at room temperature.

This subtle broadening is not axial divergence, which is a broadening towards the longer d-spacing side of the reflection. Very likely it is not an impurity either because there are no single extra reflections to fit. Some of the single reflections for which the broadening can be observed are (1 0 2), (2 0 2), (2 1 2), (0 2 2), (1 2 2) or (2 2 2). The splitting of some overlapping reflections indicates an anisotropic thermal expansion, e.g. at around $2\theta = 44.5^\circ$ the reflections (1 2 4) and (4 5 0) appear overlapped at room temperature, while they appear as two clearly separated reflections at 200 °C. But the anisotropic thermal expansion is easily modelled with lattice parameters refinement, therefore the broadening could be indicating e.g. a very subtle monoclinic or triclinic distortion happening to the orthorhombic cell with increasing temperature. Finally, similar type of broadening towards higher angles have been observed by Liu et al. [20] during in situ PXRD to LFP cells during cycling at high rates, therefore this effect could also be due to micro strain effects that appear with increasing temperature on this sample.

4.3.3.4 Refined occupancies at room temperature

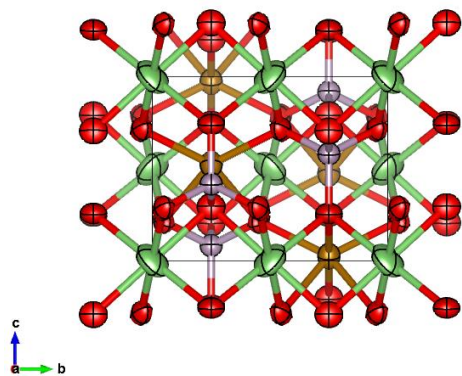
The resulting structural model for the series can be considered ordered with all indium on the iron site and all lithium and vacancies on the lithium site. On the other hand, the refined indium occupancies derived from the combined refinements for $\text{Li}_{0.96}\text{Fe}_{0.96}\text{In}_{0.04}\text{PO}_4$ and $\text{Li}_{0.92}\text{Fe}_{0.92}\text{In}_{0.08}\text{PO}_4$ are 0.031(2) and 0.066(2) respectively with errors as 3 e.s.d.

Both refinements under-estimate the indium content in about 20 %. For the sample $\text{Li}_{0.92}\text{Fe}_{0.92}\text{In}_{0.08}\text{PO}_4$ the impurity $\text{LiFeIn}(\text{PO}_4)_2$ has been observed and could explain a fraction of the missing indium. But for the case of $\text{Li}_{0.96}\text{Fe}_{0.96}\text{In}_{0.04}\text{PO}_4$ no impurities were found and the refinement still shows that it is deficient in indium. This indium deficiency is not supported by the chemical analysis by ICP-OES that will be shown later in table 4.5. Due to the high correlation of occupancy factors with several refined parameters, such as the atomic thermal displacement parameters or the background coefficients [21], the lower indium occupancy recovered with the refinements can be considered a common systematic error in this type of refinements.

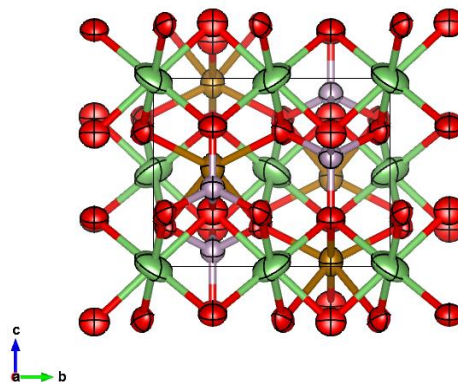
4.3.3.5 Graphic representation of the ADPs

The refined olivine structures derived from the combined refinements already discussed are plotted in figure 4.8 along their crystallographic a-axis. The atom sites are shown as 99 % thermal displacement ellipsoids. The ADPs of all the atom sites remain about the same with the expected enlargement associated with temperature. They also become larger for doped samples compared to the parent. The degree of anisotropy varies with doping. This discussion is supported by the data in table 4.2. The meaning of increased size or anisotropy for the ADPs is that the atoms stay less localised.

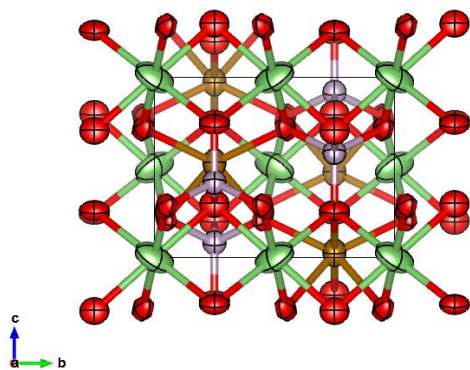
a) LiFePO_4 at room temperature.



b) $\text{Li}_{0.96}\text{Fe}_{0.96}\text{In}_{0.04}\text{PO}_4$ at room temperature.



c) $\text{Li}_{0.92}\text{Fe}_{0.92}\text{In}_{0.08}\text{PO}_4$ at room temperature.



d) $\text{Li}_{0.92}\text{Fe}_{0.92}\text{In}_{0.08}\text{PO}_4$ at 200 °C.

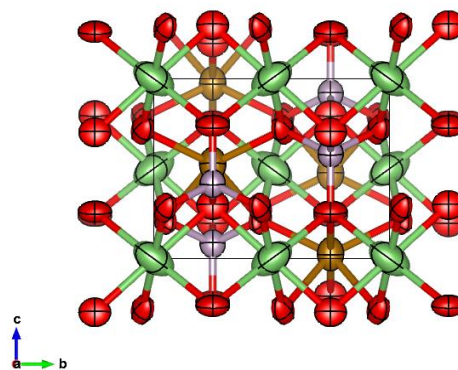


Figure 4.8. Structure models along the crystallographic a-axis representing the ADPs for each atom site. The atom site colours are green for Li, brown for Fe, purple for P and red for O. Sample composition and temperature are indicated in each panel.

4.3.3.6 Table of structural parameters for all combined refinements

This section shows the refinement fit factors and the refined structural parameters for all combined refinements presented during this chapter. The constraints used for this refinements are those imposed by the formula $[\text{Li}_{1-x}\square_x][\text{Fe}_{1-x}\text{In}_x]\text{PO}_4$ and are discussed in the corresponding sections. This information is displayed in table 4.2.

Table 4.2. Refined structural parameters for the samples with $x = 0, 0.04$ and 0.08 using the ordered model of the olivine. These are combined refinements against data collected with the diffractometers I11 at Diamond Light Source and GEM at ISIS neutron source. Error shown as 1 e.s.d.

Nominal composition:		LiFePO ₄	Li _{0.96} Fe _{0.96} In _{0.04} PO ₄	Li _{0.92} Fe _{0.92} In _{0.08} PO ₄	
Temperature		Room temperature			200 °C
I11 detector		MAC	PSD	MAC	MAC
R _{wp}		4.3978 %	3.3566 %	5.5912 %	7.7787 %
a / Å		10.328561(9)	10.330484(9)	10.330733(8)	10.349525(13)
b / Å		6.006963(5)	6.009270(5)	6.011202(4)	6.023311(7)
c / Å		4.690961(4)	4.700369(4)	4.709073(4)	4.722750(6)
Cell volume / Å ³		291.043(0)	291.793(0)	292.434(0)	294.409(1)
Site	Parameter				
Li 4a (0,0,0)	Occ. (Li)	1	0.9688(6)	0.9339(6)	0.9318(9)
	B(eq.)	1.41(3)	1.61(4)	1.47(4)	1.89(7)
	U11	0.0222(8)	0.0257(13)	0.0198(12)	0.029(2)
	U22	0.0149(8)	0.0212(12)	0.0203(11)	0.0243(19)
	U33	0.0165(8)	0.0141(12)	0.0155(12)	0.019(2)
	U12	-0.0021(6)	-0.0019(9)	-0.0049(8)	-0.0031(15)
	U13	-0.0057(8)	-0.0056(6)	-0.0021(12)	0.002(2)
	U23	-0.0060(7)	-0.0072(10)	-0.00696(10)	-0.0090(17)
Fe 4c (x,1/4, z)	Occ. (Fe)	1	0.9688(6)	0.9339(6)	0.9318(9)
	Occ. (In)	0	0.0312(6)	0.0660(6)	0.0682(9)
	x	0.28223(1)	0.28208(2)	0.28188(2)	0.28221(3)
	z	0.97467(3)	0.97427(4)	0.97384(4)	0.97416(6)
	B(eq.)	0.655(2)	0.742(3)	0.687(3)	0.952(5)
	U11	0.00858(5)	0.00952(8)	0.00834(7)	0.01116(12)
	U22	0.00679(5)	0.00774(8)	0.00693(6)	0.00973(11)
	U33	0.01004(6)	0.01175(9)	0.01160(8)	0.01676(14)
	U13	0.00058(5)	0.00039(8)	0.00021(7)	0.00039(12)

Table 4.2. (Cont.)

Nominal composition:		LiFePO ₄	Li _{0.96} Fe _{0.96} In _{0.04} PO ₄	Li _{0.92} Fe _{0.92} In _{0.08} PO ₄	
Temperature		Room temperature			200 °C
I11 detector		MAC	PSD	MAC	MAC
Site	Parameter				
P 4c (x,1/4,z)	Occ. (P)	1	1	1	1
	x	0.09497(2)	0.09490(3)	0.09485(3)	0.09517(5)
	z	0.41827(5)	0.41771(7)	0.41707(7)	0.41743(10)
	B(eq.)	0.553(3)	0.690(6)	0.616(5)	0.775(8)
	U11	0.00742(10)	0.00916(17)	0.00744(15)	0.0088(2)
	U22	0.00672(9)	0.00800(16)	0.00718(14)	0.0090(2)
	U33	0.00698(10)	0.00904(18)	0.00871(16)	0.0114(3)
	U13	-0.00005(7)	0.00009(13)	-0.00040(12)	0.00030(19)
O1 4c (x,1/4,z)	Occ. (O1)	1	1	1	1
	x	0.09661(5)	0.09760(7)	0.09850(7)	0.09937(10)
	z	0.74274(11)	0.74202(15)	0.73991(14)	0.7386(2)
	B(eq.)	0.686(8)	0.759(13)	0.740(11)	0.904(18)
	U11	0.0109(3)	0.0114(4)	0.0108(3)	0.0136(6)
	U22	0.0099(2)	0.0110(4)	0.0121(3)	0.0159(6)
	U33	0.0059(2)	0.0077(4)	0.0062(3)	0.0071(6)
	U13	-0.0006(2)	-0.0015(3)	-0.0011(3)	-0.0012(5)
O2 4c (x,1/4,z)	Occ. (O2)	1	1	1	1
	x	0.45679(5)	0.45669(7)	0.45673(6)	0.45765(10)
	z	0.20610(10)	0.20418(14)	0.20309(14)	0.2021(2)
	B(eq.)	0.658(8)	0.727(13)	0.696(11)	0.822(19)
	U11	0.0046(2)	0.0044(4)	0.0045(3)	0.0044(5)
	U22	0.0108(2)	0.0127(4)	0.0113(3)	0.0141(6)
	U33	0.0094(3)	0.0106(4)	0.0104(4)	0.0122(6)
	U13	0.0005(2)	0.0014(3)	0.0007(2)	0.0011(4)
O3 8d (x,y,z)	Occ. (O3)	1	1	1	1
	x	0.16551(4)	0.16574(5)	0.16578(5)	0.16574(8)
	y	0.04698(6)	0.04716(8)	0.04753(8)	0.04782(12)
	z	0.28455(7)	0.28377(10)	0.28287(9)	0.28304(14)
	B(eq.)	0.693(6)	0.739(9)	0.700(7)	0.873(13)
	U11	0.0110(2)	0.0114(3)	0.0109(2)	0.0132(4)
	U22	0.0070(2)	0.0078(3)	0.0065(2)	0.0080(3)
	U33	0.0084(2)	0.0089(3)	0.0092(3)	0.0128(4)
	U12	0.00271(14)	0.0032(2)	0.00297(18)	0.0040(3)
	U13	0.00191(14)	0.0019(2)	0.00220(19)	0.0040(3)
U23	0.00078(12)	0.0008(2)	0.00106(17)	0.0013(3)	

4.3.3.7 Structure solution of $\text{LiFeIn}(\text{PO}_4)_2$ and $\text{LiMgIn}(\text{PO}_4)_2$

For samples of the system $\text{Li}_{1-x}\text{Fe}_{1-x}\text{In}_x\text{PO}_4$ with nominal In content beyond the doping limit, i.e. above $x = 0.09$, a new phase appears. This phase is also formed if within the doping limit the synthetic temperature is not reached as shown at the beginning of the doping section of this chapter. This impurity did not match any pattern in the powder diffraction file version 2, i.e. PDF2 database. There were also no matching patterns in the inorganic crystal structure database, i.e. ICSD [19], for the relevant combination of cell parameters and atoms.

The best pattern on this phase was extracted from powder diffraction data on a polyphasic sample of $\text{Li}_{1-x}\text{Fe}_{1-x}\text{In}_x\text{PO}_4$ with $x = 0.15$ collected with synchrotron radiation, $\lambda = 0.825959(1) \text{ \AA}$, at beamline I11 with the position sensitive detector, i.e. PSD. The isolated pattern of this new phase, as extracted after removing the olivine phase, is shown in figure 4.9.

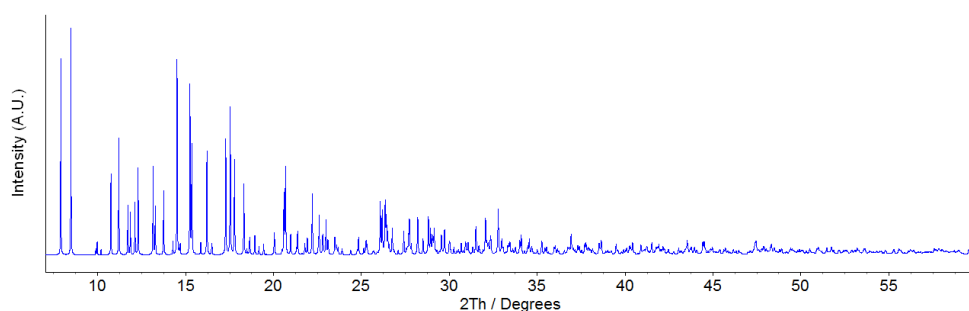


Figure 4.9. Isolated powder diffraction pattern of the new phase extracted from the powder pattern of a multiphasic sample of composition $\text{Li}_{0.85}\text{Fe}_{0.85}\text{In}_{0.15}\text{PO}_4$ after removing the olivine phase by difference.

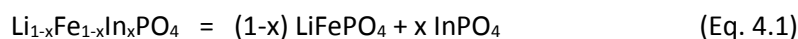
This diffraction pattern isolation was possible after indexing of the impurity peaks. It was recognised from the beginning that the unit cell that was similar to the one found in the system $\text{Li}_{1-x}\text{Mg}_{1-x}\text{In}_x\text{PO}_4$ beyond the doping limit (see Chapter 3). The pattern was indexed by using TREOR90 [22] to an orthorhombic cell. The refined cell parameters for the cells in both systems are shown in table 4.3.

Table 4.3. Refined unit cell parameters of the orthorhombic impurity indexed for the systems $\text{Li}_{1-x}\text{Mg}_{1-x}\text{In}_x\text{PO}_4$ and $\text{Li}_{1-x}\text{Fe}_{1-x}\text{In}_x\text{PO}_4$. Errors shown as 3 e.s.d.

System	a / Å	b / Å	c / Å	Volume / Å ³
Mg	13.746(3)	9.412(2)	9.260(2)	1198.0(4)
Fe	13.77776(14)	9.48761(8)	9.28519(9)	1213.74(2)

Having similar unit cell and similar relative intensities means that they are very likely isostructural. This will support assumptions to decide the cell content during the structural solution.

Both systems are the product of solid solution between two different phosphates, e.g. see equation 4.1 for the Fe system.



Only two phases are visible for compositions in the plateau, one being the olivine and another one being the indexed one. If the indexed one is not one of the known InPO_4 polymorphs, very likely contains an integer number of formula units of LiFePO_4 with it, being one unit the simplest answer. This aims to $\text{LiFeIn}(\text{PO}_4)_2$ as the main potential candidate.

On the other hand, to estimate the number of formula units per unit cell the LiFePO_4 cell volume can be used, which is about 300 \AA^3 with 4 formula units, i.e. 75 \AA^3 per formula unit. The potential candidate $\text{LiFeIn}(\text{PO}_4)_2$ should have about double the volume per formula unit, i.e. 150 \AA^3 . Dividing the volume of the indexed cell by that number we get $Z = 8$, which leads to a cell content of $\text{Li}_8\text{Fe}_8\text{In}_8\text{P}_{16}\text{O}_{64}$.

By using the software Expo 2014 [23], the diffraction pattern shown in figure 4.9 is loaded and the cell content is indicated without lithium. After the initial steps of adjusting single peak and background ranges, the indexed cell is subject to systematic absences scrutiny and the space group $Pcab$ (#61 setting 2) is selected. The solution offered after running the algorithm for direct methods yielded a structure that was initially refined within Expo 2014. The polyhedra connectivity

was already clear at this stage. The algorithm located an extra oxygen atom in an octahedral void as well.

The starting model is then input in Topas academic version 5 [16] for a Rietveld refinement. The extra oxygen is substituted by Li. All atoms of the asymmetric unit are in general positions 8c. All the occupancies are kept fixed to 1. After several cycles of refining in turn atomic positions and B_{iso} , the refinement is concluded. The resulting structure provides a good fit as can be seen in figure 4.10. The refined structural parameters are listed in table 4.4.

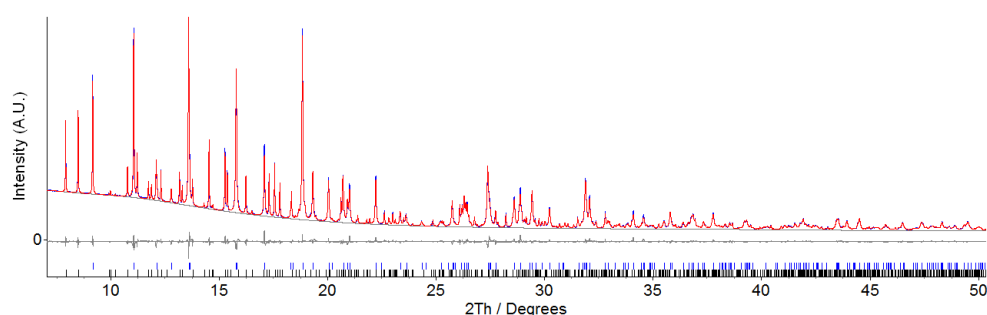


Figure 4.10. Synchrotron PXRD pattern of a sample of nominal composition $\text{Li}_{0.85}\text{Fe}_{0.85}\text{In}_{0.15}\text{PO}_4$. Multiphase Rietveld fit, red, to the data, blue. Background and difference are plotted in grey. Blue tick marks represent the olivine phase and black tick marks represent the new phase $\text{LiFeIn}(\text{PO}_4)_2$.

The structure was processed with the FINDSYM code [24] through the web-app in the ISOTROPY Software Suite web site [25]. No higher symmetry was found for this structure and the space group remained $Pcab$.

To figure out if this belongs to a new structure type, the search was done using the ICSD [19]. This is a structure $\text{ABC}(\text{XO}_4)_2$ which can be searched as $\text{BC}(\text{XO}_4)_2$ if the alkali ion is left out or as $\text{B}_2(\text{XO}_4)_2$ if both metal sites would have the same metal. Half volume is not possible, but double volume would be. There are no records of formula $\text{ABC}(\text{XO}_4)_2$ with volumes between 1080 and 1320 \AA^3 . There are some with formula $\text{BC}(\text{XO}_4)_2$ for the same volume ranges, but none of them have similar motifs or polyhedral connectivity. There are no records of formula $\text{B}_2(\text{XO}_4)_2$ for the same

volume ranges. Finally there are several structures of formula $AB_2(XO_4)_2$ for the same volume ranges with $Li_2NiS_2O_8$, described in 2001 and solved from single crystal data, being isostructural [26].

In addition to $Li_2NiS_2O_8$, other compositions have been described with the same structure type, e.g. $Li_2CoS_2O_8$ and $Li_2FeS_2O_8$ [27]. All these have been described in the setting 1 of space group #61, i.e. $Pbca$. While $Li_2FeS_2O_8$ has been probed as cathode material [27], $Li_2NiS_2O_8$ has been probed as potential magnetoelectric material [28].

Although these two new phases discovered during this thesis, $LiFeIn(PO_4)_2$ and $LiMgIn(PO_4)_2$, are not a new structure type, could be the first examples of phosphates exhibiting this structure type that are being described. These two and potential derivatives with introduced defects could be probed as new materials, at least for battery and magnetoelectric applications.

Table 4.4. Refined structural parameters of $LiFeIn(PO_4)_2$ derived from Rietveld refinement. Space group $Pcab$, #61 setting2. Cell dimensions were $a = 9.48761 \text{ \AA}$, $b = 13.77776 \text{ \AA}$ and $c = 9.28519 \text{ \AA}$ with volume = 1213.74 \AA^3 .

Wyckoff position	Atom label	x	y	z	Occ.	Biso
8c	Li1	0.21219	0.36822	0.03078	1.000	0.500
8c	In1	-0.14228	0.37735	0.40024	1.000	0.137
8c	Fe1	0.03441	0.37784	0.77864	1.000	0.606
8c	P1	-0.16544	0.51201	0.68423	1.000	0.120
8c	P2	0.07395	0.22763	0.56863	1.000	0.211
8c	O1	0.02049	0.34801	0.99634	1.000	0.200
8c	O2	-0.00584	0.52293	0.70349	1.000	0.200
8c	O3	0.22913	0.22136	0.50363	1.000	0.430
8c	O4	0.24664	0.39595	0.25023	1.000	0.700
8c	O5	0.02478	0.32370	0.53792	1.000	0.290
8c	O6	0.07201	0.22369	0.73481	1.000	0.200
8c	O7	-0.21341	0.50766	0.52803	1.000	0.700
8c	O8	-0.30924	0.41925	0.26696	1.000	0.700

The structure of $\text{LiFeIn}(\text{PO}_4)_2$ is plotted in figure 4.11 showing the typical polyhedral coordination found in this structure type.

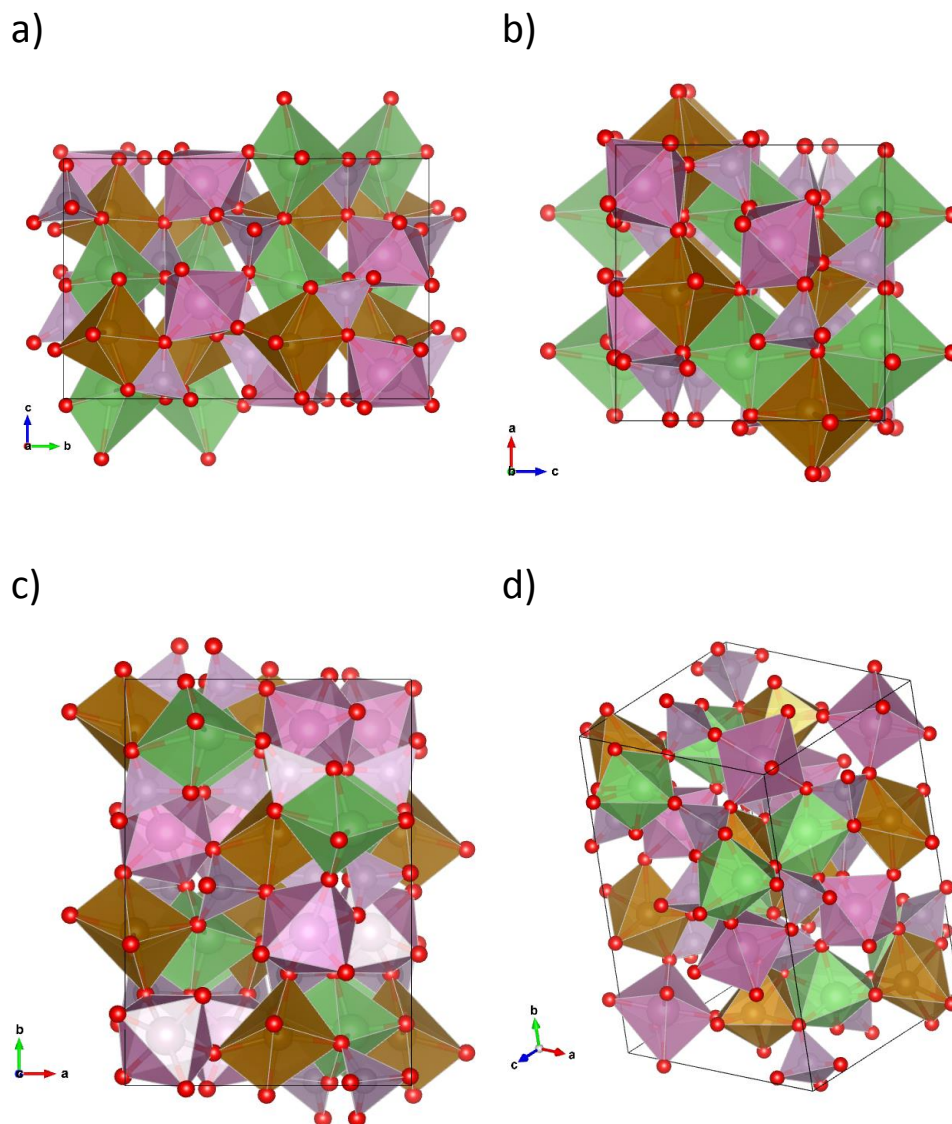


Figure 4.11. Structure of the novel phase $\text{LiFeIn}(\text{PO}_4)_2$ with the $\text{Li}_2\text{Ni}(\text{SO}_4)_2$ structure type. Panels a), b) and c) show the projection along a, b and c axes respectively. Panel d) shows a tilted version of the structure. Li, Fe, In, P and O atoms are shown in green, brown, pink octahedra, purple tetrahedra and red respectively.

The Mg analogue, i.e. $\text{LiMgIn}(\text{PO}_4)_2$, is isostructural to $\text{LiFeIn}(\text{PO}_4)_2$, and thus the Rietveld refinement of the sample of nominal composition $\text{Li}_{0.79}\text{Mg}_{0.79}\text{In}_{0.21}\text{PO}_4$ was

made by using the same model solved above just changing Fe for Mg. The small mismatch disappeared after the refinement of the atomic positions. The refinement can be seen in figure 4.12 and the refined structure, almost identical to the Fe analogue, can be seen in figure 4.13.

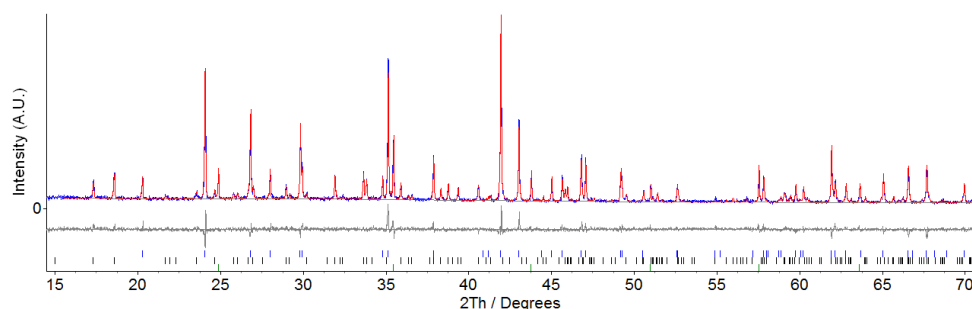


Figure 4.12. Co $K\alpha_1$ PXRD pattern of a sample of nominal composition $\text{Li}_{0.79}\text{Mg}_{0.79}\text{In}_{0.21}\text{PO}_4$. Multiphase mixed Rietveld/Pawley fit, red, to the data, blue. Background and difference are plotted in grey. Blue tick marks represent the olivine phase and black tick marks represent the new phase $\text{LiMgIn}(\text{PO}_4)_2$, both from Rietveld models. Green tick marks represent the internal standard LaB_6 , from Pawley model.

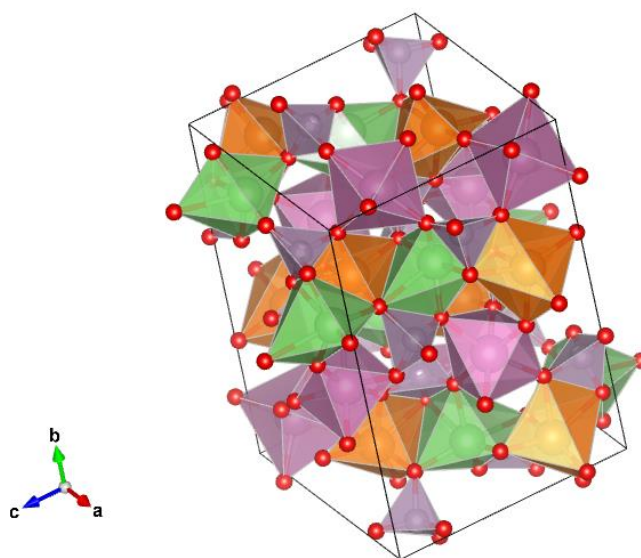


Figure 4.13. Structural model of the novel phase $\text{LiMgIn}(\text{PO}_4)_2$ with the $\text{Li}_2\text{Ni}(\text{SO}_4)_2$ structure type. Li, Mg, In, P and O atoms are shown in green, orange, pink octahedra, purple tetrahedra and red respectively.

4.4 ICP-OES

In order to confirm experimentally the nominal compositions, ICP-OES analysis was performed. The samples were digested in stirring hot concentrated nitric acid, 70 % analytical grade, and submitted for analysis. After normalising the results to phosphorous and propagating the experimental errors, the analysis match nominal compositions within 3 s.d. for all the samples, as can be seen in table 4.5.

Table 4.5. The chemical composition of three samples determined by ICP-OES and TEM-EDX. The uncertainty is shown as 3 standard deviations. Results have been normalised to phosphorous. Blank sample gave readings about zero for P, Fe, Li and In.

Nominal composition	P	Fe	Li	In
LiFePO_4	1.00(3)	0.98(4)	0.96(3)	0
$\text{Li}_{0.96}\text{Fe}_{0.96}\text{In}_{0.04}\text{PO}_4$	1.00(6)	1.00(7)	0.99(6)	0.040(3)
$\text{Li}_{0.92}\text{Fe}_{0.92}\text{In}_{0.08}\text{PO}_4$	1.00(3)	0.92(4)	0.89(3)	0.079(2)

4.5 FTIR-ATR

In order to confirm experimentally that all Li_2CO_3 present in the reaction mixture reacted, FTIR-ATR spectra were collected for the same three samples for which the chemical analysis was performed. The spectrum of Li_2CO_3 was also recorded for comparison. The sharp band of Li_2CO_3 at about 850 cm^{-1} is not present in the spectra of any of the samples, as can be seen in figure 4.14, meaning that the samples are free of it.

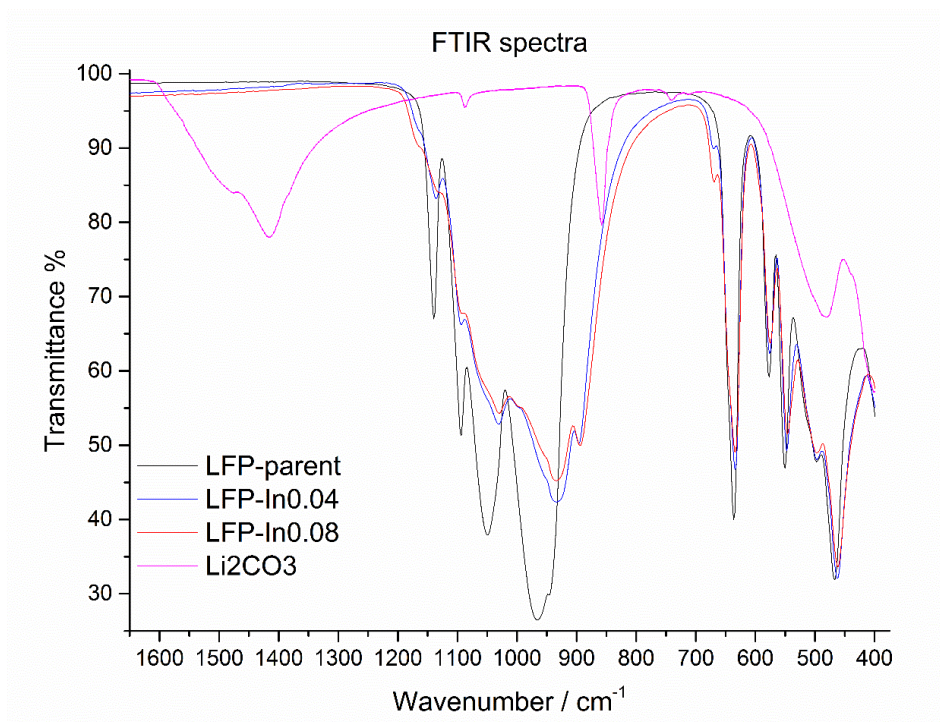


Figure 4.14. FTIR-ATR spectra of Li₂CO₃ and three samples of the series Li_{1-x}Fe_{1-x}In_xPO₄ for x = 0, 0.04 and 0.08.

4.6 Cathode testing

The ionic conductivities of these samples were not studied because it was more urgent to see their properties as cathodes compared to the parent material and therefore cathode testing was performed instead.

In order to test the cathode performance of the new materials, button cell type batteries were prepared and tested by Dr Nicholas Drewett within the Professor Laurence Hardwick group. The plots shown in this section are presented with permission from Professor Hardwick and Dr Drewett.

Materials from the series Li_{1-x}Fe_{1-x}In_xPO₄ were used to prepare the cathode of the battery. These tests were made with the original ceramic, as synthesised and without processing, for the compositions LiFePO₄ and Li_{0.96}Fe_{0.96}In_{0.04}PO₄.

The cells were prepared as follows by Dr Nicholas Drewett: the $\text{Li}_{1-x}\text{Fe}_{1-x}\text{In}_x\text{PO}_4$ active material, Super C carbon and Kynarfex binder were mixed in tetrahydrofuran, THF, in a 75:15:10 % by weight ratio, stirred and sonicated to form a slurry. This was cast on an appropriate current collector made of aluminium and dried. Electrodes were then punched out and dried overnight. Coin cells were assembled from CR2025 coin cell parts, the prepared electrodes, a glass fibre separator (Whatman) impregnated with LP30 electrolyte and a lithium (Li) metal counter electrode. In all cases, cells were sealed in a glove box under air and moisture free conditions ($\text{O}_2 < 0.1 \text{ ppm}$; $\text{H}_2\text{O} < 0.1 \text{ ppm}$). The electrochemical measurements were performed at 30°C using a Maccor Series 4000 battery cycler.

The first test was performed on the parent material. A cycling performance test was run at a rate of 0.5 C, i.e. at a charge/discharge rate that allows the theoretical capacity to be extracted/inserted in 2 hours. The output of this experiment is plotted in figure 4.15 that shows an initial capacity fading during the first few cycles and a normal capacity retention afterwards. Also the coulombic efficiency improves with cycling, i.e. the ratio between the discharge and charge capacities.

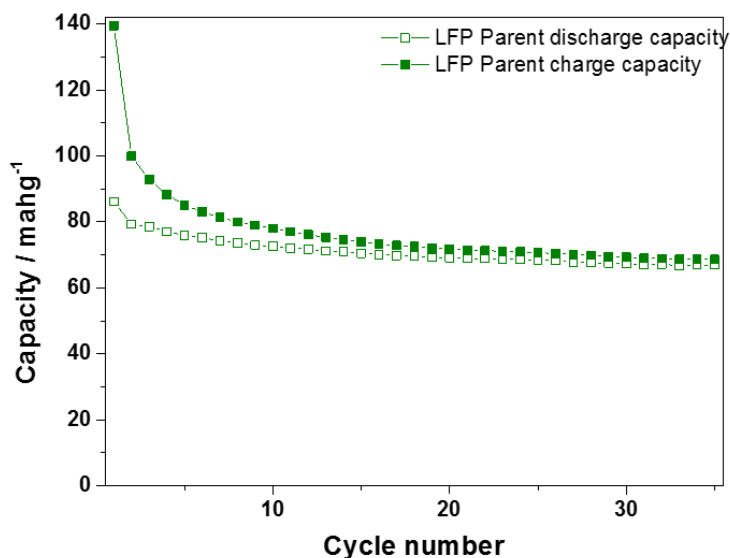


Figure 4.15. Cycling performance at 0.5 C rate, 75 mA/g, between 2.8 and 4.0 V for LiFePO_4 . Plot provided by Dr Nicholas Drewett.

The data of the charge and discharge curves during the cycling performance are shown in figure 4.16 for cycles 1 and 10. The capacity fading is observed from the first to the 10th cycle. The other feature that is worth mentioning is that the charge/discharge plateau is not as flat as in processed materials, e.g. when carbon coating is used, which is expected and has been shown previously in literature [29].

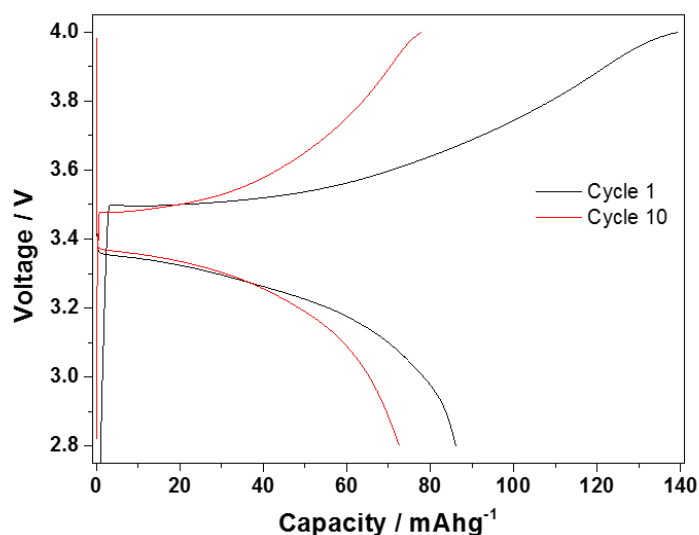


Figure 4.16. Charge and discharge curves of the LiFePO_4 cell for the first cycle, black, and for the 10th cycle, red. Plot provided by Dr Nicholas Drewett.

The second test was a comparison between the samples LiFePO_4 and $\text{Li}_{0.96}\text{Fe}_{0.96}\text{In}_{0.04}\text{PO}_4$. With this aim, an experiment that sequentially increased the C rate every 10 cycles to finally go back to a lower C rate was performed. From the output of this experiment a typical waterfall-type plot was produced which is shown in figure 4.17. For this experiment the cycling window was extended from 2.8-4.0V to 2.5-4.2V in order to cycle more capacity of the cathode.

The waterfall-type plot shows the typical loss of capacity with increasing C rates due to internal losses of the cell, e.g. the internal resistance, and finally the recovery of the capacity once the C rate is lowered again. This plot shows as well that the capacity of $\text{Li}_{0.96}\text{Fe}_{0.96}\text{In}_{0.04}\text{PO}_4$ is about 6 times lower than the capacity for the parent material LiFePO_4 .

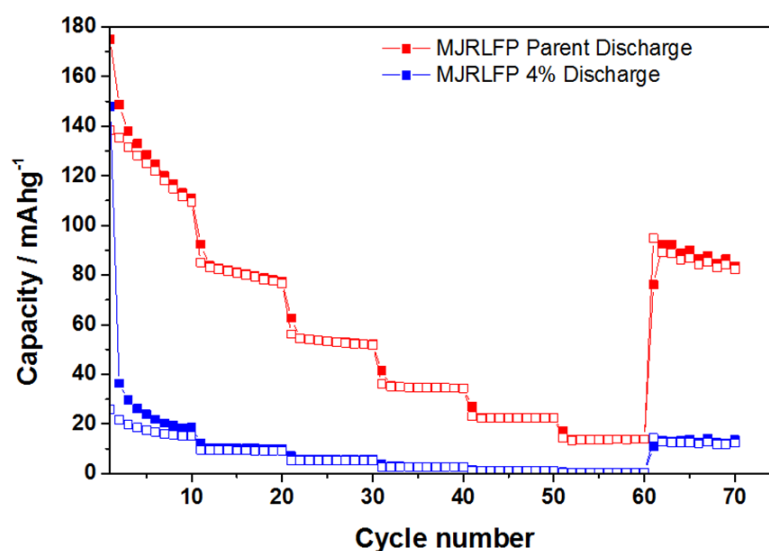


Figure 4.17. Waterfall type plot at different C rates, between 2.5 and 4.2 V for LiFePO_4 and $\text{Li}_{0.96}\text{Fe}_{0.96}\text{In}_{0.04}\text{PO}_4$. Plot provided by Dr Nicholas Drewett.

The In-doped material was expected to have 4 % lower capacity than the parent material due to the lower Li content per formula unit. However looking at the initial charge in figure 4.18, the charging voltage for the In-doped material is higher (~4 V) and has a flatter plateau, the latter indicating easier extraction of the Li-ions during the first charge compared to the parent. It should also have a higher discharge voltage, but the initial charge voltage and initial capacity are not recovered. Further cycling does not improve this as can be seen in figure 4.19 for cycle 2.

In order to clarify what was happening, an experiment for ex-situ examination of the used cathodes was designed. The ex-situ structural characterisation of reclaimed LiFePO_4 cathodes was attempted first. For two cells that were fully charged/discharged and fully charged respectively, the cathode was recovered on its aluminium current collector. X-ray diffraction of the fully charged/discharged cathode showed aluminium and LiFePO_4 as expected. X-ray diffraction of the fully charged cathode showed majorly aluminium and LiFePO_4 but almost no FePO_4 , when it should have shown only aluminium and FePO_4 . The lattice parameters of LiFePO_4 in both cathodes was the same within errors. Because the experiment did not work as expected for the parent material, it was not performed on the doped sample. The suggested method for future characterisation is the in-situ technique used e.g. by Liu et al. [20].

The initial easier extraction of the Li-ions in the battery made with $\text{Li}_{0.96}\text{Fe}_{0.96}\text{In}_{0.04}\text{PO}_4$ agrees with the structural analysis that shows an enlarging unit cell for increased doping levels. This leads to enlarged bottlenecks in the diffusion channels in addition to the Li vacancies. Therefore the doped material should have a better Li-ion mobility, which should improve charge and discharge rates. All this rests in alignment with the results for the Mg analogue presented in chapter 3.

The reason of why a large fraction of the capacity vanishes after the first charge remains unclear and more research would be needed to establish this. One of the reasons could be the lack of processing of the material, because it was used as produced for making the test cells. Literature usually shows the strong correlation between the processing of the parent material and the electrochemical performance, e.g. as shown by Chen et al. [29]. An in-situ X-ray diffraction experiment would help to clarify this as suggested above.

In conclusion, this experiment has shown that when both materials, LiFePO_4 and $\text{Li}_{0.96}\text{Fe}_{0.96}\text{In}_{0.04}\text{PO}_4$, are tested as cathode, the parent behaves as expected for a non-processed sample while the doped one exhibits much lower capacity in spite of showing a promising first charge.

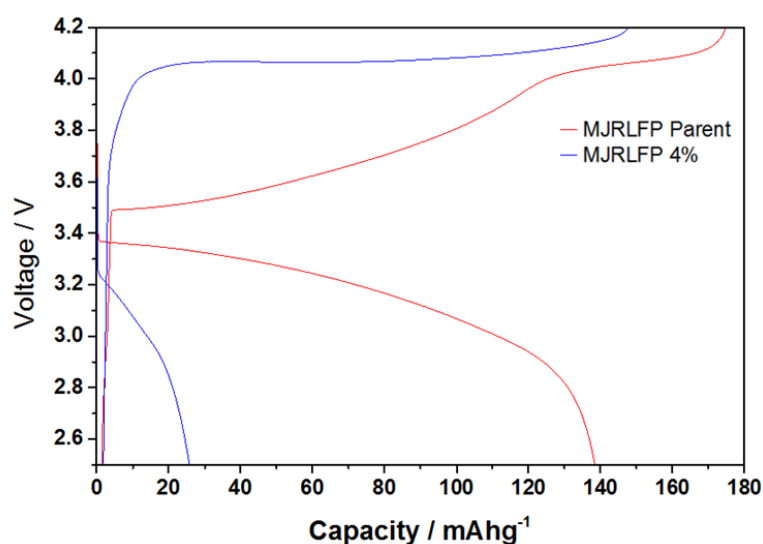


Figure 4.18. Charge and discharge curves for the first cycle between 2.5 and 4.2 V of cells made with the cathode materials LiFePO_4 , in red, and $\text{Li}_{0.96}\text{Fe}_{0.96}\text{In}_{0.04}\text{PO}_4$, in blue. Plot provided by Dr Nicholas Drewett.

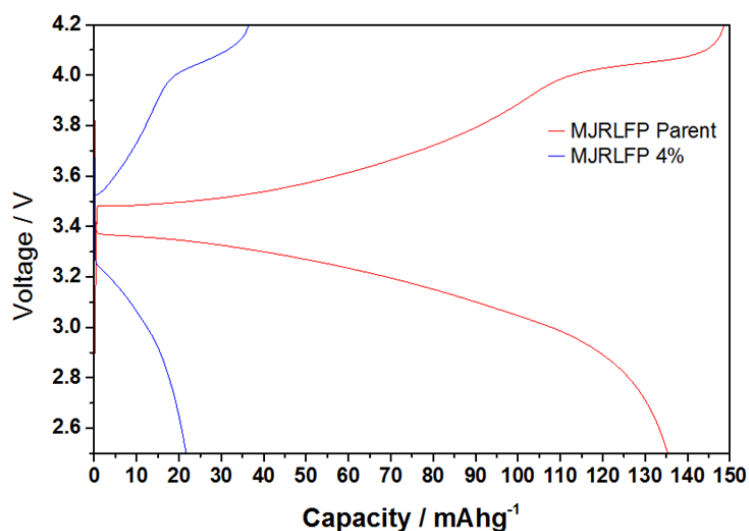


Figure 4.19. Charge and discharge curves for the second cycle between 2.5 and 4.2 V of cells made with the cathode materials LiFePO_4 , in red, and $\text{Li}_{0.96}\text{Fe}_{0.96}\text{In}_{0.04}\text{PO}_4$, in blue. Plot provided by Dr Nicholas Drewett.

4.7 Summary, conclusions and future work

The aim of the work presented in this chapter is to produce indium doped samples of LiFePO_4 with In on the Mg site and vacancies on the Li site to enhance the Li-ion mobility. Some of the limitations of the increasingly important cathode material LiFePO_4 are their low ionic and electronic conductivities. So far this has been addressed by production of carbon coatings, composites or particles of reduced size. The successful vacancy introduction in the Mg analogue during the previous chapter presented this work on LiFePO_4 as a *must do* in order to try to improve the ionic conductivity and therefore lead to the reduction of the processing cost in cathode production with this type of materials. This substitution could lead to a material with high commercial impact if the ionic conductivity is increased in the same ratio as for the Mg analogue.

Initial synthesis revealed the sensitivity of this system to traces of oxygen in the inert gas flow. This was addressed by using iron granules upstream functioning as oxygen getter. Optimisation of the synthesis temperature and profile was needed for the successful synthesis of the doped samples. The need of higher temperature

for getting single phase samples of the doped materials compared to the parent, experimentally reveal the role of the mixing entropy again in this system, in the same way as for the Mg analogue. The extra phase that appears beyond the doping limit of the system is the same that appears when the synthetic temperature is not reached. This phase is isostructural to the one that appeared in the Mg analogue under the same approach and has finally been solved in this chapter. This has led to the discovery of two new phases, $\text{LiFeIn}(\text{PO}_4)_2$ and $\text{LiMgIn}(\text{PO}_4)_2$. Finally two of the phase pure compositions have been probed as cathodes. The materials described in this chapter have been synthesised under flow of argon, with iron granules getter and in the range of temperatures from 600 °C to 850 °C.

The highest nominal doping level achieved in the series $\text{Li}_{1-x}\text{Fe}_{1-x}\text{In}_x\text{PO}_4$ was $x = 0.09$. Chemical compositions of several samples of the series were confirmed by ICP-OES. Combined Rietveld refinements on high resolution X-ray powder diffraction and neutron powder diffraction validated the substitutional pattern and the vacancy introduction. Cathode testing was performed on the samples of composition LiFePO_4 and $\text{Li}_{0.96}\text{Fe}_{0.96}\text{In}_{0.04}\text{PO}_4$. The test showed that the parent material behaves in the same way as it is described in literature for non-processed samples. On the other hand, the doped sample showed an improved first charge in accordance with the pursued higher ionic conductivity. After that, the initial capacity was never recovered. The stabilised capacity in the doped material is several times lower than for the parent, and so is the power density.

The two new phases discovered in this chapter, $\text{LiFeIn}(\text{PO}_4)_2$ and $\text{LiMgIn}(\text{PO}_4)_2$, are not a new structure type, but could be the first examples of phosphates within this structure type. The structure type was described in 2001 from single crystal data of $\text{Li}_2\text{NiS}_2\text{O}_8$. Since then other isostructural sulphates have been synthesised such as $\text{Li}_2\text{CoS}_2\text{O}_8$ and $\text{Li}_2\text{FeS}_2\text{O}_8$. The materials $\text{Li}_2\text{FeS}_2\text{O}_8$ and $\text{Li}_2\text{NiS}_2\text{O}_8$ have already been probed as cathode material and as potential magnetoelectric material respectively. The two new phases presented in this chapter and their potential derivatives offer ample opportunity for further development and discovery. Their properties could be studied to assess their suitability e.g. for battery or magnetoelectric applications.

In conclusion, synthetic work has shown that the In-doped LiFePO_4 can be made by following similar strategies as for the Mg analogue. The mixing entropy has experimentally appeared again in this system in the same way as in chapter 3. The

In-doped material has shown an initial improved charge profile with higher potential than the parent. After the first charge, the major fraction of the capacity is locked and not accessible anymore, with the reason remaining unclear. Another similarity with the Mg analogue is the structure type of the impurity that appears beyond the doping limit or when the synthetic temperature is not reached. The phase has been solved for the Fe analogue and consequently for the Mg analogue too. With the latter, in addition to the main target, this chapter has yielded two new phases that could represent the first known phosphate members of this structure type.

There are many potential lines of future work on the new materials presented in this chapter. One is to clarify why a large fraction of the capacity is locked for the $\text{Li}_{0.96}\text{Fe}_{0.96}\text{In}_{0.04}\text{PO}_4$ cell. It would be very interesting to process these materials, for a wider variety of doping levels, in the same way as the commercial LiFePO_4 and see the performance under those conditions. The microstructure could be studied with electron microscopy. The Li-ion mobility could be evaluated by AC impedance or μSR spectroscopies. From these, the AC impedance spectroscopy was not used to study the ionic conductivity because the cathode testing was considered of higher priority. The two new phases discovered, $\text{LiFeIn}(\text{PO}_4)_2$ and $\text{LiMgIn}(\text{PO}_4)_2$, could be explored as potential cathode and electrolyte respectively. For $\text{LiMgIn}(\text{PO}_4)_2$ it would be worth assessing the Mg mobility. Study of defect introduction and property relationships would also be interesting and useful. The discovery of these phases has also opened the possibility to try the synthesis of other phosphates in this structure type such as $\text{Li}_2\text{Zr}(\text{PO}_4)_2$, $\text{Li}_2\text{Ti}(\text{PO}_4)_2$ or $\text{Li}_2\text{Mn}(\text{PO}_4)_2$ to see if they can be made and to study their properties.

4.8 References

1. Ozawa, K., *Lithium-ion rechargeable batteries with LiCoO₂ and carbon electrodes: the LiCoO₂/C system*. Solid State Ionics, 1994. **69**(3-4): p. 212-221.
2. Wang, Q., P. Ping, X. Zhao, G. Chu, J. Sun, and C. Chen, *Thermal runaway caused fire and explosion of lithium ion battery*. Journal of power sources, 2012. **208**: p. 210-224.
3. Padhi, A.K., K. Nanjundaswamy, and J. Goodenough, *Phospho-olivines as positive-electrode materials for rechargeable lithium batteries*. Journal of the electrochemical society, 1997. **144**(4): p. 1188-1194.
4. Kandhasamy, S., K. Nallathamby, and M. Minakshi, *Role of structural defects in olivine cathodes*. Progress in Solid State Chemistry, 2012. **40**(1): p. 1-5.
5. Jugović, D. and D. Uskoković, *A review of recent developments in the synthesis procedures of lithium iron phosphate powders*. Journal of Power Sources, 2009. **190**(2): p. 538-544.
6. Biendicho, J.J. and A.R. West, *Thermally-induced cation disorder in LiFePO₄*. Solid State Ionics, 2011. **203**(1): p. 33-36.
7. Janssen, Y., D. Santhanagopalan, D. Qian, M. Chi, X. Wang, C. Hoffmann, Y.S. Meng, and P.G. Khalifah, *Reciprocal salt flux growth of LiFePO₄ single crystals with controlled defect concentrations*. Chemistry of Materials, 2013. **25**(22): p. 4574-4584.
8. Andersson, A.S., B. Kalska, L. Häggström, and J.O. Thomas, *Lithium extraction/insertion in LiFePO₄: an X-ray diffraction and Mössbauer spectroscopy study*. Solid State Ionics, 2000. **130**(1): p. 41-52.
9. Wang, J. and X. Sun, *Understanding and recent development of carbon coating on LiFePO₄ cathode materials for lithium-ion batteries*. Energy & Environmental Science, 2012. **5**(1): p. 5163-5185.
10. Ravet, N., Y. Chouinard, J. Magnan, S. Besner, M. Gauthier, and M. Armand, *Electroactivity of natural and synthetic triphylite*. Journal of Power Sources, 2001. **97**: p. 503-507.
11. Park, K., J. Son, H. Chung, S. Kim, C. Lee, K. Kang, and H. Kim, *Surface modification by silver coating for improving electrochemical properties of LiFePO₄*. Solid State Communications, 2004. **129**(5): p. 311-314.
12. Yuan, L.-X., Z.-H. Wang, W.-X. Zhang, X.-L. Hu, J.-T. Chen, Y.-H. Huang, and J.B. Goodenough, *Development and challenges of LiFePO₄ cathode material for lithium-ion batteries*. Energy & Environmental Science, 2011. **4**(2): p. 269-284.
13. Kim, H.-S., D.-W. Kam, W.-S. Kim, and H.-J. Koo, *Synthesis of the LiFePO₄ by a solid-state reaction using organic acids as a reducing agent*. Ionics, 2011. **17**(4): p. 293-297.
14. Hong, J., C. Wang, X. Chen, S. Upreti, and M.S. Whittingham, *Vanadium modified LiFePO₄ cathode for Li-ion batteries*. Electrochemical and Solid-State Letters, 2009. **12**(2): p. A33-A38.
15. Taylor, J., O. Arnold, J. Bilheaux, A. Buts, S. Campbell, M. Doucet, ..., and J. Zikovsky, *Mantid, A high performance framework for reduction and analysis of neutron scattering data*. Bulletin of the American Physical Society, 2012. **57**.

16. Coelho, A.A., *Topas-Academic*. A Computer Programme for Rietveld Analysis, 2004.
17. Yakubovich, O., E. Belokoneva, V. Tsirel'son, and V. Urusov, *Electron density distribution in synthetic triphylite LiFePO_4* . Vestnik Moskovskogo Universiteta, Geologiya, 1990. **45**: p. 93-99.
18. Bélar, J.-F. and P. Lelann, *ESD's and estimated probable error obtained in Rietveld refinements with local correlations*. Journal of applied crystallography, 1991. **24**(1): p. 1-5.
19. Belsky, A., M. Hellenbrandt, V.L. Karen, and P. Luksch, *New developments in the Inorganic Crystal Structure Database (ICSD): accessibility in support of materials research and design*. Acta Crystallographica Section B: Structural Science, 2002. **58**(3): p. 364-369.
20. Liu, H., F.C. Strobridge, O.J. Borkiewicz, K.M. Wiaderek, K.W. Chapman, P.J. Chupas, and C.P. Grey, *Capturing metastable structures during high-rate cycling of LiFePO_4 nanoparticle electrodes*. Science, 2014. **344**(6191): p. 1252817.
21. McCusker, L., R. Von Dreele, D. Cox, D. Louer, and P. Scardi, *Rietveld refinement guidelines*. Journal of Applied Crystallography, 1999. **32**(1): p. 36-50.
22. Werner, P.-E., L. Eriksson, and M. Westdahl, *TREOR, a semi-exhaustive trial-and-error powder indexing program for all symmetries*. Journal of Applied Crystallography, 1985. **18**(5): p. 367-370.
23. Altomare, A., C. Cuocci, C. Giacovazzo, A. Moliterni, R. Rizzi, N. Corriero, and A. Falcicchio, *EXPO2013: a kit of tools for phasing crystal structures from powder data*. Journal of Applied Crystallography, 2013. **46**(4): p. 1231-1235.
24. Stokes, H.T. and D.M. Hatch, *FINDSYM: program for identifying the space-group symmetry of a crystal*. Journal of Applied Crystallography, 2005. **38**(1): p. 237-238.
25. *ISOTROPY Software Suite, iso.byu.edu*. October 2016].
26. Isasi, J., S. Jaulmes, A. Elfakir, and M. Quarton, *Crystal structure of dilithium nickel disulfate, $\text{Li}_2\text{Ni}(\text{SO}_4)_2$* . Zeitschrift für Kristallographie-New crystal structures, 2001. **216**(1-4): p. 353-354.
27. Lander, L., M. Reynaud, G.I. Rousse, M.T. Sougrati, C. Laberty-Robert, R.J. Messinger, M.I. Deschamps, and J.-M. Tarascon, *Synthesis and electrochemical performance of the orthorhombic $\text{Li}_2\text{Fe}(\text{SO}_4)_2$ polymorph for Li-ion batteries*. Chemistry of Materials, 2014. **26**(14): p. 4178-4189.
28. Reynaud, M., J. Rodríguez-Carvajal, J.-N. Chotard, J.-M. Tarascon, and G. Rousse, *Magnetic structure and properties of orthorhombic $\text{Li}_2\text{Ni}(\text{SO}_4)_2$: A possible magnetoelectric material*. Physical Review B, 2014. **89**(10): p. 104419.
29. Chen, J.-M., C.-H. Hsu, Y.-R. Lin, M.-H. Hsiao, and G.T.-K. Fey, *High-power LiFePO_4 cathode materials with a continuous nano carbon network for lithium-ion batteries*. Journal of Power Sources, 2008. **184**(2): p. 498-502.

This page is intentionally left blank

Chapter 5

New NASICON analogue materials

5.1 Introduction

5.1.1 From the NASICON-type structure to the lithium analogues

In 1968 the crystal structure of the NASICON-type structure was described for first time for the compositions $\text{NaZr}_2(\text{PO}_4)_3$, $\text{NaGe}_2(\text{PO}_4)_3$ and $\text{NaTi}_2(\text{PO}_4)_3$ that appeared to be isostructural with space group $R\bar{3}c$ [1]. The main feature of this structure type is that it is made of typical units called the lantern motif shown in figure 5.1.a. The lantern motif is composed of two MO_6 octahedra linked by three PO_4 tetrahedra by corner sharing. The units of this motif link to each other by corner sharing to form the NASICON framework as can be seen in figure 5.1.b.

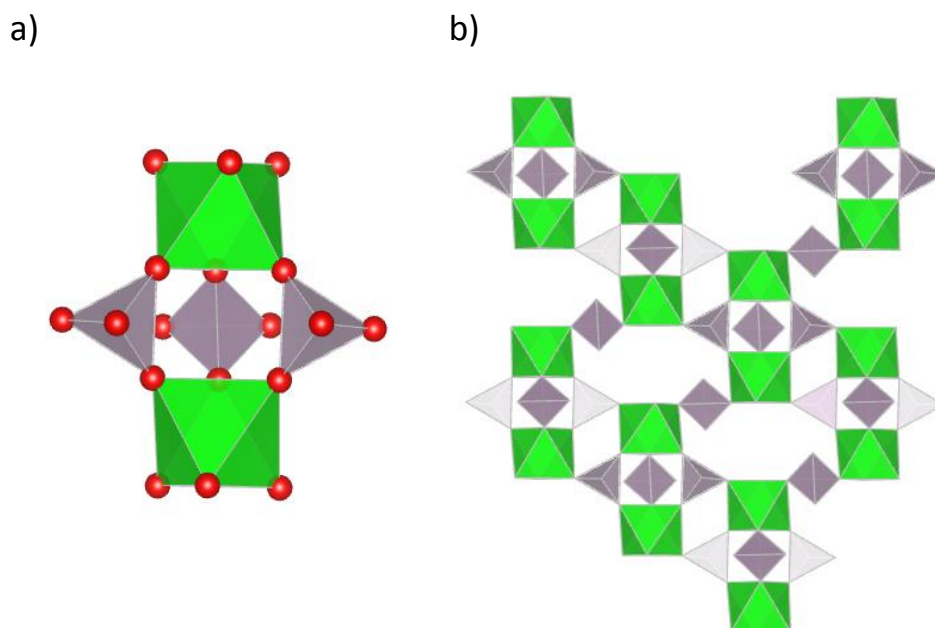


Figure 5.1. a) The building unit of the NASICON framework, the lantern motif. b) A projection of the NASICON framework showing the corner sharing connectivity between the lantern units. MO_6 octahedra and PO_4 tetrahedra are shown in green and purple respectively.

This structure type very soon became a hot topic in materials chemistry due to the study of their Na-ion conductivity. In particular, the exploration of the system $\text{Na}_{1+x}\text{Zr}_2\text{P}_{3-x}\text{Si}_x\text{O}_{12}$ showed for $x = 2$ a Na-ion conductivity of $\approx 0.2 \text{ S cm}^{-1}$ at $300 \text{ }^\circ\text{C}$ that was competitive with the value measured for β'' alumina [2]. This composition of $\text{Na}_3\text{Zr}_2[\text{PSi}_2]\text{O}_{12}$, has been referred as “the true NASICON” and it has been attributed to the Si/P substitution the ability to prevent the Na long range ordering [3].

The efficiency of the Na-ion diffusion pathways in the NASICON framework was of interest to be tested with other alkali metal cations. In particular it was investigated in order to find the trend in Li-ion conductivities in $\text{LiM}_2(\text{PO}_4)_3$ for $\text{M} = \text{Zr, Hf, Ge}$ and Ti among others. The proposed Li-ion diffusion pathway is shown in figure 5.2 where the Li site has been marked as Li1. The ion transport properties of some of these materials are shown in table 5.1.

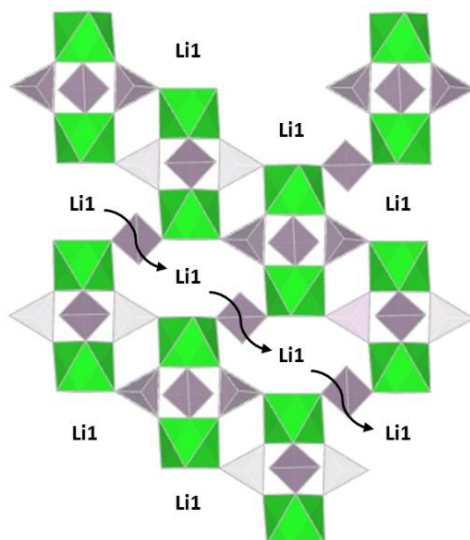


Figure 5.2. NASICON framework with the lithium site marked as Li1 and the proposed Li-ion diffusion pathway indicated with curved arrows. MO₆ octahedra and PO₄ tetrahedra are shown in green and purple respectively.

Table 5.1. Li-ion conductivity of selected NASICON analogues.

Composition	Unit cell volume / Å ³	$\sigma_{\text{bulk}} / \text{S cm}^{-1}$	T / °C	E _a / eV	References
LiZr ₂ (PO ₄) ₃	1507.5	~ 10 ⁻⁸	30	0.65	[4], [5], [6]
LiHf ₂ (PO ₄) ₃	1486	~ 10 ⁻⁵	30	0.43	[7], [5]
LiTi ₂ (PO ₄) ₃	1311	~ 10 ⁻⁷	30	0.49	[8], [5], [9]
LiGe ₂ (PO ₄) ₃	1218.1	~ 10 ⁻⁷	Room temp.	0.6	[10], [11], [9]

Table 5.2 shows the crystal chemistry of the relevant atoms in these systems. Looking at tables 5.1 and 5.2, it can be seen that the unit cell volume is linked to the ionic radius of the structural metal ion. On the other hand, there is no clear trend in conductivity or activation energy with respect to the volume. Larger unit cells in general will correlate with larger diffusion pathways. Usually in these comparisons, the conductivity follows a volcano plot vs unit cell volume, i.e. after initial conductivity increase will follow a decrease. The explanation for this has been that if the diffusion channels are too large, the ions can be trapped in potential minima [12].

Although several other applications are known for these materials, e.g. photo catalysis [13], the property on which this thesis focuses is the ionic conductivity.

Table 5.2. Crystal chemistry properties of selected atoms [14].

Element	Oxidation state	Coordination number	Effective ionic radius
Zr	+4	VI	0.72 Å
Hf	+4	VI	0.71 Å
Ti	+4	VI	0.605 Å
Ge	+4	VI	0.53 Å
Li	+1	VI	0.76 Å

5.1.2 Polymorphism

The Li analogues of NASICON are known to show a complex polymorphism, e.g. the composition $\text{LiZr}_2(\text{PO}_4)_3$ when synthesised at 1200 °C yields the α -phase while if synthesised at 900 °C yields the β -phase. Both, the rhombohedral α -phase and the orthorhombic β -phase, undergo fully reversible phase transitions to the triclinic α' -phase and the monoclinic β' -phases respectively. Both transitions occur below the transition temperatures $T_{c,\alpha} \sim 30\text{-}60$ °C and $T_{c,\beta} \sim 300$ °C as shown by Catti et al. [15, 16], i.e. α and β are the high temperature modifications while α' and β' are the low temperature modifications. The prime modifications, e.g. the triclinic with respect to the rhombohedral, retain the polyhedral connectivity and are characterised by torsions of the polyhedra.

Catti et al. refer to a bulk Li-ion conductivity of 10^{-5} S cm^{-1} for the rhombohedral α -polymorph stabilised at room temperature. This stabilisation was achieved by adding Li_3PO_4 in the synthesis [5]. The α -phase is the one shown in this chapter so far, in figures 5.1 and 5.2.

The β form is also known as anti-NASICON-type structure. The orthorhombic form is said to be an intergrowth of NASICON and anti-NASICON type structures [17]. The

main structural feature that distinguishes the NASICON-type structure from the anti-NASICON-type structure is the orientation of the lantern motif. In the case of the NASICON-type structure all the lanterns show parallel alignment as can be seen in figures 5.1 and 5.2 while for the anti-NASICON-type structure the lanterns show two types of alternating alignments [18], which can be seen in figure 5.3.

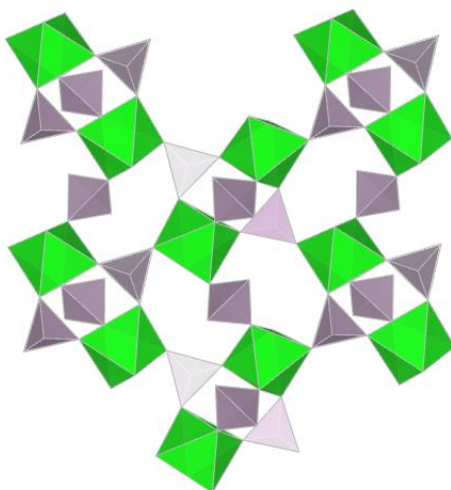


Figure 5.3. A projection of the anti-NASICON framework showing the connectivity between the lantern units. The two different orientation of the lantern motif can be observed. MO_6 octahedra and PO_4 tetrahedra are shown in green and purple respectively.

It has been shown that the transition temperature can be modulated in tens of degree through aliovalent doping, e.g. the triclinic polymorph of $\text{LiZr}_2\text{P}_3\text{O}_{12}$ at room temperature has much lower ionic conductivity than the rhombohedral NASICON stable at room temperature when a 5 % of Zr is substituted by Ca, reaching a bulk Li-ion conductivity of $1.2 \times 10^{-4} \text{ S cm}^{-1}$ at room temperature [19]. In the latter comparison the resulting stoichiometry is richer in lithium and also lithium excess is used in the synthesis. Isovalent doping has also been shown to lower the transition temperature, e.g. the solid solution between $\text{LiZr}_2(\text{PO}_4)_3$ and $\text{LiHf}_2(\text{PO}_4)_3$ shows a linear variation between the transition temperature of both end members [5]. In the same reference they show that addition of Li_3PO_4 also lowers the transition temperature.

This shows some of the structural modifications of these stoichiometries, although others are also known, such as the γ -polymorph that has been studied by Masquelier et al. in $\text{Li}_3\text{Fe}_2(\text{PO}_4)_3$ [20]. The α -polymorph of the NASICON-type structure with rhombohedral lattice is the one to which the highest ionic conductivity is attributed. In general conductivity comparisons focus on the structure, but in many cases the Li content has been increased as well, providing a higher ratio of carriers within the structure. It is worth mentioning that the phosphate content is usually not discussed as a contributor to conductivity changes. What seems clear is that the α modification offers the advantage of its three-dimensional diffusion pathways that host the most disorder distribution of Li sites [21].

5.1.3 The Li sites in the α -polymorph

In the original α -NASICON, the two sites of the Na-ions are called Na1 and Na2. Within the ribbons made of the aligned units of the lantern motif, there is a Na1 site between each pair of lanterns that corresponds to the Li1 site shown in figure 5.2. Then the Na2 site is located in the space between the ribbons, halfway between two neighbouring Na1 sites.

For the lithium analogues the situation is not far from this. There is a Li1 site with Wyckoff label 6b that correspond to the Na1. This is the Li1 site in figure 5.2. Then there is a Li2 site with Wyckoff label 18e which corresponds to the Na2, which is in the middle of the diffusion arrow in figure 5.2. Finally there is a “halfway” site located around the Li1 site with a six-fold distribution and a Wyckoff label 36f [22].

The latter site 36f is the site that Catti et al. discuss with the possibility of having the Li-ions on 6 disordered sites located off the symmetry centre for Li1 [21]. At the same time they described a new set of 3-fold disordered sites on a new Li2 site.

Arbi et al. [23] describe that Li prefer to occupy the Li1 site in systems such as $\text{LiGe}_2(\text{PO}_4)_3$ and $\text{LiTi}_2(\text{PO}_4)_3$. They also show that when $\text{LiTi}_2(\text{PO}_4)_3$ is doped with Al, the unit cell shrinks and the ionic conductivity increases having lower activation energy. On the other hand, when Ti is substituted with larger cations such as Zn, Hf or Zr, a triclinic distortion occurs and the Li is placed in a tetragonal void, M1/2,

midway between M1 and M2 in the NASICON structure such as described by Catti et al [15].

In general, the more Li sites a structure has and the closer they are to each other, the easier the hopping becomes for the mobile ions. The increase in Li content increases the population of Li-ions on interstitial sites of the NASICON crystal lattice which also contributes to increase the conductivity.

5.1.4 Opportunities for variation

Many of the compositions discussed so far share the common feature of having a single type of cation on the structural octahedral metal site of the framework. A convenient way of presenting the variety of known Li analogues is to discuss how many different cations have been attempted on the structural octahedral metal site at the same time. The selection of their ratios and oxidation states have been used to charge balance the amount of Li per formula unit.

Looking into isovalent substitutions on the M site, the single 4+ cation can be substituted with isovalent 4+ cations giving pairs 4+/4+ on the M-site that keep the Li stoichiometry of 1. A natural approach is to try solid solutions of the known compounds to produce new ones such as $\text{LiGeTi}(\text{PO}_4)_3$ [9].

Another step further is the aliovalent substitution with the aim of increasing the concentration of carrier ions per formula unit. Examples of these attempts lead to pairs 4+/3+ or 4+/2+ on the M site e.g. $\text{Li}_{1+x}[\text{Ge}_{2-x}\text{Al}_x](\text{PO}_4)_3$, with the relative high conductivity of $\approx 10^{-4} \text{ S cm}^{-1}$ at room temperature for $\text{Li}_{1.4}[\text{Ge}_{1.6}\text{Al}_{0.4}](\text{PO}_4)_3$ [10].

One more option is to change the 4+/4+ pair for a 5+/3+ pair that keep the Li stoichiometry, e.g. it is known that the material $\text{LiTaAlP}_3\text{O}_{12}$ has an ionic conductivity of $6.5 \times 10^{-7} \text{ S cm}^{-1}$ at 30 °C, which is similar to that of $\text{LiTi}_2\text{P}_3\text{O}_{12}$ but with oxidation states much more stable to Li reduction [24].

The deviation in the ratio of 1:1 for the 5+ and 3+ cations was also used to increase the amount of Li-ions per formula unit, e.g. the composition $\text{Li}_{1.2}\text{Ta}_{0.9}\text{Al}_{1.1}\text{P}_3\text{O}_{12}$, although this showed a similar conductivity to that of $\text{LiTaAlP}_3\text{O}_{12}$.

The complexity of the pattern of substitution can be increased, e.g. in the previous system the second aliovalent substitution of Ge for Ta was tried in order to increase more the concentration of Li-ions per formula unit, i.e. $\text{Li}_{1+x}[\text{Ta}_{1-x}\text{Ge}_x\text{Al}](\text{PO}_4)_3$, with the outcome of a 100-fold improvement in Li-ion conductivity for $x = 0.5$ with respect to $x = 0$ when measured at 60 °C [25]. The latter is equivalent to study samples in the ternary phase diagram for Ta-Al-Ge on the M site of the structure that lie on the line for Al = 0.5.

5.1.5 Other considerations

Hueso et al. mention in their paper [26] that the system $\text{Na}_{1+x}\text{Zr}_2\text{P}_{3-x}\text{Si}_x\text{O}_{12}$ shows a small monoclinic distortion for $1.8 < x < 2.2$ and also that ZrO_2 impurities decrease the Na-ion conductivity. With high quality diffraction data and appropriate property measurements this structural and property observations could be tested in the systems synthesised in this chapter.

Aono et al. show that for $\text{LiTi}_2(\text{PO}_4)_3$ the ionic conductivity largely increase with the incorporation of 3+ cations such as Al, Ga, Sc, In and Y up to the level of $x = 0.3$. They found that these substitutions reduced the porosity of the pellets prepared for property measurements and that this porosity was related to the ionic radius of the 3+ cation. In their opinion, the enhanced conductivity derived from the higher relative density achieved [27]. In a different paper Aono et al. show that the substitution with Al or the addition of sintering aids such as Li_2O result in both cases in reduction of porosity with a relative higher improvement in grain boundary conductivity to yield a much improved total conductivity [28]. These approaches are generally named “sintering aids”. Most of the synthesis in this chapter will use Li and P excess. It will be interesting to discuss how this will affect to either sinterability or either the crystal structure of the NASICON analogue.

Rao et al. confirm [29] that the substitution of Ti^{4+} for the isovalent larger cation Zr^{4+} in $\text{LiTi}_2(\text{PO}_4)_3$ increases the unit cell volume while slightly decreases the ionic conductivity. This is an example of the volcano type plot behaviour for conductivity vs unit cell volume.

Mestral et al. report the rate of loss of P_2O_5 from thermal phosphate decomposition at temperatures higher than 1200 °C. They describe the glass transition of a casted Ca-P-O phase which is melted with low viscosity at 1200 °C [30]. This initially would suggest that a metal phosphate is safe against decomposition below those temperatures. On the other hand, the melting and boiling points of the phosphoric acid and phosphorous oxides potentially produced as intermediates derived from the reaction precursors are not so high, e.g. P_4O_{10} melts at 340° C with no negligible vapour pressures at that temperature.

All this collection of facts show a picture of the complexity of these systems along with the substitutions that have proven to work with respect to the property tuning.

So far the historical development and the general features of these materials have been described, some difficulties and unknowns with opportunities for exploration and clarification have been presented as well. The next few subsections introduce the work described in this chapter.

5.1.6 Exploring anisotropic strain and structural distortion as potential enhancers of conductivity in $LiTaAl(PO_4)_3$ related samples

The work presented in this section was motivated by the low temperature narrowing observed with solid state NMR relaxometry on a specimen with nominal composition $Li_{0.875}Ta_{1.062}Al_{0.938}P_3O_{12}$ initially prepared by other researchers in the group. The anisotropic strain observed in the sample was proposed to be a triclinic distortion in first instance. It was interesting that preliminary AC impedance spectroscopy indicated that the ionic conductivity was at the level of samples with higher Li content per formula unit, e.g. $LiTaAl(PO_4)_3$.

With the aim of pursuing further studies within this thesis, the sample was replicated and scaled up for detailed high resolution diffraction analysis, optimisation of the processing conditions for densification and property measurements. There are many questions to answer around these samples, being the first one the confirmation of the previous results. Then a detailed structural characterisation is pursued, to check e.g. if there is any Al on the P site. It is known

that Al can be found in tetrahedral environments such as happens in the berlinite AlPO_4 . There is a very different ionic radius between P^{5+} and Al^{3+} in tetrahedral environments as shown in table 5.3, which serves to make a comparison for common tetrahedral oxyanions, e.g. $[\text{PO}_4]^{3-}$, $[\text{SiO}_4]^{4-}$ and $[\text{AlO}_4]^{5-}$. Si has been included as a known substitution in NASICON materials for comparison. It will be interesting to see if any polymorphism or transition temperatures can be observed. Finally the optimisation of the processing conditions for densification will be carried out and ionic conductivity will be measured with AC impedance and NMR spectroscopies.

Table 5.3. Crystal chemistry properties of selected atoms [14].

Element	Oxidation state	Coordination number	Effective ionic radius
P	+5	IV	0.17 Å
Si	+4	IV	0.26 Å
Al	+3	IV	0.39 Å

5.1.7 Calcium doping of $\text{LiTaAl}(\text{PO}_4)_3$ related samples

The aim of this work is to produce Ca-doped derivatives of $\text{LiTaAlP}_3\text{O}_{12}$ with higher Li content and make an accurate characterisation of the crystal structure to relate it with the change in conductivity. This could lead to higher or lower conductivities, but in any case will add to the understanding of the underlying structural chemistry that enhances conductivity. The known crystal chemistry of the cations involved are shown in table 5.4. The aim is to introduce Ca on the Ta-Al site.

Table 5.4. Crystal chemistry properties of selected atoms [14].

Element	Oxidation state	Coordination number	Effective ionic radius
P	+5	IV	0.17 Å
Al	+3	VI	0.535 Å
Ta	+5	VI	0.64 Å
Li	+1	VI	0.76 Å
Ca	+2	VI	1.00 Å

There are some questions that the work on Ca-doping will try to answer such as to explore if it is possible to substitute Ca for Ta in $\text{Li}_{1.2}\text{Ta}_{0.8}\text{Al}_{1.2}\text{P}_3\text{O}_{12}$ to increase the amount of Li per formula unit by charge balance. Also to find out which Ta/Al ratio is able to accommodate $\text{Ca}_{0.11}$ in the structure and therefore tell if this aliovalent substitution is able to increase the Li content. A detailed structural characterisation with powder diffraction data to confirm the Ca and Li location is pursued as well, to clarify if Ca goes into the NASICON framework, and to tell on which site it is. Is it on the metal Ta-Al site? Or is it on any of the Li sites proposed in literature? The latter is what its ionic radius and charge match would suggest from table 5.4. Also interesting is to search if there is any evidence of the 6 and 3-fold disordered sites described by Catti et al. for the $\alpha\text{-LiZr}_2(\text{PO}_4)_3$ or if any other sites described in literature are found. Then AC impedance and NMR spectroscopies will be used to study the temperature dependence of the ionic conductivity and clarify if the outcome is due to the change in Li-content or to the crystal structure modification.

5.1.8 New combinations of elements that retain the NASICON-type structure: Ta-Mg-Ga

For a general NASICON structure-type of formula $\text{Li}_x\text{M}_2\text{P}_3\text{O}_{12}$, the size differences of the cations located on the M site have been claimed to lead to local distortions in the NASICON framework [11]. This distortion would affect the diffusion pathway bottlenecks with the final impact of reducing the ionic conductivity. In order to reduce the size mismatch for the cations on the M site, the triple $5+/3+/2+$ of

Ta/Ga/Mg have been selected, which shows a good similarity as can be seen in table 5.5, in particular for the composition $\text{LiTaGaP}_3\text{O}_{12}$. Zr and Li have been included in the table for comparison. To the best of our knowledge, there are no NASICON analogues in the literature with this combination of elements. To produce samples with high Li content the strategy used is to increase the ratio of the lower valent cations. This is systematically tested by exploration of the ternary phase diagram.

Table 5.5. Crystal chemistry properties of selected atoms [14].

Element	Oxidation state	Coordination number	Effective ionic radius
Ga	+3	VI	0.62 Å
Ta	+5	VI	0.64 Å
Mg	+2	VI	0.72 Å
Zr	+4	VI	0.72 Å
Li	+1	VI	0.76 Å

For this system all the synthetic space is tried, offering this approach a more broad vision on the potential outcomes. This means a systematic exploration of the Ta-Mg-Ga phase diagram for the M site of the NASICON framework, generating samples in the regions where α -NASICON analogues are able to form after stoichiometric and charge balance considerations.

The major outcomes will be to show which compositions can make a phase pure NASICON analogue. For the phase pure samples, structural and compositional confirmation will be carried out with synchrotron powder diffraction data to reveal the structural features of these new phases. Also, from laboratory PXRD, the study of the NASICON phases formed in impure samples will reveal if further variation is likely within these compositions. Finally the Li-ion conductivity will be measured with AC impedance spectroscopy.

5.2 Anisotropic strain and ionic conductivity in $\text{LiTaAl}(\text{PO}_4)_3$ related samples

5.2.1 Synthesis

5.2.1.1 Revisiting the selected composition

This section focuses on the nominal composition $\text{Li}_{0.875}\text{Ta}_{1.062}\text{Al}_{0.938}\text{P}_3\text{O}_{12}$ made with $\sim 5.7\%$ Li excess and $\sim 5.4\%$ P excess. This composition was determined after applying a weight correction due to the TGA measurements on precursors shown in appendix 5.1. The resulting weights were also balanced to fit the typical NASICON stoichiometry for the metal site and the oxyanions. Some of the small scale samples presented in this section were prepared by Dr Chris Collins who helped me to start with the NASICON project.

The standard synthesis used for the small scale samples is the one previously optimised by other researchers in the group. It consisted of a conventional solid state ceramic route using high purity reactants: Li_2CO_3 99.997 % from Sigma-Aldrich, Ta_2O_5 99.99 % from Alfa Aesar, $\gamma\text{-Al}_2\text{O}_3$ 99.997 % from Alfa Aesar and $(\text{NH}_4)_2\text{H}_2\text{PO}_4$ 99.999 % from Sigma-Aldrich. All starting materials were dried at $200\text{ }^\circ\text{C}$ with the exception of $(\text{NH}_4)_2\text{H}_2\text{PO}_4$ that was used as received.

Reactants were ground with ethanol in an agate pestle and mortar for 30 minutes. When the paste was dry, it was transferred to a Pt crucible which finally was covered with an alumina lid. The crucibles were then placed in a temperature calibrated box furnace and the temperature profile used was as follows: heating at $0.5\text{ }^\circ\text{C}/\text{min}$ to $300\text{ }^\circ\text{C}$ and dwell in the range 1 – 4 hours, then heating up at $10\text{ }^\circ\text{C}/\text{min}$ to $900\text{ }^\circ\text{C}$ and dwell for 24 hours. Finally it is cooled at $10\text{ }^\circ\text{C}/\text{min}$ to room temperature. The powders were thoroughly ground in a pestle and mortar and then placed back into Pt crucibles with an alumina lid and put back into the box furnace for a second firing. The temperature profile was: heating up at $10\text{ }^\circ\text{C}/\text{min}$ to $900\text{ }^\circ\text{C}$ and dwell for 24 hours, then cool down at $10\text{ }^\circ\text{C}/\text{min}$ to room temperature. The resulting powders were finely ground and placed in vials. Laboratory PXRD were collected for all the samples.

Initially some variations are explored in order to try to understand the behaviour of the system, especially the potential triclinic distortion. This synthesis was replicated for a set of samples with the same corrected nominal composition of $\text{Li}_{0.875}\text{Ta}_{1.062}\text{Al}_{0.938}\text{P}_3\text{O}_{12}$ but with a fixed % Li_2CO_3 excess, and a range of $(\text{NH}_4)_2\text{H}_2\text{PO}_4$ excesses varying from 5.4 to 31.4 % in order to study the phase evolution. These percentages were originally chosen as integer numbers, i.e. 5 to 30, but have become those values after the corrections described at the beginning of this section. All the compositions are listed in table 5.6 with a new final formula in which the excesses have been incorporated to the formula unit for comparison. Later in this section, the synthetic work will focus in scaling up the best compositions for characterisation, processing optimisation and property measurements.

Table 5.6. Summary of compositions used to explore the effect of Li and P excess on the preferred ratio of structural cations. The four columns on the left show the sample number, the intended composition and the corresponding Li and P excesses, after applying the TGA correction factor for alumina. The column on the right shows the overall composition including the Li/P excesses. For the latter, the oxygen has not been charge balanced in order to not make the assumption that all P has oxidation state 5+.

Sample	Compositions matching a charge balanced $\text{Li}_x\text{M}_2\text{P}_3\text{O}_{12}$			Overall stoichiometry
	Nominal composition	% Li excess	% P excess	
1	$\text{Li}_{0.875}\text{Ta}_{1.062}\text{Al}_{0.938}\text{P}_3\text{O}_{12}$	5.7	5.4	$\text{Li}_{0.925}\text{Ta}_{1.062}\text{Al}_{0.938}\text{P}_{3.16}\text{O}_{12+x}$
2	$\text{Li}_{0.875}\text{Ta}_{1.062}\text{Al}_{0.938}\text{P}_3\text{O}_{12}$	8.9	6.1	$\text{Li}_{0.953}\text{Ta}_{1.062}\text{Al}_{0.938}\text{P}_{3.18}\text{O}_{12+x}$
3	$\text{Li}_{0.875}\text{Ta}_{1.062}\text{Al}_{0.938}\text{P}_3\text{O}_{12}$	8.9	11.2	$\text{Li}_{0.953}\text{Ta}_{1.062}\text{Al}_{0.938}\text{P}_{3.33}\text{O}_{12+x}$
4	$\text{Li}_{0.875}\text{Ta}_{1.062}\text{Al}_{0.938}\text{P}_3\text{O}_{12}$	8.9	16.2	$\text{Li}_{0.953}\text{Ta}_{1.062}\text{Al}_{0.938}\text{P}_{3.49}\text{O}_{12+x}$
5	$\text{Li}_{0.875}\text{Ta}_{1.062}\text{Al}_{0.938}\text{P}_3\text{O}_{12}$	8.9	21.3	$\text{Li}_{0.953}\text{Ta}_{1.062}\text{Al}_{0.938}\text{P}_{3.64}\text{O}_{12+x}$
6	$\text{Li}_{0.875}\text{Ta}_{1.062}\text{Al}_{0.938}\text{P}_3\text{O}_{12}$	8.9	31.4	$\text{Li}_{0.953}\text{Ta}_{1.062}\text{Al}_{0.938}\text{P}_{3.94}\text{O}_{12+x}$

Pawley fits to the hexagonal setting of the rhombohedral unit cell in the space group $R\bar{3}c$ were performed for all the samples. Initially, Stephens's hexagonal peak shape [31] was used in order to account for the observed hkl dependant profile

broadening. The c/a ratio and the unit cell volume for all these samples are shown in figure 5.4. These samples showed low levels of impurities that are discussed later.

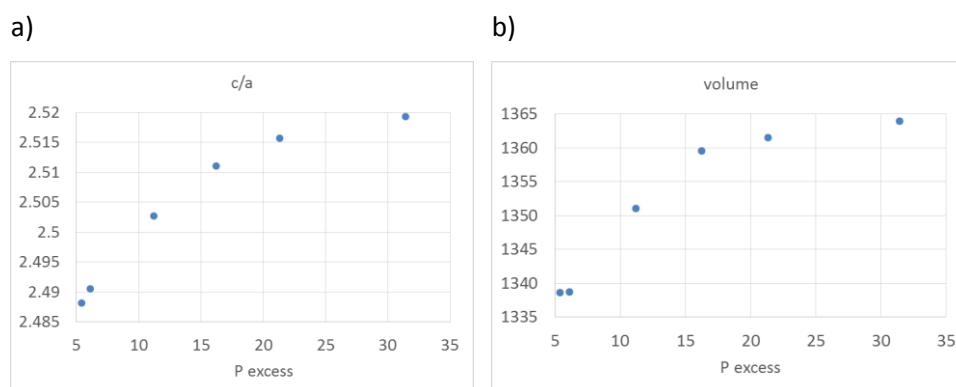


Figure 5.4. a) c/a ratio for the unit cell parameters of the series of samples of nominal composition $\text{Li}_{0.875}\text{Ta}_{1.062}\text{Al}_{0.938}\text{P}_3\text{O}_{12}$ exploring a range of Li and P excesses as stated in table 5.6. b) Unit cell volume / Å^3 for the same set of samples. Volume errors are smaller than the dot size ($1 \text{ e.s.d.} < 0.1 \text{ Å}^3$ for all samples).

There is a clear trend in lattice parameters. Comparing sample one with all the others, it seems that the Li excess affects more the c/a ratio than the unit cell volume. On the other hand it seems that the P excess forces an anisotropic change in the unit cell with a volume increase of about 2 %. The trend seems to show a change in slope above 15 % of P excess which could indicate the presence of a plateau.

The Pawley fit to the $R\bar{3}c$ phase with anisotropic Stephens's peak shape for sample 1 is shown in figure 5.5. It can be observed that the anisotropic strain is so large for some reflections, those with $l \gg h$ or k , that a free refinement of the Stephens's parameters cannot reach a satisfactory fit. Because of that a triclinic distortion is tested with a Pseudo-Voigt peak shape. The Pawley fit to the latter $P\bar{1}$ model is shown in figure 5.6 which offers a much improved fit factor R_{wp} from 7.313 % to 5.676 %.

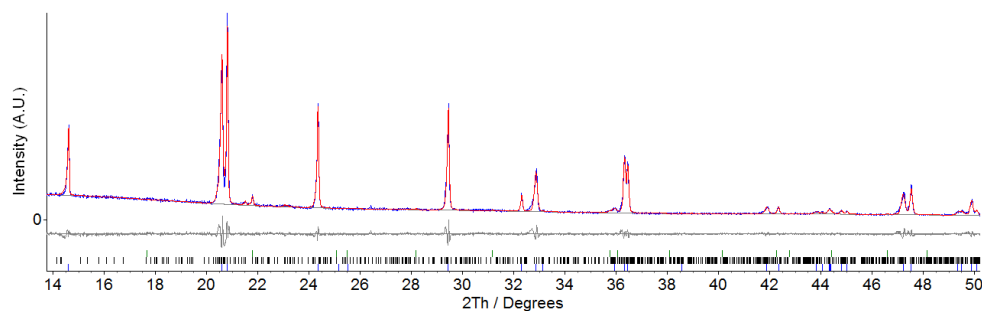


Figure 5.5. Cu $K\alpha_1$ PXRD pattern of sample 1, i.e. $\text{Li}_{0.925}\text{Ta}_{1.062}\text{Al}_{0.938}\text{P}_{3.16}\text{O}_{12+x}$. Multiphase mixed Rietveld/Pawley fit, red, to the data, blue. Background and difference are plotted in grey. Blue tick marks represent the NASICON analogue $R\bar{3}c$ phase (Pawley). Green and black tick marks represent the impurity phases $\text{AlPO}_4 C222_1$ and $\text{AlPO}_4 P1c1$ respectively (Rietveld for both). $R_{\text{wp}} = 7.313\%$.

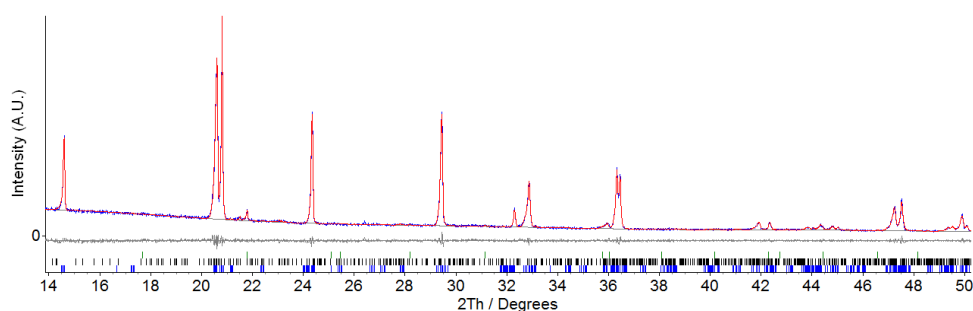


Figure 5.6. Cu $K\alpha_1$ PXRD pattern of sample 1, i.e. $\text{Li}_{0.925}\text{Ta}_{1.062}\text{Al}_{0.938}\text{P}_{3.16}\text{O}_{12+x}$. Multiphase mixed Rietveld/Pawley fit, red, to the data, blue. Background and difference are plotted in grey. Blue tick marks represent the NASICON analogue $P\bar{1}$ phase (Pawley). Green and black tick marks represent the impurity phases $\text{AlPO}_4 C222_1$ and $\text{AlPO}_4 P1c1$ respectively (Rietveld for both). $R_{\text{wp}} = 5.676\%$.

Proving that the triclinic fit is superior to the anisotropic hexagonal fit raises the question of how the triclinic unit cell would fit the whole series. The answer is in the plot of figure 5.7, showing the unit cell volume for the refined triclinic cell to all the samples. Again the trend is clearly superior to that shown in figure 5.4.b. Now the two samples with higher P excess seem to reach a plateau, which is difficult to confirm with only two samples.

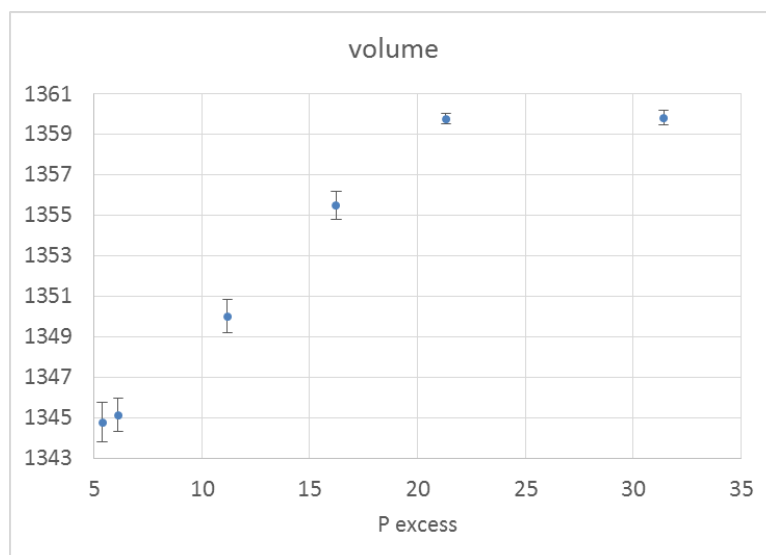


Figure 5.7. Unit cell volume / Å³ of the series of samples of nominal composition $\text{Li}_{0.875}\text{Ta}_{1.062}\text{Al}_{0.938}\text{P}_3\text{O}_{12}$ exploring a range of Li and P excesses as stated in table 5.6. Errors shown as 3 e.s.d.

The sample that is in the frontier between the incline and what seems a plateau in figure 5.7 is sample 5 or $\text{Li}_{0.953}\text{Ta}_{1.062}\text{Al}_{0.938}\text{P}_{3.64}\text{O}_{12+x}$. The Pawley fit of the hexagonal cell with anisotropic Stephens's peak shape to the laboratory PXRD pattern of sample 5 is shown in figure 5.8. It is interesting the fact that the NASICON phase for the two samples in the plateau can be fitted satisfactorily by accounting for the anisotropic strain only. The same can be observed for sample 6 as shown in figure 5.9. All the samples but sample 6 follow Vegard's law. Sample 6 shows a new impurity, which can be seen in figure 5.9 and which could indicate that the plateau is real.

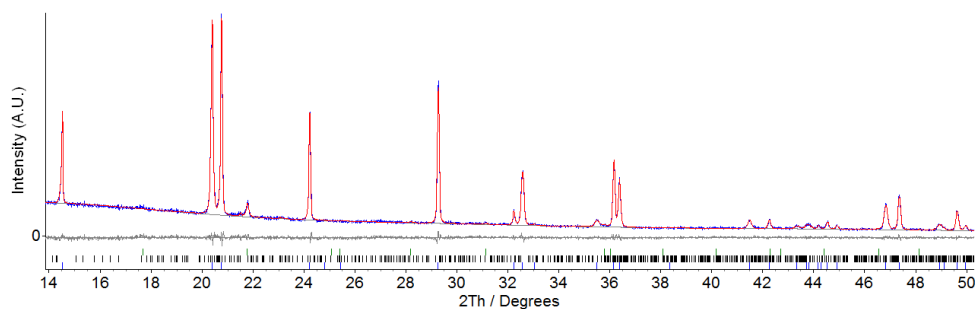


Figure 5.8. Cu $K\alpha_1$ PXRD pattern of sample 5, i.e. $\text{Li}_{0.953}\text{Ta}_{1.062}\text{Al}_{0.938}\text{P}_{3.64}\text{O}_{12+x}$. Multiphase mixed Rietveld/Pawley fit, red, to the data, blue. Background and difference are plotted in grey. Blue tick marks represent the NASICON analogue $R\bar{3}c$ phase (Pawley). Green and black tick marks represent the impurity phases $\text{AlPO}_4 C222_1$ and $\text{AlPO}_4 P1c1$ respectively (Rietveld for both).

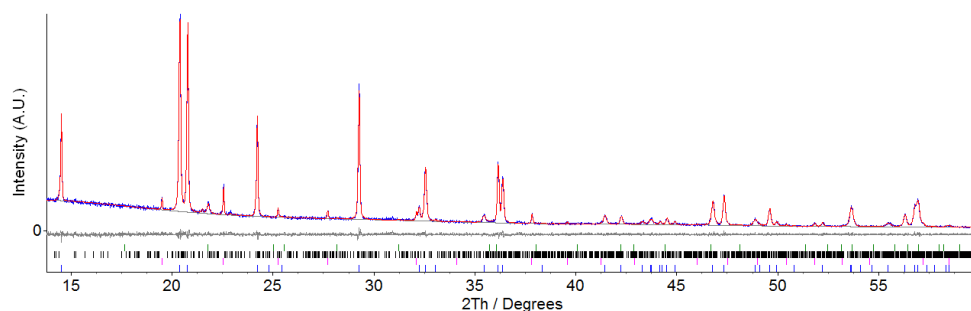


Figure 5.9. Cu $K\alpha_1$ PXRD pattern of sample 6, i.e. $\text{Li}_{0.953}\text{Ta}_{1.062}\text{Al}_{0.938}\text{P}_{3.94}\text{O}_{12+x}$. Multiphase mixed Rietveld/Pawley fit, red, to the data, blue. Background and difference are plotted in grey. Blue tick marks represent the NASICON analogue $R\bar{3}c$ phase (Pawley). Green, black and pink tick marks represent the impurity phases $\text{AlPO}_4 C222_1$, $\text{AlPO}_4 P1c1$ and $\text{Ta}_{0.5}\text{Al}_{0.5}\text{P}_2\text{O}_7$ respectively (Rietveld for all three).

For all the samples on the incline of figure 5.7, i.e. samples 1 to 5 in table 5.6, the most common impurity is AlPO_4 either as the polymorph with space group $C222_1$ or $P1c1$. But when a certain limit of P excess is exceeded a new impurity appears. This is $\text{Ta}_{0.5}\text{Al}_{0.5}\text{P}_2\text{O}_7$, a phase with the ZrP_2O_7 structure type. It was identified by structure solution as described in appendix 5.2 at the end of this chapter.

For this series of samples, some of the initial hypothesis were that Li or P could have been lost during the firings, or that a LiPO_3 glass could be present. The assignment of this extra phase in the plateau complicates the interpretation because it suggests

that some other change could be happening. This system has exhibited a typical Vegard's law behaviour with linear trend for samples 2 to 5. After the linear trend, the volume limit reached by samples 5 and 6 in table 5.6 suggests that a plateau could have been reached for which the associated new impurity would be $Ta_{0.5}Al_{0.5}P_2O_7$ as shown in figure 5.9.

These results raise more questions than answers, e.g. if the series is continued in the opposite direction, i.e. for different amounts of P defect, would another plateau be reached? Which is the actual range of NASICON analogue compositions that are represented in the incline?

Another possible interpretation is that the extra Li-P-O can be accommodated in the NASICON framework, perhaps contributing to its extension through polymerisation of PO_4 monomers. The dimers, i.e. pyrophosphates, are common in phosphate literature and have also appeared in this system in the plateau.

The rest of the section will try to find some answers from the data available for these samples, but before that some additional work is presented.

Some other related samples are shown here for the matter of leaving the record. Although they contain low level of lithium, a total splitting of the NASICON reflections have been resolved with laboratory diffractometer. These samples show how the variation of the Ta/Al ratio affects the outcome of the synthesis. This exploratory synthesis tried three new samples with compositions shown in table 5.7.

Table 5.7. Summary of compositions used to explore the effect of Ta/Al ratios for with small change in Li and P excesses. The four columns on the left show the sample number, the intended composition and the corresponding Li and P excesses, after applying the TGA correction factor for alumina. The column on the right shows the overall composition including the Li/P excesses. For the latter, the oxygen has not been charge balanced in order to not make the assumption that all P has oxidation state 5+.

Sample	Compositions matching a charge balanced $\text{Li}_x\text{M}_2\text{P}_3\text{O}_{12}$			Overall stoichiometry
	Nominal composition	% Li excess	% P excess	
7	$\text{Li}_{0.778}\text{Ta}_{1.111}\text{Al}_{0.889}\text{P}_3\text{O}_{12}$	9.10	21.23	$\text{Li}_{0.848}\text{Ta}_{1.111}\text{Al}_{0.889}\text{P}_{3.64}\text{O}_{12+x}$
8	$\text{Li}_{0.579}\text{Ta}_{1.211}\text{Al}_{0.789}\text{P}_3\text{O}_{12}$	9.81	21.07	$\text{Li}_{0.636}\text{Ta}_{1.211}\text{Al}_{0.789}\text{P}_{3.63}\text{O}_{12+x}$
9	$\text{Li}_{0.389}\text{Ta}_{1.305}\text{Al}_{0.695}\text{P}_3\text{O}_{12}$	11.54	20.97	$\text{Li}_{0.434}\text{Ta}_{1.305}\text{Al}_{0.695}\text{P}_{3.63}\text{O}_{12+x}$

This was fast exploratory work and only one firing at 900 °C was given to these three samples. The most remarkable result is that sample 9 exhibits clear splitting for some reflections of the NASICON phase as can be seen in figure 5.10. No further studies were performed on this sample due to the low lithium content. A large amount of $\text{Ta}_{0.5}\text{Al}_{0.5}\text{P}_2\text{O}_7$ appears in samples 8 and 9 while only a small amount is visible in sample 7.

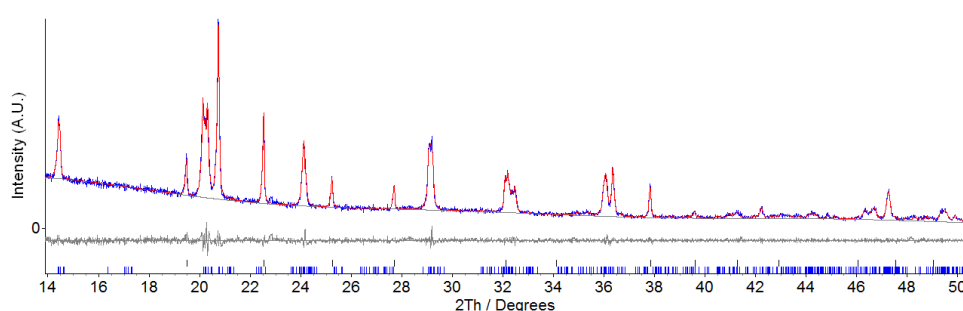


Figure 5.10. $\text{Cu K}\alpha_1$ PXRD pattern of sample 9, i.e. $\text{Li}_{0.434}\text{Ta}_{1.305}\text{Al}_{0.695}\text{P}_{3.63}\text{O}_{12+x}$. Multiphase mixed Rietveld/Pawley fit, red, to the data, blue. Background and difference are plotted in grey. Blue tick marks represent the NASICON analogue $P\bar{1}$ phase (Pawley). Black tick marks represent the impurity phase $\text{Ta}_{0.5}\text{Al}_{0.5}\text{P}_2\text{O}_7$ (Rietveld).

5.2.1.2 Scaling up selected samples

Samples 1 and 5 in table 5.6 were prepared in larger amounts for property measurements and for diffraction experiments.

For sample 1, with composition $\text{Li}_{0.925}\text{Ta}_{1.062}\text{Al}_{0.938}\text{P}_{3.16}\text{O}_{12+x}$, the synthesis was similar to the one explained in the previous section. The main differences were that the first heat treatment at 300 °C lasted for 1 hour and that the sample was reground after it before heating at 900 °C. For this sample two batches of 2 grams each were prepared for processing and preparation of pellets for AC impedance measurements. Also two more batches of 3 and 4 grams were prepared in the same way to be used as sacrificial powder during the sintering.

For sample 5, with composition $\text{Li}_{0.953}\text{Ta}_{1.062}\text{Al}_{0.938}\text{P}_{3.64}\text{O}_{12+x}$, the synthesis was similar to the one used for small scale samples with two main differences. The sample was prepared in scale of 6 grams, therefore the preparation of the precursor was made by using a Fritsch Pulverisette 7 planetary mill with zirconia milling material. The reactants were suspended in ethanol and the milling time was of 7.5 hours. The slurry was dried and homogenised. The second difference was that the first heat treatment was changed to avoid the precursor foaming from overflow the sides of the crucible. The heat treatments were carried out in Pt crucibles inside a box furnace as described here: the first heat treatment consisted of a heating ramp from room temperature to 300 °C at 0.5 °C/min but for the range 150-200 °C that was at 0.1 °C/min, then held for 4 hours at 300 °C and cooled down to room temperature at 10 °C/min. The resulting solid is then ground in agate pestle and mortar and put back to the Pt crucible for the second heat treatment which is at 900 °C for 24 hours with heating and cooling rates of 10 °C/min. After re-grinding, a second firing at 900 °C for 24 hours is repeated with same profile.

All batches of sample 1 were of the same quality. All the patterns overlapped without mismatch between each other and also compared to the sample previously prepared in the group. The impurity in these samples was assigned as AlPO_4 C222₁. One of these samples was also studied by synchrotron X-ray diffraction.

The large batch of sample 2 resulted of similar quality as in small scale synthesis. The impurity in this sample was also assigned as AlPO_4 C222₁. This sample was targeted for synchrotron and neutron powder diffraction studies.

5.2.2 TEM-EDX

TEM-EDX elemental analysis was performed on sample 1, $\text{Li}_{0.875}\text{Ta}_{1.062}\text{Al}_{0.938}\text{P}_3\text{O}_{12}$ made with 5.7 % Li excess and 5.4 % P excess, and on sample 5, $\text{Li}_{0.875}\text{Ta}_{1.062}\text{Al}_{0.938}\text{P}_3\text{O}_{12}$ made with 8.9 % Li excess and 21.3 % P excess, see table 5.6. The TEM-EDX data were collected by Dr Marco Zanella. TEM-EDX spectra and data are listed in appendix 5.3.

For the ternary diagram from sample 1, in figure 5.11, the experimental data is relatively clustered although still two or three sub-clusters are visible. These two clusters are further away from each other than the typical experimental error of 5 – 10 % would allow. It is worth mentioning that none of the measurements indicate the presence of AlPO_4 that can be seen as a minority phase in the PXRD pattern shown in figure 5.6. Under-representation of minorities in statistical populations is a well-known limitation of methods based on sampling such as TEM-EDX. On the other hand, the presence of the impurity AlPO_4 explains why the NASICON phase is slightly enriched in Ta with respect to the nominal composition indicated in red. What cannot be explained is why the NASICON clusters appear slightly deficient in P. The underlying reasons for having the two/three sub-clusters could be e.g. lack of homogeneity or a similar thermodynamic preference to form all resulting compositions.

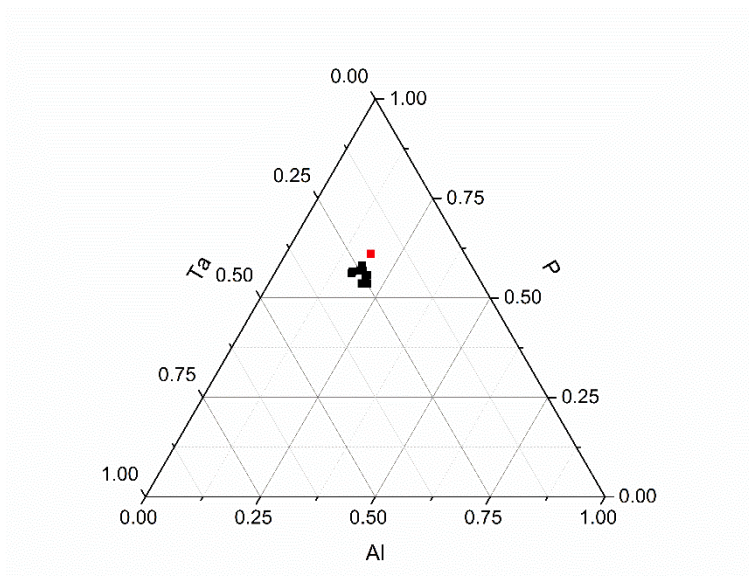


Figure 5.11. TEM-EDX derived Al-P-Ta compositions for the sample $\text{Li}_{0.875}\text{Ta}_{1.062}\text{Al}_{0.938}\text{P}_3\text{O}_{12}$ made with 5.7 % Li excess and 5.4 % P excess (sample 1). The nominal composition is marked in red.

For the ternary diagram from sample 5, in figure 5.12, the experimental data is much more spread than for sample 1. Four NASICON clusters can be observed close to the nominal composition. The two measurements lying approximately on the line $P = 0.5$ are assigned to AlPO_4 observed in the PXRD pattern shown in figure 5.8, with the shift to the left attributed to bias due to neighbour NASICON grains within the same polycrystal.

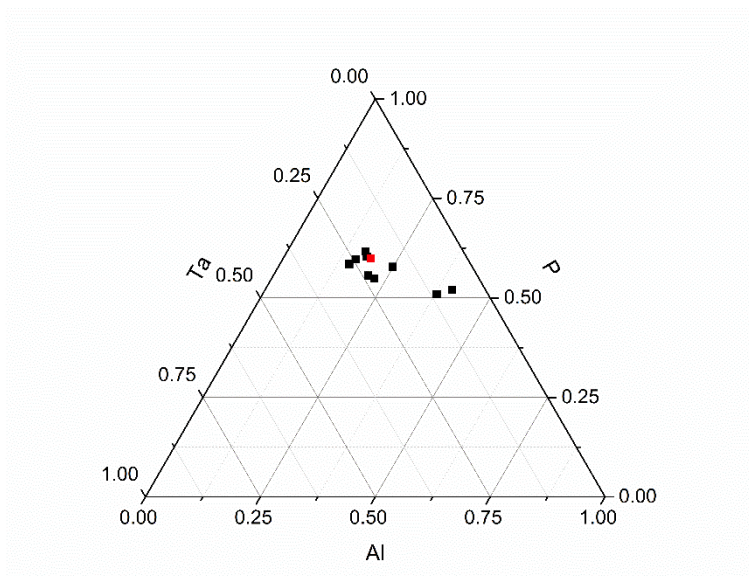


Figure 5.12. TEM-EDX derived Al-P-Ta compositions for the sample $\text{Li}_{0.875}\text{Ta}_{1.062}\text{Al}_{0.938}\text{P}_3\text{O}_{12}$ made with 8.9 % Li excess and 21.3 % P excess (sample 5). The nominal composition is marked in red.

The main conclusion from the discussion of the two Al-P-Ta ternary diagrams is that sample 1 could be single phase, but not sample 2 that could be an overlay of close compositions. The increase in P excess increases the dispersion and multiplicity of the phases around the nominal composition. This compositional variation can explain both the peak broadening and the peak splitting because, in general, different compositions have different lattice parameters.

5.2.3 Diffraction and refinements

From the two samples scaled up, sample 1 is selected for AC impedance and high resolution diffraction analysis. For PXRD the sample was loaded in a borosilicate capillary of 0.2 mm diameter. The PXRD dataset was collected with synchrotron X-ray radiation at the beamline I11 in Debye-Scherrer geometry with the MAC detectors at Diamond Light Source. The dataset analysed here was re-binned to a step size of 0.004° .

Due to the spread of the TEM-EDX data for this sample on figure 5.11, a Pawley fit was performed with the triclinic model. The software Topas academic version 5 [32] was used for this refinement. The 2θ range is set to refine from 5° to 60° . The number of coefficients of the Chebyshev-type background were set to 24 in order to achieve a good fit. The peak shape used was Pearson VII. The two AlPO_4 phases were fitted with their Rietveld models. The graphical output of the fit is shown in figure 5.13. The output parameters of the fit are shown in table 5.8.

In conclusion, the fit in figure 5.13 indicates that the triclinic model explains very accurately the diffraction pattern of sample 1, suggesting that sample 1 is a single phase sample.

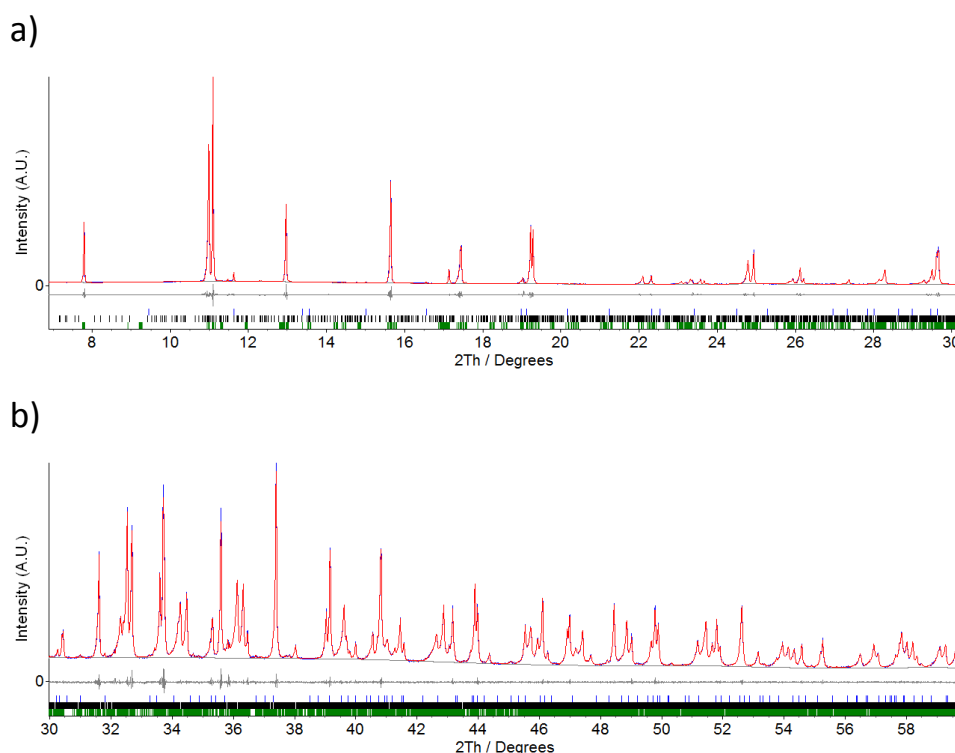


Figure 5.13. Synchrotron PXRD pattern of sample 1, i.e. $\text{Li}_{0.925}\text{Ta}_{1.062}\text{Al}_{0.938}\text{P}_{3.16}\text{O}_{12+x}$. Multiphase mixed Rietveld/Pawley fit, red, to the data, blue. Background and difference are plotted in grey. Green tick marks represent the NASICON analogue $\text{P}\bar{1}$ phase (Pawley). Blue and black tick marks represent the impurity phases AlPO_4 $\text{C}222_1$ and AlPO_4 $\text{P}1\text{c}1$ respectively (Rietveld for both). $R_{\text{wp}} = 4.668\%$.

Table 5.8. Refined unit cell parameters and refinement fit factors for sample 1, i.e. $\text{Li}_{0.925}\text{Ta}_{1.062}\text{Al}_{0.938}\text{P}_{3.16}\text{O}_{12+x}$ from a Pawley refinement with Pearson VII peak shape and the triclinic cell. Error shown as 1 e.s.d.

Space group	$P\bar{1}$
a / Å	8.56215(4)
b / Å	8.54897(3)
c / Å	21.26383(10)
α / °	90.2718(3)
β / °	89.6084(3)
γ / °	120.1749(2)
Volume / Å ³	1345.520(2)
R _{wp}	4.668 %
R _{exp}	1.524 %

5.2.4 Densification

The densification of this material was optimised in several steps for samples of the overall stoichiometry $\text{Li}_{0.925}\text{Ta}_{1.062}\text{Al}_{0.938}\text{P}_{3.16}\text{O}_{12+x}$, sample 1 from table 5.6, and builds on the methodology developed for the Ca-containing samples that will be described later on in this chapter. Here a comparison of sintering with binders is presented in order to determine the effect in relative density.

To produce high density pellets of $\text{Li}_{0.925}\text{Ta}_{1.062}\text{Al}_{0.938}\text{P}_{3.16}\text{O}_{12+x}$ the processing consisted of ball milling, cold isostatic pressing and synthetic air drying and sintering. In total nine pellets have been produced at 900 °C, 1000 °C and 1100 °C. At each temperature 3 pellets were produced, i.e. one for the powder alone, one with the binder Butvar at 2 weight % mixed in ethanol and one with the binder polyvinyl alcohol, PVA, at 2 weight % mixed in distilled water. The binder is mixed in the ball milling step. The slurry is dried under stirring at 50-60 °C. It is important to keep this drying temperature low in order to prevent the polymerisation of the binder in this step.

Pellets were pressed in a 10 mm diameter pellet die with a load of 1 Ton for the powder without binder and 500 Kg for the powders with binder. Each pellet is about 190 mg and powders with binder are much easier to make into pellets which allows the use of lower pressure. The pellets are then subject to cold isostatic pressing under a pressure of 207 MPa.

The sintering at each temperature is made at the same time for the three different pellets. The three pellets are put together and surrounded by sacrificial powder of the same composition. A thin layer of the same powder also lies between the pellets. This is contained in a platinum pouch that only touches the sacrificial powder. The Pt pouch is then placed in a boat alumina crucible.

The sintering is carried out in a tube furnace with flow of synthetic air. The temperature program consists of heating at 2 °C/min up to 250 °C and dwell for 8 hours in order to dry the samples. Then heating at 2 °C/min up to 650 °C and dwell for 1 hour in order to get rid of the binder. Then heating at 2 °C/min up to the sintering temperature and dwell for 6 hours in order to achieve the densification. Finally the furnace is cooled at 10 °C/min to room temperature. The pellets are measured and weighed and their densities are shown in table 5.9. As it can be seen in the table, in general Butvar improves relative density about 1 % versus no binder, while PVA produces lower densities.

Both sides of all pellets in table 5.9 were studied by laboratory XRD. All patterns overlap without significant mismatch showing the same level of purity for all samples as the original powder had, and showing that the sintering temperature in these ranges or the binder have not affected purity.

Table 5.9 Table with relative densities for pellets of nominal composition $\text{Li}_{0.925}\text{Ta}_{1.062}\text{Al}_{0.938}\text{P}_{3.16}\text{O}_{12+x}$.

Binder used	Sintering temperature	Relative density
None	900 °C	92.6 %
	1000 °C	93.7 %
	1100 °C	92.5 %
Butvar	900 °C	93.8 %
	1000 °C	94.8 %
	1100 °C	91.2 %
PVA	900 °C	89.3 %
	1000 °C	89.7 %
	1100 °C	87.7 %

5.2.5 Conductivity of $\text{Li}_{0.925}\text{Ta}_{1.062}\text{Al}_{0.938}\text{P}_{3.16}\text{O}_{12+x}$ sintered at 900 °C and 1000 °C

AC impedance measurements have been performed on the samples sintered at 1000 °C without binder and with Butvar from table 5.9, because these show the best density in each group. After comparing both, the sample sintered at 900 °C without binder was also studied. The samples were measured in synthetic air.

Close to room temperature the impedance Nyquist plot of the samples shows a bulk arc in the high frequency region with corrected capacitance of about $3 \times 10^{-12} \text{ F cm}^{-1}$. This is shown in figure 5.14.a from data collected at 100 °C and corresponds to a frequency range from 1 MHz to 100 kHz. The grain boundary arc can be fitted from the same dataset, see the arc between 1 kHz and 1 Hz in figure 5.14.b, with corrected capacitance in the range $2 \times 10^{-9} - 2 \times 10^{-8} \text{ F cm}^{-1}$. Finally a spike due to the electrode response is seen at low frequencies, between 0.1 Hz and 0.01 Hz in figure 5.14.b. The R and C values from each arc have been obtained from single arc fitting to the data by using the software Zview [33].

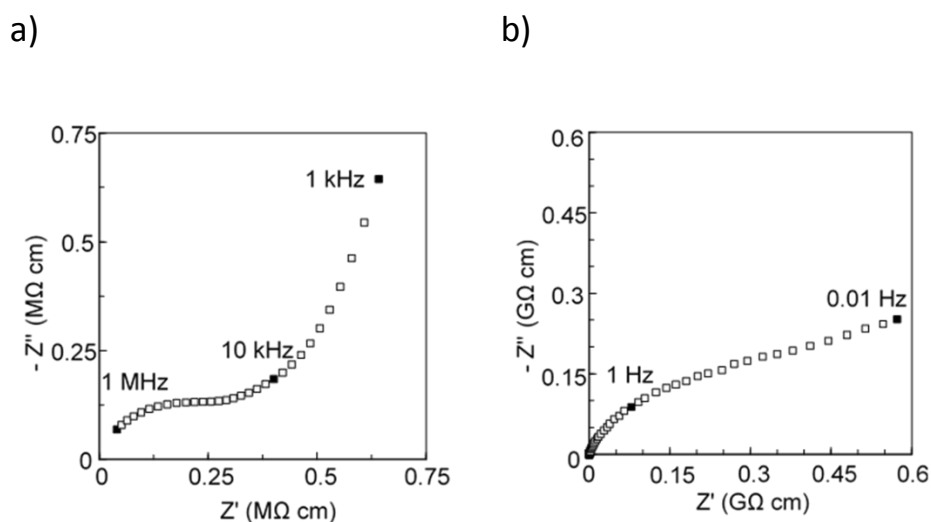


Figure 5.14. Complex plane impedance plot at 100 °C from the sample sintered at 1000 °C without binder. The detail of the high frequencies, 3 decades, is shown in a). The full dataset, 8 decades, is shown in b). These plots have been corrected for sample geometry.

When the temperature increases, the bulk element shifts to higher frequencies than the instrument can observe, i.e. above 1 MHz. This can be seen in figure 5.15.a from data collected at 300 °C where the observable arc at the high frequency end corresponds to the grain boundary, which is the same arc that can be seen in figure 5.15.b. The spike due to the electrode response is seen at low frequencies, between 10 Hz and 0.01 Hz in figure 5.15.b. The R and C values from the grain boundary arc have been obtained from single arc fitting to the data by using the software Zview [33]. In cases like this, the R value from the bulk has been obtained from the low intercept of the fit to the grain boundary arc with the Z' axis.

The conductivity for the two electroactive elements of each sample have been derived from the impedance data as explained above. The conductivity data have been used to produce an Arrhenius plot that compares the results for all three selected samples and is shown in figure 5.16.

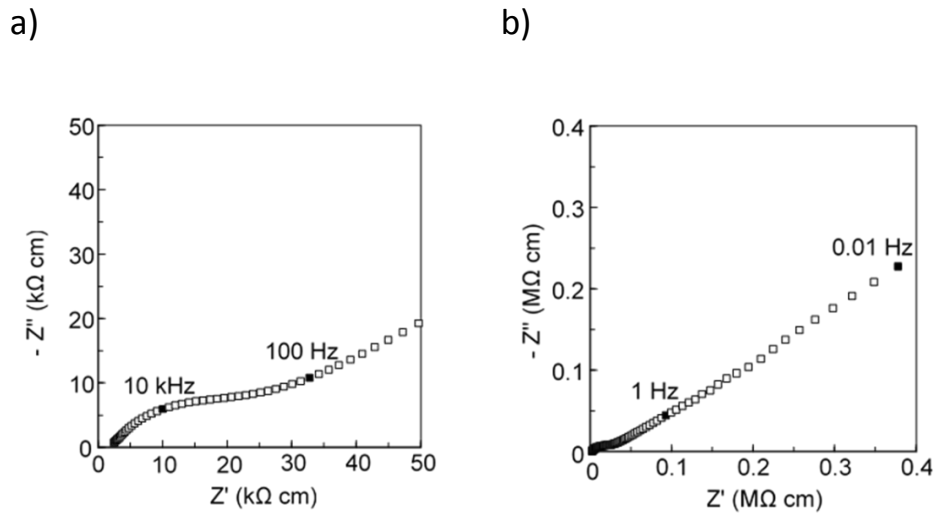


Figure 5.15. Complex plane impedance plot at 300 °C from the sample sintered at 1000 °C without binder. The detail of the high frequencies, 4 decades, is shown in a). The full dataset, 8 decades, is shown in b). These plots have been corrected for sample geometry.

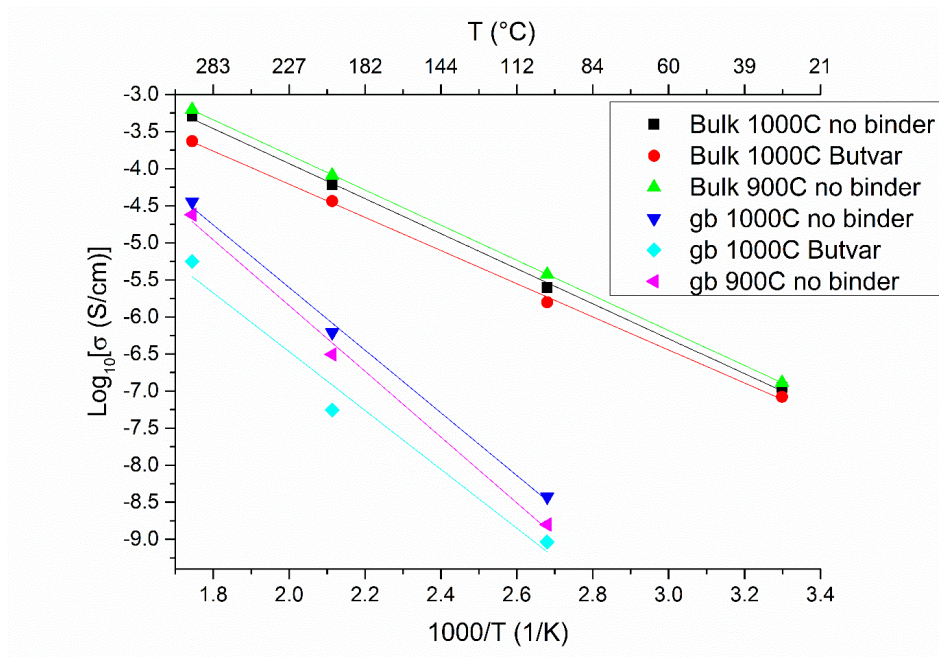


Figure 5.16. Arrhenius plot for selected samples from table 5.9. Bulk and grain boundary, gb, markers are indicated on the plot for each sample.

As can be seen in the Arrhenius plot, for the two samples sintered at 1000 °C, the one without binder has higher bulk and grain boundary conductivities than the one sintered with Butvar. Further comparison with the sample sintered at 900 °C without binder shows that the bulk conductivity is slightly higher for this sample while the grain boundary conductivity is slightly lower but still better than for the sample sintered with Butvar.

The activation energies for each sample are listed in table 5.10. As it can be seen in the table, the value for the bulk is about 0.47 eV with slightly lower value for the sample sintered with Butvar. For the grain boundary the value lies in the range 0.8 – 0.9 eV.

Table 5.10. Activation energies for both electroactive elements of the measured samples. Errors shown as 1 σ .

Sample	Bulk E_a / eV	Grain boundary E_a / eV
Sintered at 1000 °C with no binder	0.468(11)	0.84(5)
Sintered at 900 °C with no binder	0.4694(11)	0.88(6)
Sintered at 1000 °C with Butvar	0.443(10)	0.79(12)

The best bulk conductivity at 30 °C was measured for the pellet without binder sintered at 900 °C, for which the value is $1.3 \times 10^{-7} \text{ S cm}^{-1}$, similar to the literature value given for the total conductivity of $\text{LiTaAl}(\text{PO}_4)_3$ which is $6.5 \times 10^{-7} \text{ S cm}^{-1}$. On the other hand, the activation energy obtained for the bulk in this study is the same that is reported in literature for the total conductivity [24].

5.3 Li-Ta-Ca-Al-P-O series constrained to $\text{Li}_{2x}[\text{Ta}_{1.55-x}\text{Ca}_{0.11}\text{Al}_{0.33+x}](\text{PO}_4)_3$

5.3.1 Synthesis

5.3.1.1 Samples of $\text{Li}_{1.55}\text{Ta}_{0.78}\text{Ca}_{0.11}\text{Al}_{1.11}\text{P}_3\text{O}_{12}$ with a range of P excess

The initial target of this system had nominal composition $\text{Li}_{1.55}\text{Ta}_{0.78}\text{Ca}_{0.11}\text{Al}_{1.11}\text{P}_3\text{O}_{12}$ which was initially synthesised with additional 5 % of Li excess and additional 20 % of P excess following optimisation carried out by Dr Chris Collins who helped me to start with the NASICON project.

The synthesis of the samples were made by conventional solid state ceramic route using high purity reactants: Li_2CO_3 99.997 % from Sigma-Aldrich, Ta_2O_5 99.99 % from Alfa Aesar, CaCO_3 99.95 % from Alfa Aesar, $\gamma\text{-Al}_2\text{O}_3$ 99.997 % from Alfa Aesar and $(\text{NH}_4)\text{H}_2\text{PO}_4$ 99.999 % from Sigma-Aldrich. All starting materials were dried at 200 °C with the exception of $(\text{NH}_4)\text{H}_2\text{PO}_4$ that was used as received. For all the samples in this section the reactant Al_2O_3 has been considered pure and the correction presented in appendix 5.1 has not been used.

Reactants were ground with ethanol in an agate pestle and mortar for 30 minutes. When the paste was dry, it was transferred to a Pt crucible which finally was covered with an alumina lid. The crucibles were then placed in a temperature calibrated box furnace and the temperature profile used was as follows: heating at 0.5 °C/min to 300 °C and dwell for 4 hours. Then heating up at 10 °C/min to 900 °C and dwell for 24 hours. Finally it is cooled at 10 °C/min to room temperature.

The powders were thoroughly ground in a pestle and mortar and then placed back into Pt crucibles with alumina lid and put back into the box furnace for a second firing. The temperature profile was: heating up at 10 °C/min to 900 °C and dwell for 24 hours. Then it was cooled down at 10 °C/min to room temperature. The resulting powders were finely ground and placed in vials. Laboratory PXRD were collected for all the samples.

This synthesis was replicated for a set of samples with the same nominal composition of $\text{Li}_{1.55}\text{Ta}_{0.78}\text{Ca}_{0.11}\text{Al}_{1.11}\text{P}_3\text{O}_{12}$ with still an additional fixed 5 % Li_2CO_3

excess, but with a range of $(\text{NH}_4)\text{H}_2\text{PO}_4$ excesses varying in the range from 20 to 70 % in order to study the phase evolution.

Pawley fits to the hexagonal setting of the rhombohedral unit cell in the space group $R\bar{3}c$ was performed for all the samples. Stephens's hexagonal peak shape [31] was used in order to account for the observed hkl dependant profile broadening. The c/a ratio and the unit cell volume for all these samples are shown in figure 5.17.

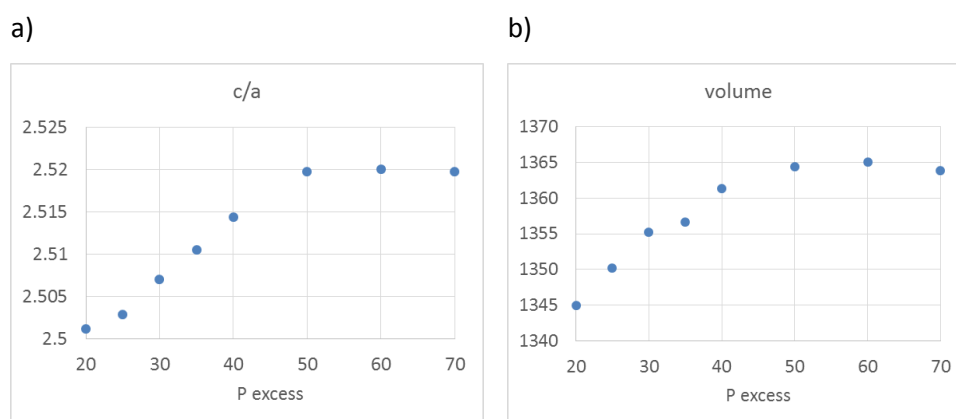


Figure 5.17. a) c/a ratio for the unit cell parameters of the series of samples of nominal composition $\text{Li}_{1.55}\text{Ta}_{0.78}\text{Ca}_{0.11}\text{Al}_{1.11}\text{P}_3\text{O}_{12}$ exploring a range of P excess. All samples were made with 5 % Li excess. b) Unit cell volume / Å^3 for the same set of samples. Volume errors are smaller than the dot size (1 e.s.d. $< 0.2 \text{ Å}^3$ for all samples but for 70 % sample for which 1 e.s.d. $< 0.45 \text{ Å}^3$).

Both quantities being studied, the c/a ratio and the unit cell volume, follow Vegard's law. They increase linearly up to a limit, 50 % of P excess, and then reach a plateau. The samples forming the plateau also exhibit a new impurity. The impurity before the plateau was AlPO_4 . In the plateau the impurity that arises is $\text{Ta}_{0.5}\text{Al}_{0.5}\text{P}_2\text{O}_7$. This lattice parameter determination was made without internal standard.

The Stephens's parameters that account for the anisotropic strain of the rhombohedral phase profile are plotted in figure 5.18. Zeta is the Lorentzian mixing parameter, i.e. the refined fraction of Lorentzian vs Gaussian in the peak shape. For each (h k l) reflection, s004 indicates the broadening in the l direction, s400

indicates the broadening in the h and k directions (a = b in the hexagonal crystal system) and s202 indicates de broadening that happens in both directions, h and l.

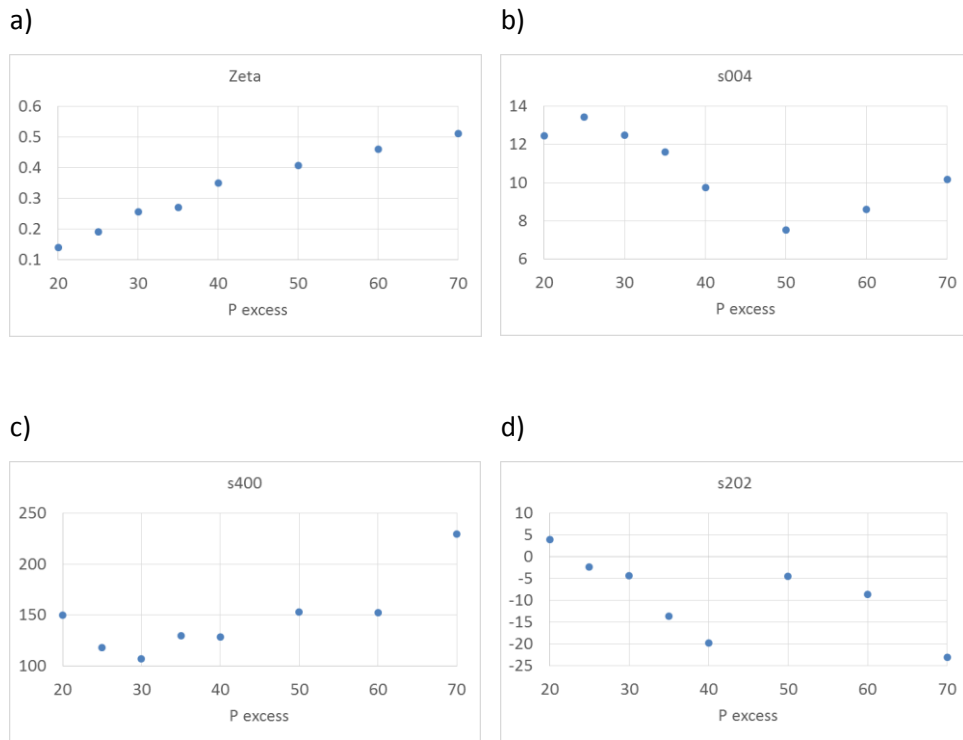


Figure 5.18. Refined Stephens's parameters that describe the anisotropic strain for the set of samples of nominal composition $\text{Li}_{1.55}\text{Ta}_{0.78}\text{Ca}_{0.11}\text{Al}_{1.11}\text{P}_3\text{O}_{12}$ with 5 % Li excess and with a range of 20 to 70 % of P excess. Zeta, the Lorentzian mixing parameter, is shown in a), s004, s400 and s202 are shown in b), c) and d) respectively.

It can be seen from figure 5.18 that the Lorentzian fraction increases with P excess. s400 shows no correlation with P excess, while s004 and s202 show clear change when the plateau is reached. The diffraction pattern for the samples with 40 % and 70 % P excesses are shown in figure 5.19 and 5.20.

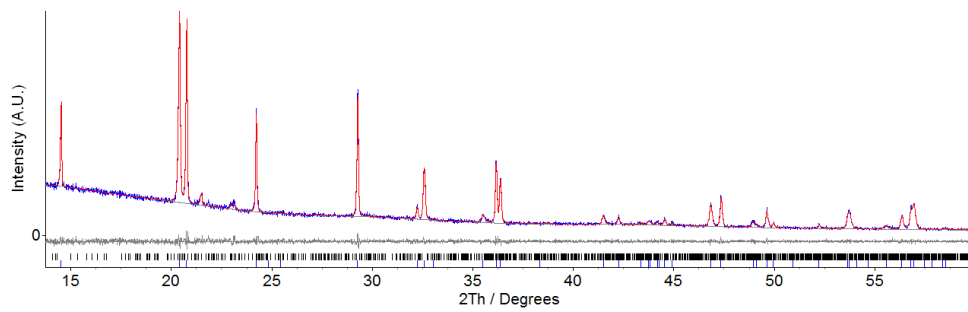


Figure 5.19. Cu $K\alpha_1$ PXRD pattern of $\text{Li}_{1.55}\text{Ta}_{0.78}\text{Ca}_{0.11}\text{Al}_{1.11}\text{P}_3\text{O}_{12}$ made with 5 % Li excess and 40 % P excess. Multiphase mixed Rietveld/Pawley fit, red, to the data, blue. Background and difference are plotted in grey. Blue tick marks represent the NASICON analogue phase (Pawley). Black tick marks represent the impurity phase AlPO_4 (Rietveld).

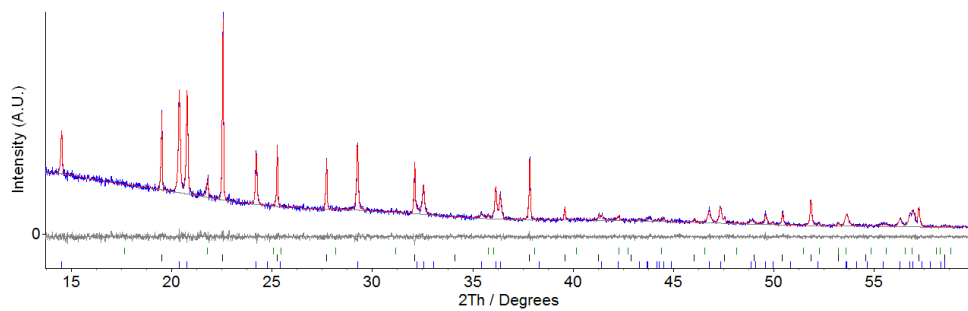


Figure 5.20. Cu $K\alpha_1$ PXRD pattern of $\text{Li}_{1.55}\text{Ta}_{0.78}\text{Ca}_{0.11}\text{Al}_{1.11}\text{P}_3\text{O}_{12}$ made with 5 % Li excess and 70 % P excess. Multiphase mixed Rietveld/Pawley fit, red, to the data, blue. Background and difference are plotted in grey. Blue tick marks represent the NASICON analogue phase (Pawley). Green and black tick marks represent the impurity phases AlPO_4 and $\text{Ta}_{0.5}\text{Al}_{0.5}\text{P}_2\text{O}_7$ respectively (Both as Rietveld).

The conclusion from this series is that there is a definite change in unit cell volume and c/a ratio that follows Vegard's law, after which it reaches a plateau at the same time that new impurities arise. This is correlated to the amount of P excess in the sample, which also correlates with the peak shape anisotropy observed in the PXRD patterns.

5.3.1.2 Ca_{0.11} line exploration

The samples already presented were still impure. With the aim of pursuing a phase pure sample, more exploration was carried out in the synthetic space of this system. The impurity found below the plateau is AlPO₄ which could mean that there is an excess of Al in the precursor mixture. This is suggesting to search for a sample with less Al in. The fraction of Ca on the M site is kept the same for this search because one of the aims of this section is to introduce Ca in the NASICON framework.

If we consider a fixed amount of Ca in the ternary diagram of Ta-Ca-Al for the M site of the NASICON structure, when the Al content is reduced, the Ta fraction is increased, reducing also the level of Li to meet the charge balance. This can be seen in figure 5.21 where the composition already explored is plotted as a filled red square. The set of new samples is plotted as open blue squares and the one that appeared phase pure in laboratory diffractometer is plotted as a filled green square. In addition, the literature composition Li_{1.2}Ta_{0.9}Al_{1.1}P₃O₁₂ reported by Thangadurai et al. [24] is plotted as a black circle for comparison.

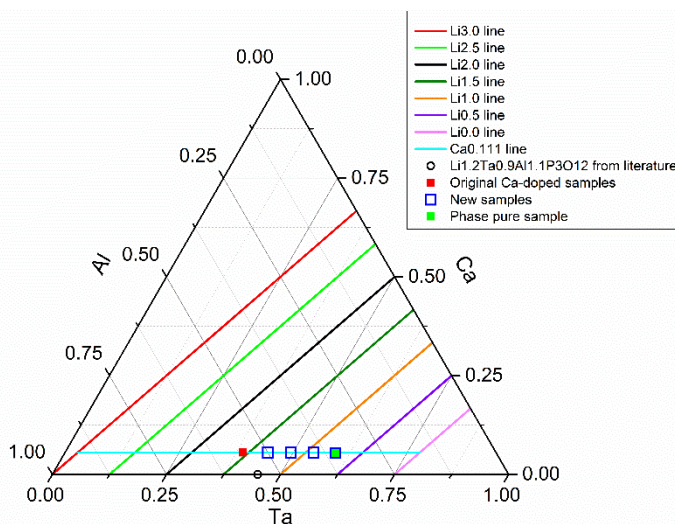


Figure 5.21. Ternary diagram showing the synthetic space in Ta-Ca-Al for the M site of the NASICON-type structure. The coloured contour lines indicate the amount of Li per formula unit that would correspond to a NASICON analogue with those cation ratios on the M site. The coloured squares represent the samples that were synthesised, as explained in the legend and in the text.

All the new samples were made by adding 5 % of Li excess and 20 % of P excess to the nominal compositions. Similar study of the c/a ratio and the unit cell volume was carried out on this samples of the series $\text{Li}_{2x}[\text{Ta}_{1.555-x}\text{Ca}_{0.11}\text{Al}_{0.333+x}](\text{PO}_4)_3$. The quantities c/a and unit cell volume / \AA^3 derived from Pawley fits to the hexagonal setting of the $R\bar{3}c$ unit cell are shown in figure 5.22. This lattice parameter determination was made with no internal standard. The c/a ratio can be compared with the values in figure 5.17. In figure 5.22 no plateau has been reached but the sample for $x = 0.366$ has reached a c/a value beyond the plateau in figure 5.17 which would indicate that this is a different composition. When the Stephens's anisotropic strain parameters for the same sample with $x = 0.366$, shown in figure 5.23 are compared with those in figure 5.18 it can be seen that the Lorentzian mixing parameter, s_{004} and s_{400} are very similar. This result would suggest that the peak anisotropy is not correlated with the Ta/Al ratio.

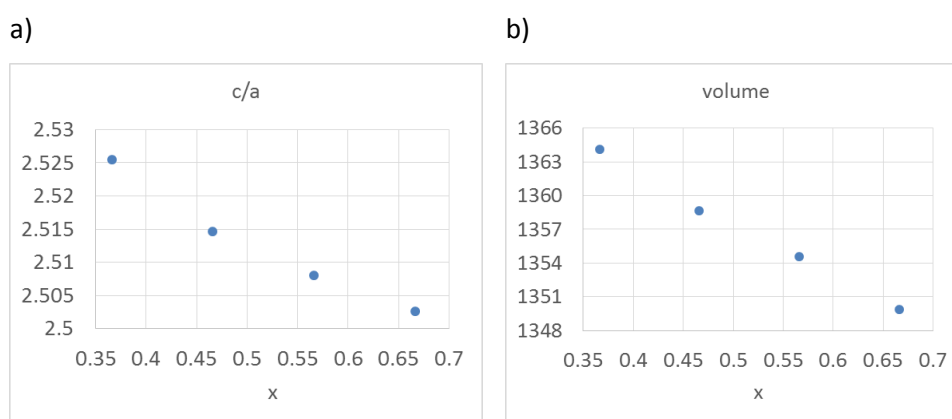


Figure 5.22. a) c/a ratio for the unit cell parameters of the samples of nominal composition $\text{Li}_{2x}[\text{Ta}_{1.555-x}\text{Ca}_{0.11}\text{Al}_{0.333+x}](\text{PO}_4)_3$ with $x = 0.366, 0.466, 0.566$ and 0.666 . All samples were made with additional 5 % Li excess and 20 % P excess with respect to the nominal composition. b) Unit cell volume / \AA^3 for the same set of samples. Volume errors are smaller than the dot size (1 e.s.d. $< 0.1 \text{\AA}^3$ for all samples).

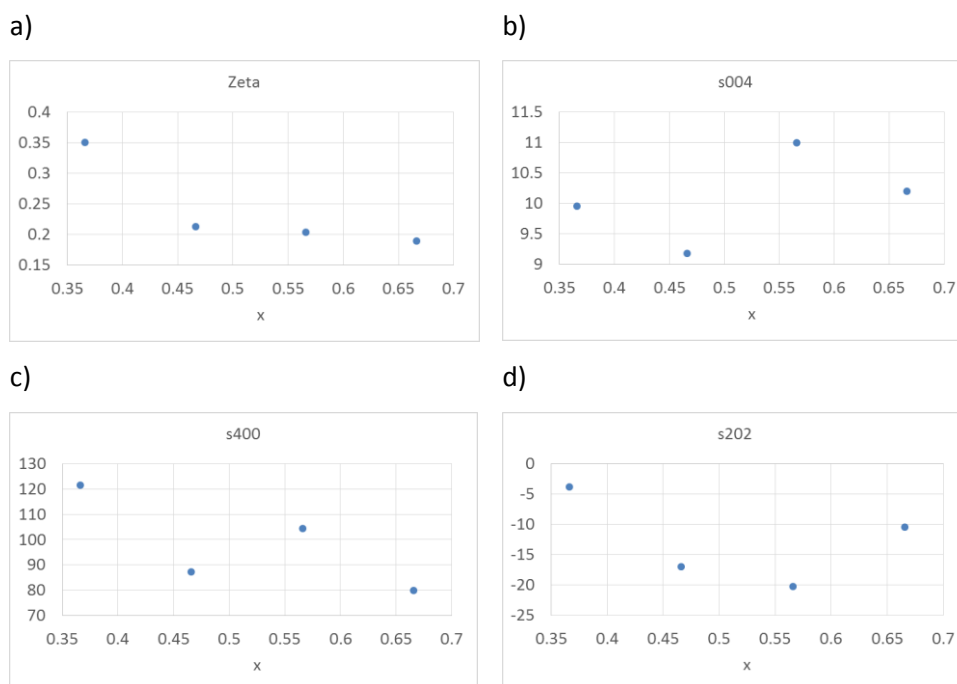


Figure 5.23. Refined Stephens's parameters that describe the anisotropic strain for the same set of samples of nominal composition $\text{Li}_{2x}[\text{Ta}_{1.555-x}\text{Ca}_{0.11}\text{Al}_{0.333+x}](\text{PO}_4)_3$ with $x = 0.366, 0.466, 0.566$ and 0.666 . All samples were made with additional 5 % Li excess and 20 % P excess with respect to the nominal composition. Zeta, the Lorentzian mixing parameter, is shown in a), s004, s400 and s202 are shown in b), c) and d) respectively.

Samples for $x = 0.566$ and 0.666 show the same impurity phase observed before for the range of P excesses in samples of nominal composition $\text{Li}_{1.55}\text{Ta}_{0.78}\text{Ca}_{0.11}\text{Al}_{1.11}\text{P}_3\text{O}_{12}$, i.e. AlPO_4 $P1c1$. The pattern for $x = 0.566$ is shown in figure 5.24. For the sample with $x = 0.466$, a second polymorph of AlPO_4 appear, i.e. AlPO_4 $P1c1$ and AlPO_4 $C222_1$ are observed at the same time.

Finally the sample for $x = 0.366$ showed to be phase pure, i.e. the composition $\text{Li}_{0.734}\text{Ta}_{1.187}\text{Ca}_{0.108}\text{Al}_{0.705}\text{P}_3\text{O}_{12}$, as can be seen in figure 5.25. Although this composition has less Li than the non-doped sample described in literature, the fact that it showed a clean hexagonal phase made it interesting to scale it up for further studies.

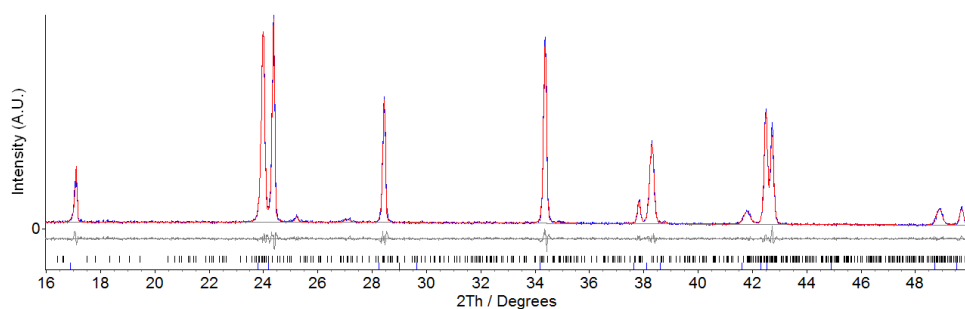


Figure 5.24. Co $K\alpha_1$ PXRD pattern of $\text{Li}_{1.13}\text{Ta}_{0.99}\text{Ca}_{0.11}\text{Al}_{0.9}\text{P}_3\text{O}_{12}$ made with 5 % Li excess and 20 % P excess. Multiphase mixed Rietveld/Pawley fit, red, to the data, blue. Background and difference are plotted in grey. Blue tick marks represent the NASICON analogue phase (Pawley). Black tick marks represent the impurity phase AlPO_4 (Rietveld).

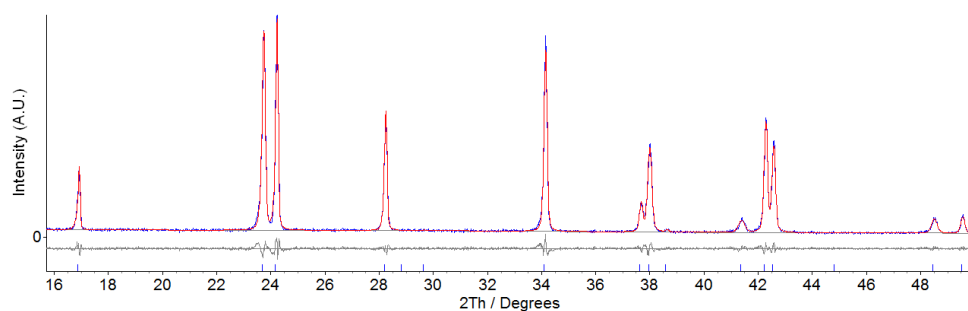


Figure 5.25. Co $K\alpha_1$ PXRD pattern of $\text{Li}_{0.734}\text{Ta}_{1.187}\text{Ca}_{0.108}\text{Al}_{0.705}\text{P}_3\text{O}_{12}$ made with 5 % Li excess and 20 % P excess. Pawley fit, red, to the data, blue. Background and difference are plotted in grey. Blue tick marks represent the NASICON analogue phase.

5.3.1.3 Scaled up sample

The best sample found so far is $\text{Li}_{0.734}\text{Ta}_{1.187}\text{Ca}_{0.108}\text{Al}_{0.705}\text{P}_3\text{O}_{12}$ made with 5 % Li excess and 20 % P excess. The c/a ratio, unit cell volume and Stephens's anisotropic strain parameters have already been discussed. The sample is scaled up for neutron diffraction and property measurements. The low temperature step was modified after small scale exploration in order to avoid the precursor foaming from overflow the sides of the crucible.

For the large sample, 5 grams, the precursor mixture was milled by using a Fritsch Pulverisette 7 planetary mill with zirconia milling material. The milling time was of 7.5 hours. The heat treatments were carried out in Pt crucibles inside a box furnace. The first heat treatment consisted of a heating ramp from room temperature to 300 °C at 0.5 °C/min but for the range 150-200 °C that was at 0.1 °C/min, then held for 4 hours at 300 °C and cooled down to room temperature at 10 °C/min. The resulting solid is then ground in agate pestle and mortar and put back to the Pt crucible for the second heat treatment which is at 900 °C for 24 hours with heating and cooling rates of 10 °C/min. For this sample, the second firing at 900 °C was not given. The sample was ground to fine powders and saved in a vial.

Laboratory PXRD showed that there is a majority $R\bar{3}c$ phase identified as the Li-containing NASICON analogue and the minority phase $AlPO_4$ $C222_1$ for $Li_{0.734}Ta_{1.187}Ca_{0.108}Al_{0.705}P_3O_{12}$ as can be seen in figure 5.26.

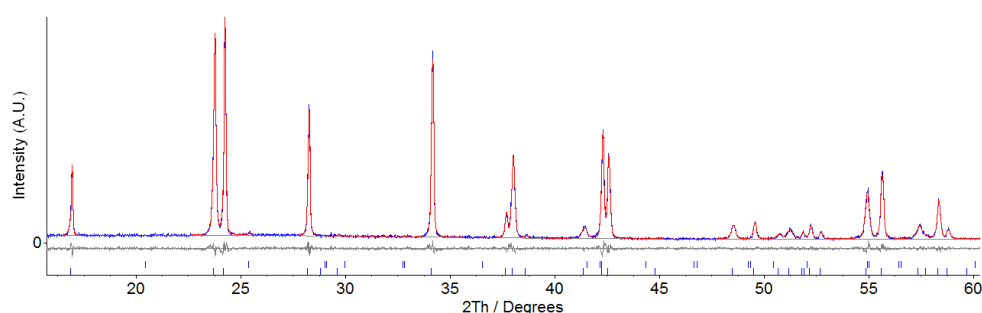


Figure 5.26. Co $K\alpha_1$ PXRD pattern of $Li_{0.734}Ta_{1.187}Ca_{0.108}Al_{0.705}P_3O_{12}$ made with 5 % Li excess and 20 % P excess. Multiphase mixed Rietveld/Pawley fit, red, to the data, blue. Background and difference are plotted in grey. Blue tick marks represent the NASICON analogue phase. Black tick marks represent the impurity phase $AlPO_4$ (Rietveld).

As previously stated, for the Ca-containing samples, the TGA correction for alumina has not been applied to the nominal compositions. If the sample were corrected for the alumina deficiency, the nominal composition for this sample would be $Li_{0.715}Ta_{1.197}Ca_{0.109}Al_{0.694}P_3O_{12}$. The corresponding new Li and P excesses have not been calculated. The corrected composition is not very different from the original one. Because of that and for keeping unity, during the rest of the chapter the

sample will be referred to using the original nominal composition. The correction has been highlighted because it was considered of importance for the synthesis of these and other systems using the same precursor for aluminium.

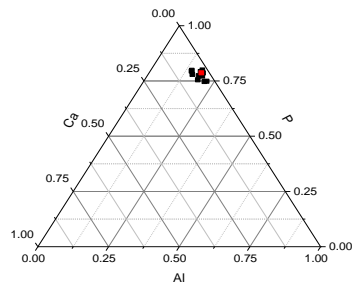
5.3.2 TEM-EDX

TEM-EDX analysis was performed in order to confirm the chemical composition of the sample that was scaled up, i.e. $\text{Li}_{0.734}\text{Ta}_{1.187}\text{Ca}_{0.108}\text{Al}_{0.705}\text{P}_3\text{O}_{12}$ made with 5 % Li excess and 20 % P excess. The PXRD pattern of this sample is shown in figure 5.26. This sample was also subject to high resolution PXRD and AC impedance measurements. The TEM-EDX data were collected by Dr Marco Zanella. TEM-EDX spectra and data are listed in appendix 5.3.

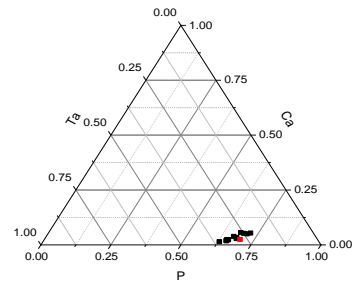
The ternary diagrams derived from TEM-EDX analysis for this sample are shown in figure 5.27, which shows the compositional ratios recovered for all cations but Li. Although the nominal value, shown in red, is approximately in the centre of the measurements, the overall feature is that the dispersion is larger for the panels in which Ta is represented, i.e. panels b), c) and d). This along with the fact that data on panel a) appear more focused, would indicate that the ratio Ca/Al is more stable in the phosphate than the Ta ratio to the other elements. The conclusion is an inhomogeneity in the sample for which the grains with more Ta would have less Li due to charge balance and conversely the grains with less Ta would have more Li. There are no data points to represent the small AlPO_4 impurity seen in PXRD, which is normal because sampling methods usually miss under-represented populations.

From these results the conclusion is that there is a range of compositions in the sample that average the nominal value. Although this composition is not completely single phase, it is the purest Ca-doped sample achieved in large scale so far. This is the sample for which more work is devoted to in the rest of the section.

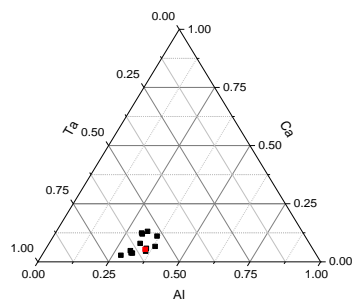
a)



b)



c)



d)

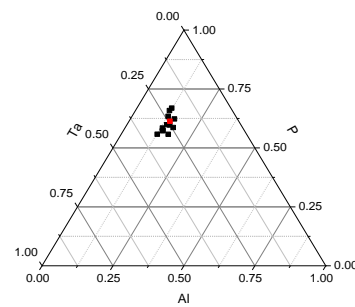


Figure 5.27. TEM-EDX derived compositions for the sample $\text{Li}_{0.734}\text{Ta}_{1.187}\text{Ca}_{0.108}\text{Al}_{0.705}\text{P}_3\text{O}_{12}$ made with 5% Li excess and 20% P excess. The nominal composition is marked in red.

5.3.3 Diffraction and refinements

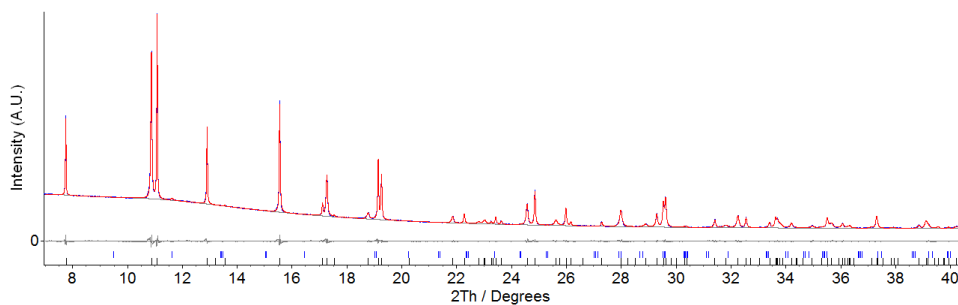
High resolution diffraction data were collected for the scaled up sample of composition $\text{Li}_{0.734}\text{Ta}_{1.187}\text{Ca}_{0.108}\text{Al}_{0.705}\text{P}_3\text{O}_{12}$ made with 5 % Li excess and 20 % P excess. For PXRD the sample was loaded in a borosilicate capillary of 0.2 mm diameter. The PXRD dataset was measured with synchrotron X-ray radiation at the beamline I11 in Debye-Scherrer geometry with the PSD detector at Diamond Light Source.

Due to the spread of the TEM-EDX data for this sample on figure 5.27, a Pawley fit was performed with the hexagonal cell. The software Topas academic version 5 [32] was used for this refinement. The 2θ range is set to refine from 7° to 76° . The number of coefficients of the Chebyshev-type background were set to 24. The peak shape used was Stephens's hexagonal. The AlPO_4 phase was fitted with its Rietveld model. The graphical output of the fit is shown in figure 5.28. The output parameters of the fit are shown in table 5.11. The refined values of the anisotropic strain parameters [31] are shown in table 5.12.

In conclusion, comparing the refinement of this sample with the refinement of $\text{Li}_{0.925}\text{Ta}_{1.062}\text{Al}_{0.938}\text{P}_{3.16}\text{O}_{12+x}$ in figure 5.13, it can be seen that $\text{Li}_{0.734}\text{Ta}_{1.187}\text{Ca}_{0.108}\text{Al}_{0.705}\text{P}_3\text{O}_{12}$ made with 5 % Li excess and 20 % P excess shows a larger unit cell volume that is mainly driven by a longer c axis. This may be in agreement with either a larger Ta/Al ratio or a successful Ca-doping, due to the larger Ca^{2+} ionic radius compared with the other cations in the structure (see table 5.4).

The R_{wp} value of this refinement is much lower than the R_{wp} value for the fit in figure 5.13. The same happens for R_{exp} as can be seen in the corresponding tables for each refinement, meaning that the ratios $R_{\text{wp}}/R_{\text{exp}}$ for each refinement are not far from each other, i.e. both models are of similar quality. The much lower R-factors for this refinement are due to the larger background fraction with respect to the measured intensities of the diffraction pattern. It leads to a larger sum in the denominator of the equations of the R-factors R_{wp} and R_{exp} shown in chapter 2, making both values smaller.

a)



b)

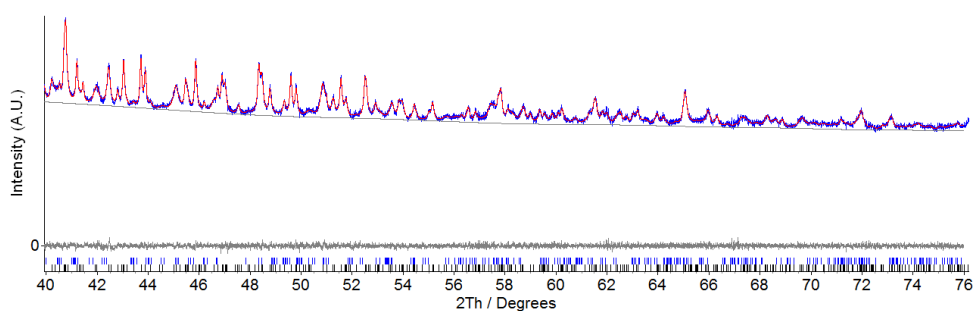


Figure 5.28. Synchrotron PXRD pattern from the sample of composition $\text{Li}_{0.734}\text{Ta}_{1.187}\text{Ca}_{0.108}\text{Al}_{0.705}\text{P}_3\text{O}_{12}$ made with 5 % Li excess and 20 % P excess. Multiphase mixed Rietveld/Pawley fit, red, to the data, blue. Background and difference are plotted in grey. Black tick marks represent the NASICON analogue $R\bar{3}c$ phase (Pawley). Blue tick marks represent the impurity phase AlPO_4 $C222_1$ (Rietveld). $R_{\text{wp}} = 1.253\%$.

Table 5.11. Refined unit cell parameters and refinement fit factors for the sample of composition $\text{Li}_{0.734}\text{Ta}_{1.187}\text{Ca}_{0.108}\text{Al}_{0.705}\text{P}_3\text{O}_{12}$, made with 5 % Li excess and 20 % P excess, from a Pawley refinement with Stephens's hexagonal peak shape and the hexagonal cell. Error shown as 1 e.s.d.

Space group	$R\bar{3}c$
$a / \text{\AA}$	8.55086(9)
$c / \text{\AA}$	21.5563(8)
Volume / \AA^3	1364.98(6)
R_{wp}	1.253 %
R_{exp}	0.367 %

Table 5.12. Refined values of anisotropic strain parameters for the sample of composition $\text{Li}_{0.734}\text{Ta}_{1.187}\text{Ca}_{0.108}\text{Al}_{0.705}\text{P}_3\text{O}_{12}$, made with 5 % Li excess and 20 % P excess. The best fit refining all parameters produce $R_{\text{wp}} = 1.253 \%$. The R_{wp} produced when each anisotropic parameter and ζ are individually set to zero are shown for comparison. ζ is the Lorentzian mixing parameter. Error shown as 1 e.s.d.

Parameter	Value	R_{wp}
S_{400}	83(2)	3.263 %
S_{004}	9.1(3)	2.151 %
S_{202}	-7(2)	1.272 %
ζ	0.71(8)	2.634 %

5.3.4 Densification

The densification of this material was optimised in several steps for samples of the composition $\text{Li}_{0.734}\text{Ta}_{1.187}\text{Ca}_{0.108}\text{Al}_{0.705}\text{P}_3\text{O}_{12}$ made with 5% Li excess and 20% P excess.

Initially using powder ground with pestle and mortar, uniaxial pressing and sintering at 900 °C in air gave a relative density below 70 % as can be seen in table 5.13 for pellets 1 and 2. Then a previously published protocol that focuses in dry atmosphere was used [34]. The powder was dried between 3 to 6 days at 200 °C and the pellet die was kept hot at 70 °C until it was needed. Once on the bench, as soon as the pellet die temperature allowed its manipulation, the powder was loaded in it and the 10 mm diameter pellet was made while still hot by application of a load of 1000 Kg for 10 seconds with the uniaxial press. Then, the firing of pellet 3 was done in O₂ and the sintering of pellet 4 was done in synthetic air for comparison. As it can be seen in table 5.13 for pellets 3 and 4, this method did not offer any advantage with respect to the previous processing. The relative densities in table 5.13 are still low because these were initial trials, and the optimised conditions discovered later were not applied to these samples yet.

Table 5.13. Summary of the sintering optimisation trials at 900 °C for samples of composition $\text{Li}_{0.734}\text{Ta}_{1.187}\text{Ca}_{0.108}\text{Al}_{0.705}\text{P}_3\text{O}_{12}$ made with 5% Li excess and 20% P excess.

Pellet number	Sintering conditions	Sintering gas	Relative density
1	Ramp rates of 5 °C/min 900 °C for 12 hours	Air	63.2 %
2	Ramp rates of 5 °C/min 900 °C for 12 hours	Oxygen	64.5 %
3	Ramp rates of 5 °C/min 900 °C for 12 hours	Oxygen	63.0 %
4	Ramp rates of 5 °C/min 900 °C for 12 hours	Synthetic air	62.9 %

These pellets were crushed and powdered in order to check the phase purity. All four powders resulted of the same level of purity, overlap without significant mismatch and are similar to that of the original sample showed in figure 5.26.

Using fresh powder from the same batch a number of pellets of 8 mm diameter were sintered in air at higher temperatures for 6 hours. These pellets resulted bended or showing lack of regularity and the relative densities measured are less reliable, because it is more difficult to measure their volume with the calliper. For sintering temperatures of 1100 °C, 1200 °C, 1300 °C and 1350 °C, the estimated relative densities were 82.9 %, 82.3 %, 88.1 % and 91.1 % respectively.

These pellets made at higher temperature were crushed and ground to powder in order to check the phase purity at each temperature. An increase in crystallinity is observed with temperature up to 1200 °C while the level of purity of these samples is about the same as for pellets 1 to 4 in table 5.13. See figure 5.29. Samples sintered at 1300 °C showed decomposition into other secondary phases such as TaPO₅ and CaO(Al₂O₃)₂ while for the sample sintered at 1350 °C the impurity TaPO₅ dominates the PXRD pattern. At these high temperatures the loss of P₂O₅ is documented in calcium phosphates [30], which explains the arising impurities such as TaPO₅.

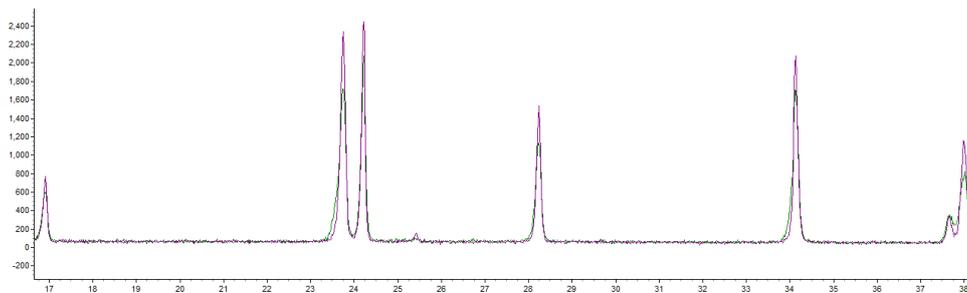


Figure 5.29. Overlapped laboratory diffraction patterns of powders from pellets sintered at 900 °C, green, and 1200 °C, purple. The increased crystallinity can be appreciated. The peak at $2\theta = 25.5^\circ$ is the AlPO₄ reflection.

From table 5.13 it seems that for a fixed temperature, the change in sintering gas or pellet drying has no effect on the densification of this material. The first attempt for improving density without increasing the temperature was to ball mill the powder, then form pellets with pellet die by using the uniaxial press as before, and

finally to apply isostatic pressure with the cold isostatic press. After that, the pellets were sintered in air without any drying pre-treatment at 900 °C and at higher temperatures for comparison, as shown in table 5.14. The heating rate above 900 °C was reduced in order to avoid pellet bending and other regularity defects previously observed when heating at rates of 10 °C/min up to temperatures of 1100 °C or above. All the relative densities were below 90 %. No particle size analysis was performed on these samples.

Table 5.14. Summary of the sintering optimisation trials at selected different temperatures for samples of composition $\text{Li}_{0.734}\text{Ta}_{1.187}\text{Ca}_{0.108}\text{Al}_{0.705}\text{P}_3\text{O}_{12}$ made with 5% Li excess and 20% P excess. The pellets were made from ball milled powder and were cold isostatically pressed.

Pellet number	Sintering conditions	Sintering gas	Relative density
5	Ramp rates of 5 °C/min 900 °C for 12 hours	Air	72.0 %
6	Ramp rate of 10 °C/min to 900 °C then ramp at 2 °C/min to 1300 °C and dwell for 6 hours	Air	85.5 %
7	Ramp rate of 10 °C/min to 900 °C then ramp at 2 °C/min to 1350 °C and dwell for 6 hours	Air	81.2 %

In order to increase the relative densities to levels above 90 %, the optimisation continued. Powders were firstly ball milled in ethanol in amount of 2.5 g for 3 hours using the planetary mill equipment already described. Fractions of 0.2 g of dried powder were made into 10 mm diameter pellets by using uniaxial pressure of 120 MPa. The next step was cold isostatic pressing by using hydrostatic pressure of 200 MPa. Two pellets were placed together and surrounded by powder of the same composition in a Pt pouch. The former sacrificial powder was not ball milled. The Pt pouch contained in a boat alumina crucible was placed in a tube furnace with flow of compressed air from BOC. The temperature was raised from room temperature to 250 °C at 2 °C/min. The pellets were held at that temperature for 8 hours in order

to get the material dried. Then the temperature was raised at 5 °C/min until 900 °C and then at 2 °C/min until 1100 °C. The latter temperature was held for 6 hours in order to allow the material to sinter and densify. Finally the pellets were cooled down at 10 °C/min. After removal of the sacrificial crust, the pellets were slightly polished. Diameter and thickness of the pellets were measured for determination of pellet density. This process was repeated for another two pellets sintered at 1200 °C. A summary with relative densities is shown in table 5.15.

Table 5.15. Summary of the sintering optimisation trials at selected different temperatures for samples of composition $\text{Li}_{0.734}\text{Ta}_{1.187}\text{Ca}_{0.108}\text{Al}_{0.705}\text{P}_3\text{O}_{12}$ made with 5% Li excess and 20% P excess. The pellets were made from ball milled powder, cold isostatically pressed, surrounded of sacrificial powder and packed in a Pt pouch for sintering in synthetic air.

Pellet number	Sintering conditions	Sintering gas	Relative density
8	Ramp rate of 5 °C/min to 900 °C then ramp at 2 °C/min to 1100 °C and dwell for 6 hours	BOC compressed air	90.6 %
9	Ramp rate of 10 °C/min to 900 °C then ramp at 2 °C/min to 1100 °C and dwell for 6 hours	BOC compressed air	90.6 %
10	Ramp rate of 10 °C/min to 900 °C then ramp at 2 °C/min to 1200 °C and dwell for 6 hours	BOC compressed air	91.8 %
11	Ramp rate of 10 °C/min to 900 °C then ramp at 2 °C/min to 1200 °C and dwell for 6 hours	BOC compressed air	90.5 %

Pellets 8 and 11 in table 5.15 were crushed and ground with pestle and mortar. Pellets 9 and 10 were saved as candidates for AC impedance spectroscopy. The phase purity of the pellets sintered at each temperature was assessed from the powders of pellets 8 and 11 by laboratory PXRD. These powders were also submitted for NMR spectroscopy to be carried out within the group of Dr Frédéric Blanc. The NMR data will be published elsewhere. It was observed that the powder

from the pellet sintered at 1200 °C had better crystallinity while both presented about the same level of purity, which was similar to that of the original powder. Powders from samples sintered at 1100 °C and 1200 °C showed about the same relative density. That is why the best densification is considered to be the one at 1100 °C in order to reduce the possibility of Li loss. The AC impedance measurements of pellet 9 will be discussed in the next section.

5.3.5 Conductivity of $\text{Li}_{0.734}\text{Ta}_{1.187}\text{Ca}_{0.108}\text{Al}_{0.705}\text{P}_3\text{O}_{12}$ sintered at 1100 °C

A pellet of $\text{Li}_{0.734}\text{Ta}_{1.187}\text{Ca}_{0.108}\text{Al}_{0.705}\text{P}_3\text{O}_{12}$ made with 5% Li excess and 20% P excess, pellet 9 from table 5.15 with 90.6 % relative density, was selected for AC impedance spectroscopy. Higher relative density would have been desired for impedance measurements, ideally in the range 95 – 100 %. It is not clear why higher densities were not accessible.

Before painting the electrodes for AC impedance measurements, phase purity was assessed with XRD patterns collected from both sides of the pellet. These patterns confirmed that the sintered material conserved the same level of purity as when it was synthesised, containing only an extra weak reflection assigned to AlPO_4 , as described in previous refinements.

For AC impedance measurements silver pasted electrodes were mounted on the sides of the pellet by painting and drying the paste. Silver wires were attached to the electrodes by using the same silver paste. For the pellets with silver electrodes no mesh was used, the wire was attached directly to the pellet with its end folded to help make better adhesion with the silver paste.

AC impedance was measured in synthetic air starting at the higher temperature which was 500 °C. The rest of the temperatures were 400, 300, 200, 100 and 25 °C. Identification of electroactive elements was done with the capacitance values by using the table from Irvine et al. [35].

The AC impedance complex plane plot at 500 °C of the sample can be seen in figure 5.30. Three electroactive elements are visible: at high frequencies a partially visible arc with capacitance of $2 \times 10^{-12} \text{ F cm}^{-1}$ and $\rho = 19.6 \text{ k}\Omega \text{ cm}$ (from high intercept of a fitted arc to the data). This element is assigned to the bulk. At medium frequencies

there is another arc with capacitance of $2 \times 10^{-5} \text{ F cm}^{-1}$ and $\rho = 46.7 \text{ k}\Omega \text{ cm}$ (from circle fit to the data). The capacitance associated with this arc is too large for being due to the grain boundary and therefore is assigned to the electrode response following the table from Irvine et al. [35]. At low frequencies there is a spike which is due to the electrode response.

Not having an arc associated to the grain boundary suggests that the sample is electrically homogeneous, e.g. because it has the same composition as the bulk or the grains make a continuous network without grain boundaries.

For the rest of the discussion electrode response and sample-electrode interface response, as tabulated by Irvine et al [35], will be used as synonyms.

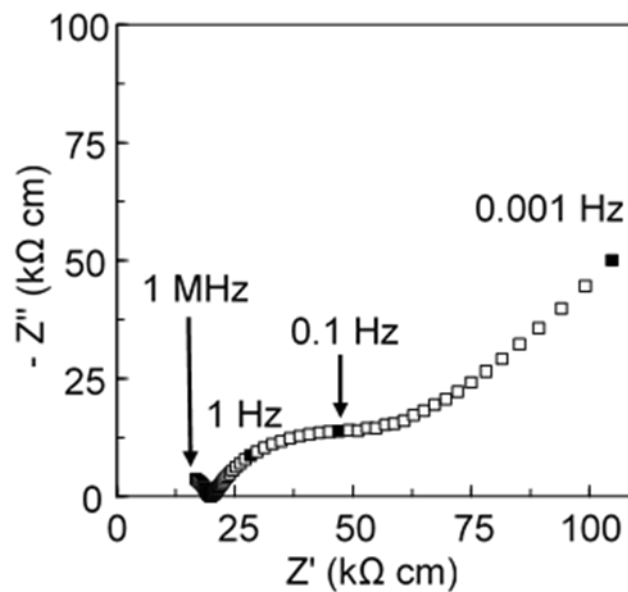


Figure 5.30. AC impedance complex plane plot at 500 °C for a sample of $\text{Li}_{0.734}\text{Ta}_{1.187}\text{Ca}_{0.108}\text{Al}_{0.705}\text{P}_3\text{O}_{12}$ made with 5 % Li excess and 20 % P excess sintered at 1100 °C, with relative density of 90.6 %.

The Nyquist plot of the same sample at 300 °C is shown in figure 5.31. At high and medium frequencies, 1 MHz to 1 kHz, an arc with capacitance of $2 \times 10^{-12} \text{ F cm}^{-1}$ and $\rho = 1.7 \text{ M}\Omega \text{ cm}$ (from high intercept of a fitted arc to the data) can be seen. This arc

is assigned to the bulk. At low frequencies a partially visible arc with capacitance of $1.1 \times 10^{-5} \text{ F cm}^{-1}$ and $\rho = 40 \text{ M}\Omega \text{ cm}$ (from circle fit to the data) which is assigned to the sample-electrode interface for the reason discussed above. In this case the spike is not visible at the low frequency end because it has been shifted outside the minimum observed frequency, i.e. 0.001 Hz.

Finally, at room temperature only the bulk arc can be observed as shown in figure 5.32.

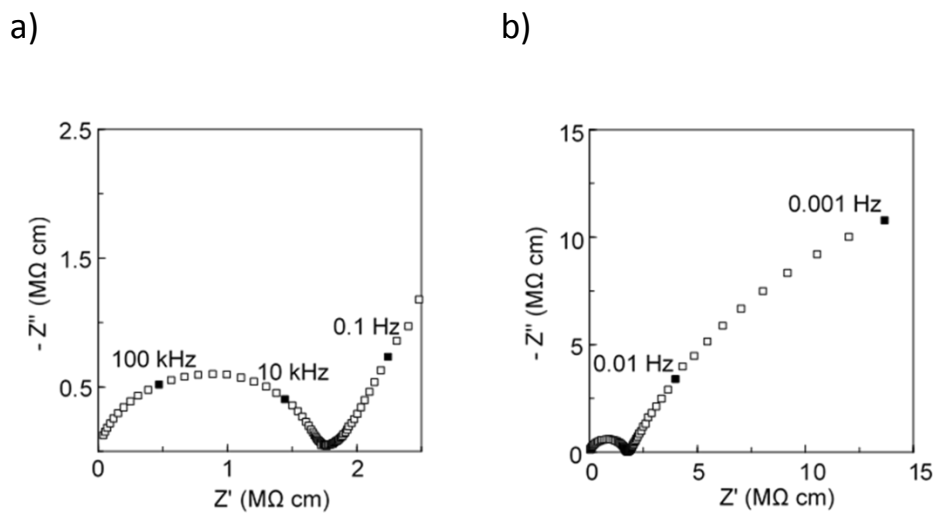


Figure 5.31. AC impedance complex plane plots at 300 °C for a sample of $\text{Li}_{0.734}\text{Ta}_{1.187}\text{Ca}_{0.108}\text{Al}_{0.705}\text{P}_3\text{O}_{12}$ made with 5 % Li excess and 20 % P excess sintered at 1100 °C, with relative density of 90.6 %. The whole dataset is shown in b) and the detail of the high frequency region is shown in a).

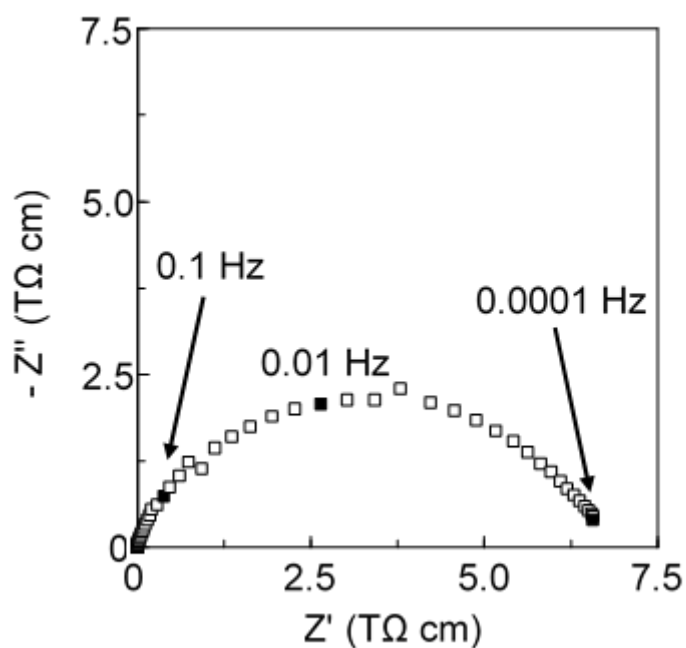


Figure 5.32. AC impedance complex plane plot at 25 °C for a sample of $\text{Li}_{0.734}\text{Ta}_{1.187}\text{Ca}_{0.108}\text{Al}_{0.705}\text{P}_3\text{O}_{12}$ made with 5 % Li excess and 20 % P excess sintered at 1100 °C, with relative density of 90.6 %.

The conductivity values for the two electroactive elements derived from the impedance data have been used to produce an Arrhenius plot that is shown in figure 5.33, from which the activation energies are calculated after the corresponding least squares linear fits.

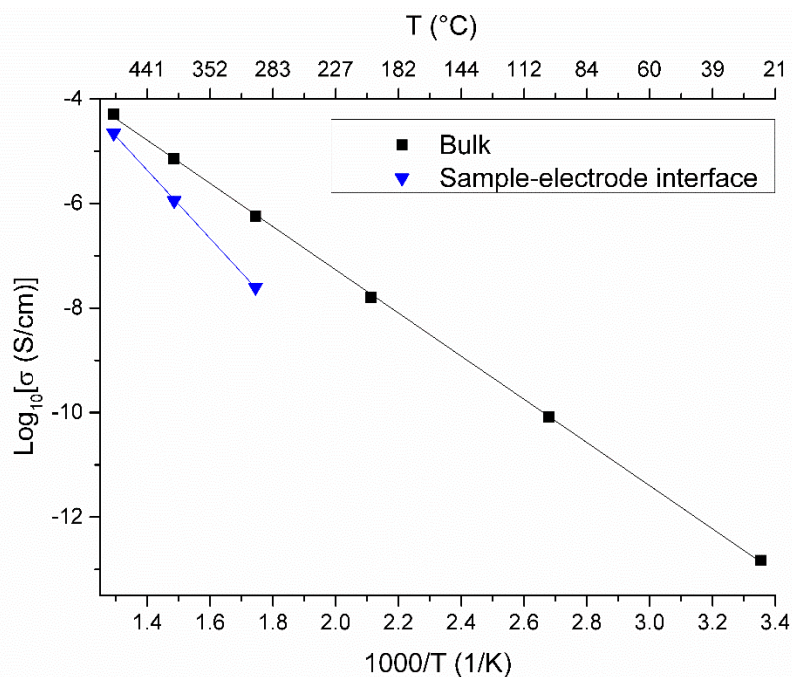


Figure 5.33. Arrhenius plot for the sample of $\text{Li}_{0.734}\text{Ta}_{1.187}\text{Ca}_{0.108}\text{Al}_{0.705}\text{P}_3\text{O}_{12}$ made with 5 % Li excess and 20 % P excess sintered 1100 °C, with relative density of 90.6 %. Bulk and sample-electrode interface markers are indicated on the plot.

The arc associated with the electrode response is only visible or partially visible in the complex plane at or above 300 °C. For the arc assigned to the electrode response, the activation energy has been calculated and is of 1.3 eV. On the other hand the bulk has an activation energy of 0.8 eV and a conductivity at 25 °C of $1.5 \times 10^{-13} \text{ S cm}^{-1}$, which is a very low conductivity.

This material has much lower bulk conductivity than the composition $\text{Li}_{0.925}\text{Ta}_{1.062}\text{Al}_{0.938}\text{P}_{3.16}\text{O}_{12+x}$ studied before for which it was $1.3 \times 10^{-7} \text{ S cm}^{-1}$ at 30 °C. The bulk activation energy is also higher meaning that the Li transport is more difficult in this material. It could be either because of the lower Li content or because of the Ca blocking the diffusion pathways. In order to answer the structural question, a more homogeneous sample would be needed for diffraction studies.

5.4 Li-Ta-Ga-Mg-P-O series

5.4.1 Synthesis

As it was said in the introduction of this chapter, the aim for the study of this system was to try a new combination of atoms, with similar ionic radii among them, which have not been found in NASICON analogues literature. For the new phases, characterisation and property measurements would be carried out. Dr Chris Collins helped me to start with this NASICON project.

The synthesis of this system was very ambitious from the beginning with the intention of exploring the whole ternary phase diagram in Ta-Mg-Ga in the region where potential NASICON analogue phases can form. The synthesis has followed similar standard protocol used in the previous sections, i.e. ceramic solid state route with the higher temperature step at 900 °C and the use of 5% Li excess and 20% of P excess was the experimental strategy. The main difference is that the second firing at 900 °C was not given to these samples and the only additions have been the reactants Ga₂O₃ (99.999 %, Alfa Aesar, dried at 200 °C) and MgO (99.95 %, Alfa Aesar, dried and decarbonated at 950 °C) in order to supply the stoichiometric amounts of elements needed to prepare the samples. The compositions synthesised are presented in figure 5.34.

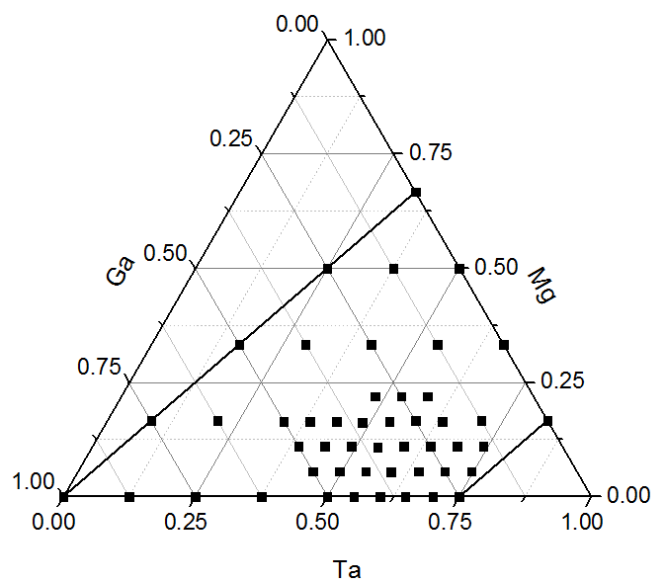


Figure 5.34. Set of synthesised samples, black squares, presented on the ternary phase diagram showing the stoichiometric ratios of Ta-Mg-Ga for the samples of composition $\text{Li}_x\text{Ta}_y\text{Mg}_z\text{Ga}_t\text{P}_3\text{O}_{12}$ where $y + z + t = 2$ and x is calculated to balance the charge, i.e. $x = 9 - 5y - 2z - 3t$. The field where these samples can form is delimited by lines in the diagram.

After the synthesis, all 48 samples were studied by laboratory PXRD. The powder pattern from every sample was searched for the NASICON α phase and for any extra peak. The latter were matched to impurities of sensible compositions for most of the cases. A ternary plot with the outcome of this synthesis is shown in figure 5.35.

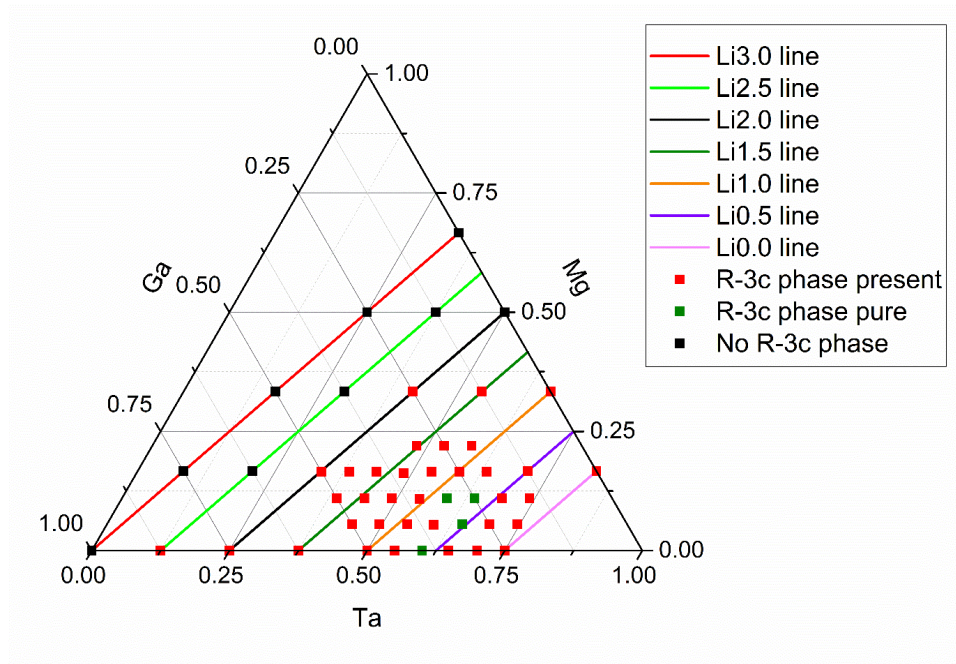


Figure 5.35. Ternary phase diagram with all the samples synthesised for this system. The samples with high purity and those that contain the α -NASICON analogue phase are indicated in green and red respectively.

The typical Pawley fits to laboratory PXRD data are shown in figures 5.36 and 5.37 for phase pure and poly-phasic samples respectively.

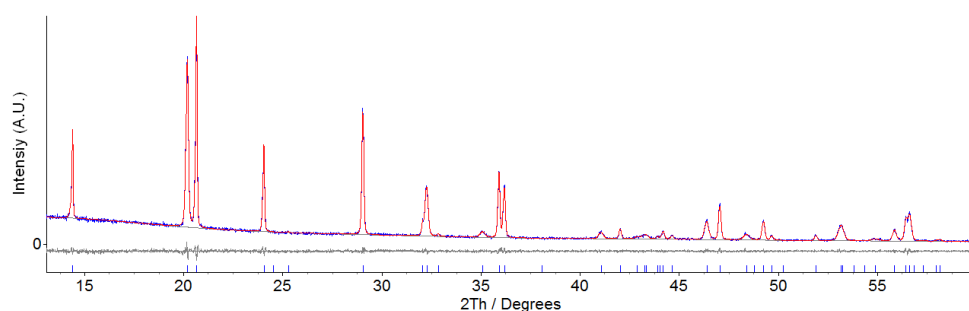


Figure 5.36. Cu $K\alpha_1$ PXRD pattern of $\text{Li}_{0.86}\text{Ta}_{1.18}\text{Mg}_{0.22}\text{Ga}_{0.6}\text{P}_3\text{O}_{12}$ made with 5 % Li excess and 20 % P excess. Pawley fit, red, to the data, blue. Background and difference are plotted in grey. Blue tick marks represent the NASICON analogue phase.

It can be seen in figure 5.35 that there are two polyphasic samples that show the rhombohedral phase without having any Ga in them. They are the compositions $\text{LiTa}_{1.333}\text{Mg}_{0.667}\text{P}_3\text{O}_{12}$ and $\text{Ta}_{1.667}\text{Mg}_{0.333}\text{P}_3\text{O}_{12}$ both of them made with 5 % Li excess and 20 % P excess. From the two, the only potential candidate as Li-ion conductor would be $\text{LiTa}_{1.333}\text{Mg}_{0.667}\text{P}_3\text{O}_{12}$. The Pawley fit to the laboratory PXRD data of $\text{LiTa}_{1.333}\text{Mg}_{0.667}\text{P}_3\text{O}_{12}$ is shown in figure 5.37. This sample could be related to the known $\text{Li}_{0.25}\text{Ta}_{1.75}\text{P}_3\text{O}_{12}$ [36] because the lattice parameters are close to the literature values. On the other hand the impurity could not be matched to any PDF2 phase. It was indexed to a monoclinic cell of lattice parameters $a = 14.313(3)$, $b = 3.3627(5)$, $c = 9.952(2)$, $\beta = 112.823(13)$ and volume = 441.5(2) with errors as 1 e.s.d. by using TREOR 90 [37]. A search in ICSD for volume and crystal system did not produce any sensible candidate.

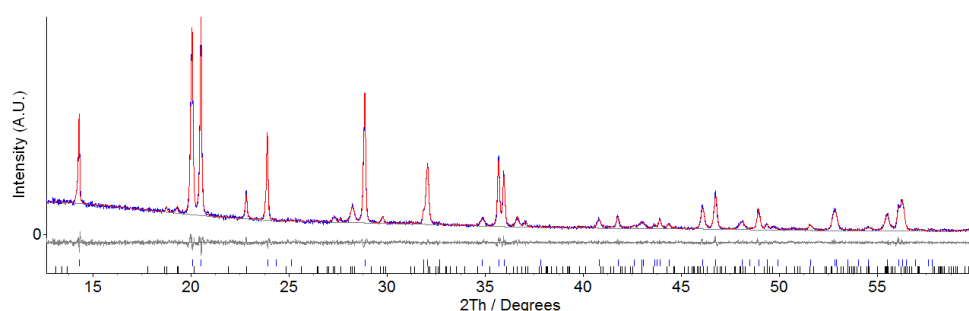


Figure 5.37. $\text{Cu K}\alpha_1$ PXRD pattern of $\text{LiTa}_{1.333}\text{Mg}_{0.667}\text{P}_3\text{O}_{12}$ made with 5 % Li excess and 20 % P excess. Multiphase Pawley fit, red, to the data, blue. Background and difference are plotted in grey. Blue tick marks represent the NASICON analogue phase. Black tick marks represent the indexed impurity phase explained in the text.

In order to clarify the behaviour of the system, the lattice parameters in the hexagonal setting of all rhombohedral phases with space group $R\bar{3}c$ were studied from PXRD. The samples were classified taking into account the c/a ratio and the unit cell volume. The numerical data for all samples extracted from Pawley fits without internal standard are listed in table 5.16.

Table 5.16. Summary of the lattice parameters of all rhombohedral $R\bar{3}c$ phases in the 39 samples of the system that presented the unit cell of interest. All samples were made with 5 % Li excess and 20 % P excess which are not indicated in the nominal composition. The only exception is sample 25 that was made with 72 % Li excess and 55 % P excess by mistake. The phase pure samples are listed with numbers 8, 12, 15 and 16. Error is shown as 3 e.s.d.

Sample number	Nominal Composition	Lattice parameters			
		a / Å	c / Å	c/a ratio	Volume / Å ³
1	Ta _{1.5} Ga _{0.5} P ₃ O ₁₂	8.590(3)	22.114(11)	2.574(2)	1413.1(1.2)
2	Ta _{1.667} Mg _{0.333} P ₃ O ₁₂	8.6278(9)	22.186(4)	2.5714(5)	1430.2(4)
3	Li _{0.41} Ta _{1.295} Ga _{0.705} P ₃ O ₁₂	8.5835(13)	21.969(5)	2.5594(7)	1401.7(5)
4	Li _{0.2} Ta _{1.4} Ga _{0.6} P ₃ O ₁₂	8.5846(10)	21.910(5)	2.5523(7)	1398.4(5)
5	Li _{0.33} Ta _{1.39} Mg _{0.11} Ga _{0.5} P ₃ O ₁₂	8.5870(6)	21.947(3)	2.5559(4)	1401.50(9)
6	Li _{0.13} Ta _{1.49} Mg _{0.11} Ga _{0.4} P ₃ O ₁₂	8.5920(9)	21.973(4)	2.5574(5)	1404.8(4)
7	Li _{0.26} Ta _{1.48} Mg _{0.22} Ga _{0.3} P ₃ O ₁₂	8.5945(5)	22.047(2)	2.5652(3)	1410.33(7)
8	Li _{0.53} Ta _{1.29} Mg _{0.11} Ga _{0.6} P ₃ O ₁₂	8.5869(4)	21.875(2)	2.5475(3)	1396.9(2)
9	Li _{0.46} Ta _{1.38} Mg _{0.22} Ga _{0.4} P ₃ O ₁₂	8.5940(5)	22.001(2)	2.5600(3)	1407.2(2)
10	Li _{0.5} Ta _{1.417} Mg _{0.333} Ga _{0.25} P ₃ O ₁₂	8.6081(7)	22.017(2)	2.5577(3)	1412.8(2)
11	Li _{0.8} Ta _{1.1} Ga _{0.9} P ₃ O ₁₂	8.5900(4)	21.7176(2)	2.5282(2)	1387.8(2)
12	Li _{0.6} Ta _{1.2} Ga _{0.8} P ₃ O ₁₂	8.5871(4)	21.794(2)	2.5380(2)	1391.8(2)
13	Li _{0.93} Ta _{1.09} Mg _{0.11} Ga _{0.8} P ₃ O ₁₂	8.5889(4)	21.701(2)	2.5266(3)	1386.4(2)
14	Li _{0.731} Ta _{1.188} Mg _{0.107} Ga _{0.705} P ₃ O ₁₂	8.584(3)	21.792(8)	2.5388(12)	1390.5(1.1)
15	Li _{0.86} Ta _{1.18} Mg _{0.22} Ga _{0.6} P ₃ O ₁₂	8.5925(4)	21.770(2)	2.5336(2)	1391.9(2)
16	Li _{0.66} Ta _{1.28} Mg _{0.22} Ga _{0.5} P ₃ O ₁₂	8.5928(6)	21.855(3)	2.5434(4)	1397.5(3)
17	Li _{0.79} Ta _{1.27} Mg _{0.33} Ga _{0.4} P ₃ O ₁₂	8.5990(7)	1.864(3)	2.5426(4)	1400.1(3)
18	LiTaGaP ₃ O ₁₂	8.5762(2)	21.631(5)	2.5222(7)	1377.8(5)
19	Li _{1.053} Ta _{1.082} Mg _{0.217} Ga _{0.701} P ₃ O ₁₂	8.5894(4)	21.660(2)	2.5217(2)	1383.9(2)
20	Li _{0.99} Ta _{1.17} Mg _{0.33} Ga _{0.5} P ₃ O ₁₂	8.5985(6)	21.769(2)	2.5317(3)	1393.86(8)
21	LiTa _{1.333} Mg _{0.667} P ₃ O ₁₂	8.6433(9)	21.902(4)	2.5340(5)	1417.0(4)
22	Li _{1.33} Ta _{0.89} Mg _{0.11} GaP ₃ O ₁₂	8.5854(8)	21.594(3)	2.5152(4)	1378.4(3)
23	Li _{1.13} Ta _{0.99} Mg _{0.11} Ga _{0.9} P ₃ O ₁₂	8.5894(6)	21.641(2)	2.5194(3)	1382.7(3)
24	Li _{1.26} Ta _{0.98} Mg _{0.22} Ga _{0.8} P ₃ O ₁₂	8.5908(5)	21.643(2)	2.5193(3)	1383.3(2)
25	Li _{1.39} Ta _{0.97} Mg _{0.324} Ga _{0.705} P ₃ O ₁₂	8.5946(5)	21.679(2)	2.5224(3)	1386.8(2)
26	Li _{1.19} Ta _{1.07} Mg _{0.33} Ga _{0.6} P ₃ O ₁₂	8.5969(6)	21.718(2)	2.5262(3)	1390.1(2)
27	Li _{1.32} Ta _{1.06} Mg _{0.44} Ga _{0.5} P ₃ O ₁₂	8.6033(8)	21.702(3)	2.5225(4)	1391.1(3)
28	Li _{1.12} Ta _{1.16} Mg _{0.44} Ga _{0.4} P ₃ O ₁₂	8.6056(7)	21.748(2)	2.5271(4)	1394.8(2)
29	Li _{1.5} Ta _{0.75} Ga _{1.25} P ₃ O ₁₂	8.5857(12)	21.557(4)	2.5108(6)	1376.2(5)
30	Li _{1.46} Ta _{0.88} Mg _{0.22} Ga _{0.9} P ₃ O ₁₂	8.5895(7)	21.581(2)	2.512(4)	1378.9(2)
31	Li _{1.52} Ta _{0.96} Mg _{0.44} Ga _{0.6} P ₃ O ₁₂	8.6010(8)	21.647(3)	2.5167(4)	1386.8(3)

32	$\text{Li}_{1.5}\text{Ta}_{1.083}\text{Mg}_{0.667}\text{Ga}_{0.25}\text{P}_3\text{O}_{12}$	8.6301(12)	21.781(2)	2.5238(2)	1404.89(11)
33	$\text{Li}_{1.66}\text{Ta}_{0.78}\text{Mg}_{0.22}\text{GaP}_3\text{O}_{12}$	8.5898(8)	21.540(3)	2.5076(4)	1376.4(3)
34	$\text{Li}_{1.79}\text{Ta}_{0.77}\text{Mg}_{0.33}\text{Ga}_{0.9}\text{P}_3\text{O}_{12}$	8.5937(5)	21.515(2)	2.5036(3)	1376.1(2)
35	$\text{Li}_{1.59}\text{Ta}_{0.87}\text{Mg}_{0.33}\text{Ga}_{0.8}\text{P}_3\text{O}_{12}$	8.5911(8)	21.636(3)	2.5184(4)	1382.9(3)
36	$\text{Li}_2\text{Ta}_{0.5}\text{Ga}_{1.5}\text{P}_3\text{O}_{12}$	8.5860(14)	21.482(5)	2.5019(8)	1371.4(6)
37	$\text{Li}_{1.99}\text{Ta}_{0.67}\text{Mg}_{0.33}\text{GaP}_3\text{O}_{12}$	8.5951(5)	21.497(2)	2.5011(2)	1375.3(2)
38	$\text{Li}_2\text{Ta}_{0.833}\text{Mg}_{0.667}\text{Ga}_{0.5}\text{P}_3\text{O}_{12}$	8.6121(14)	21.638(4)	2.5125(6)	1389.8(5)
39	$\text{Li}_{2.5}\text{Ta}_{0.25}\text{Ga}_{1.75}\text{P}_3\text{O}_{12}$	8.590(3)	21.417(13)	2.493(2)	1368.8(1.4)

In order to extract useful information from the content of the table 5.16, the data were plotted in different ways. The most reliable value in this table is the c/a ratio. The rest of the values in the table have a stronger correlation with the zero error of the diffractometer which refined to values from $-0.0162(12)$ to $0.0267(10)^\circ$ with errors shown as 1 e.s.d.

The first plot presented in figure 5.38 shows the volume vs c/a ratio. It can be seen that the phase pure samples, indicated in green, are located in the middle of the distribution. There is an approximate variation in volume from 1370 to 1420 \AA^3 and the phase pure samples have an average volume of 1395 \AA^3 . The variation in volume is about 3.5 % of the cell volume which is relatively significant. This means that although other phases are accessible, only a restricted range of compositions can be made phase pure with the experimental approach used in this section.

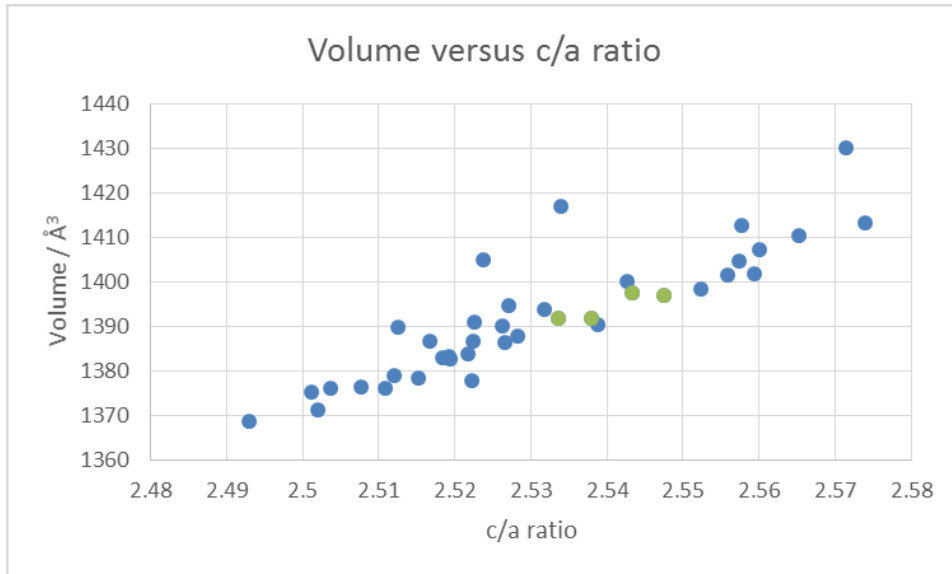


Figure 5.38. Plot of the volume vs c/a for all samples from table 5.16. The phase pure samples are represented in green. Errors are smaller than the dot size.

The second plot presented in figure 5.39 shows the lattice parameters c vs a . It can be seen that the phase pure samples, indicated in green, are located again in the middle of the distribution close to each other. No other trends can be found from this representation. The scatter indicates that there is no correlation between the unit cell edge lengths a and c for these samples. The conclusion is the same as from the plot in figure 5.38, i.e. related phases could be made phase pure under different experimental conditions.

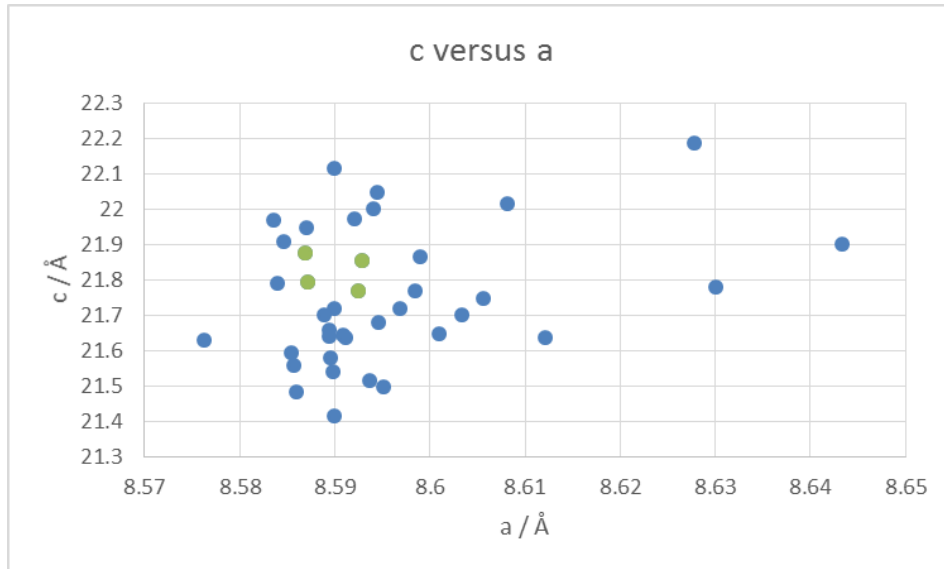


Figure 5.39. Plot of the lattice parameters c versus a , for all samples from table 5.16. The phase pure samples are represented in green. Errors are smaller than the dot size.

Finally the third plot is presented in figure 5.40. It shows the c/a ratio vs sample number in table 5.16. The sample number follows the order of the Li isoclines in figure 5.35 from the Ta axis to the Mg axis, i.e. after listing the samples in isocline for no Li, the samples in the gap from the first two isoclines are listed, then samples in isocline for $\text{Li}_{0.5}$ and so on.

It can be seen that the phase pure samples, indicated in green, are located in the first half of the list with very similar c/a ratio compared with the c/a range accessible. This leads to the same conclusion as before that more phases than those achieved in this section could be made phase pure in this synthetic field. It would be interesting to isolate and characterise the phases in both ends of the c/a ratio range. A summary with the four samples that resulted phase pure and were scaled up is shown in table 5.17.

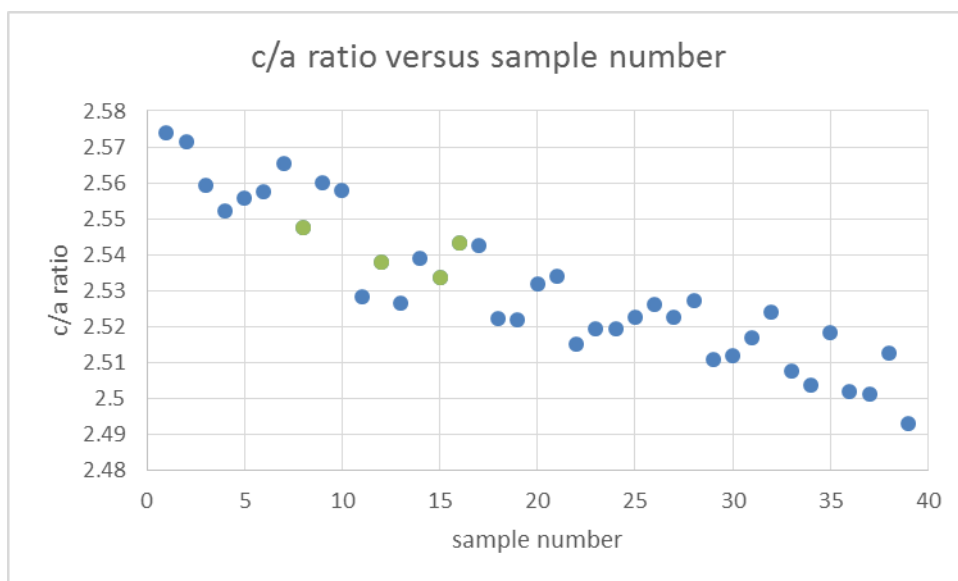


Figure 5.40. Plot of the c/a ratio versus the sample number in table 5.16. The phase pure samples are represented in green. Errors are smaller than the dot size.

Table 5.17. Summary of compositions of phase pure samples. The sample number refers to the number in table 5.16. All samples were made with 5 % Li excess and 20 % P excess which are not indicated in the nominal composition. The column on the right shows the overall composition including the Li/P excesses. For the latter, the oxygen has not been charge balanced in order to no make the assumption that all P has oxidation state 5+.

Sample Number	Nominal composition	Overall stoichiometry including Li and P excesses
8	$\text{Li}_{0.53}\text{Ta}_{1.29}\text{Mg}_{0.11}\text{Ga}_{0.6}\text{P}_3\text{O}_{12}$	$\text{Li}_{0.56}\text{Ta}_{1.29}\text{Mg}_{0.11}\text{Ga}_{0.6}\text{P}_{3.6}\text{O}_{12+x}$
12	$\text{Li}_{0.6}\text{Ta}_{1.2}\text{Ga}_{0.8}\text{P}_3\text{O}_{12}$	$\text{Li}_{0.63}\text{Ta}_{1.2}\text{Ga}_{0.8}\text{P}_{3.6}\text{O}_{12+x}$
15	$\text{Li}_{0.86}\text{Ta}_{1.18}\text{Mg}_{0.22}\text{Ga}_{0.6}\text{P}_3\text{O}_{12}$	$\text{Li}_{0.90}\text{Ta}_{1.18}\text{Mg}_{0.22}\text{Ga}_{0.6}\text{P}_{3.6}\text{O}_{12+x}$
16	$\text{Li}_{0.66}\text{Ta}_{1.28}\text{Mg}_{0.22}\text{Ga}_{0.5}\text{P}_3\text{O}_{12}$	$\text{Li}_{0.69}\text{Ta}_{1.28}\text{Mg}_{0.22}\text{Ga}_{0.5}\text{P}_{3.6}\text{O}_{12+x}$

5.4.2 Diffraction and refinements

The sample 12 in table 5.17 has the composition $\text{Li}_{0.6}\text{Ta}_{1.2}\text{Ga}_{0.8}\text{P}_3\text{O}_{12}$ made with 5 % Li excess and 20 % P excess. The sample was loaded in a 0.2 mm diameter borosilicate capillary for synchrotron PXRD data collection with the diffractometer I11 at Diamond Light Source. The diffraction pattern was collected with the position sensitive detector, PSD. The I11 diffraction pattern of this sample presents anisotropic peak broadening that initially was modelled by using the Stephens's anisotropic peak shape for hexagonal unit cells. Using Pawley fits, the fit factor of the rhombohedral $R\bar{3}c$ cell with Stephens's hexagonal was compared with the fit factor of a derived triclinic cell with pseudo-Voigt peak shape and $P\bar{1}$ symmetry. The refined unit cell parameters and the fit factors are presented in table 5.18. The refined values of anisotropic strain parameters [31] are shown in table 5.19. The graphical output of these two refinements can be seen in figures 5.41 and 5.42.

Table 5.18. Refined unit cell parameters and refinement fit factors for the sample with composition $\text{Li}_{0.6}\text{Ta}_{1.2}\text{Ga}_{0.8}\text{P}_3\text{O}_{12}$ made with 5 % Li excess and 20 % P excess. Data from Pawley refinements with anisotropic peak shape and the triclinic cell with standard pseudo-Voigt peak shape. Error shown as 1 e.s.d.

Peak shape	Stephens	Pseudo-Voigt
Space group	$R\bar{3}c$	$P\bar{1}$
a / Å	8.58995(2)	8.5883(4)
b / Å	-	8.5904(2)
c / Å	21.7803(11)	21.7982(4)
α / °	90	89.947(2)
β / °	90	90.236(4)
γ / °	120	119.945(2)
Volume / Å ³	1391.799(9)	1393.50(9)
R_{wp}	1.26 %	1.11 %

Table 5.19. Refined values of anisotropic strain parameters for $\text{Li}_{0.6}\text{Ta}_{1.2}\text{Ga}_{0.8}\text{P}_3\text{O}_{12}$ (5%Li/20%P). The best fit refining all parameters produce $R_{\text{wp}} = 1.26\%$. The R_{wp} produced when each anisotropic parameter and ζ are individually set to zero are shown for comparison. ζ is the Lorentzian mixing parameter. Error shown as 1 e.s.d.

Parameter	Value	R_{wp}
S_{400}	93.2(4)	6.99 %
S_{004}	7.91(5)	3.06 %
S_{202}	-12.8(4)	1.35 %
ζ	0.660(3)	3.68 %

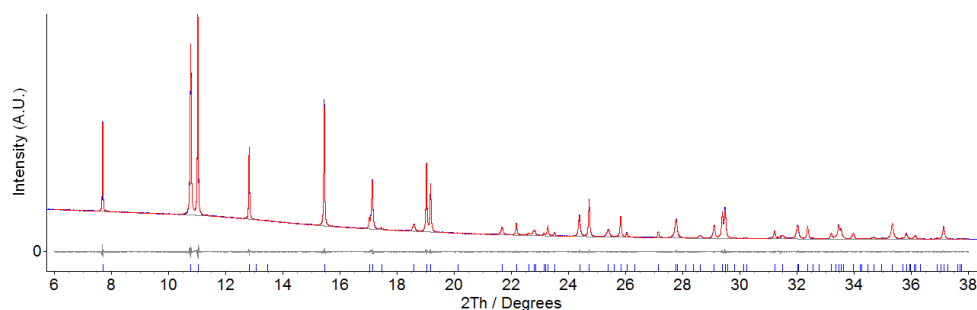


Figure 5.41. Synchrotron PXRD pattern from the sample of composition $\text{Li}_{0.6}\text{Ta}_{1.2}\text{Ga}_{0.8}\text{P}_3\text{O}_{12}$ made with 5 % Li excess and 20 % P excess. Pawley fit, red, to the data, blue. Background and difference are plotted in grey. Blue tick marks represent the NASICON analogue in space group $R\bar{3}c$. $R_{\text{wp}} = 1.26\%$.

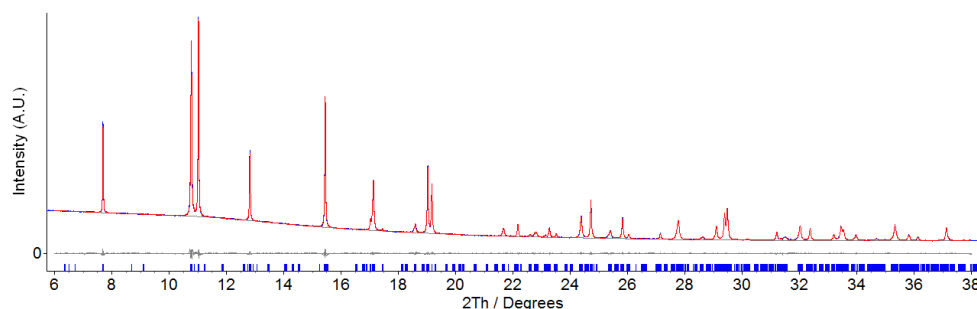


Figure 5.42. Synchrotron PXRD pattern from the sample of composition $\text{Li}_{0.6}\text{Ta}_{1.2}\text{Ga}_{0.8}\text{P}_3\text{O}_{12}$ made with 5 % Li excess and 20 % P excess. Pawley fit, red, to the data, blue. Background and difference are plotted in grey. Blue tick marks represent the NASICON analogue in space group $P\bar{1}$. $R_{\text{wp}} = 1.11\%$.

Future work on these samples would include performing Rietveld refinements in both space groups to confirm if these findings are consistent when a structural model is included. After that, the same type of analysis for the rest of the phase pure samples would be useful to study how different the four samples are to each other and how they compare with known phases.

5.4.3 Densification

Samples 12 and 15 in table 5.17, i.e. samples with compositions $\text{Li}_{0.6}\text{Ta}_{1.2}\text{Ga}_{0.8}\text{P}_3\text{O}_{12}$ and $\text{Li}_{0.86}\text{Ta}_{1.18}\text{Mg}_{0.22}\text{Ga}_{0.6}\text{P}_3\text{O}_{12}$ both of them made with 5 % Li excess and 20 % P excess, were prepared for AC impedance measurements. The powders were thoroughly ground in pestle and mortar, dried for two days at 200 °C and made into pellets by using the uniaxial press.

The pellets were then sintered in Pt crucibles in a box furnace. The temperature program consisted of heating at 0.5 °C/min up to 300 °C and dwell for 12 hours in order to dry the samples. Then heating at 5 °C/min up to 850 °C and dwell for 6 hours in order to sinter the materials. Finally the furnace is cooled at 10 °C/min to room temperature.

The resulting pellets were weighed and measured in order to determine their densities. These densities were compared to the crystallographic densities of the nominal compositions in order to get the relative densities, which resulted of 59 % and 73 % for samples 12 and 15 respectively. These relative densities are lower than those ideally needed for AC impedance spectroscopy, probably due to incomplete sintering. The optimisation of this densification process would follow similar lines to those used for the two previous systems, i.e. to include ball milling and cold isostatic pressing in the procedure, and then test some higher sintering temperatures, e.g. 900 and 1000 °C.

5.4.4 Conductivity of $\text{Li}_{0.6}\text{Ta}_{1.2}\text{Ga}_{0.8}\text{P}_3\text{O}_{12}$ and $\text{Li}_{0.86}\text{Ta}_{1.18}\text{Mg}_{0.22}\text{Ga}_{0.6}\text{P}_3\text{O}_{12}$

The two pellets sintered in the previous section were selected for AC impedance spectroscopy. Phase purity was assessed with XRD patterns collected from both sides of each pellet. The silver paste used for making the electrodes of these pellets was dried at 100 °C. Silver wire was attached to the electrodes by using the same silver paste and drying method.

AC impedance was measured in air using an open tube furnace, starting at the higher temperature which was 300 °C. Then impedance data were collected at 250 °C and 200 °C as well. Capacitance values were used to identify the electroactive elements as indicated by Irvine et al. [35].

From the AC impedance plots at 300 °C, figure 5.43, only one electroactive element was visible for these two samples in the range of frequencies observed, from 10 MHz to 0.01 Hz. This element was the bulk which appeared as an arc starting at the origin with corrected capacitance in the range of $1.4 - 1.7 \times 10^{-12} \text{ F cm}^{-1}$. The arc assigned to the bulk had a resistivity $\rho = 1.31 \text{ M}\Omega \text{ cm}$ for sample 12 and of $254 \text{ k}\Omega \text{ cm}$ for sample 15 (from circle fit to the data in both cases). For sample 15 a small spike, which is smaller than the bulk circle, is visible. It is too small for recognising it either as an arc or as a spike from the electrode response. At lower temperatures only the arc corresponding to the bulk could be recognised.

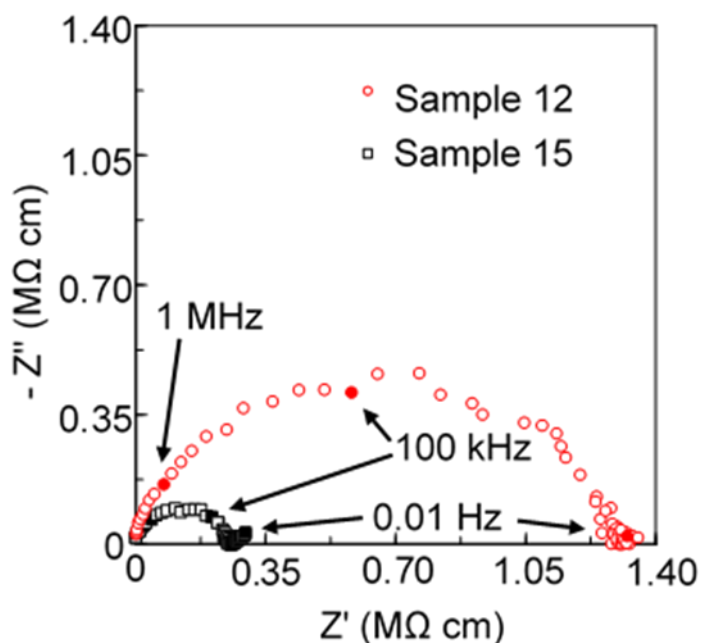


Figure 5.43. AC impedance complex plane plot at 300 °C for samples 12 and 15 of compositions $\text{Li}_{0.6}\text{Ta}_{1.2}\text{Ga}_{0.8}\text{P}_3\text{O}_{12}$ and $\text{Li}_{0.86}\text{Ta}_{1.18}\text{Mg}_{0.22}\text{Ga}_{0.6}\text{P}_3\text{O}_{12}$ respectively, made with 5 % Li excess and 20 % P excess.

The conductivity values for the bulk of each sample derived from the impedance data have been used to produce an Arrhenius plot that is shown in figure 5.44, from which the activation energies are calculated after the corresponding least squares linear fits. The bulk for these two samples has an activation energy in the range of 0.8 – 0.9 eV. The conductivity properties of these two samples are summarised in table 5.20.

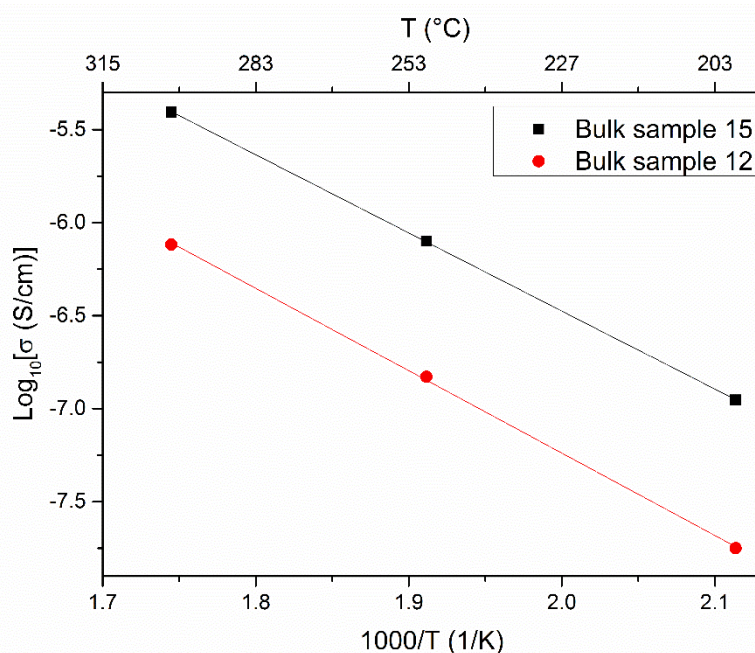


Figure 5.44. Arrhenius type plot showing the bulk conductivity for the samples $\text{Li}_{0.6}\text{Ta}_{1.2}\text{Ga}_{0.8}\text{P}_3\text{O}_{12}$ (sample 12) and $\text{Li}_{0.86}\text{Ta}_{1.18}\text{Mg}_{0.22}\text{Ga}_{0.6}\text{P}_3\text{O}_{12}$ (sample 15), both of them made with 5 % Li excess and 20 % P excess. Additional data on these two samples are listed in table 5.20.

Table 5.20. Conductivity data for selected samples of the system derived from AC impedance spectroscopy. Both samples were made with 5 % Li excess and 20 % P excess which are not indicated in the nominal composition. E_a errors shown as 1σ .

Sample Number	Nominal composition	Relat. density	Conductivity data		
			$\sigma_{\text{bulk}}(300 \text{ }^\circ\text{C})$	$E_{a,\text{bulk}}$	C_{corr}
12	$\text{Li}_{0.6}\text{Ta}_{1.2}\text{Ga}_{0.8}\text{P}_3\text{O}_{12}$	59 %	$7.6 \times 10^{-7} \text{ Scm}^{-1}$	0.878(16) eV	$1.4 \times 10^{-12} \text{ Fcm}^{-1}$
15	$\text{Li}_{0.86}\text{Ta}_{1.18}\text{Mg}_{0.22}\text{Ga}_{0.6}\text{P}_3\text{O}_{12}$	73 %	$3.9 \times 10^{-6} \text{ Scm}^{-1}$	0.832(4) eV	$1.7 \times 10^{-12} \text{ Fcm}^{-1}$

From these two samples, sample 12 has similar bulk conductivity and bulk activation energy, in the range 200 – 300 °C, as $\text{Li}_{0.734}\text{Ta}_{1.187}\text{Ca}_{0.108}\text{Al}_{0.705}\text{P}_3\text{O}_{12}$ studied previously in this chapter. On the other hand, sample 15 is about 10 times more conductive than sample 12 in agreement with a higher Li content, but still 100 times less conductive than $\text{Li}_{0.925}\text{Ta}_{1.062}\text{Al}_{0.938}\text{P}_{3.16}\text{O}_{12+x}$ at 300 °C. The bulk activation energy of sample 15 is similar to that of sample 12.

All these results were obtained from samples with low relative densities as shown in table 5.20 and commented above. Low density can lead to open porosity and electrode roughness, which could lead to values with additional errors.

5.5 Summary, conclusions and further work

The introduction of this chapter gives an overview of the NASICON Li-ion analogues, some of their conductivities and the variety of their doping patterns. The structure of the most common polymorphs is presented along with the arrangement of the lantern motif that lead to the structural frameworks. Some other considerations such as the description of the Li sites in the α -polymorph are also presented.

After the introduction, this chapter is divided into three blocks of content. The first one describes the synthesis of $\text{LiTaAl}(\text{PO}_4)_3$ related samples, their characterisation, densification and property measurements. In the second part, a new Ca-containing NASICON analogue is pursued with the aim of increasing the Li content in samples related again to $\text{LiTaAl}(\text{PO}_4)_3$. Densification and property measurements are performed on the best composition. Finally, in the third block, the new combination of atoms Ta-Mg-Ga are tried to explore the regions of the ternary diagram where the charge balance would be compatible with potential NASICON analogue phases. The samples are screened and selected phase pure specimens are studied in more detail.

For the section that studies the $\text{LiTaAl}(\text{PO}_4)_3$ related samples, the main motivation was a sample found interesting from NMR Li-dynamics studies and also because potentially was presenting a triclinic distortion with similar Li-ion conductivity as the rhombohedral phase. This led to study the effect of different P excess in the sample of nominal composition $\text{Li}_{0.875}\text{Ta}_{1.062}\text{Al}_{0.938}\text{P}_3\text{O}_{12}$ made with $\sim 5.7\%$ Li excess and $\sim 5.4\%$ P excess, which finally showed the Vegard's law with a plateau and an impurity, $\text{Ta}_{0.5}\text{Al}_{0.5}\text{P}_2\text{O}_7$. The fits also showed to be superior when made with a triclinic cell in $P\bar{1}$ rather than with the rhombohedral in $R\bar{3}c$. TEM-EDX data showed that samples with lower P excess were more homogenous. The densification was tried at three different temperatures without and with two different binders. All pellets without binder and with Butvar resulted in relative densities above 90 %

while those with PVA were below 90 %. The most dense pellets were subject to AC impedance measurements and showed a bulk conductivity and E_a similar to the total conductivity and E_a given in literature for $\text{LiTaAl}(\text{PO}_4)_3$. During this section the alumina TGA correction highlighted in Appendix 5.1 was used. For the assignment of the phase $\text{Ta}_{0.5}\text{Al}_{0.5}\text{P}_2\text{O}_7$, it was needed some structure solution work, which is described in Appendix 5.2.

For the Ca-containing NASICON analogues, the first target composition derived from the substitution of Ta^{5+} for Ca^{2+} and Li^+ in $\text{Li}_{1.2}\text{Ta}_{0.9}\text{Al}_{1.1}\text{P}_3\text{O}_{12}$. The target composition of $\text{Li}_{1.55}\text{Ta}_{0.78}\text{Ca}_{0.11}\text{Al}_{1.11}\text{P}_3\text{O}_{12}$ was attempted for a range of P excess. However, none of these samples resulted pure, always showing aluminium containing impurities. To get rid of these impurities, a new set of Ca-doped samples were synthesised to explore the synthetic space for Al-deficient samples that keep the same fraction of Ca. Finally the sample of nominal composition $\text{Li}_{0.734}\text{Ta}_{1.187}\text{Ca}_{0.108}\text{Al}_{0.705}\text{P}_3\text{O}_{12}$ made with 5% Li excess and 20% P excess appeared to be phase pure. TEM-EDX analysis confirmed that the nominal composition was correct although with some dispersion. Synchrotron X-ray diffraction data was fitted to the hexagonal cell after accounting for the anisotropy in the peak shape. The processing conditions were optimised for $\text{Li}_{0.734}\text{Ta}_{1.187}\text{Ca}_{0.108}\text{Al}_{0.705}\text{P}_3\text{O}_{12}$ reaching relative densities slightly above 90 % and AC impedance spectroscopy was used to determine the Li-ion conductivity that resulted in a value of $1.5 \times 10^{-13} \text{ S cm}^{-1}$ at 25 °C with $E_a \approx 0.8 \text{ eV}$ for the bulk.

The Li-Ta-Ga-Mg-P-O series was an ambitious project in which 48 samples explored the whole synthetic space wherein potential NASICON phases would form. The experimental approach was to make the samples with 5 % Li excess and 20 % P excess. Four compositions resulted in phase pure samples with close lattice parameters between them. The study showed evidence that a larger variation in lattice parameters is accessible in this system which would indicate that several other compositions could be isolated by changing the experimental approach. Selected compositions were subject to AC impedance measurements showing a bulk conductivity and E_a in between of the two systems previously presented in this chapter.

In conclusion, the work carried out in this chapter give evidence that the addition of extra Li-P-O to these systems is not just a sintering aid that increase

density/conductivity, but that the modification of the overall stoichiometry lead to unit cell changes that follow Vegard's law. This involves a unit cell volume change, along with a loss in homogeneity of the sample observed by TEM-EDX. Subtle triclinic distortion was suggested by anisotropic peak broadening in PXRD and finally supported by superior trends when using the triclinic cell for Pawley fits. Densification procedures have been developed for two of these systems achieving relative densities over 90 %. The AC impedance measurements on the best samples of these systems have shown that the bulk conductivities and E_a lie in the same range as the total conductivities published for $\text{LiTaAl}(\text{PO}_4)_3$ or below.

The further work suggested for $\text{LiTaAl}(\text{PO}_4)_3$ related samples is to isolate phase pure samples at the maximum and minimum unit cell volumes found in this thesis. Still search if a lower unit cell volume can be reached by searching for the low end plateau by using lower or negative P excess. The same applies to the Ca-doped samples, i.e. find the maximum volume variations that can be achieved and isolate again phase pure materials at the ends for structural and conductivity studies. For the Ta-Mg-Ga system the lattice parameters have shown a uniform distribution for all values with no accumulation of samples at any end suggesting that further change in lattice parameters would be possible. Initial further work could try to isolate the already shown extreme cells for characterisation and extend the study on those samples to find new plateaus at each end. Finally the development of a digestion method suitable for ICP-OES analysis would be useful, so that the data gathered in this way could support the TEM-EDX results.

5.6 Appendix 5.1: TGA of selected reactants

TGA was performed to some of the precursors of the cations on the M site of the NASICON structure. This analysis was made in order to double check if there was any weight loss during heating as it has been shown in literature for Al_2O_3 [38].

For Ta_2O_5 one experiment with 110 mg of sample was run. For CaCO_3 one experiment with 36 mg of sample was run. These two precursors did not show significant weight loss and were considered pure.

For Al_2O_3 two samples in the range 40-50 mg were run independently. The weight loss found in literature was closely replicated in these two separate experiments as can be seen in figures 5.45 and 5.46.

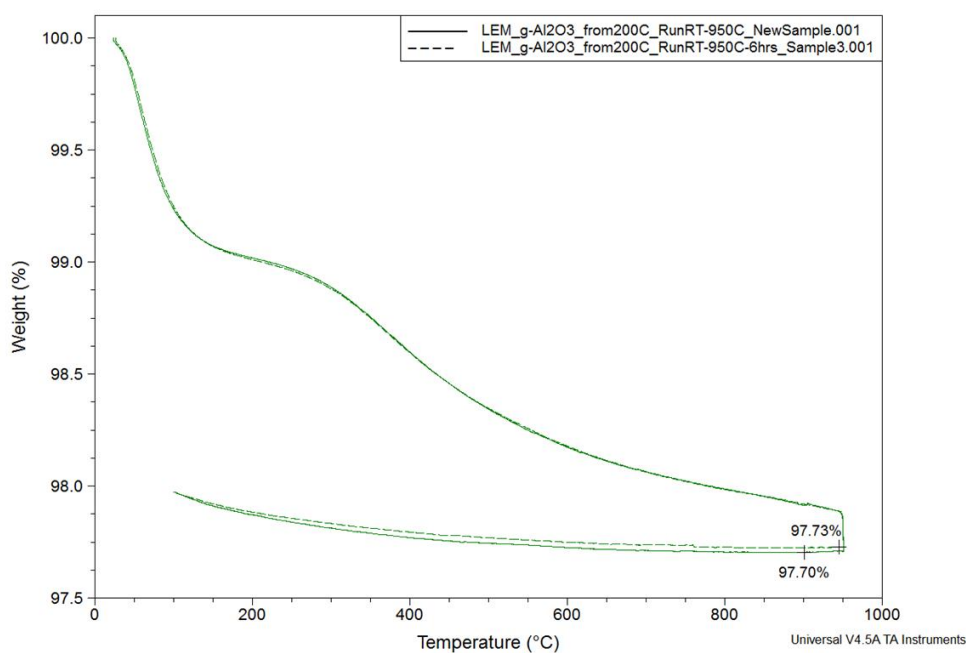


Figure 5.45. Outcome of the both replications of the TGA experiment to Al_2O_3 . This plot shows the gravimetric data against temperature in °C.

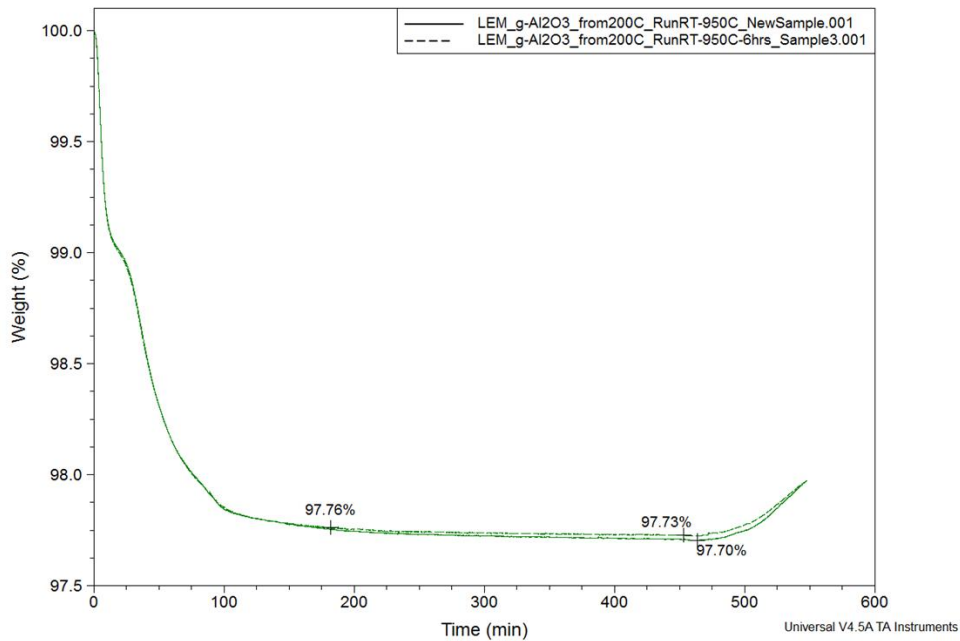


Figure 5.46. Outcome of the both replications of the TGA experiment to Al₂O₃. This plot shows the gravimetric data against time in minutes.

Alumina was kept in the oven at 200 °C until the preparation of the TGA experiment, which tried to replicate the usual process of weighing materials for synthesis in order to get a reliable factor to be applied in potential compositional corrections. It has been found that the average correction from the two experiments on Al₂O₃ is 2.3 % of weight loss.

5.7 Appendix 5.2: Structure solution of $Ta_{0.5}Al_{0.5}P_2O_7$

For samples with P excess over the limit that lead to the unit cell volume plateau, the impurity $Ta_{0.5}Al_{0.5}P_2O_7$ appears. This impurity did not match any pattern in the powder diffraction database version 2, PDF2. There were also no matching patterns in the inorganic crystal structure database, ICSD, for the relevant combination of atoms. Although this material had its lattice parameters reported [39], the absence in the two databases commonly used by the author led to the need of its structure solution as explained below. This basic structural characterisation enabled the identification with Rietveld refinements needed for explaining the systems studied in this chapter.

The best pattern on this phase was extracted from the difference of a Pawley fit to a polyphasic sample with 70 % P excess. This isolated pattern, as extracted, is shown in figure 5.47.

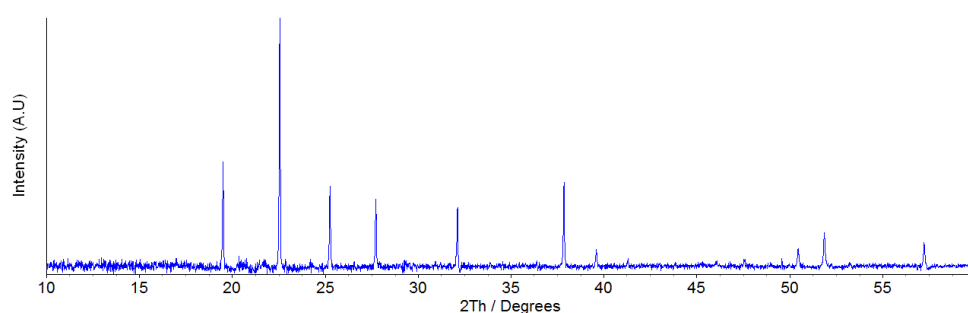


Figure 5.47. Pattern of the unknown phase extracted from a multiphasic sample after a fit to the known phases.

After peak position extraction with Fullprof [40] the position and intensity of the single profiles were refined in Topas academic version 5 [32]. The same profile, a refined Pseudo-Voigt peak shape, was used for all peaks. This was done within the original Pawley fit to the NASICON phase that contains the zero error correction. Finally, the refined positions were indexed by using TREOR 90 [37] and several solutions found.

The solution with lower cell volume was the one with lower number of Bragg reflections with zero intensities. The cell dimensions were then searched in the ICSD and a list with several matches found. The obvious one was WP_2O_7 with ZrP_2O_7 structure type. Then following the crystal chemistry arguments discussed in the introduction of the chapter for the NASICON framework, the structure was solved by analogy: W^{4+} for $0.5 Ta^{5+} + 0.5 Al^{3+}$. The refinement was easy and the small mismatch in intensities disappeared after refining the atomic positions for phosphorous and oxygen. The refined structural parameters are shown in table 5.21. The structure is plotted in figure 5.48 showing the typical polyhedral coordination found in this structure type.

Table 5.21. Refined structural parameters for $Ta_{0.5}Al_{0.5}P_2O_7$. Space group $P\bar{a}3$, #205/setting1. Cubic cell with $a = 7.8804(5)$. Error shown as 3 e.s.d.

Site	Atom	Wyckoff	X	Y	Z	Occ	Biso
Ta/Al	Ta	4a	0	0	0	0.502	0.779
Ta/Al	Al	4a	0	0	0	0.498	0.779
P	P	8c	0.38861	0.38861	0.38861	1	2.284
O1	O1	4b	0.5	0.5	0.5	1	5.347
O2	O2	24d	0.22233	0.07371	0.94227	1	5.347

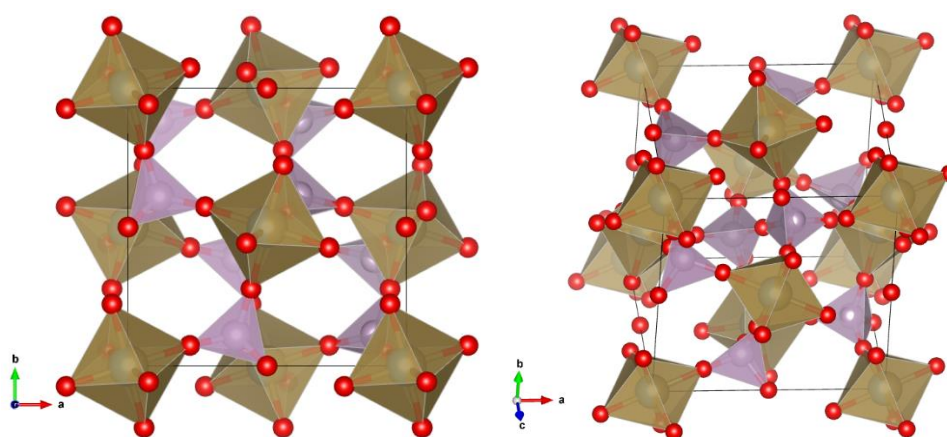


Figure 5.48. Structure of $Ta_{0.5}Al_{0.5}P_2O_7$ phase with the ZrP_2O_7 structure type. a) shows the projection along the c axis and b) is a tilted version that allow to see the “dumbbell” unit P_2O_7 .

5.8 Appendix 5.3: TEM-EDX spectra of NASICON samples.

5.8.1 Sample of overall composition $\text{Li}_{0.925}\text{Ta}_{1.062}\text{Al}_{0.938}\text{P}_{3.16}\text{O}_{12+x}$ (sample 1).

This section presents the TEM-EDX measurements for the sample $\text{Li}_{0.875}\text{Ta}_{1.062}\text{Al}_{0.938}\text{P}_3\text{O}_{12}$ made with 5.7 % Li excess and 5.4 % P excess (sample 1). Figures 5.49 and 5.50 show the first two spectra of the ten measurements shown in table 5.22.

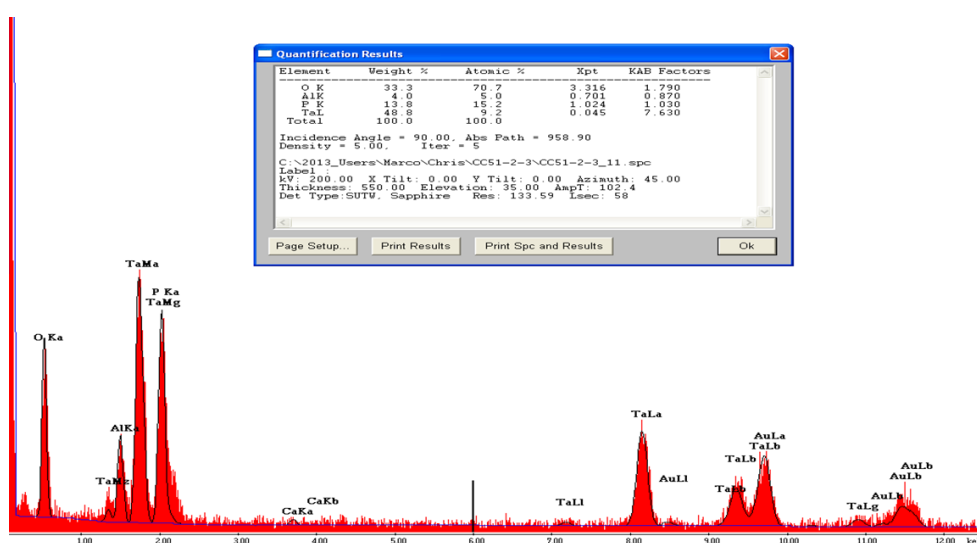


Figure 5.49. TEM-EDX spectrum for measurement 1 of sample $\text{Li}_{0.875}\text{Ta}_{1.062}\text{Al}_{0.938}\text{P}_3\text{O}_{12}$ made with 5.7 % Li excess and 5.4 % P excess (sample 1).

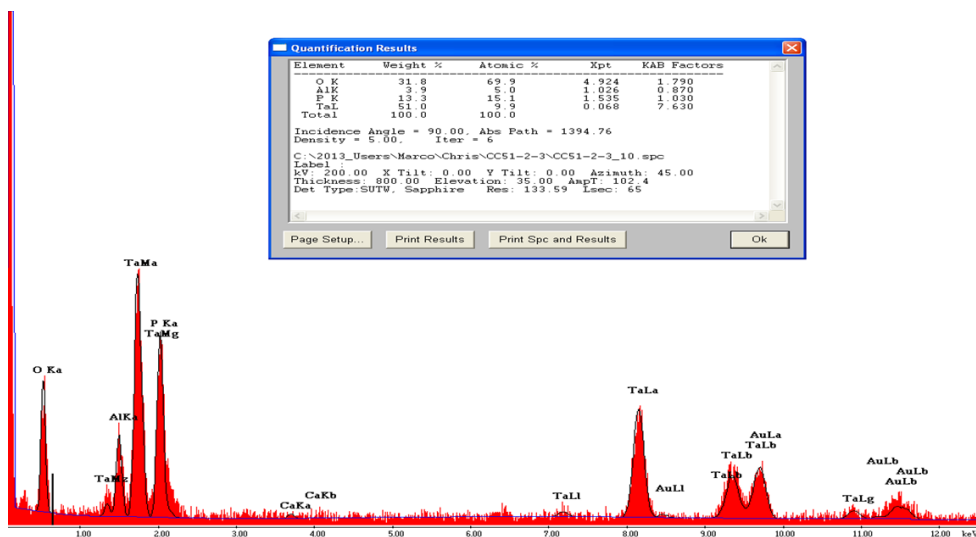


Figure 5.50. TEM-EDX spectrum for measurement 2 of sample $\text{Li}_{0.875}\text{Ta}_{1.062}\text{Al}_{0.938}\text{P}_3\text{O}_{12}$ made with 5.7 % Li excess and 5.4 % P excess (sample 1).

Table 5.22. Atom % quantification produced by the instrument as extracted from the TEM-EDX spectra for the sample $\text{Li}_{0.875}\text{Ta}_{1.062}\text{Al}_{0.938}\text{P}_3\text{O}_{12}$ made with 5.7 % Li excess and 5.4 % P excess (sample 1).

Measurement number	O	Al	P	Ta
1	70.7	5	15.2	9.2
2	69.9	5	15.1	9.9
3	70.3	5.3	15	9.4
4	70.2	5	15.5	9.3
5	70.4	4.6	15.8	9.1
6	70.7	4	15.3	9.9
7	70.5	4.4	16.1	8.9
8	70	4.1	15.8	10
9	70.3	4.5	15.9	9.3
10	69.5	5.2	16.1	9.3

The EDX quantification was corrected with correction factors for each element. The correction factors for this sample were 1.15, 1.01 and 0.75 for Al, P and Ta respectively. For each element, the final value was calculated by application of equation 5.1.

$$\text{Final value} = \text{Measured value} \times \text{Correction factor} \quad (\text{Eq. 5.1})$$

After application of the correction factors the new table 5.23 was produced.

Table 5.23. Relative atom quantification after application of the correction factors for the sample $\text{Li}_{0.875}\text{Ta}_{1.062}\text{Al}_{0.938}\text{P}_3\text{O}_{12}$ made with 5.7 % Li excess and 5.4 % P excess (sample 1).

Measurement number	O	Al	P	Ta
1	70.7	5.75	15.352	6.9
2	69.9	5.75	15.251	7.425
3	70.3	6.095	15.15	7.05
4	70.2	5.75	15.655	6.975
5	70.4	5.29	15.958	6.825
6	70.7	4.6	15.453	7.425
7	70.5	5.06	16.261	6.675
8	70	4.715	15.958	7.5
9	70.3	5.175	16.059	6.975
10	69.5	5.98	16.261	6.975

Finally this table was normalised so that every row adds up to 100 and the relevant three columns were plotted to form the ternary diagram shown in figure 5.11.

5.8.2 Sample of overall composition $\text{Li}_{0.953}\text{Ta}_{1.062}\text{Al}_{0.938}\text{P}_{3.64}\text{O}_{12+x}$ (sample 5).

This section presents the TEM-EDX measurements for the sample $\text{Li}_{0.875}\text{Ta}_{1.062}\text{Al}_{0.938}\text{P}_3\text{O}_{12}$ made with 8.9 % Li excess and 21.3 % P excess (sample 5). Figures 5.51 and 5.52 show the first two spectra of the nine measurements shown in table 5.24.

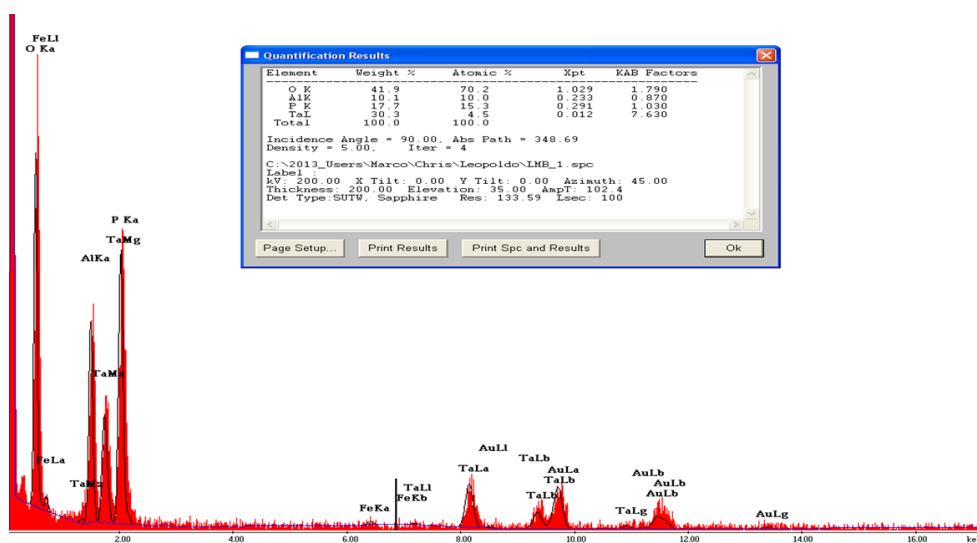


Figure 5.51. TEM-EDX spectrum for measurement 1 of sample $\text{Li}_{0.875}\text{Ta}_{1.062}\text{Al}_{0.938}\text{P}_3\text{O}_{12}$ made with 8.9 % Li excess and 21.3 % P excess (sample 5).

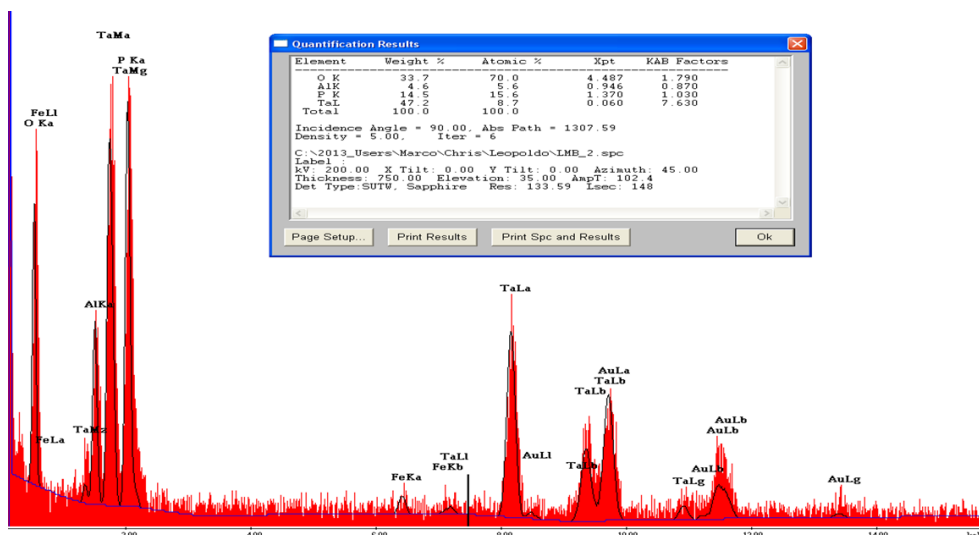


Figure 5.52. TEM-EDX spectrum for measurement 2 of sample $\text{Li}_{0.875}\text{Ta}_{1.062}\text{Al}_{0.938}\text{P}_3\text{O}_{12}$ made with 8.9 % Li excess and 21.3 % P excess (sample 5).

Table 5.24. Atom % quantification produced by the instrument as extracted from the TEM-EDX spectra for the sample $\text{Li}_{0.875}\text{Ta}_{1.062}\text{Al}_{0.938}\text{P}_3\text{O}_{12}$ made with 8.9 % Li excess and 21.3 % P excess (sample 5).

Measurement number	O	Al	P	Ta
1	70.2	10	15.3	4.5
2	70	5.6	15.6	8.7
3	70	4.5	17.2	8.3
4	70.5	4.2	17.3	8
5	69.6	5.2	16	9.2
6	70	3.7	16.3	9.9
7	70	11	16	3
8	70.8	6.2	16.4	6.6
9	70.1	3.9	16.7	9.2

The EDX quantification was corrected in the same way as for the previous sample. The correction factors for this sample were the same as for the previous sample, i.e. 1.15, 1.01 and 0.75 for Al, P and Ta respectively. After application of the correction factors the new table 5.25 was produced.

Table 5.25. Relative atom quantification after application of the correction factors for the sample $\text{Li}_{0.875}\text{Ta}_{1.062}\text{Al}_{0.938}\text{P}_3\text{O}_{12}$ made with 8.9 % Li excess and 21.3 % P excess (sample 5).

Measurement number	O	Al	P	Ta
1	70.2	11.5	15.453	3.375
2	70	6.44	15.756	6.525
3	70	5.175	17.372	6.225
4	70.5	4.83	17.473	6
5	69.6	5.98	16.16	6.9
6	70	4.255	16.463	7.425
7	70	12.65	16.16	2.25
8	70.8	7.13	16.564	4.95
9	70.1	4.485	16.867	6.9

Finally this table was normalised so that every row adds up to 100 and the relevant three columns were plotted to form the ternary diagram shown in figure 5.12.

5.8.3 Ca-doped sample.

This section presents the TEM-EDX measurements for the sample $\text{Li}_{0.734}\text{Ta}_{1.187}\text{Ca}_{0.108}\text{Al}_{0.705}\text{P}_3\text{O}_{12}$ made with 5 % Li excess and 20 % P excess. Figures 5.53 and 5.54 show the first two spectra of the ten measurements shown in table 5.26.

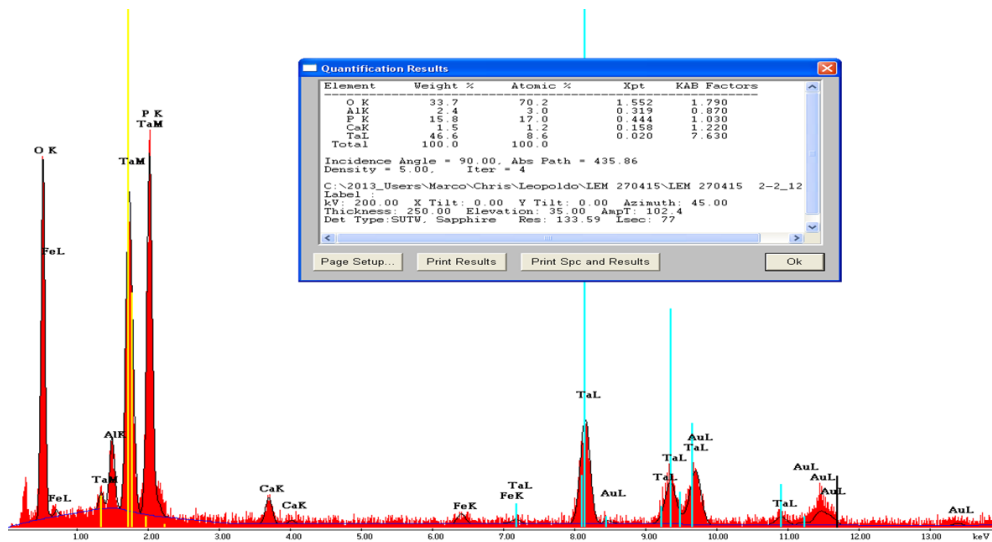


Figure 5.53. TEM-EDX spectrum for measurement 1 of sample $\text{Li}_{0.734}\text{Ta}_{1.187}\text{Ca}_{0.108}\text{Al}_{0.705}\text{P}_3\text{O}_{12}$ made with 5 % Li excess and 20 % P excess.

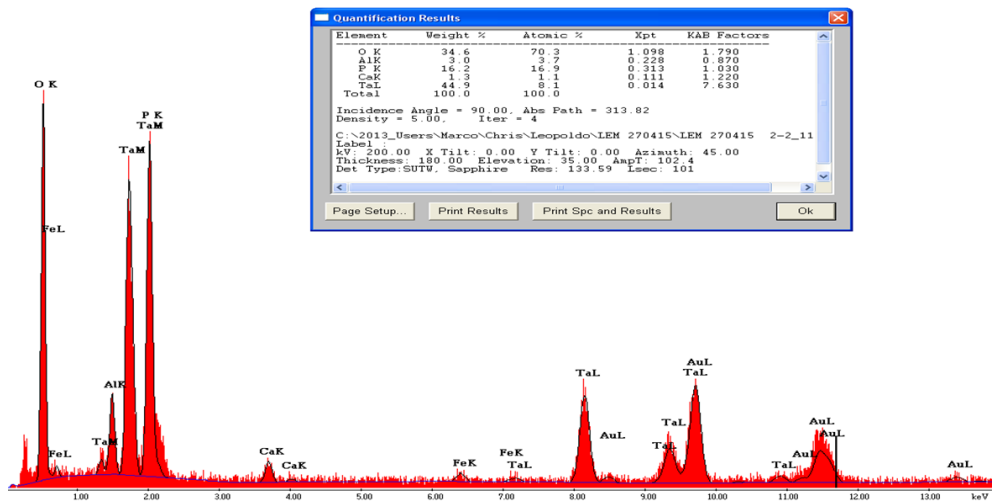


Figure 5.54. TEM-EDX spectrum for measurement 2 of sample $\text{Li}_{0.734}\text{Ta}_{1.187}\text{Ca}_{0.108}\text{Al}_{0.705}\text{P}_3\text{O}_{12}$ made with 5 % Li excess and 20 % P excess.

Table 5.26. Atom % quantification produced by the instrument as extracted from the TEM-EDX spectra for the sample $\text{Li}_{0.734}\text{Ta}_{1.187}\text{Ca}_{0.108}\text{Al}_{0.705}\text{P}_3\text{O}_{12}$ made with 5 % Li excess and 20 % P excess.

Measurement number	O	Al	P	Ca	Ta
1	70.2	3	17	1.2	8.6
2	70.3	3.7	16.9	1.1	8.1
3	69.7	2.9	18.1	1.1	8.2
4	70	4.1	16.2	0.7	9.1
5	70.5	3.3	16	0.8	9.4
6	69.5	3	18.6	1.2	7.8
7	69.7	3.7	16.6	0.6	9.4
8	69.6	3.2	16.1	0.5	10.5
9	69.6	3.4	15.9	0.4	10.7
10	70.1	4	15.3	0.5	10.2
11	70.3	3	15	0.3	11.4
12	70.1	3.3	15.6	0.4	10.6

The EDX quantification was corrected in the same way as for the previous samples. The correction factors for this sample were the same as for the previous samples with the addition of the factor for Ca, i.e. 1.15, 1.01, 1.17 and 0.75 for Al, P, Ca and Ta respectively. After application of the correction factors the new table 5.27 was produced.

Table 5.27. Relative atom quantification after application of the correction factors for the sample $\text{Li}_{0.734}\text{Ta}_{1.187}\text{Ca}_{0.108}\text{Al}_{0.705}\text{P}_3\text{O}_{12}$ made with 5 % Li excess and 20 % P excess.

Measurement number	O	Al	P	Ca	Ta
1	70.2	3.45	17.17	1.404	6.45
2	70.3	4.255	17.069	1.287	6.075
3	69.7	3.335	18.281	1.287	6.15
4	70	4.715	16.362	0.819	6.825
5	70.5	3.795	16.16	0.936	7.05
6	69.5	3.45	18.786	1.404	5.85
7	69.7	4.255	16.766	0.702	7.05
8	69.6	3.68	16.261	0.585	7.875
9	69.6	3.91	16.059	0.468	8.025
10	70.1	4.6	15.453	0.585	7.65
11	70.3	3.45	15.15	0.351	8.55
12	70.1	3.795	15.756	0.468	7.95

Finally this table was normalised so that every row adds up to 100 and the relevant three columns were plotted to form the ternary diagram shown in figure 5.27.

5.9 References

1. Hagman, L.O. and P. Kierkegaard, *The crystal structure of $\text{NaMe}_2^{\text{IV}}(\text{PO}_4)_3$; $\text{Me}^{\text{IV}} = \text{Ge, Ti, Zr}$* . Acta Chem. Scand, 1968. **22**(6): p. 1822-32.
2. Goodenough, J., H.-P. Hong, and J. Kafalas, *Fast Na^+ -ion transport in skeleton structures*. Materials Research Bulletin, 1976. **11**(2): p. 203-220.
3. Boilot, J., G. Collin, and P. Colomban, *Crystal structure of the true nasicon: $\text{Na}_3\text{Zr}_2\text{Si}_2\text{PO}_{12}$* . Materials research bulletin, 1987. **22**(5): p. 669-676.
4. Petit, D., P. Colomban, G. Collin, and J. Boilot, *Fast ion transport in $\text{LiZr}_2(\text{PO}_4)_3$: Structure and conductivity*. Materials research bulletin, 1986. **21**(3): p. 365-371.
5. Kuwano, J., N. Sato, M. Kato, and K. Takano, *Ionic conductivity of $\text{LiM}_2(\text{PO}_4)_3$ ($M = \text{Ti, Zr, Hf}$) and related compositions*. Solid State Ionics, 1994. **70**: p. 332-336.
6. Sudreau, F., D. Petit, and J. Boilot, *Dimorphism, phase transitions, and transport properties in $\text{LiZr}_2(\text{PO}_4)_3$* . Journal of Solid State Chemistry, 1989. **83**(1): p. 78-90.
7. Aono, H., E. Sugimoto, Y. Sadaoka, N. Imanaka, and G.-y. Adachi, *Electrical properties and crystal structure of solid electrolyte based on lithium hafnium phosphate $\text{LiHf}_2(\text{PO}_4)_3$* . Solid State Ionics, 1993. **62**(3-4): p. 309-316.
8. Delmas, C., A. Nadiri, and J. Soubeyroux, *The nasicon-type titanium phosphates $\text{ATi}_2(\text{PO}_4)_3$ ($A = \text{Li, Na}$) as electrode materials*. Solid State Ionics, 1988. **28**: p. 419-423.
9. Martínez-Juárez, A., C. Pecharrromán, J.E. Iglesias, and J.M. Rojo, *Relationship between Activation Energy and Bottleneck Size for Li^+ Ion Conduction in NASICON Materials of Composition $\text{LiMM}'(\text{PO}_4)_3$; $M, M' = \text{Ge, Ti, Sn, Hf}$* . The Journal of Physical Chemistry B, 1998. **102**(2): p. 372-375.
10. Yamamoto, H., M. Tabuchi, T. Takeuchi, H. Kageyama, and O. Nakamura, *Ionic conductivity enhancement in $\text{LiGe}_2(\text{PO}_4)_3$ solid electrolyte*. Journal of power sources, 1997. **68**(2): p. 397-401.
11. Francisco, B.E., C.R. Stoldt, and J.-C. M'Peko, *Lithium-ion trapping from local structural distortions in sodium super ionic conductor (NASICON) electrolytes*. Chemistry of Materials, 2014. **26**(16): p. 4741-4749.
12. Bachman, J.C., S. Muy, A. Grimaud, H.H. Chang, N. Pour, S.F. Lux, O. Paschos, F. Maglia, S. Lupart, P. Lamp, L. Giordano, and Y. Shao-Horn, *Inorganic Solid-State Electrolytes for Lithium Batteries: Mechanisms and Properties Governing Ion Conduction*. Chem Rev, 2016. **116**(1): p. 140-62.
13. Palla, S., G. Ravi, J. Reddy, N.K. Veldurthi, R. Velchuri, G. Prasad, N. Munirathnam, and M. Vithal, *Characterization, conductivity and photocatalytic studies of $\text{AHfM}(\text{PO}_4)_3$ ($A = \text{Na and Ag; M} = \text{Ti and Zr}$) powders synthesized by sol-gel method*. Journal of sol-gel science and technology, 2013. **67**(3): p. 507-518.
14. Shannon, R.t., *Revised effective ionic radii and systematic studies of interatomic distances in halides and chalcogenides*. Acta Crystallographica Section A: Crystal Physics, Diffraction, Theoretical and General Crystallography, 1976. **32**(5): p. 751-767.
15. Catti, M., S. Stramare, and R. Ibberson, *Lithium location in NASICON-type Li^+ conductors by neutron diffraction. I. Triclinic α' - $\text{LiZr}_2(\text{PO}_4)_3$* . Solid State Ionics, 1999. **123**(1): p. 173-180.

16. Catti, M., N. Morgante, and R. Ibberson, *Order–Disorder and Mobility of Li⁺ in the β'- and β-LiZr₂(PO₄)₃ Ionic Conductors: A Neutron Diffraction Study*. Journal of Solid State Chemistry, 2000. **152**(2): p. 340-347.
17. Tran Qui, D. and S. Hamdoune, *Structure of the orthorhombic phase of Li_{1+x}Ti_{2-x}In_xP₃O₁₂, x = 1.08*. Acta Crystallographica Section C: Crystal Structure Communications, 1988. **44**(8): p. 1360-1362.
18. Masquelier, C. and L. Croguennec, *Polyanionic (phosphates, silicates, sulfates) frameworks as electrode materials for rechargeable Li (or Na) batteries*. Chemical reviews, 2013. **113**(8): p. 6552-6591.
19. Xie, H., J.B. Goodenough, and Y. Li, *Li_{1.2}Zr_{1.9}Ca_{0.1}(PO₄)₃, a room-temperature Li-ion solid electrolyte*. Journal of Power Sources, 2011. **196**(18): p. 7760-7762.
20. Masquelier, C., C. Wurm, J. Rodriguez-Carvajal, J. Gaubicher, and L. Nazar, *A powder neutron diffraction investigation of the two rhombohedral NASICON analogues: γ-Na₃Fe₂(PO₄)₃ and Li₃Fe₂(PO₄)₃*. Chemistry of materials, 2000. **12**(2): p. 525-532.
21. Catti, M., A. Comotti, and S. Di Blas, *High-Temperature Lithium Mobility in α-LiZr₂(PO₄)₃ NASICON by Neutron Diffraction*. Chemistry of materials, 2003. **15**(8): p. 1628-1632.
22. Lang, B., B. Ziebarth, and C. Elsässer, *Lithium ion conduction in LiTi₂(PO₄)₃ and related compounds based on the NASICON structure: a first-principles study*. Chemistry of Materials, 2015. **27**(14): p. 5040-5048.
23. Arbi, K., J. Rojo, and J. Sanz, *Lithium mobility in titanium based Nasicon Li_{1+x}Ti_{2-x}Al_x(PO₄)₃ and LiTi_{2-x}Zr_x(PO₄)₃ materials followed by NMR and impedance spectroscopy*. Journal of the European Ceramic Society, 2007. **27**(13): p. 4215-4218.
24. Thangadurai, V., A.K. Shukla, and J. Gopalakrishnan, *New lithium-ion conductors based on the NASICON structure*. Journal of Materials Chemistry, 1999. **9**(3): p. 739-741.
25. Leo, C., G.S. Rao, and B. Chowdari, *Fast ion conduction in the Li-analogues of Nasicon, Li_{1+x}[(Ta_{1-x}Ge_x)Al](PO₄)₃*. Journal of Materials Chemistry, 2002. **12**(6): p. 1848-1853.
26. Hueso, K.B., M. Armand, and T. Rojo, *High temperature sodium batteries: status, challenges and future trends*. Energy & Environmental Science, 2013. **6**(3): p. 734-749.
27. Aono, H., E. Sugimoto, Y. Sadaoka, N. Imanaka, and G.-y. Adachi, *Ionic conductivity and sinterability of lithium titanium phosphate system*. Solid State Ionics, 1990. **40**: p. 38-42.
28. Aono, H., E. Sugimoto, Y. Sadaoka, N. Imanaka, and G.y. Adachi, *Ionic conductivity of solid electrolytes based on lithium titanium phosphate*. Journal of the electrochemical society, 1990. **137**(4): p. 1023-1027.
29. Rao, A.V., V. Veeraiah, A.P. Rao, B.K. Babu, and K.V. Kumar, *Influence of Zr⁴⁺ doping on structural, spectroscopic and conductivity studies of lithium titanium phosphate*. Ceramics International, 2014. **40**(9): p. 13911-13916.
30. De Mestral, F. and R. Drew, *Calcium phosphate glasses and glass-ceramics for medical applications*. Journal of the European Ceramic Society, 1989. **5**(1): p. 47-53.
31. Stephens, P.W., *Phenomenological model of anisotropic peak broadening in powder diffraction*. Journal of Applied Crystallography, 1999. **32**(2): p. 281-289.

32. Coelho, A.A., *Topas-Academic*. A Computer Programme for Rietveld Analysis, 2004.
33. *Zview software*. Scribner Associates, Inc. <http://www.scribner.com>. 2017].
34. Aguesse, F., J.M. López del Amo, V. Roddatis, A. Aguadero, and J.A. Kilner, *Enhancement of the Grain Boundary Conductivity in Ceramic $\text{Li}_{0.34}\text{La}_{0.55}\text{TiO}_3$ Electrolytes in a Moisture-Free Processing Environment*. *Advanced Materials Interfaces*, 2014. **1**(7).
35. Irvine, J.T., D.C. Sinclair, and A.R. West, *Electroceramics: characterization by impedance spectroscopy*. *Advanced Materials*, 1990. **2**(3): p. 132-138.
36. Sukhanov, M., E. Gobechiya, Y.K. Kabalov, and V. Pet'kov, *Synthesis and structure of new framework phosphates $\text{Li}_{1/4}\text{M}_{7/4}(\text{PO}_4)_3$ ($\text{M} = \text{Nb}, \text{Ta}$)*. *Crystallography Reports*, 2008. **53**(6): p. 974-980.
37. Werner, P.-E., L. Eriksson, and M. Westdahl, *TREOR, a semi-exhaustive trial-and-error powder indexing program for all symmetries*. *Journal of Applied Crystallography*, 1985. **18**(5): p. 367-370.
38. Becerra, M.-E., N.-P. Arias, O.-H. Giraldo, F.-E. López-Suárez, M.-J. Illán-Gómez, and A. Bueno-López, *Alumina-supported manganese catalysts for soot combustion prepared by thermal decomposition of KMnO_4* . *Catalysts*, 2012. **2**(3): p. 352-367.
39. Varga, T., A.P. Wilkinson, M.S. Haluska, and E.A. Payzant, *Preparation and thermal expansion of $(\text{M}^{\text{III}}_{0.5}\text{M}^{\text{IV}}_{0.5})\text{P}_2\text{O}_7$ with the cubic ZrP_2O_7 structure*. *Journal of Solid State Chemistry*, 2005. **178**(11): p. 3541-3546.
40. Rodríguez-Carvajal, J., *Recent developments of the program FULLPROF*. Commission on powder diffraction (IUCr). Newsletter, 2001. **26**: p. 12-19.

Chapter 6

Summary

During this thesis, the synthesis and characterisation of new ceramic materials with potential application in the field of Li-ion conductors have been carried out.

Chapter 1 introduced the topic of Li-ion conductors and Li-ion batteries along with a literature review of the most prominent Li conducting solid state electrolyte materials.

Chapter 2 offered a description of the synthesis and characterisation methods used throughout the thesis. Special attention was paid to the buffer pellet technique that virtually allows to use a crucible of the same material than the one that is being synthesised, reducing in this way the possibility of contamination. Then the main core of the chapter is about powder diffraction of X-rays and neutrons. Finally other physical characterisation techniques such as AC impedance spectroscopy are introduced.

Chapter 3 describes the work performed on the parent material LiMgPO_4 with the aim of developing a potential solid state electrolyte for Li-ion batteries. The olivine structure is an interesting target due to the growing importance of the cathode material LiFePO_4 . LiMgPO_4 is isostructural to LiFePO_4 but with all elements in a highly preferred oxidation state that prevents electronic conductivity, thus complying with the first requirement of an electrolyte material. The new materials prepared during this chapter were made with the aim of introducing Li-vacancies in the structure in order to increase the mobility of the Li-ion and therefore increase the ionic conductivity of the material. One of the strategies was the doping with 3+ cations, M^{3+} , to give the series $\text{Li}_{1-x}\text{Mg}_{1-x}\text{M}_x\text{PO}_4$ with Li-vacancies on the Li site. The dopant elements for the aliovalent substitutions were chosen both by computational screening with DFT calculations and by ionic radii similarity. Several series were developed and studied in search for the doping limit and Vegard's law. The Li-ion conductivity was probed in the series with major fraction of substitution.

The most interesting series of chapter 3 was $\text{Li}_{1-x}\text{Mg}_{1-x}\text{In}_x\text{PO}_4$ with a doping limit of $x = 0.17$. For this series full structural characterisation, with chemical analysis and powder neutron and X-ray diffraction, was performed. AC impedance and NMR spectroscopy studies indicated an increase in Li-ion conductivity with doping level, which corresponds to increasing unit cell volumes. The results of this part of the thesis were published in Chemistry of Materials in 2015. The second best series by level of doping was $\text{Li}_{1-x}\text{Mg}_{1-x}\text{Sc}_x\text{PO}_4$ with a doping limit of $x = 0.04$. The Sc-doped series also showed unit cell expansion with doping. The series $\text{Li}_{1-x}\text{Mg}_{1-x}\text{Ga}_x\text{PO}_4$ did not produce phase pure samples but showed a monoclinic distortion of the olivine unit cell that would need further work. These Ga-doped samples showed a decrease in unit cell volume for the olivine phase, which inspired the following attempt in which the idea was to reduce the unit cell volume of an In-doped sample using co-doping with Ga. Samples of this series, with composition $\text{Li}_{0.85-x}(\text{Mg}_{0.85-x}\text{In}_{0.15}\text{Ga}_x)\text{PO}_4$ were pursued, but all the co-doped samples contained secondary phases. Another co-doping attempt was based on the ionic radii similarity of Li and Mg. With the idea of creating gateways between the 1D Li channels, compositions of the series $\text{Li}_{0.85+x}(\text{Mg}_{0.85-x}\text{In}_{0.15}\text{Li}_x)\text{PO}_4$ were attempted. The resulting phase pure samples in the range $x = 0$ to $x = 0.05$ showed a linear trend in lattice parameters that indicate that some modification was achieved. Determining whether this modification was the desired gateway will require further work.

In chapter 3 also Zr-doping was attempted with the series $\text{Li}_{1-2x}\text{Mg}_{1-x}\text{Zr}_x\text{PO}_4$. The study of this system did not produce phase pure samples but revealed the existence of a solid solution between $\text{Mg}_3(\text{PO}_4)_2$ and LiMgPO_4 which inspired the last series of this chapter. Samples of the series $\text{Li}_{1-2x}\text{Mg}_{1+x}\text{PO}_4$ showed a doping limit of $x = 0.1$. The AC impedance measurements on a sample of composition $\text{Li}_{0.8}\text{Mg}_{1.1}\text{PO}_4$ revealed that the bulk Li-ion conductivity for this sample was 2 – 3 orders of magnitude lower than for LiMgPO_4 at 400 °C, with a higher activation energy than the parent material.

Most of the doping attempts in chapter 3 pursued the Li vacancy on the Li site with the dopant on the Mg site. The last one, the Mg-doped series, attempted to place Mg atoms and Li vacancies both on the Li site. The Mg dopant atom on the Li site would block the 1D Li channels, explaining in this way the lower bulk conductivity and higher activation energy than for the parent. Finally, the ranking of

substitutions derived from computational screening was correct with the meaning that the calculated relative doping enthalpies translated into maximum vacancy fraction in the experimental realisation. The mixing entropy term correctly predicted the need for higher temperatures in the synthesis of the doped structures.

Chapter 4 describes the doping of LiFePO_4 with indium. This was tried in search of a high degree of doping and Li-vacancy introduction in the same way as it was achieved for the parent material LiMgPO_4 . In order to accomplish this, a method optimised for the synthesis of In-doped samples of LiFePO_4 was developed. The series $\text{Li}_{1-x}\text{Fe}_{1-x}\text{In}_x\text{PO}_4$ again needed higher temperature than the parent material to be formed, highlighting in this way the role of the mixing entropy in these solid solutions. The doping limit for this series was found at $x = 0.09$. Chemical analysis and neutron and X-ray powder diffraction confirmed the composition and structure. Cathode testing was performed for the parent material and for the sample with $x = 0.04$. The first charge showed for the doped sample an improved flatter plateau with higher potential than for the parent but after that about 80 % of the capacity is lost for cycling. It would be interesting to do more work on this system in order to clarify why the capacity is lost. The microstructure could be studied with electron microscopy. The Li-ion mobility could also be studied by AC impedance or μSR spectroscopies.

During this work on LiFePO_4 it was also found that the impurity phase that appeared beyond the doping limit was isostructural to the phase that appeared for the Mg analogue under the same approach. The structure of this new phase was finally solved during this chapter by application of direct methods to a powder diffraction pattern collected with synchrotron X-ray radiation. In this way two new phases were discovered with compositions $\text{LiFeIn}(\text{PO}_4)_2$ and $\text{LiMgIn}(\text{PO}_4)_2$. These phases belong to the structure type of $\text{Li}_2\text{NiS}_2\text{O}_8$ but could be the first phosphates described in this structure type. These two new phases discovered in this chapter present an excellent opportunity to open a new line of research on this new type of phosphates. Apart from studying these two new phases, other potential new phases to attempt with this structure type could be $\text{Li}_2\text{ZrP}_2\text{O}_8$, $\text{Li}_2\text{TiP}_2\text{O}_8$ or $\text{Li}_2\text{MnP}_2\text{O}_8$ in order to see if they can be made and to study their properties.

Chapter 5 describes the work on Li analogues with the NASICON-type structure. It is structured in three blocks of content. The first block shows the work on compositions related to $\text{LiTaAl}(\text{PO}_4)_3$. Exploratory synthesis with different levels of P excess, in the sample of nominal composition $\text{Li}_{0.875}\text{Ta}_{1.062}\text{Al}_{0.938}\text{P}_3\text{O}_{12}$ made with $\sim 5.7\%$ Li excess, revealed that the series followed Vegard's law with the new impurity $\text{Ta}_{0.5}\text{Al}_{0.5}\text{P}_2\text{O}_7$ appearing in the plateau. The samples were investigated with X-ray diffraction showing that fits using a triclinic cell in $P\bar{1}$, rather than the rhombohedral cell in $R\bar{3}c$, were superior. A method for the densification of this material was developed and relative densities above 90 % were achieved when sintering the powder alone and when sintering the powder with the binder Butvar. AC impedance spectroscopy on the sintered materials showed Li-ion bulk conductivity and activation energy values similar to the total conductivity values published for $\text{LiTaAl}(\text{PO}_4)_3$.

The second block of chapter 5 describes attempts of Ca-doping in two nominal compositions derived again from $\text{LiTaAl}(\text{PO}_4)_3$. The exploratory work followed similar lines than for the undoped samples. A range of P excess was tried in a sample of nominal composition $\text{Li}_{1.55}\text{Ta}_{0.78}\text{Ca}_{0.11}\text{Al}_{1.11}\text{P}_3\text{O}_{12}$, but none of the samples resulted phase pure. Further exploratory work searching for Al-deficient samples produced a phase pure sample of nominal composition $\text{Li}_{0.734}\text{Ta}_{1.187}\text{Ca}_{0.108}\text{Al}_{0.705}\text{P}_3\text{O}_{12}$ made with 5% Li excess and 20% P excess. This sample was studied in more detail with synchrotron X-ray radiation showing anisotropic peak broadening. The densification method developed for this composition achieved relative densities above 90 %. AC impedance spectroscopy showed a bulk Li-ion conductivity of $1.5 \times 10^{-13} \text{ S cm}^{-1}$ at 25 °C with $E_a \approx 0.8 \text{ eV}$.

The third block of chapter 5 describes how the phase diagram Li-Ta-Mg-Ga-P-O has been investigated in search for new Li-ion analogues with the NASICON-type structure. 48 samples were prepared with the experimental approach of using 5 % of Li excess and 20 % of P excess. Four compositions resulted in phase pure materials with close lattice parameters among them. However, by studying the lattice parameters of all samples, it was shown that much larger variation in lattice parameters is accessible in this synthetic field. This means that other compositions could be isolated by changing the experimental approach. AC impedance measurements showed that the bulk ionic conductivity of these samples were

intermediate with respect to the previous both systems studied in the same chapter.

One of the major conclusions from the NASICON analogues work is that the systematic addition of the elements Li-P-O to a nominal NASICON composition produces lattice parameters variations that follow Vegard's law, which would deserve further study. Densification procedures have been developed for the two systems derived from $\text{LiTaAl}(\text{PO}_4)_3$ to allow measurement of their conductivities. Finally the phase diagram of Li-Ta-Mg-Ga-P-O has been explored producing phase pure samples with the NASICON-type structure and showing evidence that other compositions in this synthetic field are accessible. Interesting future work on these systems would try to isolate phase pure samples at both ends of the cell volume variations found for each system. The development of a digestion method for these compositions in order to perform ICP-OES analysis would be very useful as well. Finally Li-ion conductivity assessment of the new samples would complete the study.

Synthesis of solid state electrolytes with high Li-ion conductivity that are stable against the electrodes of the battery on cycling remain a challenge. The methodologies developed for the Li-ion technology will have the pioneering value of being translated into technologies based on other ions such as Na.

The research on solid state Li-ion conductors in the form of advanced ceramics will continue and breakthrough materials will be discovered. This thesis show how many modifications can be made by choosing one starting composition such as LiMgPO_4 . On the other hand, this thesis also shows how common is to discover new phases when new modifications are being pursued. There are a huge amount of new phases and derivatives still to be discovered and some of them will be the key to new developments. The high complexity of some equilibria make of this work a task which outcome is difficult to predict. Future technologies will be fed by these and other discoveries.

This page is intentionally left blank